

# Lawrence Berkeley National Laboratory

## LBL Publications

### Title

Micro-Scale Mass-Transfer Variations during Electrodeposition

### Permalink

<https://escholarship.org/uc/item/2qf3t2zv>

### Author

Sutija, D P, Ph.D. Thesis

### Publication Date

1991-08-01

### Copyright Information

This work is made available under the terms of a Creative Commons Attribution License, available at <https://creativecommons.org/licenses/by/4.0/>



# Lawrence Berkeley Laboratory

UNIVERSITY OF CALIFORNIA

## Materials & Chemical Sciences Division

### Micro-Scale Mass-Transfer Variations during Electrodeposition

D.P. Sutija  
(Ph.D. Thesis)

August 1991



LOAN COPY 1  
Circulates 1  
for 4 weeks 1  
Bldg. 50 Library.  
Copy 2

LBL-30825



## **DISCLAIMER**

This document was prepared as an account of work sponsored by the United States Government. While this document is believed to contain correct information, neither the United States Government nor any agency thereof, nor the Regents of the University of California, nor any of their employees, makes any warranty, express or implied, or assumes any legal responsibility for the accuracy, completeness, or usefulness of any information, apparatus, product, or process disclosed, or represents that its use would not infringe privately owned rights. Reference herein to any specific commercial product, process, or service by its trade name, trademark, manufacturer, or otherwise, does not necessarily constitute or imply its endorsement, recommendation, or favoring by the United States Government or any agency thereof, or the Regents of the University of California. The views and opinions of authors expressed herein do not necessarily state or reflect those of the United States Government or any agency thereof or the Regents of the University of California.

Micro-scale Mass-Transfer Variations  
During Electrodeposition

Davor P. Sutija  
Ph. D. Thesis

Department of Chemical Engineering  
University of California

and

Material Sciences Division  
Lawrence Berkeley Laboratory  
University of California  
Berkeley, CA 94720

August, 1991

This work was supported by the Assistant Secretary for  
Conservation and Renewable Energy, Office of Transportation Technologies,  
Electric/Hybrid Propulsion Division of the U.S. Department of Energy  
under Contract No. DE-AC03-76SF00098.

# Micro-scale Mass-Transfer Enhancement at Electrode Surfaces

by

Davor Peter Sutija

## Abstract

Results of two studies on micro-scale mass-transfer enhancement are reported:

1. Profiled cross-sections of striated zinc surfaces deposited in laminar channel flow were analyzed with fast-fourier transforms (FFT) to determine preferred striation wavelengths. Striation frequency (20 - 70 per cm.) increases with current density until a minimum separation between striae of 150  $\mu\text{m}$  is reached. Beyond this point, independent of substrate used, striae meld together and form a relatively smooth, nodular deposit.

Substrates equipped with artificial micron-sized protrusions result in significantly different macro-morphology in zinc deposits. Micro-patterned electrodes (MPE) with hemispherical protrusions 5  $\mu\text{m}$  in diameter yield thin zinc striae at current densities that ordinarily produce random nodular deposits. MPEs with artificial hemi-cylinders, 2.5  $\mu\text{m}$  in height and spaced 250  $\mu\text{m}$  apart, form striae with a period which matches the spacing of the micron-sized ridges.

The emergence of striations is ascribed to the combination of instantaneous three-dimensional nucleation and fast, concentration-dependent kinetics. Striae appear, in general, in the linear overpotential regime; consequently, the zinc reaction is sensitive to small changes in mass-transport and ohmic drop in the vicinity of growing nodules.

2. A novel, corrosion-resistant micromosaic electrode was fabricated on a silicon wafer. Measurements of mass-transport enhancement to a vertical micromosaic electrode caused by parallel bubble streams rising inside of the diffusion boundary-layer demonstrated the presence of two co-temporal enhancement mechanisms: surface-renewal increases the limiting current within five bubble diameters of the rising column, while bubble-induced laminar flows cause weaker enhancement over a much broader swath.

The enhancement caused by bubble curtains is predicted accurately by linear superposition of single-column enhancements. Two columns of smaller H<sub>2</sub> bubbles generated at the same volumetric rate as a single column of larger bubbles cause higher peak and far-field enhancements. The effect is ascribed to the higher frequency of the smaller bubbles, and the larger total drag exerted on the surrounding fluid.

Signature: \_\_\_\_\_

*Charles W. Tobias*

Committee Chairman

Til min kjaereste, Unni

## Acknowledgements

I will always remember fondly the weekly group meetings in building 62: Linzer torte, Earl Grey, and "rat biscuits." It was an experience which bonded us as a group, filled us with wisdom, and a place where we learned what it meant to be scientists. I am grateful to Professor Charles W. Tobias for many insights, some given, others surmised. The unspoken values that he stands for, honesty, elegance, and frugality, taught me more than any formal lesson.

It was my good fortune to have had Dr. Rolf H. Muller as my co-advisor. There was always time in his busy schedule for our meetings, which solved many of my stumbling blocks and often delved into the difficult details of experimental work.

While outside of my thesis research, I would also like to acknowledge the generous guidance of Prof. J. M. Prausnitz. His interest in the hermeneutics of science was the starting point for many challenging discussions, and a collaboration that I was honored to participate in.

The entire staff of the Microlab, Department of Electrical Engineering, U.C. Berkeley was always available for consultation, professional help, and timely repairs. The design and fabrication of micro-patterned and micro-mosaic electrodes was only possible with their efforts, and the availability of this unique facility. I feel privileged to have had the opportunity to work there.

The help of Henry Chan, Electronics Shop, College of Chemistry, in writing software for the upgraded data acquisition system in use with the micromosaic experiments is gratefully acknowledged. Stuardo Robles and

Sang Yi both did experimental work on zinc striations as undergraduate research assistants. The preparation of photographs for the thesis involved extraordinary help from Marilyn Sam and the entire LBL photolab staff. Many thanks.

The Tobias/Muller group has always been a source of assistance, especially Ken Jordan, whose help with programming was invaluable, and Laura McVay, for aid with the SEM. I wish Gerd Matzen the same enjoyment with this project that I experienced ... for seven years.

The figures in the thesis were expertly prepared by my wife, Unni Byrkjeland, whose help and love has been my inspiration.

The author was supported as a doctoral student by the Fannie and John Hertz Foundation. This work was supported by the Assistant Secretary for Conservation and Renewable Energy, Office of Transportation Technologies, Electric/ Hybrid Propulsion Division of the U. S. Department of Energy under Contract No. DE-AC03-76SF00098.

## TABLE OF CONTENTS

Acknowledgements .....	iii
Table of Contents .....	v
Abstract .....	1
Part I: The Emergence of Striated Zinc Electrodeposits	
1. Introduction and Literature Review .....	1
2. Experimental Procedures .....	26
3. Striation Frequency on Flat and Micro-Profiled Electrodes .....	41
4. Theoretical Analysis of Striation Emergence .....	89
Part II: Mass-Transport by Rising Bubble Curtains	
5. Introduction and Literature Review .....	119
6. Experimental Procedures .....	133
7. Mass-transfer to Vertical Electrodes .....	152
Nomenclature .....	213
References .....	215
Appendix A - Micro-profiled Electrode Fabrication .....	234
Appendix B - Creation of the New Micro-mosaic Electrode .....	242
Appendix C - Impurity Analysis of Zinc Solutions .....	273
Appendix D - Computer Programs for Statistical Analysis .....	274
Appendix E - Program for Bubble Data Acquisition .....	296



## Part I - The Formation of Striated Zinc Electrodeposits

### Chapter 1 - Introduction and Literature Review

#### 1.1. *Introduction and Scope of Present Work*

Storage battery technology has a distinguished history; its pedigreed past is associated with the names of Volta, Faraday, Galvani, and Edison, as well as the perhaps less-widely known Bunsen or Plante'. Yet the conversion of chemical to electrical energy and its recovery in rechargeable cells still contains unresolved problems, the result of an apparent failure to capitalize on promising ideas. Consider the case of zinc-halide rechargeables, whose behavior in one particular aspect is the object of the present inquiry.

When H. H. Dow, founder of the eponymous chemical company, presented details of his new discovery to the Inaugural meeting of the American Electrochemical Society in 1902, he found to his chagrin that the zinc-bromide storage battery had already been patented more than a decade earlier [4,4a,4b]. Even at the turn of the century, the concept of rechargeable batteries using zinc in combination with an acidic halide solution seemed worth pursuing. To this day, the full development of such systems has remained an elusive goal.

Dow's interlocutors were already aware of the system's limitations. While one member of the academy worried about the need for a separator to keep apart the zinc and the bromine, Dow himself pointed out the primary obstacle: the zinc electrode refused to behave during the charging process! "The zinc will deposit in crystals," lamented the inventor, "and the crystals will cross the cell and short-circuit it ...." Such "crystals", examined in much greater detail in subsequent decades [13], have been

named dendrites in recognition of their tendency to form branched tree-like structures. Dendrites have a deleterious effect on battery performance, since they pierce through almost any conceivable barrier, growing across the cell and providing an alternative pathway for the electric current. In this way, the charging process is prematurely ended, since the current is no longer passing through solution, and therefore, no more zinc is plated out. Furthermore, during discharge dendrites dissolve unevenly and often disintegrate, littering the cell bottom with metal particles which permanently lower battery capacity. Their prevention is necessary to achieve maximum battery cycle life.

Part of this task consists in understanding the fundamental causes underlying the morphologies which precede the formation of dendrites. In most modern zinc-halide rechargeable battery systems, forced convection is used to increase the rate of mass-transfer to the zinc electrode surface [7]. As a result of the complex behavior of zinc during deposition, the direction of flow is actually imprinted into the resulting deposit; ridges and valleys aligned in the direction of flow appear in the first minutes of deposition. Such features, named striations by workers in our laboratory, form an apparently periodic structure [17,22-24]. After substantial charging, striation ridges become the preferred location for the emergence of dendrites, and are the direct precursors for this detrimental morphology [17]. Our goal is to understand the mechanism for the formation of zinc striae in acidic solutions.

While the appearance of striated electrodeposits occurs in several metals at high current densities where diffusion-limited mass-transport variations lead to changes in deposit thickness, zinc is unique since zinc striae appear at low fractions of limiting current (typically less than 10 percent) [17]. In fact, zinc striae occur only up to a certain current density, approximately  $40 \text{ mA/cm}^2$  in channel flow, above which a nodular, yet smoother deposit emerges. This is doubly perplexing, since roughness usually increases with current density, and furthermore, in a "kinetically-limited regime" such periodic morphological patterns seem difficult to explain. The wide disparity in deposit

thickness perpendicular to the direction of flow cannot be ascribed to portions of the electrode being depleted of the reactant. Rather, a complicated interaction must exist between the first stages of electrocrystallization (when sub-micron three-dimensional growth centers emerge) and the subsequent morphology. The largest growth centers seem to grow fastest (all nodules in this group are fairly uniform in size). At some height, they begin to interact with the flow field, and the transport to the surface may vary slightly. They begin to elongate in the direction of flow and form a 'string of pearls' downstream, as nodules in their wake tend to also be favored for growth. This 'string' smooths itself out until it becomes one of a number of parallel strands in a corrugated landscape [22-27,30]. Figure 1.1 shows striae obtained by Jaksic and Faltemier in both rotating disk and channel-flow cells, under conditions of both laminar and turbulent flow [17].

By measuring surface profiles and quantifying deposit characteristics, we are able to correlate electrode behavior with process parameters such as the galvanostatically-applied current. Until now, most evaluations of zinc deposit morphology were qualitative in nature; our study is aimed at determining quantitative changes in striation frequency. By using a variety of substrates, and a range of current densities, we are able to distinguish between the effects of nucleation (at short times) from those of deposit growth rate (at longer times). To show how small protrusions (equal in size and density to randomly occurring zinc growth centers) can drastically alter the resulting morphology, we designed and fabricated micropatterned electrodes with hemispherical features with a radius of  $2.5\ \mu\text{m}$  [32]. By determining the spacing and orientation of these artificial nodules *ab initio*, we are able to further separate nucleation-induced morphological changes from those that arise from changes in applied total current. Artificial striae were also produced using the same technique, and their effect was studied.

The next section reviews the state-of-the-art in zinc-halide batteries, while the rest of the introduction provides a foundation for the phenomenological theory of striation formation given in Chapter 4.

## 1.2. Zinc-Halide Rechargeable Batteries

Acidic zinc-halide batteries are attractive because of their low material costs, non-toxicity, fast kinetics, and large cell voltages (2.32 V for  $\text{ZnCl}_2$  and 1.85 V for  $\text{ZnBr}_2$  batteries) [7]. These systems operate at room temperature, a natural advantage over sodium-sulfur cells, and have a moderately high energy density. Current interest in rechargeables has focused on two separate applications: 1) Stationery devices for utility load-leveling and 2) as power sources for electric vehicles. The requirements for these two systems differ substantially. Vehicle batteries involve stringent weight limitations and size considerations, combined with higher peak discharge-rate demands and the need to limit leakage. The likelihood is that the first commercial-scale use of electric vehicles will be in fleets of delivery vans for use in cities. Typical urban van use consists of short driving distances (under 120 miles/day) with numerous brief idle off-times. This duty cycle is inefficient for internal combustion engines, where ignition and start-up consume energy and add wear, but is not a hindrance for electric vehicles. The lower maintenance costs of electric vehicles will offset some of their disadvantages, such as less power for acceleration. On the other hand, load-leveling applications need high energy efficiency batteries and require units which deliver long cycle lifetimes with deep discharge. The primary criterion determining acceptance for this application is a low unit cost, which zinc systems promise (currently \$ 100 – 200 per KWHr of capacity) [3,6].

In the United States, at least, the two applications generated separate research programs, which engendered fragmentation of the total research effort. The need for protecting proprietary information also hindered joint development efforts, since a large

portion of DOE-funded research was done by the private sector (i.e. Exxon, Gould, Johnson Controls, Energy Research Corp., etc.) [3,6,8]. Further specialization occurred as one company worked on a given halide system (either bromide or chloride) to the exclusion of the other. This was necessitated, in part, by the different techniques envisioned in storing the pure halogen reactant as shown in the schematic diagrams of the two battery systems (Fig. 1.2).

Both the  $\text{ZnCl}_2$  and the  $\text{ZnBr}_2$  batteries involve a flow system. The chloride battery design is potentially simpler, however, since the chloride is stored in a separate chilled compartment as a hydrate, and requires no separator. The bromide battery design incorporates a quaternary ammonium compound (such as N-ethyl N-methyl morpholinium bromide or MEMBr) which complexes with the bromine to form an immiscible liquid phase. The  $\text{ZnBr}_2$  battery requires a separator to prevent the bromine from being transported to the zinc electrode and reacting spontaneously.

The main electrochemical limitations in addition to mechanical problems have tended to be low energy efficiency (approx. 60%) and limited cycle life. Exxon's research project (dating from 1979-1987, when Exxon sold the technology to Johnson Controls) was typical of U.S. efforts [1,6]. They were funded by DOE and Ford to test  $\text{ZnBr}_2$  batteries. The best result achieved was 1400 shallow cycles, but using more realistic "quasi-random" cycling, batteries failed before 500 cycles were achieved. Furthermore, packs of 8 and 78 cells, which are necessary in practical applications, were limited to 400 and 100 cycles respectively as of 1983 [1,2]. By 1987, a pack of 8 1/2-KWhr cells (600 cm<sup>2</sup> area) had attained 640 cycles, with a specific energy of 80 - 85 Wh/kg and a peak power in excess of 150 Wh/kg [1]. The main failure modes were a severe warping of the carbon-plastic electrodes (used for cost-effective extrudability), and the presence of an oily residue caused by electrode degradation. Mechanical problems such as pump motor burnouts also contributed to short cycle life. A severe kinetic penalty was also paid by using extrudable materials, since the exchange current ( $i_0$ ) on

the carbon electrodes was low, ranging from 0.1 - 0.3 mA/cm<sup>2</sup>. More recent work by the Energy Research Corporation using Gould technology and by Johnson Controls, in cooperation with Sandia Labs, did not improve things markedly [8]. The Energy Research Corp. reported that their stack tests gave energy efficiencies of 60% for a total of 300 cycles with 30-cell packs, with an 872 cm<sup>2</sup> area each.

The zinc-chloride effort, with research led by Energy Development Assoc., was shelved even earlier, though a pilot plant near New York City was designed and tested in 1986 [3]. No new interest has been shown in this country after that date.

The Japanese are still researching these promising battery systems, however [5,10,11]. They have coordinated work on competing battery systems for load-leveling applications, with utilities directly involved in the planning and development stages. The Japanese effort, dubbed the "Moonlight Project," is organized by the Agency of Industrial Science and Technology (AIST), in collaboration with MITI and NEDO, the agency responsible for developing new energy resources [11]. Their final goal is the development of a 1 MW / 8 MWh electric-energy storage pilot plant having an AC-AC energy efficiency of 70% and a service life of 1500 cycles. The total budget over twelve years, at current 1990 exchange rates, exceeds \$ 100 million. The three most prominent candidates for this application were determined to be the two zinc-halide systems, as well as the high-temperature sodium-sulfur battery.

Pilot plant tests at Tatsumi, using lead-acid batteries and 60kW-class modules operated not only as a load-leveler, but also as a high-quality power source for automatic frequency control and voltage regulation of the Kansai power grid. Over the next three years, the lead-acid modules will be replaced with advanced battery designs including the two zinc-halide systems [11]. MEIDENSHA is leading ZnBr<sub>2</sub> development [5], and has tested single cells with DC-DC energy efficiencies (the same efficiencies quoted in the description U.S. efforts) of 80% for 500 cycles. As in the Exxon system, electrode warpage was the eventual cause of battery failure. The

Furukawa Electric Co. did concurrent work on a 60kW-class  $\text{ZnCl}_2$  system [10], also producing single cells with 80% energy efficiency, with both 15kW-class and 60kW-class stacks performing at an initial energy efficiency of over 75%. The reaction of chlorine lowered the electrolyte pH, however, and the pitch carbon electrodes were no longer chemically stable. As carbon corrosion occurred, the electrolyte changed color and  $\text{CO}_2$  was evolved. The high initial efficiency of these cells was due in part to the use of a novel ruthenium-oxide catalyst at the chloride electrode, promoting its voltage efficiency considerably. The Japanese consortium hopes to reach its goal of a 1MW storage facility by the end of 1991, although a recent report states that the choice of battery will be by a sodium-sulfur cell stack [12]. The U.S. has no such plans. *Caveat Lector.*

### 1.3. *Striated Zinc Electrodeposits*

The discovery of striations in metal deposition or dissolution is neither very recent nor particularly uncommon. Observations of striated markings have been made in copper, nickel, iron, as well as zinc electrodes. Levich [40] uses the striated surface of a corroding metal to demonstrate the distribution of streamlines near the surface of a rotating disk. Rogers and Taylor [54,55], and later Hill and Rogers [43,44] studied spirals that emerged during the electrodeposition of copper on a rotating disk. Their results were at relatively high currents, at a point where the current-voltage curve was very steep. What distinguishes zinc striae, as noted above, is their occurrence at low currents (less than 10% of the limiting value) and disappearance at higher currents.

Work in our laboratory on zinc striae began in 1976 [22-27]. Jaksic observed striae in both rotating-disk and channel-flow cells. He attributed the spiral markings to counter-rotating vortices which he likened to Taylor and Taylor-Goertler vortices found in other flow geometries. Although the evidence was circumstantial at best, his hypothesis had some plausibility, as it explained the remarkable parallelness and apparent periodicity of the phenomena. Jaksic continued his investigations by

determining the effect of additives on the emergence of striae. The result was perhaps somewhat disappointing: striae persisted under all conditions below a threshold current density. The addition of cationic, anionic, and non-ionic Zonyl fluoro-surfactants had the predicted effect of smoothing the striae (the additives act as leveling agents), but they did not affect the emergence or number density of the striae. The number density of striae was also shown to be independent of rotation speed in the RDE experiments, and the upper current density limit was determined to be  $80 \text{ mA/cm}^2$  for  $\text{ZnCl}_2$  electrolytes and  $15 \text{ mA/cm}^2$  for  $\text{ZnSO}_4$  electrolytes.

Collaborating with Jaksic, Faltemier [17] extended the experimental analysis to include observations under turbulent flow in channel electrodes. He also conclusively showed that striae were scale-independent; increasing the electrode length and width by a factor often did not change the observed morphology. The average pitch remained constant, and striae covered the entire electrode, appearing almost instantaneously everywhere after an induction time. A close examination of Faltemier's photographic records [Fig. 4.16 in 17] shows that the striae appear to abruptly end, then reappear downstream. The average distance between neighboring striae remains constant, but only a few striations seem to extend continuously from the leading to the trailing edge. This is not often the case in the smaller electrodes, but the length scale over which the striae merged and reappeared in the large cell may make it unlikely to occur on a small electrode.

Faltemier studied the effect of deposition parameters on striation frequency. He determined that the Reynold's number has, counterintuitively, no effect on the striation spacing. This directly contradicts the Jaksic hypothesis concerning Taylor-Goertler vortices since the strength of the flow would change the vortex amplitude and therefore the striation spacing. This hypothesis had already been weakened since one would have to suppose two counter-rotating vortices between each striation pair, and the spacing between such pairs is often too narrow to accommodate circular vortices. Faltemier did



notice one important change in spacing as one went from laminar to turbulent flow in flow-channel experiments, however. In laminar flow, the spacing was not affected by the amount deposited (referred to as loading), while in turbulent flow, a longer deposition time lowered the frequency to a new stable value. At short times, frequency was equivalent in both laminar and turbulent flow, but at long times, laminar flow gave a higher frequency of striae. This may have been caused by striation melding, which may occur more quickly in turbulent flow. Rotating disk studies, all done in the laminar region, gave no difference in striation density with an increase in  $Re$  from 200 - 3000 [17].

In a master's project, Tsuda [34] examined the effect of inorganic impurities on striation formation. He found that the impurities plate out selectively on the striae, and may change striae spacing somewhat. Under all conditions, however, including the use of ultra-pure zinc solutions, striae eventually appeared. Only by pulse-plating, which changes nucleation density, were striae eliminated. Nucleation number density was identified as an important parameter in determining striae frequency.

Tsuda [34] also measured the angle formed by striae on the surface of an RDE, and found that it conformed to Cochran and Von Karman's analytic solutions for the flow lines at the surface of a disk [39,41,42]. These logarithmic spirals were precisely the correct angle, and Tsuda's work rebutted a less accurate measurement of dissolution spiral angles by Johnson and Turner [45]. Those authors had maintained that the spirals were Archimedean, and although the difference is small, the consonance between Tsuda's and Cochran's results shows that dissolution spirals and striae follow the flow lines close to the disk surface.

Much of Tsuda, Jaksic, and Faltemier's work was duplicated by Yee and Jorne [58,59]. Yee and Jorne worked in the same two flow systems, but also extended the experiments to the rotating hemisphere. There, they measured spiral angles and also found them to conform to the theoretically predicted value for the flow-lines at the

surface. In a recent paper, these authors maintain that this may allow sub-micron visualization of flow lines. This does not seem to follow; there is no proof that using striae for flow visualization will work in other geometries.

Since nucleation was shown by Tsuda [34] to change dramatically with increasing current density, the next project by Anderson focused on measuring the number density of micron-sized zinc growth centers as a function of overpotential [14]. Anderson determined that surface preparation differences contributed significantly to the nucleation density differences he observed. There was a correlation between overpotential and nucleation density, but it was not a dependable one. On the average, nodule density increased by 200-1000 nodules per  $\text{cm}^2$  per mV. What made the experimental task more difficult was the heterogeneity of some surfaces, notably glassy carbon. Glassy carbon had regions of high nucleation density bordering on regions with very few nuclei.

Anderson reported that Union Carbide HOPG graphite was more active than either platinum or Gould synthetic graphite. This resulted in higher nodule densities and smaller super-polarizations on the HOPG surface. He also showed that this nodule density stayed roughly constant as a function of loading over a range from 50 to 450 milli-Coulombs/ $\text{cm}^2$ . After 50 milli-Coulombs has been deposited (equivalent to a zinc thickness of 235 Angstroms averaged over the geometric area), all nucleation and nodule emergence is already over [14]. This is in consonance with the work of McBreen [51,52] on glassy carbon, where the authors determined from current transients that the zinc nucleation happened instantaneously, rather than progressively as in the case of silver deposition.

McVay [30,31] was the first to successfully observe the emergence of striae *in situ*. She combined a long-range microscope objective on a traveling stage with a video camera/cassette-recorder to record the growth of zinc nodules. The resolution achieved was about 1  $\mu\text{m}$  [31]. McVay showed that nodules coalesce and elongate both

downstream and upstream, though predominantly in the former direction [30]. The elongation is not uniform, and there is a strong preference for upstream and downstream nodules to join, even if there is some misalignment. Subsequently, forming striae fill in the space between elongating nodules afterwards.

An important observation was that striae appeared in the absence of any significant gas evolution, with a current efficiency often approaching 100%. This rebuts arguments by Hsie and Selman [56,57] that striae form as a result of bubble wakes. Such claims are also found in the literature on zinc electrowinning [80], and must be discarded, since they are not based on direct observation. In Selman's case, use of a rotating cylinder meant that evolved gas accumulated on the cathode during zinc deposition. This does not imply that striae must have emerged as a direct consequence. Jaksic [16] and more recently the present author, also photographed striae bypassing attached bubbles. The striae are present around the bubble, as well as in its wake. At low pH, where bubble evolution is heaviest, experiments often yield no striae since attached bubbles prevent convection at the surface.

Jorne has measured the change in striation frequency as a function of applied current density, and reported a non-linear dependence in both the rotating disk and channel flow systems. The striation frequency increases with the 0.4 power of the applied current; their results are shown in Fig 1.3 [58]. Selman's group also made such measurements, and found a linear dependence instead. Faltemier's results, although sparse, correspond more closely with a linear dependence. One difference is the assumption that at very low currents, the frequency will go to zero, which is tacitly used by Jorne. In the case of channel flow, the collected data were taken over a relatively narrow current density range, so that discrimination between these two hypotheses is difficult if one excludes a data point at the origin. At low currents, the background hydrogen evolution dominates and the striae become very thick and "mesa"-shaped rather than sinusoidal. In such cases, both the actual zinc current and the striation

spacing are not easily determined.

#### 1.4. *Kinetics and Mechanisms of the $Zn^{+2}/Zn$ Electrode Reaction*

Other authors have studied zinc deposition from acid-halide electrolytes in detail, notably the research groups of Landau, Cahan, and Selman. Two joint projects headed by Landau [47,48], and funded by the EPRI (Electric Power Research Institute) focused on modeling of dendrite emergence and determination of kinetic parameters for the zinc deposition reaction. Orthogonal Collocation methods were used to determine the current and potential distribution on an electrode in a flow cell, while stability analysis of small perturbations was used to determine the conditions under which dendrites emerge. A pseudo-stable region was identified where the interface was not absolutely stable, but over the time scale of battery charging, dendrites may be avoided.

Since zinc is a rather reversible metal, the determination of the exchange current density at high zinc ion concentrations requires the passage of substantial charge in a short period of time, and is complicated by a roughening of the electrode surface after three-dimensional (3D) nucleation. The active surface area of growing nodules is difficult to determine, and the existence of a nucleation overpotential (a resistance to the formation of nuclei in the first place), only further complicates the analysis. As a result of these factors, the estimates for  $i_0$  at 1M zinc ion concentration literally range from well under  $1\text{mA}/\text{cm}^2$  to about  $250\text{ mA}/\text{cm}^2$ . Fig. 1.4 from [48] summarizes the literature values of the exchange current density.

Potential step experiments by Jorne [74,75] and Anderson [14] obtained values of the zinc exchange current in acidic electrolytes between  $1\text{-}2\text{ mA}/\text{cm}^2$ , which are consistent with work by Hauser on zinc dissolution [21], but considerably lower than other reported measurements [48, 49]. Yamashita reported that in a solution that was oxygen-free, he obtained an exchange-current density well below  $1\text{mA}/\text{cm}^2$ , when measuring small currents near the zinc equilibrium potential. Both Hauser's work and

Yamashita's does not pertain to the case where 3D zinc growth centers appear, which may have a significantly higher activity than the exchange-current density for 2D deposition or dissolution indicates.

Ordinarily, a potential-step experiment, such as Anderson's, would be the ideal method for determining reaction kinetics. Cyclic voltammetry is inferior since the surface properties depend on its history before passing through the overpotentials of interest. It cannot be counted on to yield quantitatively accurate  $i_0$  values. In this case, however, potential step experiments may also be inappropriate, since the entire surface is not uniformly active. Deposition is primarily confined to 3D nodules which grow as deposition proceeds. Only a small portion of the electrode surface is covered by growth centers and the activity of these zinc clusters exceeds the averaged result obtained from the overall kinetics.

Nucleation processes also change the real surface area as a function of deposition time. While at short times the active area is smaller than the geometric area, at some time the roughness amplitude is large enough so that the real area is substantially larger than the apparent geometric value. It has been reported that the real surface of a rough zinc deposit is 3-5 times greater than the geometric value. This means that the local current density becomes much lower as deposition proceeds [50].

A change in applied overpotential may drastically change the nucleation characteristics, since nucleation usually occurs at imperfections on the surface and the energy required for nucleation varies among different surface sites. Thus, with an increased overpotential, more sites become available.

McBreen [51] reported that on glassy carbon electrodes there exists a threshold overpotential of 40 mV past the zinc equilibrium potential before any zinc nucleates. Anderson [14] obtained similar results on other substrates, including on polycrystalline zinc. Only background currents due to hydrogen evolution could be detected until the overpotential was greater than 40 mV. Such a nucleation overpotential may be partially

masked on Tafel plots, since the background hydrogen current obscures accurate zinc current measurements near the zinc equilibrium potential. The assumptions in such plots, 1) that there is only one Faradaic process occurring, 2) that the only overpotential is a kinetic or surface one, and 3) that the kinetics follow a simple Butler-Volmer model, may all have to be reassessed in the case of zinc.

The complex interaction between applied potential, deposition time, and real surface area complicates any macroscopic kinetic analysis. It obscures the actual exchange current for the zinc reaction on an active nodule, which is the parameter necessary for determining the variation in overpotential occurring during the striation formation process.

Two alternatives to determine the proper  $i_0$  on active surfaces exist. One is to extrapolate the exchange current from data at low concentrations such as the work of Hurlen et al. [65,71-73], where the  $i_0$  is three orders of magnitude smaller, the other is to measure the growth rate of a single, uniformly active surface such as the tip of a dendrite. The second method, used by Landau [48], yields an exchange current density of over 250 mA/cm<sup>2</sup>. It may overestimate the real value, however, since the ohmic drop is changing as the dendrite grows toward the counter electrode. Extrapolation, and recent data by Jorne [47,48,49], instead give a value for  $i_0$  of approximately 100mA/cm<sup>2</sup>, which is still much higher than the values of Anderson [14]. In our theoretical work in Chapter 4, we will use this last value as the best approximation available for the true value of  $i_0$ .

### 1.5. *Nucleation Theory, Stability Theory, and Ohmic Advantage*

The electrodeposition of metals proceeds by the adsorption and discharge of ions at an electrode surface. The energy of the surface is spatially heterogeneous, so that through the process of surface diffusion, the discharged metal atom moves to a position of minimum energy. The edges of partially completed atomic layers, or the

existence of crystalline defects provide a suitable location for the incorporation of the discharged atom into the underlying lattice. When such locations are non-existent, or when the discharged atoms are sufficiently energetic, new stable structures are formed through the process of nucleation. Nucleation can be of three basic types: 1) atom-scale nucleation leading to 2-dimensional (2D) film growth, 2) 3-dimensional (3D) growth of screw dislocations, and most importantly for our work, 3) the nucleation of 3D clusters which grow into sub-microscopic hemispherical nodules. These are shown schematically in Fig. 1.5.

The study of nucleation began in the 1930's with the work of Volmer [111], Kaischew and Stranski [108], but was greatly enhanced in the 1950's with the development of potentiostatic experimentation by Fleischmann. A review of this research area is given in Fleischmann and Thirsk [104], with more recent work described in Abyaneh and Fleischmann [95]. The first two types of nucleation and crystal growth were easier to analyze, and dominate the growth of metal at very low overpotentials. Budevski [100] studied a dislocation-free silver single-crystal and observed current changes as 2-D monolayers formed and then grew over the entire exposed electrode area. In a potentiostatic experiment, every time a layer was completed the current would fall, as part of the overpotential was used to overcome the energy barrier necessary to form a new atomic layer. From the theoretical side, Avrami proposed the first nucleation model in 1946 [96]. His work was not confined to the case of 2-D nucleation, but it proved difficult to study more complicated 3-D nucleation experimentally. Furthermore, the currents predicted from the analysis of the 2D nucleation models significantly underestimated the real currents obtained during electrodeposition.

In 1949, Burton, Cabrera and Frank [101] found that screw dislocations (3D dislocations that are self-perpetuating, shown in Fig. 1.5b) may account for the high deposition rates often reported. In fact, experimental photos of pyramidal structures with clear crystallographic orientations seemed to corroborate this theory. Fleischmann

and Thirsk, however, proposed that 3D nucleation may also occur at surface inclusions, as illustrated in Fig. 1.5c. Once the size of the inclusion is large enough, it will become stable from the perspective of thermodynamics. That is, the tendency for the inclusion of high-curvature to dissolve will be more than compensated by the predicted rate at which it will incorporate new atoms. Their model assumed that the number of such inclusions on a surface was fixed, but that the probability of nucleation at each site was a function of overpotential. More recent models modify this position by claiming that the number of sites available was, in fact, a function of potential as well, and that at smaller overpotentials the sites were completely unavailable. The difference between these two models can be determined by studying the characteristics of nucleation at long times, when the low energy sites are completely nucleated, but higher-energy sites are available. The first theory predicts that new nucleation occurs at such long times, while the second does not. It is not necessary to believe that either theory is correct for all metal deposition reactions, since both quasi-instantaneous and progressive nucleation may occur under different conditions. Fletcher's experiments are the most noteworthy in distinguishing between the competing nucleation models.

The growth of these nucleated sites has also been studied. Fletcher [105, 106], in the 1970's used micro-electrodes to confine experimentation to a single growing nodule, and thus deconvolute the current signal caused by a single nodule from increases due to progressive nucleation. He confirmed that the nuclei emerge at atomic imperfections on the crystal surface where phase transformation requires marginally less energy. These grow at a diffusion limited rate by hemispherical diffusion, until the boundary layers of the individual nuclei begin to overlap. Through growth, these nuclei become microscopic nodules which continue to grow and limit further nucleation in their vicinity. At some point in time, the area of these nodules becomes large enough that they no longer grow at a limiting rate, further nucleation stops, and the active growth centers continue to grow, albeit at a slower rate.



Milchev [109-110] proposed a model that accounts for the enhanced growth of nodules after the initial diffusion-controlled growth period has passed. At longer times, when the height of the nodule exceeds a critical value, the nodule becomes sufficiently ohmically favored that it continues to grow at a faster rate than the surrounding surface.

Work has also been done on determining how deposits form into periodic structures. A great deal of work has been done, especially by Mullins and Sekerka [92,93], on the melt-crystal interface, which is partially analogous to electrodeposition (since a new solid phase is formed in response to a thermodynamic driving force). Instabilities occur at such interfaces, resulting in a sinusoidally-shaped boundary. Mullins-Sekerka instability analysis showed that certain wavelengths grew faster than others, and that the deposit eventually was composed only of the fastest growing single wavelength.

Landau [48] used Mullins-Sekerka analysis to examine the growth of dendrites during electrodeposition. Landau calculated that at sufficiently long times, dendrites will emerge under most deposition conditions. At moderate deposition rates, however, a pseudo-stable region exists. Within this region, the formation time for dendrites is so long that they do not appear.

While stability analysis may eventually be helpful in determining the long-time stable striation wavelength, a proper stabilizing, restoring force has not been identified. The origin of striations is also a separate issue, and must have something to do with the nature of flow in the wake of zinc growth centers. Thus, analysis of the characteristics of flow around 3D obstacles is pertinent to determining the causes for the emergence of striations.

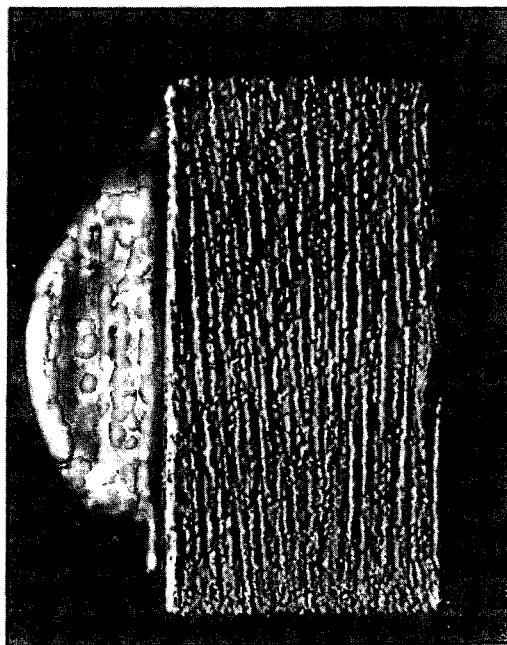
### 1.6. *Flow Around 3-D Obstacles*

The flow pattern around a 3-dimensional obstacle in a channel flow-cell cannot be calculated either analytically or in the general case, even numerically. The computational requirements are still prohibitive, especially in a situation where the surface is changing shape continuously, as in electrochemical metal deposition. When a protrusion is large enough, however, it is reasonable to assume that flow detachment occurs, and that transport in the wake of such a feature will be different from that of the surrounding flat surface. Since computations are not yet feasible, it is necessary to determine the mass-transport enhancement by empirical methods.

In our laboratory, Carlson [15] looked at deposition around 1mm-sized obstacles and found localized enhancement that stretched downstream for a distance equal to several obstacle diameters. Enhancement also occurred to the sides and in front of the protrusion. Fig. 1.6 shows the results for copper deposition near the limiting current [15]. Hanson [20] and Fischl [18,19] did similar experiments for smaller slabs placed normal to the flow. These obstacles were both larger and smaller than the diffusion boundary layer thickness. For obstructions of the smallest size, hemi-cylinders 256  $\mu\text{m}$  in height, enhancements of up to 50% were obtained. The enhancement Fischl measured was an overall value, so no information on localization of the enhancement was obtained. It can be argued that the effect was confined to a region near the features, since the addition of more obstacles kept increasing the total enhancement. Previous work by McLarnon using interferometry also determined that objects that were larger than the calculated diffusion boundary layer caused a distortion of the concentration field, and a narrowing of the boundary layer, for a distance downstream that was much greater than the diameter of the obstacle [29]. Focke [112], doing electrodeposition in a low-aspect ratio channel saw areas of enhancement at a distance downstream from the obstacle, as well as in the immediate wake.

Recent computational work in fluid mechanics agrees with this experimental work. One paper [113] shows Carlson-type localized detachment and vortex-formation, while another [114] shows Focke-like downstream eddies in the case of a moving wall with an attached obstacle.

While none of the experimental work used features that were as small as the nodules which precede striation formation, computer simulations show that the size of the nodule may be very small and still cause flow separation. In addition to the size, the shape of the obstacle determines whether separation occurs. In general, 2D models or axisymmetric models tend to show even greater amounts of wake recirculation. Flow around the nodule tends to stabilize the flow, so that direct comparison between flow around a bump and over a hemi-cylinder is inappropriate. Nevertheless, the elongation of zinc nodules in the direction of flow, seen by both Jaksic and McVay, suggests that mass-transport must be somehow facilitated in this region. By comparison to macroscopic experiments, it is quite likely that recirculation is the reason.



a. Flow channel electrode

RE 5300, 45 MIN



b. Rotating disc electrode

400 RPM, 40 MIN

XBB 784-11239F

 $1 \text{ M ZNCL}_2$ , PH 2.4,  $30 \text{ MA/CM}^2$ 

Figure 1.1. Striated Zinc Electrodeposits [17].

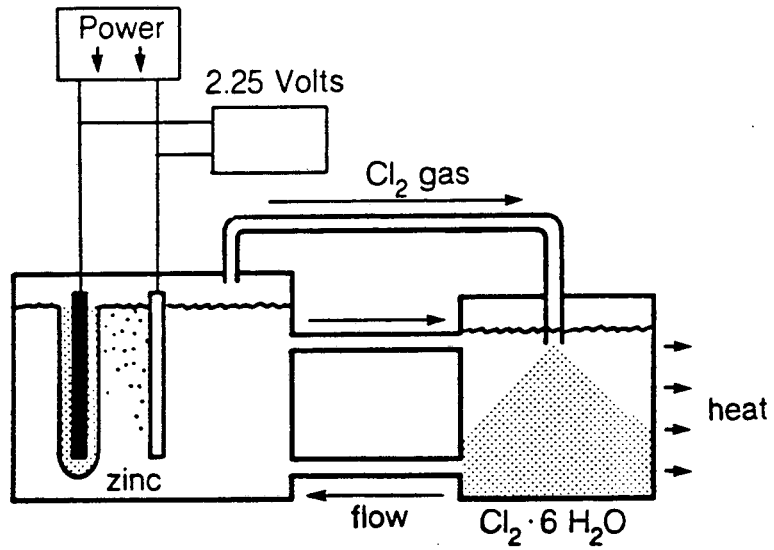
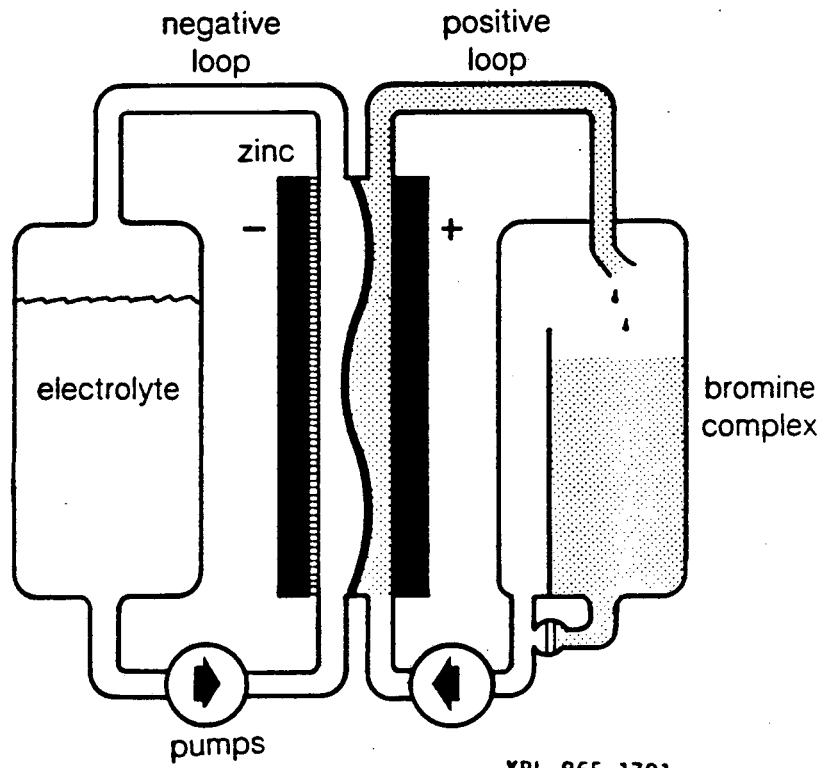


Figure 1.2A: Zinc/Chlorine Rechargeable Battery [7,30]



XBL 865-1791

Figure 1.2B: Zinc/Bromine Rechargeable Battery [7,30]

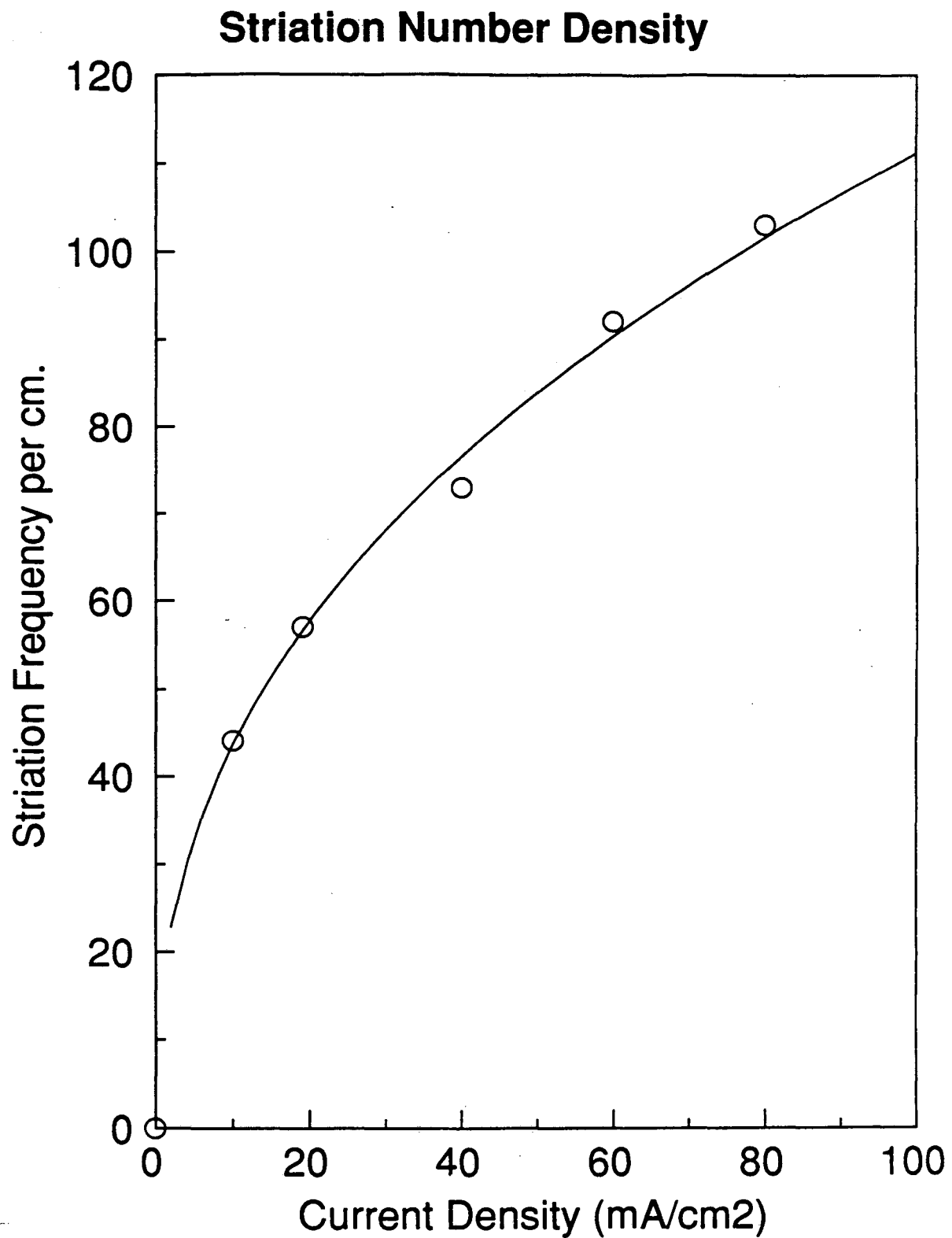
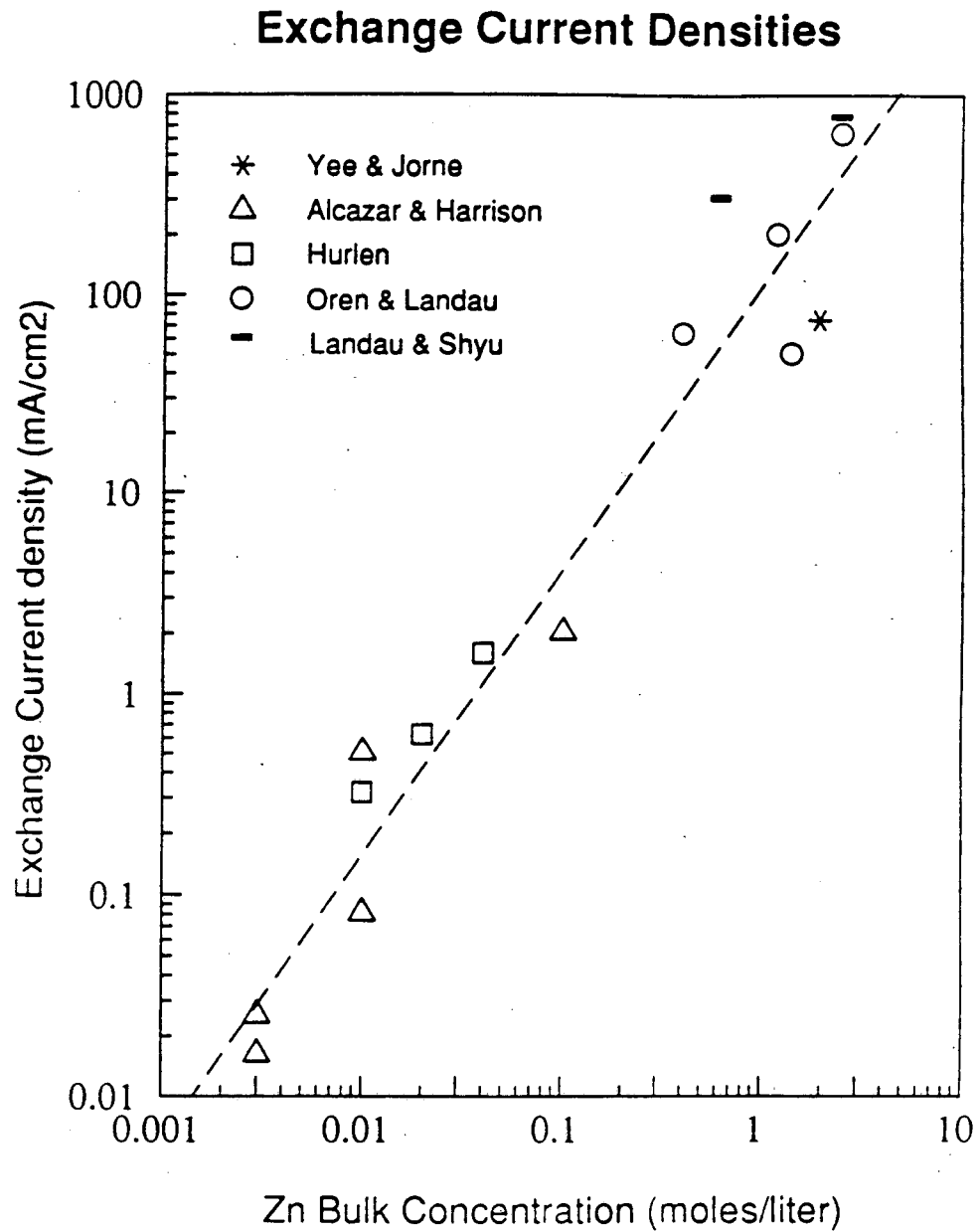


Fig. 1.3 Striation number density versus current density on a rotating-disc electrode, from data by Yee and Jorne [58].



XBL 915-1107

Fig. 1.4 Zinc deposition exchange current densities as a function of bulk concentration (moles/liter). Based on Landau et al. [48].

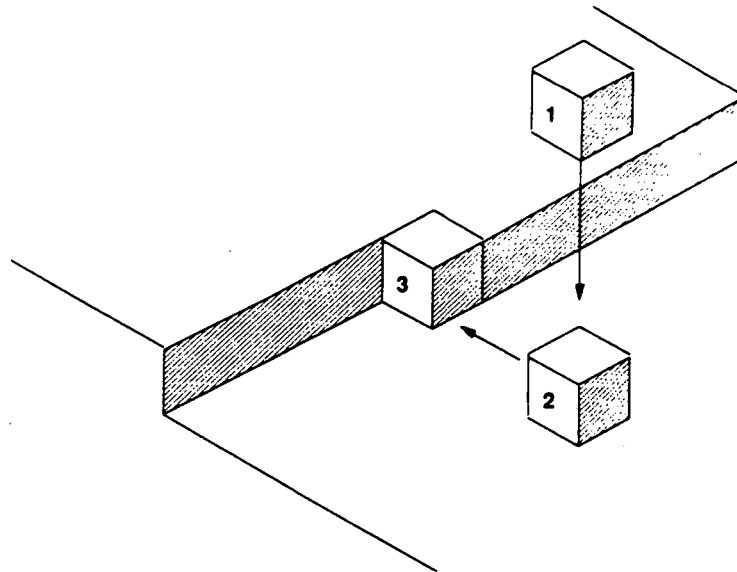


Fig. 1.5a. Classic model of 2-dimensional electrodeposition by 1) ad-atom adsorption, 2) discharge, and 3) surface diffusion to a low-energy kink site.

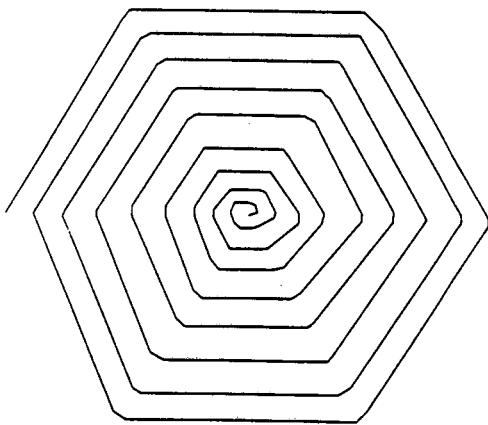


Fig. 1.5b. Screw dislocation

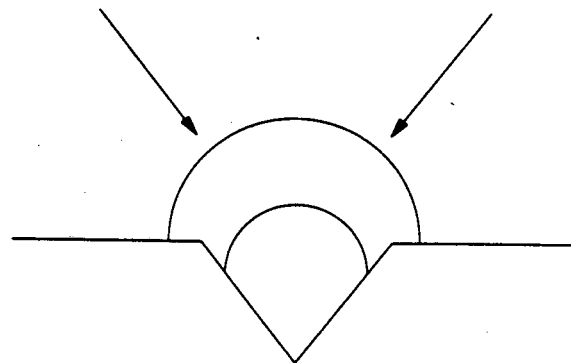


Fig. 1.5c. 3-D nucleation



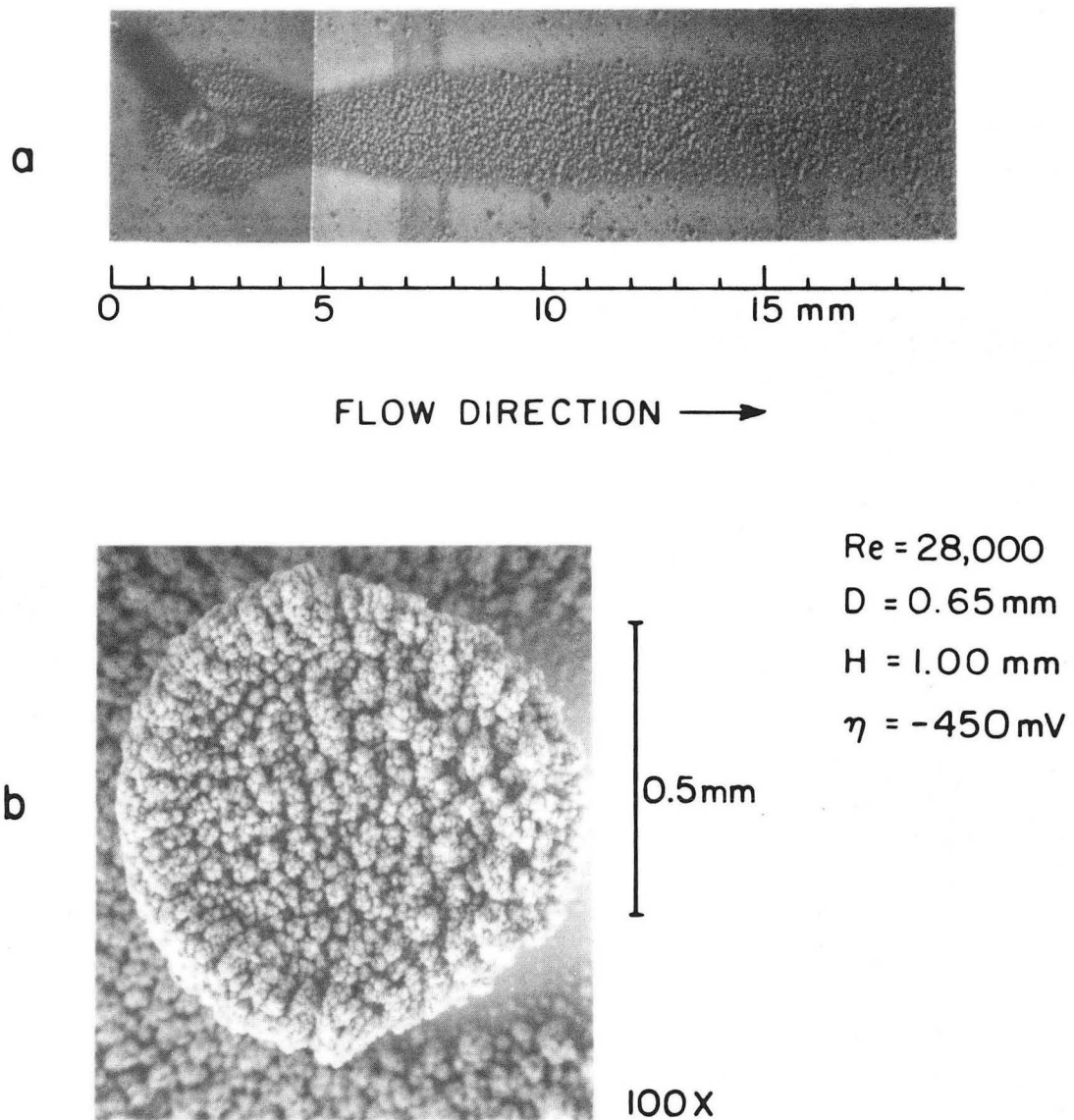


Figure 1.6. Copper deposition in turbulent channel flow around a 1 mm cylindrical protrusion [15]. The enhancement region extends 15 diameters downstream.

XBB 740-6952A

## Chapter 2 - Experimental Procedures

### 2.1 *Experimental Apparatus*

#### 2.1.1 Electrolysis Flow cell

The deposition of zinc was performed galvanostatically in a channel flow cell (shown in Fig. 2.1), under laminar conditions and over a range of current densities and flow velocities. The channel has a 10 mm x 6 mm rectangular cross-section, and contains a removable planar cathode (with a geometric area of 0.45 - 0.50 cm<sup>2</sup> and two sacrificial zinc anodes of equivalent area, set in the walls perpendicular to the cathode. Figure 2.2 from [17] shows the electrode arrangement in greater detail. A long entrance length (equivalent to 50 channel hydraulic diameters) ensures fully-developed flow at the electrode surface. The cell is made of polypropylene and transparent polymethyl methacrylate, through which the cathode may be observed and videotaped through a microscopy set-up developed by McVay [30]. The flow rate was measured by a rotameter which was calibrated using distilled water. The calibration chart, Fig. 2.3, shows a linear relationship between rotameter reading and flow rate for practically the entire measurable range (which corresponds to  $Re = 200 - 5000$  for the flow cell used in this work). The experiments were conducted at  $Re = 2000$ . The tank at the left of Fig. 2.1 was used for storage of excess electrolyte, and had a capacity of 20 liters, though only 4 - 6 liters of solution was usually used. Drifts in flow rate were corrected manually, and were usually not significant.

The current was controlled by a PAR 173 potentiostat, and the total charge passed was measured by a PAR 175 Digital coulometer or manually by multiplying the applied current by the time of the experiment. Typical runs used a current density of 5-60 mA/cm<sup>2</sup> with 20 Coulombs total charge passed.

### 2.1.2 Electrodes

The cathodes used in this study were of two types. The first variety consisted of rectangular synthetic graphite and platinum electrodes attached to a brass core by silver epoxy, and encased in non-conductive epoxy resin. The electrode assembly was then heat-cured and machined to the desired cylindrical diameter of 2 cm. The active area of these electrodes ranged from 0.45 - 0.50 cm<sup>2</sup>.

The second electrode type, used for the studies in Chapter 4, was the micro-profiled electrode (MPE). The geometric area was also 0.5 cm<sup>2</sup>, but superimposed on the optically-smooth substrate are artificial hemispherical growth centers with a radius of 2.5 μm or artificial striae, with a diameter of 10 - 20 μm. The substrate was a polished copper square, which was subsequently covered with an evaporated gold layer of 1.0 μm thickness, then patterned photolithographically. The patterned layer defined the growth center and striae geometry, which was created by pulse-plating gold in the exposed areas. Scanning electron micrographs of the resulting substrate are given in Fig. 2.4 and 2.5. The design of the MPE is described in the author's M.S. thesis [33], while the details of fabrication are given in Appendix A. The process allows the creation of 28 separate electrodes simultaneously from a single patterned square, with the individual electrodes diced by spark erosion machining. Appendix A gives a detailed fabrication sequence. The electrode holders were made of Teflon, 2 cm in diameter, with a brass core with a rectangular orifice for the replaceable MPE substrate.

The anodes were pieces of zinc with an exposed area of 0.36 cm<sup>2</sup> each. Electrical contact was made by a silver wire to the back of the anode. The wire and all sides of the anode, except the front face, were insulated from the electrolyte.

### 2.1.3 Electrolyte Solutions

All solutions used in this study were prepared from analytical grade chemicals. Experiments were performed in a variety of zinc sulfate, zinc chloride, and zinc bromide electrolytes, either unsupported or supported with potassium sulfate, potassium chloride, or potassium bromide. Some runs on acidified zinc chloride solutions were also performed. The chemicals used were:

- (1) Baker Analyzed Zinc Bromide
- (2) Mallinckrodt AR-grade Zinc Chloride
- (3) Baker Analyzed Zinc Sulfate 7-Hydrate
- (4) Fisher Scientific Potassium Bromide
- (5) Fisher Scientific Potassium Chloride
- (6) Baker Analyzed Potassium Sulfate
- (7) Baker Dilut-it Analytical Hydrochloric Acid

## 2.2 *Details of Operation*

### 2.2.1 Electrolyte Preparation

Zinc halide solutions were prepared in four-liter batches, with a 1M zinc ion concentration. Purification by cementation with zinc dust eliminates trace metal impurities such as Fe, Cu, Mn, and Co, which may catalyze hydrogen evolution and lower the current efficiency of the zinc deposition reaction. The dust is added to the solution (10 grams/liter), then the solution is heated to 90 ° C while being stirred by a magnetic stirrer. The solution is kept heated for four hours, then cooled and filtered. Residual cloudiness because of zincate ion formation is eliminated by refiltration.

Appendix C gives a chemical analysis of a typical 1M zinc bromide solution by atomic absorption analysis.

### 2.2.2 Electrode Polishing

All substrates were polished using 600 grit sandpaper, then 6 $\mu\text{m}$  diamond paste, and finally 1  $\mu\text{m}$  diamond paste on a nylon cloth using Buehler Automet Lapping Oil. Samples were cleaned between each polishing step in an ultrasonic bath of Liqui-nox detergent and distilled water; they were then rinsed with acetone, methanol, and finally double-rinsed in distilled water before the next polishing step. This procedure ensures that particles are not carried from one polishing step to another.

The polishing was done on a stationary nylon cloth and care was taken so that the electrode would not wobble during polishing. The most important criterion for successful polishing was determined to be the curvature of the substrate rather than small micro-roughness. This is especially true if spectral analysis of the profile is used. Striation heights are approximately 30-80  $\mu\text{m}$ : a bowing as little as one tenth of this amount in the original polished electrode is sufficient to introduce spurious peaks into the measured power spectrum of a striated zinc deposit. The maximum allowed bowing was 2.0  $\mu\text{m}$ , while the roughness ( $R_a$ ) of the surface usually ranged from 0.15 to 0.30  $\mu\text{m}$ . Figure 2.6 shows a typical polished surface, whose profile was scanned on the Taylor-Hobson profilometer described in the following section. Note the gap between the platinum substrate and the epoxy resin. While it is significant in size, the area used for spectral measurements was confined to the middle 4mm of the platinum surface, so that this gap would not affect the measurements. Over this region, the bowing is substantially smaller, usually less than 1.0  $\mu\text{m}$ , or a slope of one part per twenty thousand. Table 2.1 gives actual roughness and bowing measurements for acceptable electrode surfaces; those outside of specifications were re-polished with a succession of sandpaper grades, then with the afore-mentioned polishing procedure.

### 2.2.3 Experimental Procedure

After polishing, the electrodes were degreased with successive rinses in acetone, methanol and doubly-distilled water, then stored in a sealed dessicator until use. The electrodes were placed in the flow cell, and sealed with Teflon tape to prevent leaks. The PAR 173 potentiostat was set to the desired current and the timed experiment begun until 20 coulombs were passed (some experiments were also done at different loadings ranging from 5 coulombs to 75 coulombs charge passed).

After the experiment, the electrode was removed, rinsed with distilled water, and again stored in a dessicator until profiled and photographed.

### 2.2.4 Macro-photography

Macro-photographs of the substrate were taken either in the metallographic laboratory at Lawrence Berkeley Labs or in the microfabrication facility in the electrical engineering department at U.C. Berkeley. In either case, the magnification used was about 40x, and the lighting was placed at an acute angle to the surface to highlight the corrugations. Polaroid Type 45 film gave the most satisfactory results. It has moderate contrast and exposure times of less than 30 seconds. Lower-speed polaroid films require longer exposure times, which give poorer quality photographs because of excessive blurriness caused by stage vibration.

### 2.2.5 Profilometry

After photographing the substrate, nine separate profiles of the electrode cross-section were taken on Taylor-Hobson Talysurf 10 digital profilometer, shown in Fig. 2.7. Fig. 2.8 shows the electrode holder and a closeup of how a scan was taken (Note: In this work, the profiles were taken in the direction perpendicular to the flow direction, not as shown in the photograph). The profilometer is interfaced to an IBM XT compatible computer, and a software program provided by the vendor allows for automatic data

acquisition. The program is called TS10, and allows the user to set up the proper speed and range for the scan. The density of digital data points can be adjusted by changing the 'cutoff' length. Within one cutoff, there are 230 data points. The profilometer uses the first cutoff to level the substrate, so that the first 230 data points are lost to further analysis, but the collected profile is generally level across the scan length. A number of statistical tests can be done with this software, such as measuring the peak-to-peak or RMS roughness of a zinc deposit surface profile. Skewness, kurtosis, and other parameters were obtained but were not found to be useful.

The deposit profiles were taken 1 mm apart starting one millimeter from the leading edge of the platinum, carbon or gold active area. All nine profiles were then stored in the computer, re-leveled, and translated to a standard ASCII file by DATPRN, a Basic program listed in Appendix D written by Mr. Ken Jordan, a graduate coworker. The ASCII files contained the central portion of each scan (the middle 3.7 mm of the electrode), and after processing by two other BASIC routines written by the author, the data was imported into a LOTUS spreadsheet.

Batch programs ran each profile through the Fortran spectral power density estimation routines and other statistical tests (autocorrelation, and maximum entropy method). The batch programs, Lotus macros, and Fortran subroutines are all listed in Appendix D. The Fortran subroutines were taken from **Numerical Recipes** [118], and were adapted for our use by the author and an undergraduate research assistant, Sang Yi. Plotting of the data was done with LOTUS Picgraph and FREELANCE.

Table 2.1: Electrode Polishing Sequence	
STEP	Polishing Technique
1	#1 Sandpaper and Buehler Lapping Oil
2	#0 Sandpaper and Buehler Lapping Oil
3	6 $\mu\text{m}$ Diamond Paste
4	1 $\mu\text{m}$ Diamond Paste
Between Steps	De-greasing w/ Acetone, and Rinsing w/ Distilled H <sub>2</sub> O

Table 2.2: Flatness Measurements of Polished Electrodes				
Electrode	Front		Back	
	R <sub>a</sub> ( $\mu\text{m}$ )	R <sub>T</sub> ( $\mu\text{m}$ )	R <sub>A</sub> ( $\mu\text{m}$ )	R <sub>T</sub> ( $\mu\text{m}$ )
1	0.12	1.5	0.20	1.7
2	0.35	1.9	0.23	1.7
3 *	0.15	2.4	0.48	2.9
4	0.49	1.4	0.13	1.6
5	0.19	2.3	0.28	1.7
6	0.42	2.5	0.20	1.3
7	0.50	1.5	0.26	2.0
8	0.15	1.5	0.20	1.4

\* Electrode #3 was rejected as being inadequately polished and was redone. The results shown above were for one typical batch of eight Pt electrodes. In general, the carbon electrodes were easier to polish, and had R<sub>A</sub> and R<sub>T</sub> values that were half as large after polishing.

$\bar{R}_A$  (Average RMS Roughness) = 0.25  $\mu\text{m}$ , sdev. = 0.11 $\mu\text{m}$ ; tolerance = 0.4  $\mu\text{m}$ .

$\bar{R}_T$  (Maximum Vertical Dev.) = 1.71  $\mu\text{m}$  (Tolerance = 2.0  $\mu\text{m}$ ); Slope  $\approx 1$   $\mu\text{m}$  per mm.



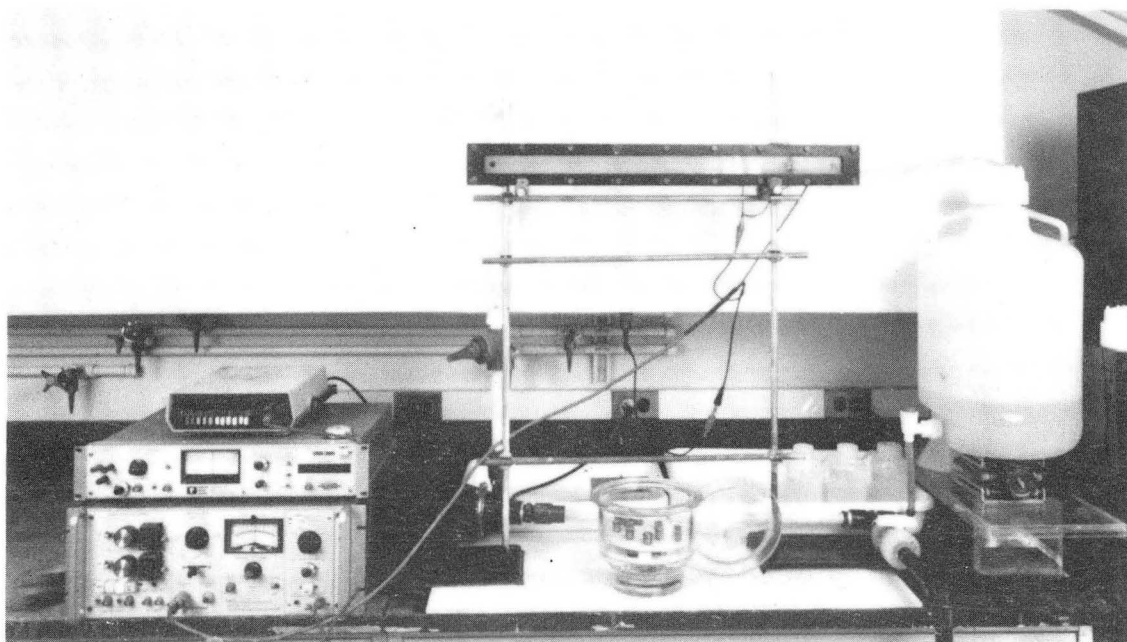


Figure 2.1. Zinc deposition flow cell. The channel has a 50-diameter entrance length, and a clear lucite sidewall for in-situ observation of striation emergence and growth. CBB 884-4398A

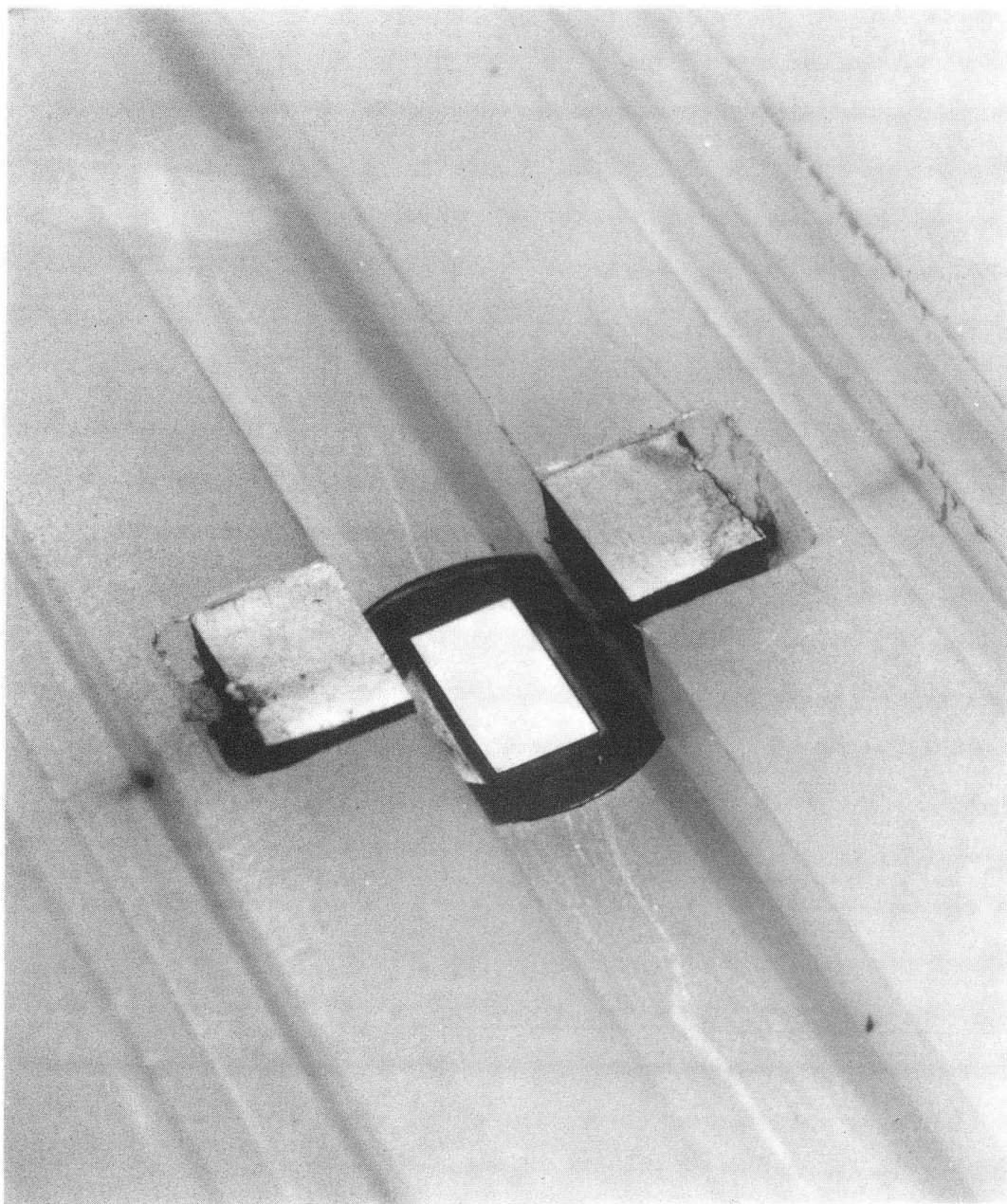


Figure 2.2. Electrode placement. The cathode, shown in the bottom of the channel, is a 2 cm wide replaceable plug. The sacrificial zinc anodes, placed in the walls perpendicular to the cathode, maintain the solution concentration uniform during deposition. CBB 820 - 10747A

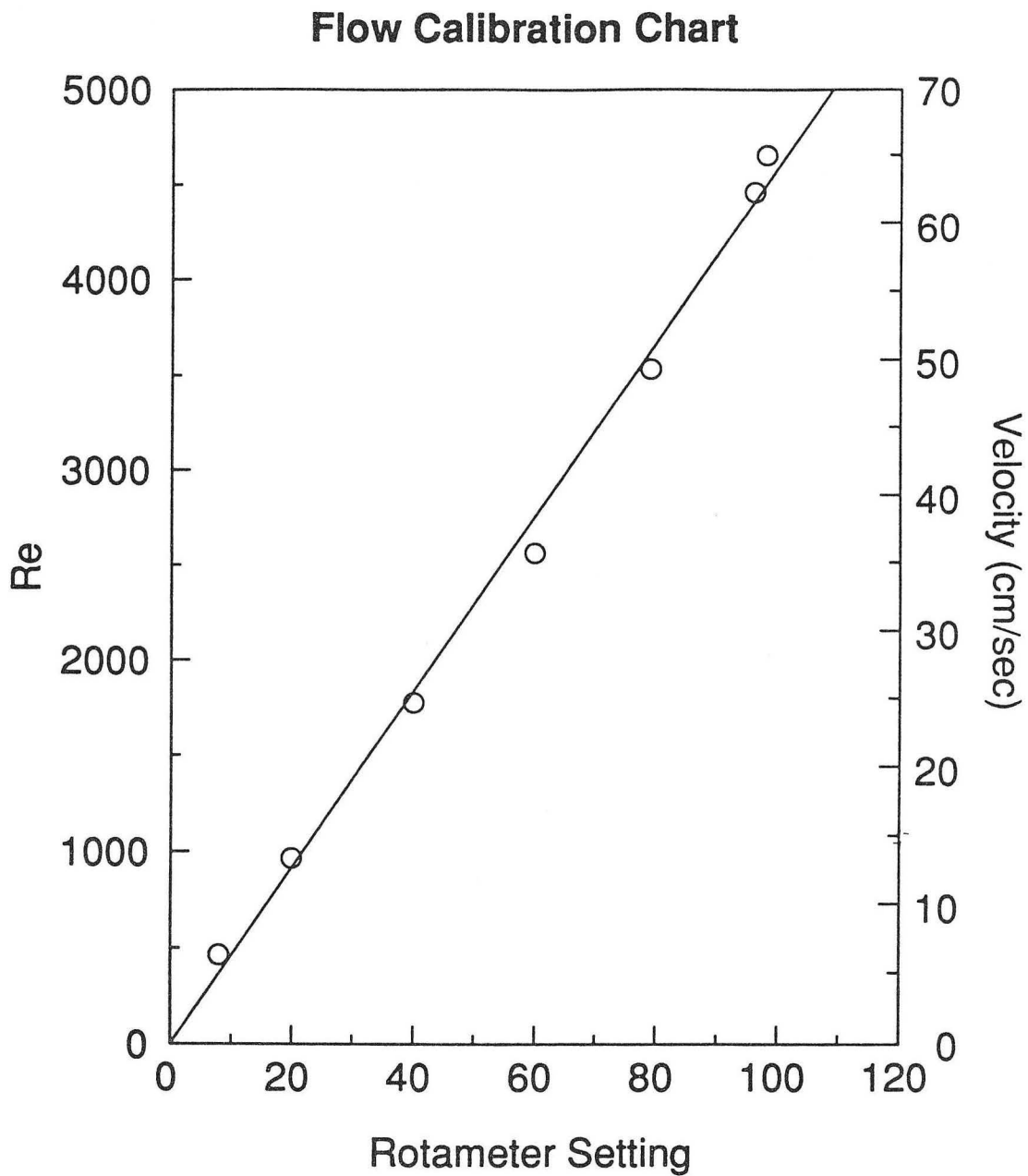


Figure 2.3 Calibration chart for the Gilmont rotameter used in the zinc deposition flow cell. A stainless-steel pellet was used as a float, and a linear relationship between rotameter setting and flowrate was measured over the entire practical range ( $Re = 500 - 4500$ ).

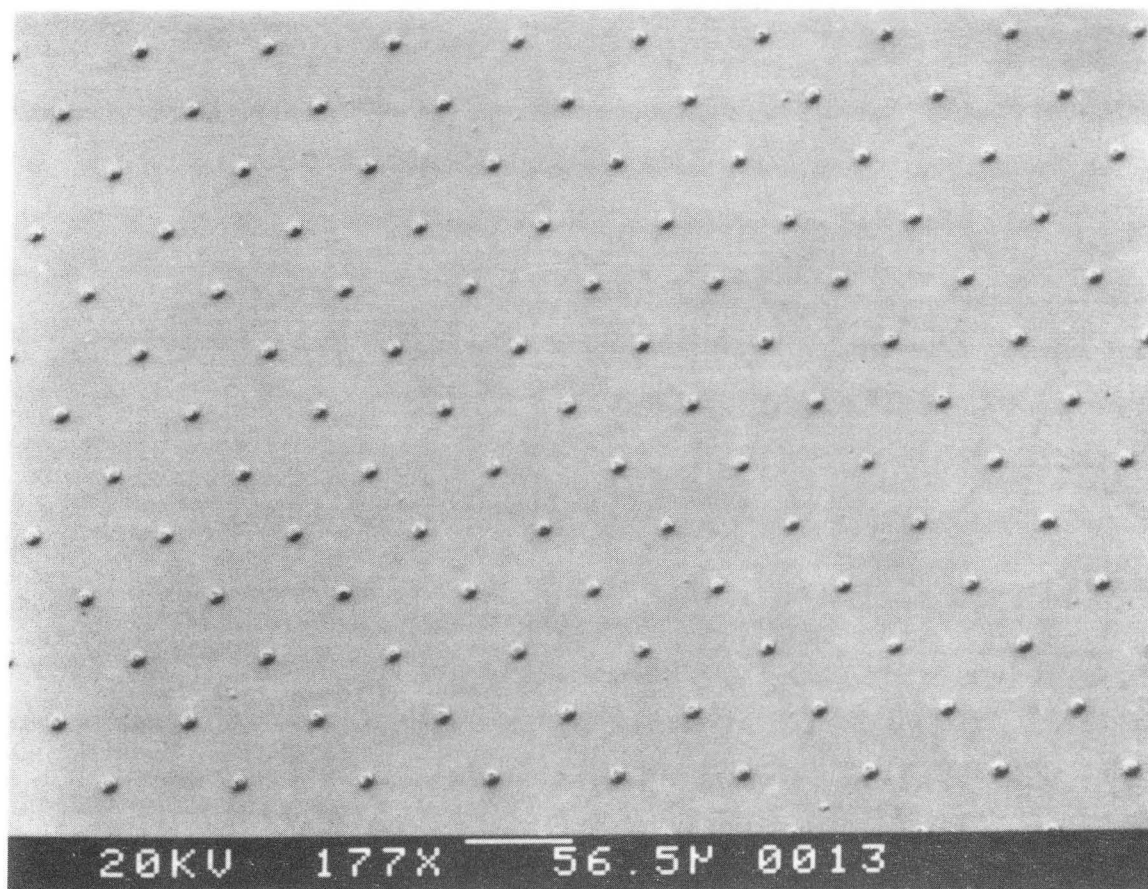


Figure 2.4. A scanning-electron micrograph of a micro-patterned electrode substrate with a triangular array of 5  $\mu\text{m}$  hemispherical protrusions. The MPE is made by pulse-plating gold through a mask onto a gold-plated copper substrate.

XBB 884 - 3428A

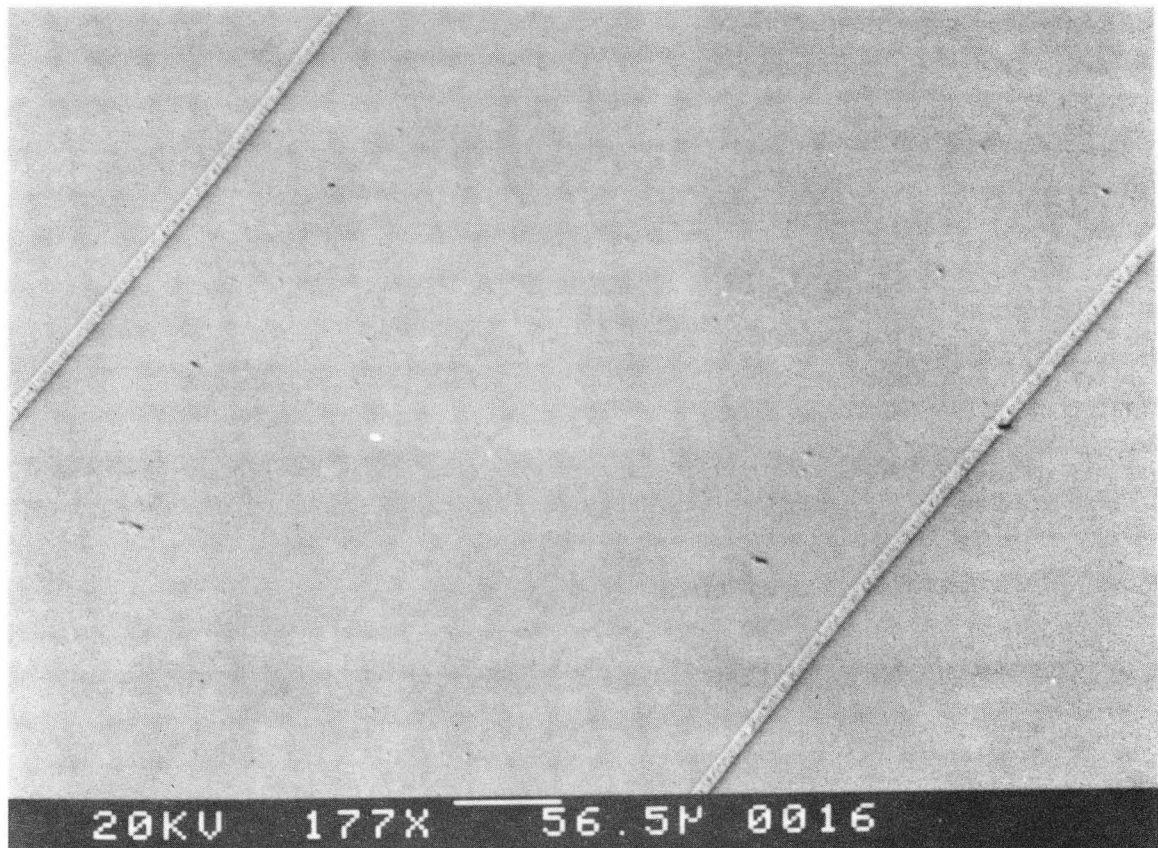


Figure 2.5. A scanning-electron micrograph of a micro-patterned electrode substrate with parallel hemi-cylindrical ridges, 20  $\mu\text{m}$  in diameter. The ridges mimic the effect of emerging striae. XBB 884-3431A

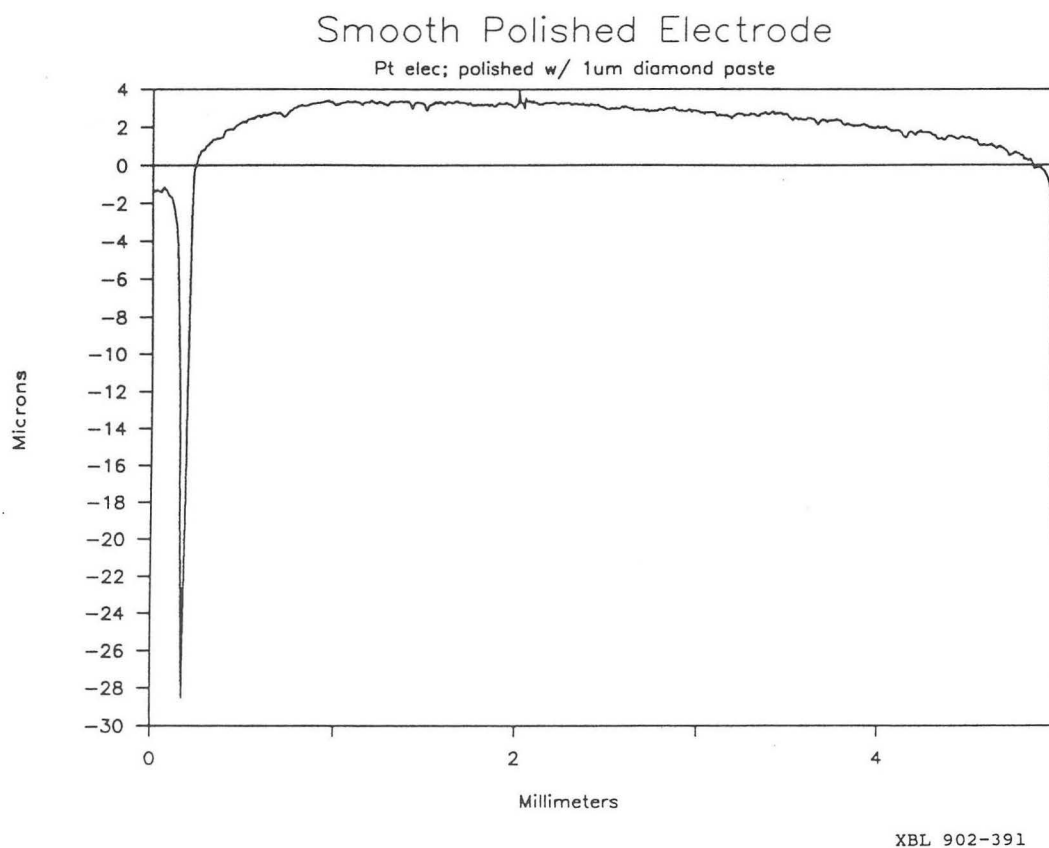


Figure 2.6 Profile of a polished platinum substrate before use. The electrode has a 30  $\mu$ m deep groove at the point where the platinum meets the epoxy, but over the center 80% where zinc deposit profiles are obtained, the surface shows less than 2.0  $\mu$ m of bowing, and no scratches deeper than 1.0  $\mu$ m.



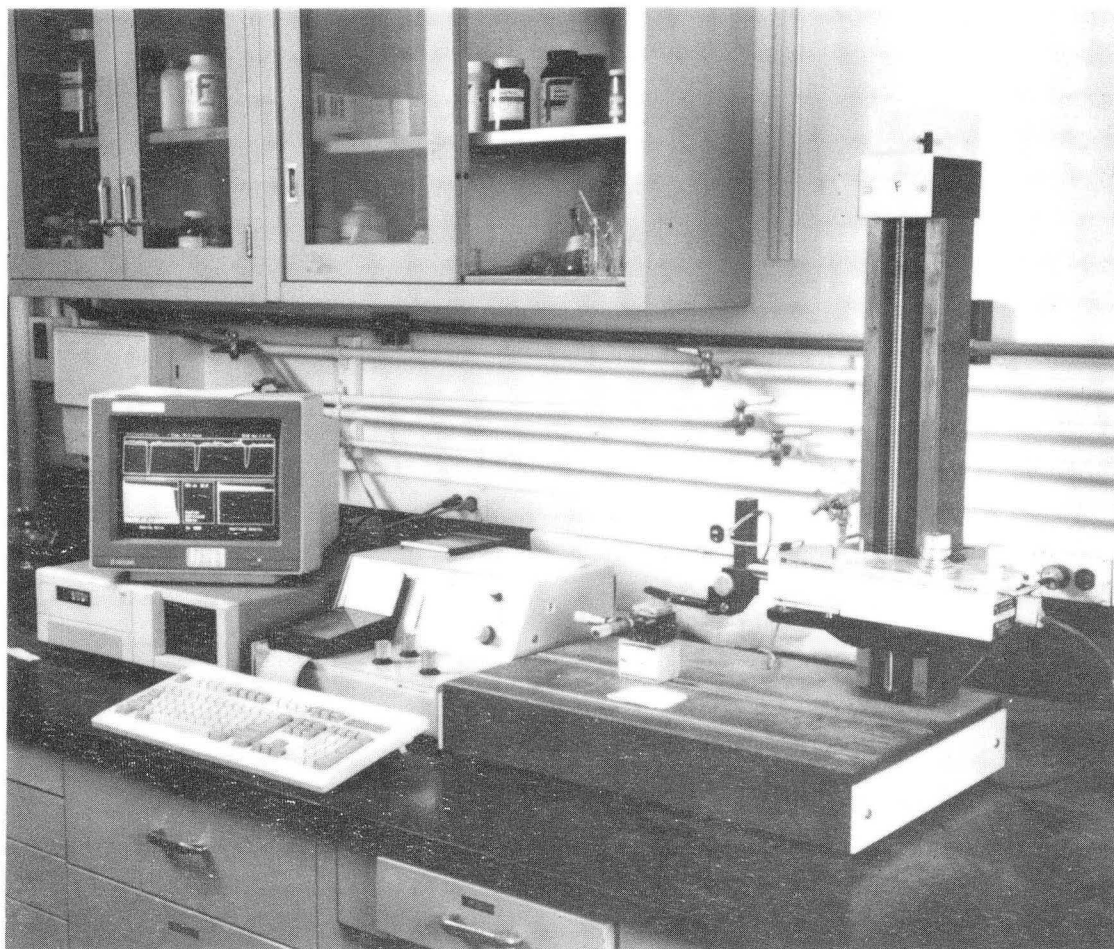


Figure 2.7. Talysurf 10 profilometer. Computer control of the scan and digital data acquisition facilitate spectral power density analysis of striation cross-sectional heights. CBB 900-9315B

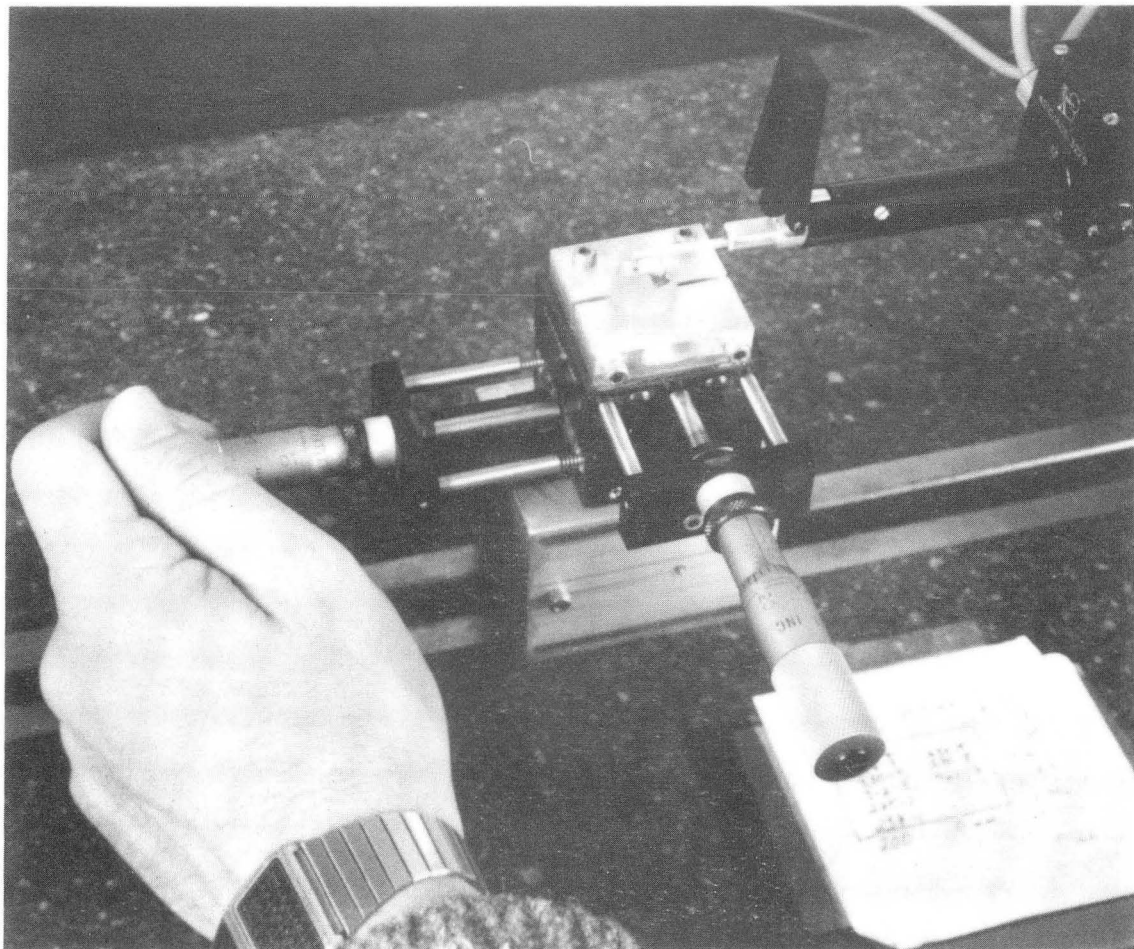


Figure 2.8. Detailed view of a profilometric scan. In the figure, the scan is taken down the length of the 1 cm cathode. Ordinarily, the cross-section of a striated zinc deposit was taken instead. The micrometer precisely positions the stylus. CBB 900-9311B



## Chapter 3 - Striation Periodicity on Flat and Micro-Profiled Electrodes

### 3.1 Macro-photography and Morphology Characterization

A series of deposition experiments were performed over a broad range of current densities to determine the conditions under which striations formed in zinc chloride, zinc sulfate and zinc bromide solutions after extensive deposition. The zinc concentration in all of the reported experiments was one molar, and the pH was approximately 5.2. Fig. 3.1 and 3.2 summarize the results of these runs, which were all done at a uniform loading of 75 Coulombs ( $150 \text{ C/cm}^2$ ) in a channel flow cell at  $Re = 2000$ .

Figure 3.1 shows results for the runs with a zinc chloride solution. At low current densities,  $10 \text{ mA/cm}^2$  or less, the deposit is mesa-shaped or grooved, rather than sinusoidal. Bare surface is evident between adjacent striae at these low current densities. From  $15 \text{ mA/cm}^2$  to  $70 \text{ mA/cm}^2$ , well-developed striations appear, with a clearly periodic appearance. An upper limit for striae emergence occurs at approximately  $70 \text{ mA/cm}^2$  in experiments without supporting electrolyte. Above this value, some markings develop at the leading edge of the electrode, but do not cover the entire electrode surface. These markings are similar to an individual striae, but do not seem periodic in nature and rarely extend over the entire electrode length. They may be caused by single large protrusions. At still higher currents, the electrode becomes macroscopically smooth. Only under magnification can the nodular nature of the deposit be seen.

Similar results were obtained in solutions with a different anion, and in solutions containing a supporting electrolyte, as shown in Fig. 3.2. With supporting electrolyte, striae are replaced at low current densities by a rough, nodular deposit. This may be caused by the substantially lower resistivity of solutions containing potassium salts. The transference number of zinc does not change much, however; it is already small (and possibly negative), even without a supporting electrolyte [81,83,84,86,88].

Macro-photos of zinc deposited from a 1M  $\text{ZnBr}_2$  solution after 75 Coulombs ( $150 \text{ C/cm}^2$ ) were passed show a dramatic change in morphology as a function of the applied galvanostatic current density (Fig. 3.3 - 3.7). The photographs show progressively thinner striae as current density is increased for the same loading, flow rate, and electrolyte. This is in agreement with results obtained previously by Jaksic and Faltemier [17,22-24]. At  $4 \text{ mA/cm}^2$ , the striae are square, mesa-like structures. They become more rounded, and sinusoidal at higher current densities up to  $40 \text{ mA/cm}^2$ , when they become confined to the center of the electrode in the spanwise direction. This confinement is probably due to the inhomogeneity in the current distribution on the electrode in the spanwise direction. At the sides of the electrode, the current density is about 25% higher than in the center. The melding and disappearance of striae would, therefore, tend to occur first at the side edges and move progressively inward.

There is evidence of melding in the higher current density experiments, as striae coalesce together as they grow downstream. The explanation for this may be two-fold. While striae generally originate upstream, the back edge of the electrode also forms striated markings which may be out-of-phase with respect to their upstream counterparts. When the two merge, the misalignment may force two upstream striations to coalesce into a downstream feature appearing between them. McVay has shown in her *in-situ* studies that emerging striae tend to grow towards other nodules in the downstream direction even if they are slightly offset from each other (cf. Ch. 1 and [31]).

### 3.2 Statistical Tests for Periodicity

Several questions can be investigated and answered by profiling the cross-section of striated zinc deposits: the location on the electrode surface where striae originate, how they develop with time, and importantly, ascertaining whether this morphological inhomogeneity is periodic in the spanwise direction. A typical profile is illustrated in Fig. 3.8. The vertical axis has been expanded to show the relative size of the

features. At these deposition conditions, the cross-section exhibits periodic low-amplitude waves. The ratio of the deposit thickness between peaks and valleys decreased with increasing galvanostatic current density. At  $40 \text{ mA/cm}^2$ , the peaks were twice as high as the valleys, while at  $10 \text{ mA/cm}^2$  and below, the valleys were often bare, with the substrate clearly seen between striae.

Two statistical techniques (using subroutines from [118]) were used in the present study: auto-correlation analysis and fast-Fourier transform spectral power density estimation (FFT SPD). Both methods attempt to do the same thing, which is to identify the frequencies of the periodic signals which determine the shape of the input function. They work equally well on time-varying signals or, as in our case, on spatially-varying heights of a zinc deposition profile, although each has distinct advantages and limitations. Autocorrelations work better on signals with one characteristic time-varying component, even if the component is not sinusoidal (such as a constant square-wave), while spectral methods are better at identifying the components of an additive signal.

### 3.3 *Autocorrelation Analysis*

Autocorrelation analysis determined the length scale over which the amplitudes of the waveform are correlated. If the original input is perfectly sinusoidal and of long duration relative to its period, the autocorrelation function will be a normalized, phase-shifted replica of the input. The maximum in the autocorrelation function will invariably occur at the origin, and each successive maximum will be of equal intensity, spaced apart by the wavelength of the input sinusoid. Most often, however, the input function will be imperfect in a number of ways. The input may be of limited duration or length, or consist of a signal having a mixture of frequencies distorted by white noise. In this case, the output auto-correlation function will still be periodic, but the amplitude of the peaks will be diminished at distances away from the origin.

The autocorrelation is accomplished by taking the original waveform and shifting it by a delay  $\tau$ , as shown in Fig. 3.9 from [117], and then computing the correlation average ( $\Psi$ ) over the observation interval,  $2T$ , as in Eq. 3.1:

$$\Psi = \lim_{t \rightarrow \infty} \frac{1}{2T} \int_{-T}^T x(t) y(t) dt. \quad (3.1)$$

where  $x(t)$  = value of input function.

$y(t)$  = value of phase-shifted function:  $y(t) = x(t+\tau)$ .

and  $2T$  = number of data points in observation interval.

Several caveats limit the information content of the autocorrelation function that is obtained, however. First, the input function must have an average value (DC component) which vanishes over the chosen input data [117]. In the case of zinc striations, an average height must be calculated and subtracted from the height at each data point. The height is then normalized by the most extreme deviation from this mean value. The occurrence of a single sharp feature will depress the relative amplitude of neighboring features, and consequently, depress the correlation function generally, for phase-shifts  $\tau > 0$ .

Second, and more importantly, the observation interval is finite in length, which creates new problems. Since sinusoidal functions are orthogonal, frequencies that are not equal to (or multiples of) the delay will cancel out, so that the only contributors to the correlation function at a given delay  $\tau$  will be wavelengths of the delay frequency or an integer multiple. In the case of finite signal inputs, orthogonal frequencies are not expected to cancel, and may contribute spuriously to the autocorrelation output [115,117,118]. This is especially true at delays close to  $\tau = T$ , since the autocorrelation is symmetric around this point. The most useful information (strongest correlations) are obtained when the periodic component of the input has a wavelength such that  $\tau \ll T$ .

Third, the input waveform may be composed of various components summed together. In this case, the output waveform has a multiplicity of features. Peklenik [120], in Fig. 3.10, has characterized and grouped typical autocorrelation plots by their most salient features. Input waves that are noise-free are deterministic and give the clearest outputs, but information may be gleaned from the other wave types as well. Fig. 3.11 shows the result when the input consists of additive waveforms of varying intensity. In these cases, the autocorrelation would show the strongest peaks for a wavelength of intermediate length if the two components were *in phase* with one another. As the phase of the two frequencies begins to differ, the autocorrelation becomes difficult to interpret, since the frequencies interfere both constructively and destructively.

The results obtained for high amplitude striations, after 75 C ( $150 \text{ C/cm}^2$ ) are deposited, give the sharpest and most periodic peaks. Fig. 3.12 shows the results for deposition at  $10 \text{ mA/cm}^2$  from a zinc chloride solution. The auto-correlation is rather saw-toothed, which corresponds to a square-wave input. At long deposition times, then, the striae lose their sinusoidal shape and become taller, with steeper side slopes and broader crests.

Statistically significant results are also obtained for the analysis of profiles of smaller amplitude, but the correlation coefficient rarely exceeds 0.3. This value for the correlation coefficient still exceeds the threshold for significance. The threshold lies between 0.1 and 0.15, one wavelength from the origin, and decreases as the square root of the distance parameter [118]. Figure 3.13 shows spectra taken from profiles on two separate electrodes at the same distance downstream from the leading edge. While the peaks are not identical in amplitude, there is a remarkable similarity in the average period between successive peaks. This period corresponds to the observed striation frequency on the original zinc profile, which was deposited at  $20 \text{ mA/cm}^2$  on a platinum electrode in a zinc sulfate solution.

The advantage of autocorrelation is that information can be obtained at several electrode positions, and the resulting spectra directly compared. Figure 3.14 shows that, with superimposed autocorrelations of profiles taken at various distances from the leading edge on a single electrode, striation frequencies shift slightly as striae meld downstream. Although the shift is small, at three wavelengths it becomes discernible; there is a monotonic increase in frequency as one moves downstream from the leading edge. In other instances, not illustrated, the striations towards the trailing edge of the deposit are again spaced more widely apart.

The explanation for this behavior lies in the way striae emerge and propagate. Larger nodules at the edges are the first to extend themselves and form a pattern before the rest of the electrode. This may occur because the leading and trailing edges have an ohmic advantage, since the electrode is bounded by an insulator. Figures 3.15 and 3.16 show that the autocorrelation function at the leading and trailing edge is weakly periodic when only 10 C (20 C/cm<sup>2</sup>) has been deposited. The rest of the electrode does not yield spectra with distinct periods. There is no reason to suppose that the periods at the leading and trailing edge are phase-aligned, however. As the striae at the front propagate downstream (the preferred direction), they meet an out-of-phase array, and shift sideways slightly as the two proto-striations meld.

The results at 10 C (20 C/cm<sup>2</sup>) are important for understanding how striae emerge. The deposit is rough, but of relatively uniform average thickness from front to back, as seen in Figure 3.17. There is a distribution in the size of individual nodules, but before striae emerge, the leading edge is not (on the average) thicker than the middle of the electrode. By now, however, a weak patterning has already occurred at the leading edge, as evidenced by the autocorrelation results. This patterning seems to accelerate local growth, because after the passage of 20 C (40 C/cm<sup>2</sup>), the regions 1mm from the leading and trailing edges are, on the average, 50% thicker than the center portion of the electrode, as shown in Fig. 3.18.

### 3.4 *Fourier Analysis and Spectral Power Estimation*

While the autocorrelation results provide information on deposit conditions at various locations on the electrode surface, the quality of the output waveform is limited by noise and determination of a single correlation distance is not always possible. The relatively low correlation coefficient indicates that perhaps more than one wavelength could be characteristic of a particular striation profile and that noise may be obscuring the actual correlation distances. Fast Fourier transform decompose the waveform into an orthogonal set of sine and cosine functions. This is advantageous because the entire scan, not just half of it, is used in determining the power of periodic components in the cross-sectional morphology of the zinc deposit. Noise contributes a background-level to the spectrum, but does not alter the frequencies into which the waveform is decomposed. Multiple peaks, or sidebands, are identified separately, and accounted for by comparison with the shape of the zinc profile.

A Fourier transform carries phase information as the power at a given frequency is partitioned into separate coefficients for the sine and cosine functions. These coefficients are the amplitude of the component function. The phase information may be useful in some applications, but in our case it was found to be essentially random. There is no precise reference point at which to start the profilometric scan, so the data is not phase-locked to the striation frequency.

To reduce noise by averaging the transform signal, one must first eliminate the phase angle of the component functions, since signals with random phase angle will sum to zero (i.e. if our signal has random phase angle, it too will vanish upon summation). Summing the squares of the amplitude of the sine and cosine components eliminates the phase but retains a measure of the amplitude for a single spectral frequency. The resulting spectrum is called the Spectral Power Density (SPD). SPDs may be summed and averaged to provide data with less relative noise. For each experimental condition, a total of 27 profiles were obtained, nine profiles on each of three different

electrodes plated at the same conditions. They were analyzed separately, and normalized individually by the frequency of largest amplitude. Their SPDs were then included in the normalized average which is presented in the following figures.

In obtaining the Fourier transform, advantage is taken of the "FFT" algorithm by adopting a choice of  $N$  data values, where  $N$  is a power of two,  $N = 2^P$ . In our data sets, the number of data points was never exactly equal to 1024 or 2048 (the powers of two closest to the measured number of data points in each 3.7 mm scan), so zeros were appended to the data set to bring the total up to the required value. This is a standard procedure, known as zero-padding. The percentage of appended zeros ranged from only a couple to 8% of our data set, so that even at low frequencies, an integral number of striation wavelengths was included in each data set. Tests were performed to determine whether the padding operation distorted the resulting Fourier spectrum. Doubling the number of appended zeros from 20 to 40, shifted the maximum power of the output spectra by a negligible amount (approx. 1%).

The first Fourier spectra obtained had peaks that were obscured by noise, to the point that the largest signal amplitude was only twice as strong as the background power. Two types of noise were apparent: 1) flicker noise ( $1/f$  noise) which decreases as the reciprocal of the frequency, and an additional low frequency noise that is caused by bowing of the electrode surface. Although the platinum substrates had been carefully polished on a wheel, there was a slight bowing from the side to the center of the active area. Since striation wavelengths are also of relatively low frequency, the electrodes had to be repolished on a flat nylon cloth (cf. chapter 2), to eliminate the overlap between the two signals.

The frequencies that are determined by Fourier analysis range from one per scan length to the Nyquist limit at the upper frequency end. The Nyquist limit [118] states that a minimum of two data points must be taken per cycle for a frequency component to be resolved. Each of our Fourier transforms used 512 equally-spaced data points out



of the 2048 taken over 3.7 mm, and the output resolved frequencies up to 256 wavenumber, equivalent to a wavelength of less than 14  $\mu\text{m}$ . The rest of the points were also used in separate Fourier transforms, and the results were averaged. Taking four transforms over the same data set reduces the variance of each frequency power estimate from 100% to 25% [118].

A third source of possibly spurious peaks is known as aliasing, which often occurs if there is substantial power at frequencies higher than the Nyquist limit. As seen below, this is not the case in our data set, as the amplitude of small-scale roughness is much smaller than the striation height. No appreciable power was seen in the spectra close to the Nyquist limit. The visually observed number of striae ranged from 5 to 25 per scan length, and it was over this region of wavenumbers that striation peaks were expected, far from the Nyquist limit of 256 (where only small-scale roughness was expected to contribute to the spectrum).

In addition to repolishing and the averaging of multiple SPDs to reduce noise, an additional technique was employed to mitigate the effects of finite scan length on the results. The data set was "windowed," which means that it was multiplied by a function before Fourier transformation. This windowing function must have the property that its value is zero at the beginning and end of the scan, and rises to a maximum value of unity at the center of the data set, around which point the function is symmetric.

The most common windows used for finite data sets are a triangular (linear) or parabolic (quadratic) function. Their purpose is to weight the data set to diminish the effect of points that lie close to the ends of the scan. Since the data are "wrapped" around themselves to form a continuous signal by the Fourier algorithm, discontinuities at the ends may create unwanted spurious power. By windowing the data, any such discontinuities are damped. In practice, the zero-padding of the data was distributed evenly between the beginning and end of the data set, thus avoiding any discontinuities. In this case, the windowing serves a second function, to dampen the importance of the

zero-padded data, leaving only the 'true' data to contribute to the power spectrum. Transforming data without use of an explicit tailing function corresponds to the implicit use of a "square" window, which rises vertically to one at the first data point, and remains there for the duration of the scan.

As Bracewell acknowledges in his pithy recent review in *Science*, "Much practical technique is involved [in Fourier analysis]." He goes on to warn about the pitfalls of both zero-padding and windowing, particularly the appearance of oscillations in the power spectra obtained. The use in this work of these noise-reduction techniques is justified on the basis of accepted general practice [118], and by the sharp, oscillation-free spectra obtained as a result. After noise reduction, power at wavenumbers above 60 rarely exceeded 0.01 (normalized by the peak power), and averaged only 0.002 for wavenumbers between 100 and 256.

For ease of comparison, the results are all plotted using the wavenumber as the horizontal axis, which is equivalent to the frequency of striations over the 3.7 mm scan length. Table 3.1 converts this to a striation wavelength; it should be noted that each frequency bin is representative of power from halfway from the preceding discrete frequency bin to halfway towards the following one. Thus, wavenumber 12 is the average power for striation wavelengths between 291 and 345  $\mu\text{m}$ .

The range of operating conditions tested was limited by the need to obtain representative spectra, with as little variance as possible. Three parameters were varied in the experiments on flat electrodes: total charge passed, applied galvanostatic current density, and solution composition (anion type and supporting electrolyte concentration were changed; zinc ion concentration kept constant).

The results for a range of charge passed are shown in Figures 3.19a, b and c. At 10 Coulombs ( $20 \text{ C/cm}^2$ ), there is still no distinctive sharp peak present. The power at a wavenumber of one, caused by the slight bowing of the electrode after polishing, dominates other spectral features. The remaining power falls off with higher frequency,

typical of noise caused by random roughness. With the passage of 15 C ( $30 \text{ C/cm}^2$ ), however, a single sharp peak occurs at a wavenumber of eight ( $\lambda \approx 470 \mu\text{m}$ ). This peak does not immediately shift with increased loading, and is still the largest at 25 C ( $50 \text{ C/cm}^2$ ). In both cases, however, a weaker secondary peak occurs at wavenumber 16. This bimodal distribution is observed in the original profile, shown in Fig. 3.8. There seem to be two distances, one between large nearest neighbors, another between these large peaks and smaller ones that are growing in between the earlier striae. There is a third frequency which can be seen in the 25 C spectrum, centered on wavenumber 11. By 30 and 50 C ( $100 \text{ C/cm}^2$ ), the distribution becomes narrower and the power becomes concentrated at this intermediate frequency between the two predominant peaks seen at shorter deposition times.

Each power spectrum is an average of three separate experiments, not redeposition on an electrode that has been tested and then replaced in the flow cell. It is then even more remarkable that the same periodicities emerge after deposition of 15 and 25 C and that congruence on a single peak at wavenumber 11 or 12 ( $\lambda \approx 310\text{--}330 \mu\text{m}$ ) takes place at 30 and 50 Coulombs of charge passed ( $60\text{--}100 \text{ C/cm}^2$ ).

In general, at the same amount of charge passed, the frequency of striations will increase as the current density is raised, as in Figure 3.20 (the same effect is also seen in Figure 3.27, discussed below). In both the complexing chloride and the non-complexing sulfate solutions, the peaks shift to higher frequencies as the rate of deposition is increased. The lack of difference in spectra between the two solutions is seen more clearly in Fig. 3.21, where the spectra for experiments at three different current densities are superimposed. The largest peaks occur within a distance of two bins, or less, of each other in all three cases, and the shape of the spectrum is similar as well.

Differences emerge only at the highest current densities tested, in regions where striae are confined to the leading edge of the electrode. Such leading-edge striations are not usually observed in deposits plated in a sulfate solution, but occur regularly in

chloride solutions. The spectra in Fig. 3.22 shows the difference between the leading edge and the electrode average for the case of deposits obtained at 50 and 60 mA/cm<sup>2</sup>. At 50 mA/cm<sup>2</sup>, a peak at wavenumber 12 is clearly seen in the leading edge (defined as the first 3 mm of the electrode length) spectrum, while it is much weaker for the whole electrode (average of all 9 scans taken). By 60 mA/cm<sup>2</sup>, the average spectrum is completely dominated by the low-frequency global current distribution, while the leading edge still bears a small signal from periodic striated structures.

It is of interest to define the highest current density at which striations emerge. A number of researchers [17,58,59], claim to have obtained striae at current densities above 60 mA/cm<sup>2</sup>. If one plates zinc for a much longer time than is necessary to obtain striae at low current densities, the roughness of the deposit becomes substantial, increasing the actual electrode area. After prolonged deposition, the current density based on the real area declines to progressively lower values, and not surprisingly, striae emerge as evident in the spectrum obtained from a deposit plated with 90 C (180 C/cm<sup>2</sup>) of zinc at 120 mA/cm<sup>2</sup> in an unsupported chloride electrolyte. The period observed is identical to the one obtained at 50 C (100 C/cm<sup>2</sup>) and 20 mA/cm<sup>2</sup> in Fig. 3.19c. It seems that the period of striations at long deposition times is not as dependent on the applied current density based on geometric area. This may be because the active electrode area is now much larger, and the range of actual current densities smaller. It seems reasonable that as the current density based on the real area falls, wider striations would become favored, since they are the ones that emerge in experiments at low current densities at short times.

This result may explain the discrepancy between the macro-morphology of zinc deposited in chloride versus sulfate electrolytes. As shown in Figure 3.1, striations are obtained in chloride electrolytes at much high current densities after the deposition of 150 C/cm<sup>2</sup>, than from sulfate solutions. After the deposition of 40 C/cm<sup>2</sup>, however, the SPDs of zinc deposits plated from each of the two solutions was practically identical.

As the substrates become rougher, the effect of ohmic advantage must be more important. Deposition in chloride solutions, which have a significantly lower resistivity still lead to the development of striations at these longer deposition times, while use of the more resistive sulfate solutions will not. If ohmic considerations outweigh the advantage of recirculation in the wake of the nodule, elongation and alignment caused by variations in concentration polarization will not occur.

Experiments with well-supported zinc chloride electrolyte solutions were performed on both platinum and graphite substrates. Fig. 3.23 through 3.26 show macrophotographs of the zinc deposits obtained. They are qualitatively similar to the results in zinc-bromide solutions which are shown in Fig. 3.3-3.7. The SPD spectra (Fig. 3.27) show peaks at the same wavenumbers as deposits plated from unsupported chloride and sulfate electrolytes. On changing the substrate to Gould graphite-loaded polymer, the striation density at a given current density, measured by the most prominent peak in the obtained power spectrum, changes as summarized in Fig. 3.28. Results on both platinum and carbon both show a dependence of striation number on current density, but the slope is higher for the carbon substrate. This means that the current density for the transition from striated to nodular growth occurred at a lower value for the carbon substrates, and for both substrates occurred below  $50 \text{ mA/cm}^2$ . At sufficiently high current densities, striae meld to form a pattern with a lower density, then at still higher deposition rates form a noduled, unstriated surface. The difference between the two substrates can be correlated to the nucleation characteristics reported by Tsuda [34] and Anderson [14]. Zinc nucleates better on platinum substrates at low current densities; as a consequence, higher striation frequency is to be expected. What stays roughly constant is the critical frequency at which striae no longer develop. Above this cutoff frequency, the striae do not seem to be morphologically stable; they either meld or emerging nodules coalesce before the striated pattern appears.

### 3.6 Deposition on Micro-Profiled Electrodes

The effect of precisely-patterned arrays of surface features on the resulting zinc morphology was examined using the micro-profiled electrode (MPE), whose fabrication is described in [33] and Appendix A. Both nodule arrays and artificial striae (hemicylinders) were used in the zinc deposition experiments. The first trials were completed before the profilometry apparatus was available, so the results are qualitative. As shown above, plating on different substrates (platinum vs. graphite) made a difference in the spacing of striations at the same deposition conditions because of differences in the nucleation characteristics of the substrate. A more direct way to examine this was by using artificially-patterned substrates, where the density, distribution, and orientation of surface features is determined *a priori*, independent of the applied galvanostatic current density,  $i$ .

Plating zinc on a flat platinum electrode at  $30 \text{ mA/cm}^2$  in a well-supported chloride solution, results in a nodular deposit after the passing of  $90 \text{ C}$  ( $180 \text{ C/cm}^2$ ). If the working electrode is replaced with a micro-patterned gold substrate, striations are evident at the same plating conditions, as seen in Fig. 3.29. The top photo in the figure shows a deposit obtained on a polished substrate used as a control, while the deposits at lower left and right were plated on micro-profiled electrodes with different surface features.

The number density of the striae depends on the underlying pattern. An MPE with artificial nodules,  $2.5 \text{ }\mu\text{m}$  in height and spaced  $50 \text{ }\mu\text{m}$  apart in both square- and triangular-pitched arrays yielded fine striations with a estimated wavelength of approximately  $140 \text{ }\mu\text{m}$ . This value was obtained from counting ridges in macro-photos of the resulting deposit. Such a large number of striae do not persist in deposits on flat, control electrodes after such thick deposits are grown, regardless of the applied current density. Electrodes patterned with artificial striations  $2.5 - 3.0 \text{ }\mu\text{m}$  in height,  $20 - 40 \text{ }\mu\text{m}$  in width, spaced  $200 \text{ }\mu\text{m}$  apart, and aligned in the direction of flow, also developed a zinc

deposit characterized by much wider striations. The period of the striations was equal to the spacing of the artificial hemi-cylinders.

Experiments on artificially profiled substrates were used to test whether the orientation of the pre-existing surface features also had an effect on the resulting morphology. Artificial hemi-cylindrical obstacles identical in size to the ones described above, were placed perpendicular to the direction of flow. Thick striae aligned in the flow direction were also obtained, independent of the orientation of the curved obstacle. This is not as surprising as it may appear, however, since the spacing was similar to that obtained at long times in unsupported electrolyte.

Spacing of the nodules is also critical. Experiments with nodules spaced  $500\ \mu\text{m}$  apart, showed little difference from the morphology on flat, polished electrodes. The addition of a few, widely-spaced  $2.5\ \mu\text{m}$  protrusions does little to alter the total number density of growth centers. More recent work on patterned electrodes at lower current densities ( $10$  and  $20\ \text{mA}/\text{cm}^2$ ) in an unsupported sulfate electrolyte also gave negative results; there were no differences in the morphology compared to that obtained at equivalent current densities on polished substrates. The striation frequency on the patterned substrates, both nodules and hemi-cylinders, was nearly identical to that obtained on control electrodes.

A set of experiments was done on flat electrodes to try to explain these divergent results at different current densities. Since the distance between nodules on the artificially-patterned substrates is small, they correspond to the nodule density obtained on flat electrodes after initial deposition at a high current density. If such a well-nucleated electrode was then grown slowly, would striae still emerge? Results on the profiled electrodes seemed to indicate that they would, and that after enough time, the growth rate would determine the striation spacing at low current densities. To investigate this possibility, a platinum electrode was plated for  $2\ \text{C}/\text{cm}^2$  at  $100\ \text{mA}/\text{cm}^2$ , then grown at  $20\ \text{mA}/\text{cm}^2$  until an additional  $38\ \text{C}/\text{cm}^2$  were passed. The resulting deposit

had striations localized in the front half of the electrode, with a frequency close to the value obtained for deposits grown at  $40 \text{ mA/cm}^2$ . Thus, deposits with a dense spacing of nodules, but grown slowly, show features which are characteristic of electrodes deposited galvanostatically at an intermediate current density.

### 3.7 Conclusions

The following conclusions may be drawn from the profiles obtained, and from the determination of preferred striation wavelengths by auto-correlation analysis and spectral power density estimation:

1) Striae emerge after the deposition of 15 - 20 Coulombs of deposit ( $30 - 40 \text{ C/cm}^2$ ) at current densities well below the exchange current density, which is taken to be  $100 \text{ mA/cm}^2$  (from [49]), and at only 8% or less of the diffusion-limited current density. This is in agreement with prior work by Faltemier [17].

2) At short times, the range of current densities over which striae develop is independent of the anion in solution, and also independent of the presence of supporting electrolyte. Some differences emerge after 75 C ( $150 \text{ C/cm}^2$ ) are deposited, however. This may account for disagreement in the range of current densities over which striae have been reported. Jaksic [22] and Faltemier [17] obtained striations at current densities up to  $80 \text{ mA/cm}^2$  in rotating disk experiments, and Yee and Jorne [58, 59] at even higher rates, but only after the passage of much larger amounts of charge. Striae were obtained in this study at  $120 \text{ mA/cm}^2$ , but only after depositing 90 Coulombs, when the real surface area greatly exceeds the geometric area.

3) The shape of striae changes from sinusoidal to square shaped as deposition time increases. The shape at a given loading is a function of current density, since at low current densities the valleys appear to be entirely quiescent even at short times (no zinc deposition is observed). The only possible reaction between striae at  $4-8 \text{ mA/cm}^2$  seems to be the evolution of hydrogen. Striae form more quickly at low current



densities, and the ratio in deposit thickness between top and valley is smaller at higher current densities.

4) Melding of striations may be caused by misalignment near the back electrode edge between two sets of striae, one growing upstream and the other downstream.

5) The formation of a periodic structure at the leading and trailing edges accelerates the deposition rate locally by increasing the real surface area of the deposit and concurrently increasing the average deposit height. This is a self-accelerating process, since the increased average height gives the leading and trailing edges greater ohmic and concentration advantages over the rest of the deposit.

6) Striation frequency varies with loading, as the spacing induced by nucleation is replaced by a new, perhaps flow-determined spacing. At  $20 \text{ mA/cm}^2$  in sulfate solution, a bimodal power spectrum was replaced by a spectrum with a single peak of intermediate frequency after more charge was passed.

7) Striation density is a strong function of current density, as reported by Jaksic [22-24], Faltemier [17], Jorne [58, 59], and Selman [56, 57], but is independent of solution anion composition or the presence or absence of supporting electrolyte.

8) Replacing a substrate with another material with different nucleation characteristics changes the frequency of striae obtained at a given deposition rate. The narrowest stable striae do not depend on the substrate, however. Above a threshold frequency, striae meld and the observed power spectrum becomes bi-modal, with power also concentrated at a frequency of half the expected value.

9) Patterned substrates have a remarkable effect at high current density, where striations may not otherwise occur. At  $30 \text{ mA/cm}^2$  and after plating 90 Coulombs in a well-supported zinc-chloride electrolyte ( $1\text{M ZnCl}_2 + 2\text{M KCl}$ ), the use of MPEs with artificial nodules results in thin striae while using electrodes patterned with micron-sized ridges results in the formation of thicker striae. The periodicity of the thick striae matches the spacing of the hemi-cylindrical ridges. Thick striae also occur if the lines

are oriented perpendicular to flow. Electrodes with two patterns of lines followed the behavior determined by upstream features, while the use of MPEs with only a sparse array of nodules gave negative results.

At lower current densities, the artificially-patterned electrodes do not give deposits that are greatly different from the control electrode, and at  $10 \text{ mA/cm}^2$  no difference is seen in the striation number density. This suggests that a critical density of nuclei is necessary to form striae; altering this density significantly with the use of densely packed nodules results in a qualitative difference in the resulting macro-morphology of the zinc deposit.

10) Striations are usually characterized by a single period characteristic of the current density at which the zinc is plated, although the peak in the power spectra is broader than a single bin for averaged spectra. This is caused by a distribution of peak spacings on different electrodes. The proper frequency may also fall between bins, leading to some broadening which is an artifact of the method. Zinc plated first at a high current density, then at a lower one, where striae ordinarily occur, have a striation density characteristic of a galvanostatic current density intermediate to the two values at which the deposit was actually plated.

These results lend plausibility to a scenario where growth centers emerge through a competition for current, and through a directional recirculation of the flow, elongate and align, forming striations.

**This page left intentionally blank.**

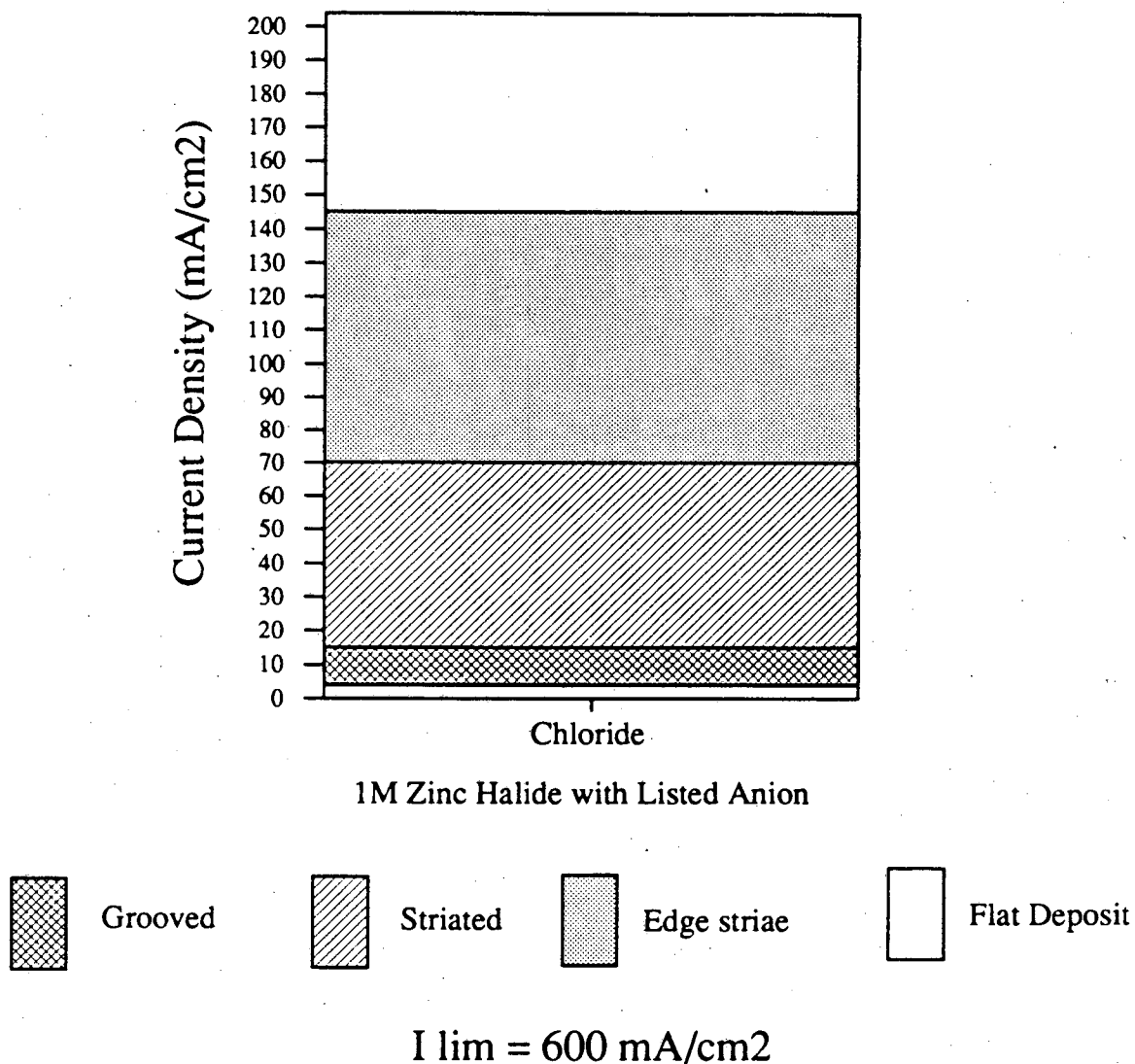
**This page left intentionally blank.**

**This page left intentionally blank.**

**Table 3.1: Wavenumbers and Striation Wavelength**

Striation Frequency per Scan Length	Corresponding Wavelength ( $\mu\text{m}$ )
5	750
6	625
7	536
8	469
9	417
10	375
12	313
14	268
16	234
18	210
20	181
22	170

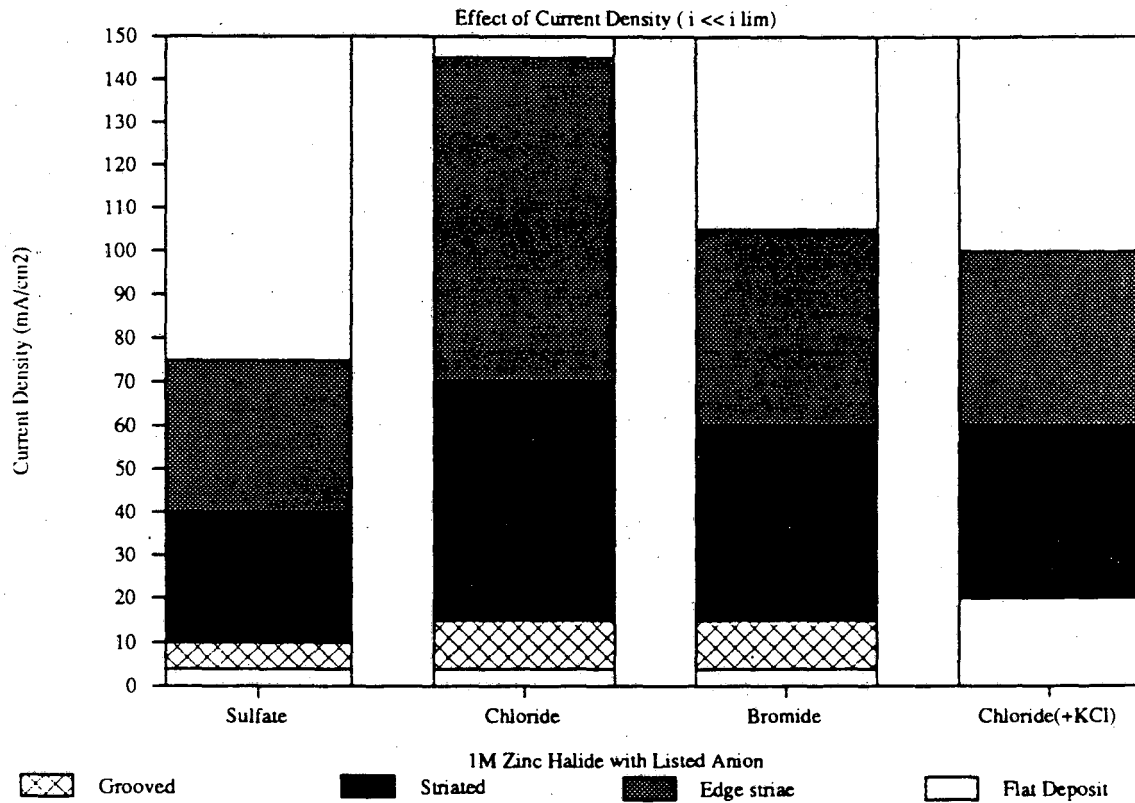
## Effect of Current Density ( $i \ll i_{lim}$ )



XBL 9011-3564

Figure 3.1 Zinc macro-morphology after deposition of  $180 \text{ C/cm}^2$  as a function of current density. At low deposition rates, the surface is marked by broad, mesa-shaped grooves. At intermediate current densities, striae appear, up to  $60 - 80 \text{ mA/cm}^2$ , when the surface becomes smoother. Up to  $130 - 150 \text{ mA/cm}^2$ , the leading edge contains a few short striae which do not propagate the length of the electrode.

## Morphology of Zinc Electrodeposits



XBL 902-448

Figure 3.2 Zinc macro-morphology after deposition of  $180 \text{ C/cm}^2$  as a function of current density and electrolyte composition. The range of current densities over which striae appear varies only slightly depending on the presence of supporting electrolyte and the degree of zinc-ion complexation.



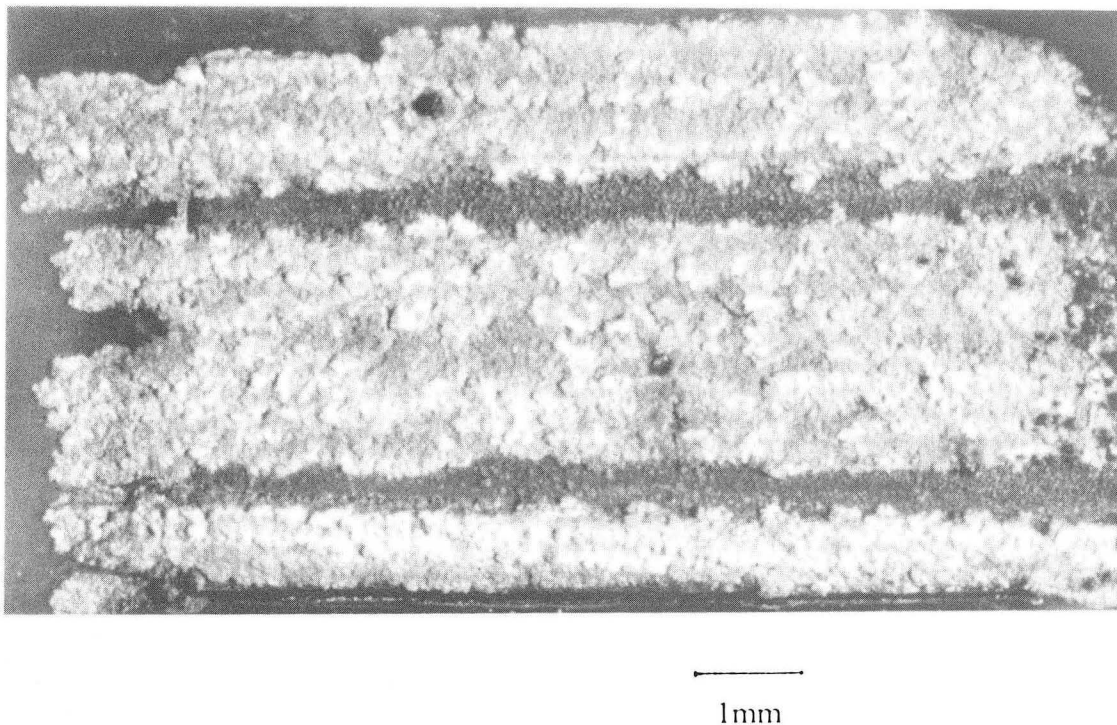
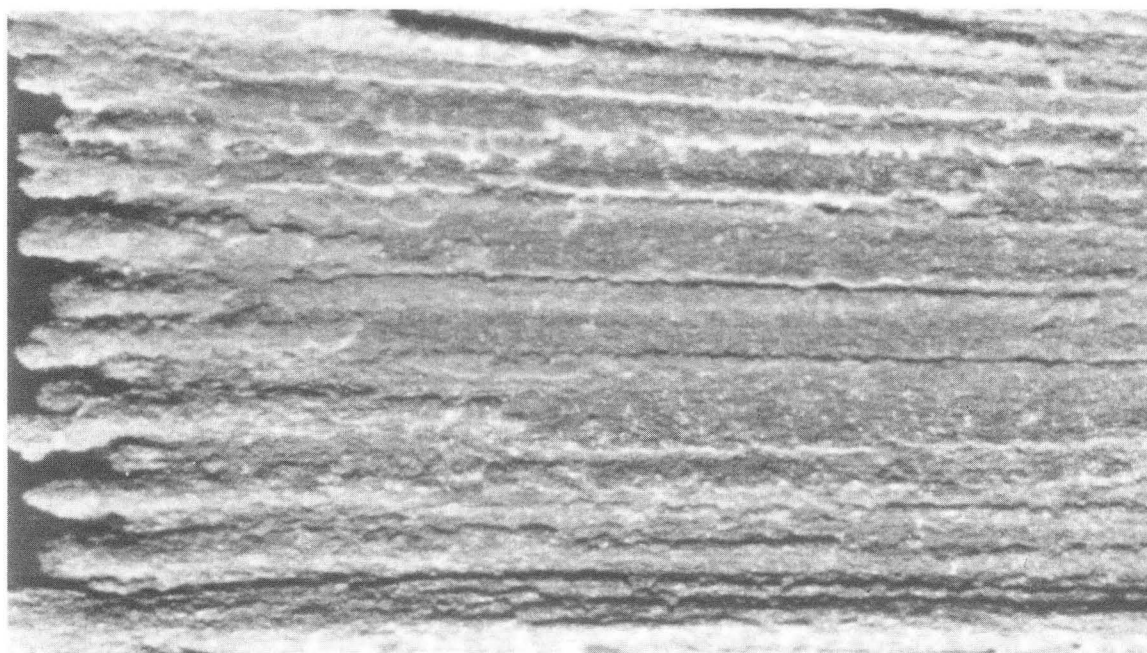


Fig. 3.3 Striated Zinc Deposit ( $4 \text{ mA/cm}^2$ ,  $40\text{C/cm}^2$ ) XBB 886-6451A

Fig. 3.3-3.7 Zinc striations deposited at constant current over a range of current densities ( $4 - 40 \text{ mA/cm}^2$ ) in a channel flow cell from a  $1\text{M ZnBr}_2$  solution at  $\text{Re} = 2000$ . The current densities over which striations appear are all below 10% of the measured limiting current. The dimensions in all five figures are the same; the electrode length is 1.0 cm and the width is 0.5 cm.



1mm

Fig. 3.4 Striated Zinc Deposit ( $10 \text{ mA/cm}^2$ ,  $40\text{C/cm}^2$ )

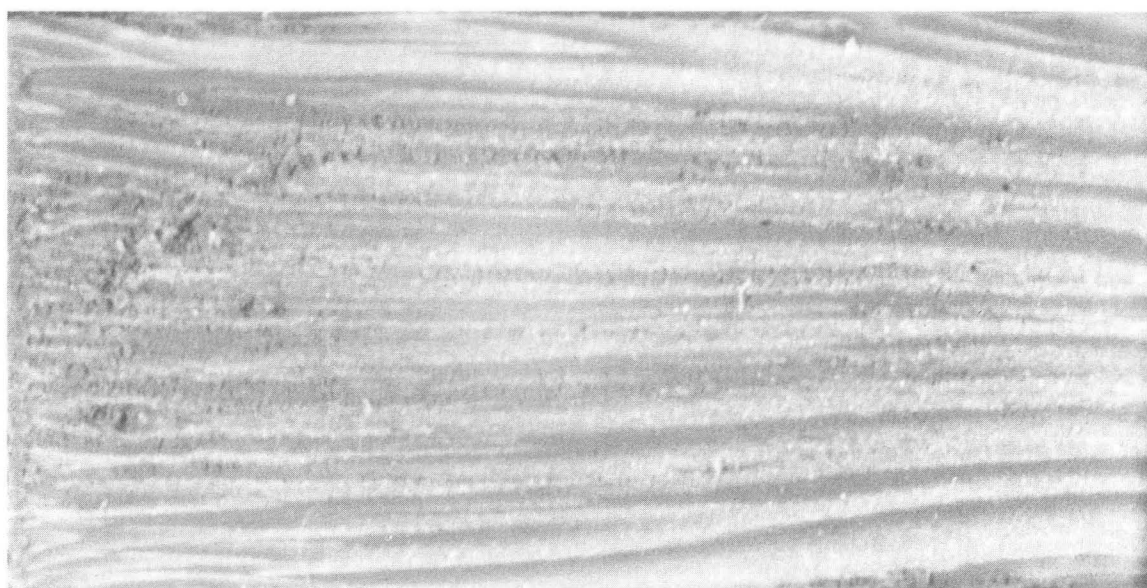
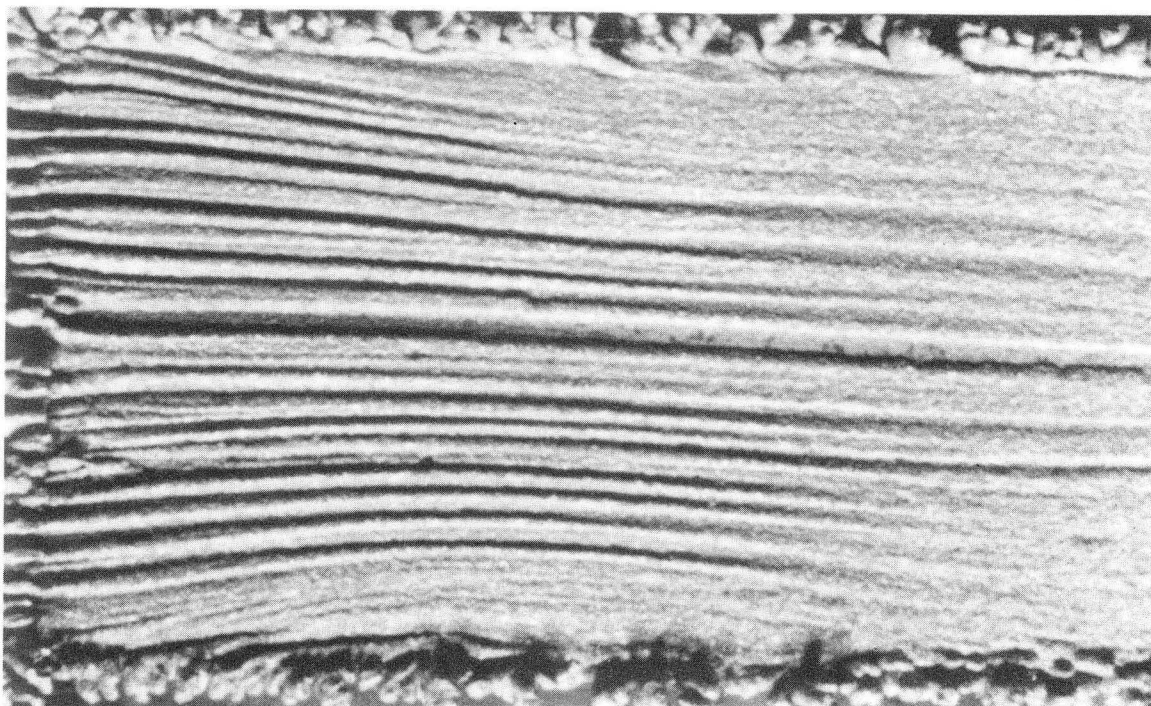


Fig. 3.5 Striated Zinc Deposit ( $20 \text{ mA/cm}^2$ ,  $40\text{C/cm}^2$ ) XBB 886-6448 A



1mm

Fig. 3.6 Striated Zinc Deposit ( $30 \text{ mA/cm}^2$ ,  $40 \text{ C/cm}^2$ )

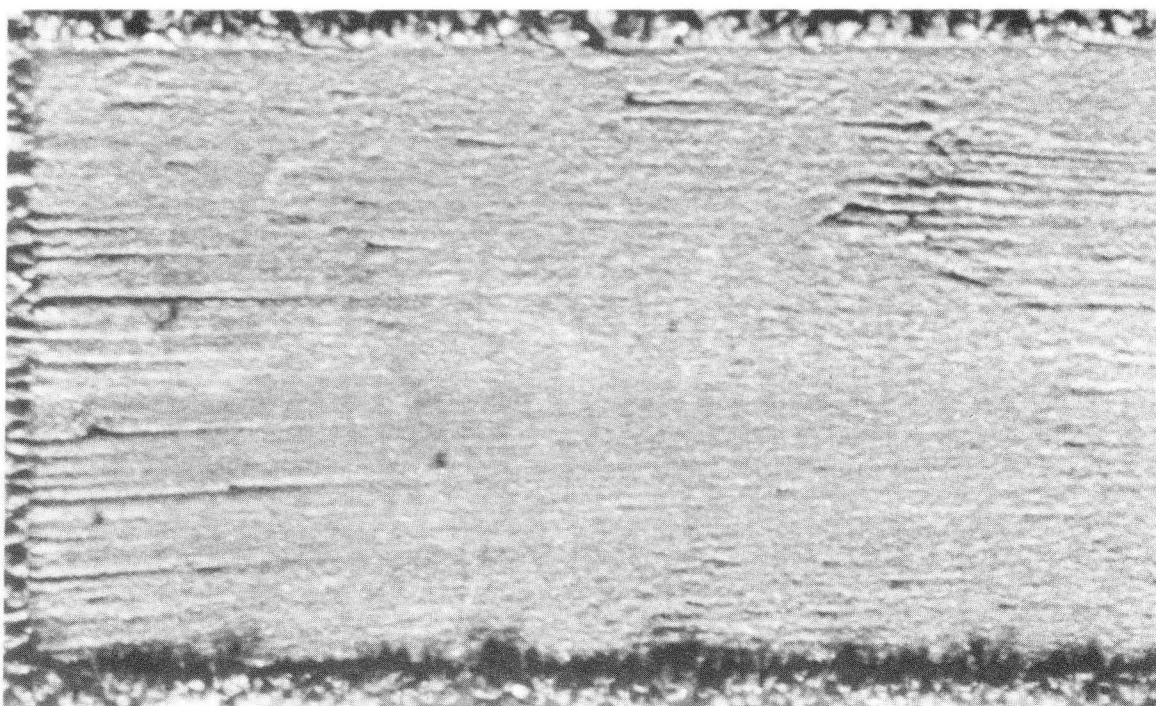
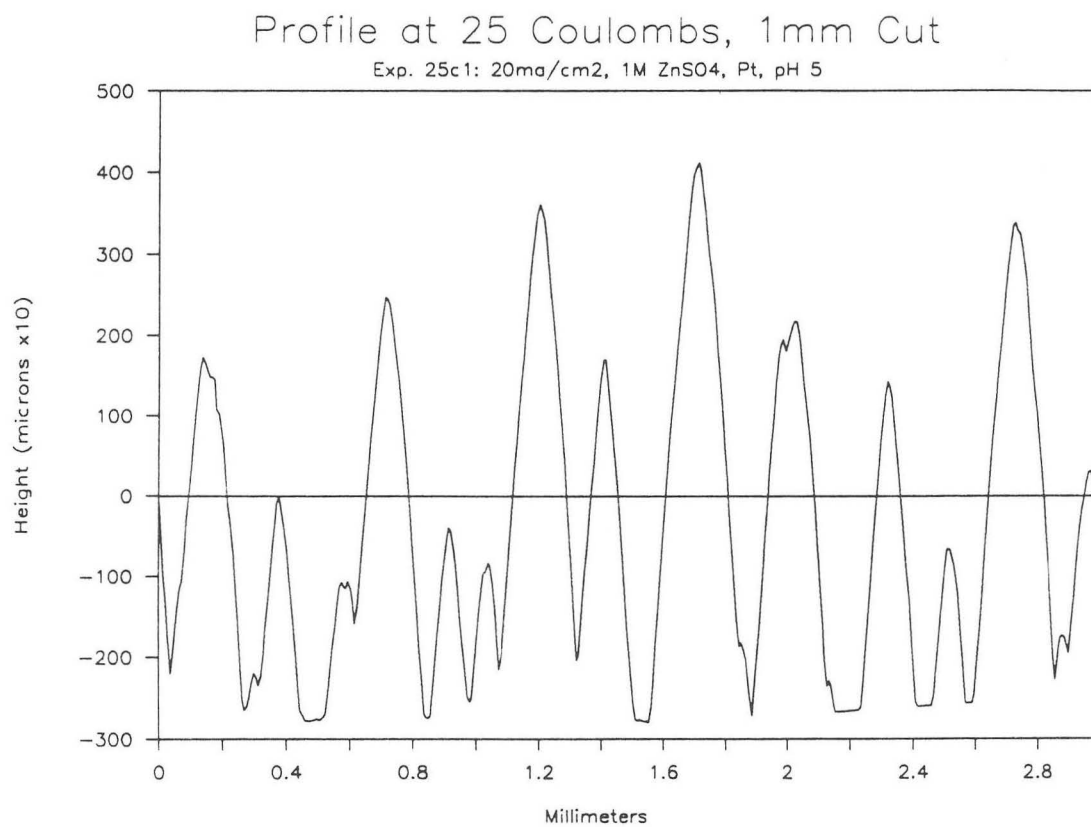


Fig. 3.7 Striated Zinc Deposit ( $40 \text{ mA/cm}^2$ ,  $40 \text{ C/cm}^2$ ) XBB 886-6460 A



XBL 902-363

Figure 3.8 Cross-sectional profile of a striated zinc deposit scanned 1 mm from the leading edge. The deposit was plated at a rate of  $20 \text{ mA/cm}^2$  from a  $1\text{M ZnSO}_4$  unsupported electrolyte, pH 5. Two periods are evident in the SPD, the distance between neighboring peaks, and the period between nearest tall ridges.

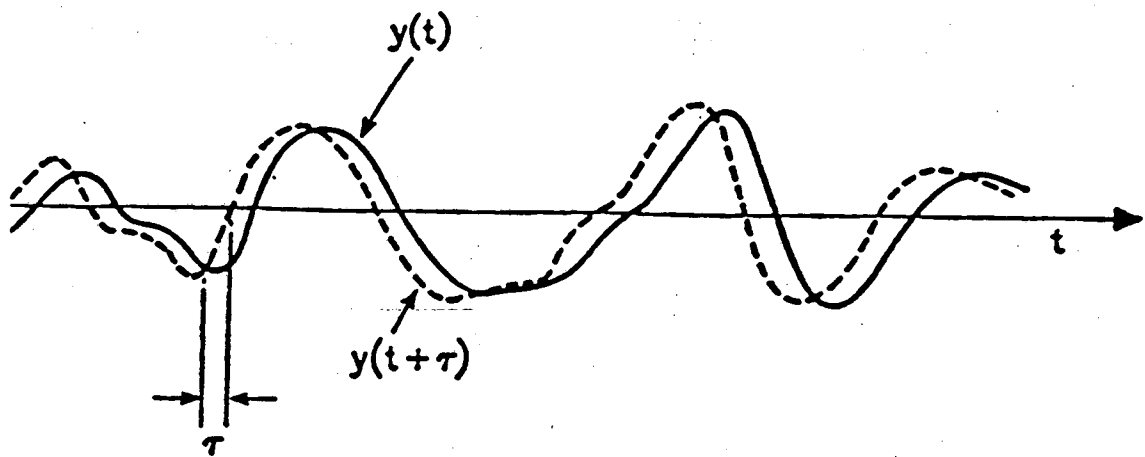


Figure 3.9 Auto-correlations of a function are calculated in an analogous manner to shifting the function by a delay  $\tau$  and multiplying the function by itself at all points, then normalizing the sum of the product by the maximum value for all shifts  $\tau$ . A correlation of one occurs at  $\tau=0$  and whenever the function matches the shifted function  $y(t + \tau)$  exactly.


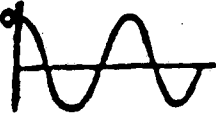

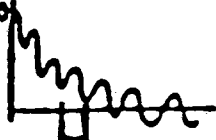

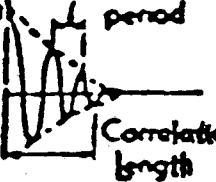
PEKLENIK TYPOLOGY		
GROUP	WAVEFORM	AUTO CORRELATION
I	 <p>Deterministic</p>	
II	 <p>Additive</p>	
III	 <p>Modulated</p>	

Figure 3.10 Grouping of auto-correlations according to type, in the manner of Peklenik [120]. A deterministic function of arbitrary phase will produce a phase-shifted auto-correlation. More complicated input signals will result in weaker correlations with increasing distance from the origin, and may display more than one correlation period.

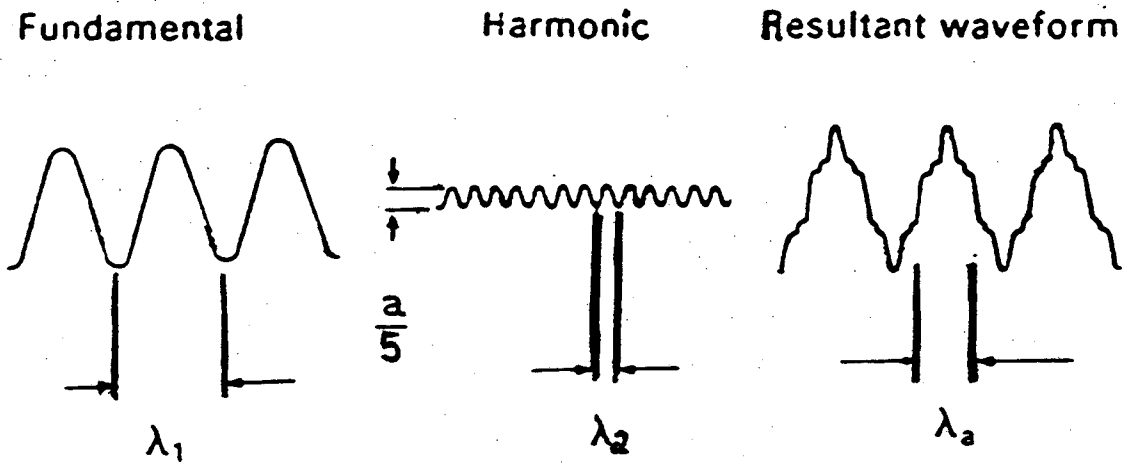


Figure 3.11. Addition of a weak harmonic to a fundamental frequency gives the resulting waveform an intermediate period which appears in its Fourier decomposition. From a figure in [120].

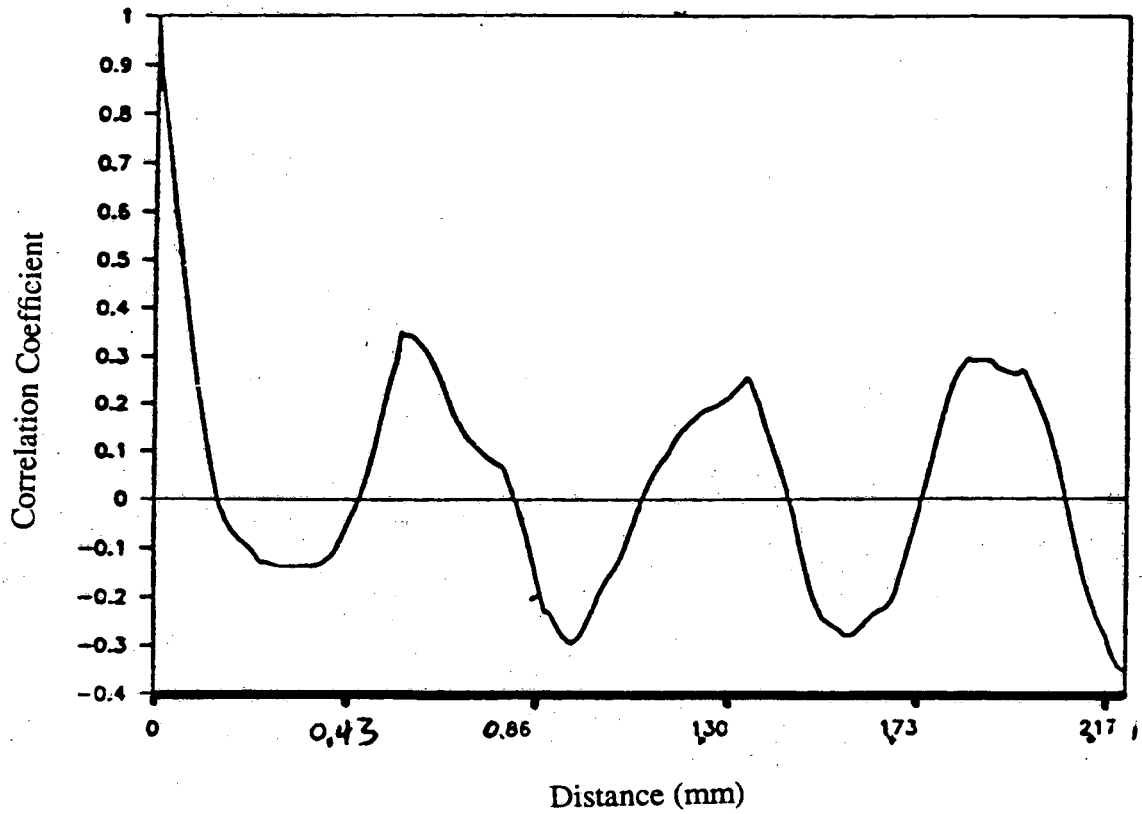


Figure 3.12. Auto-correlation of a deposit cross-section with high-amplitude striations. The saw-toothed auto-correlation function implies that the input was square-waved; the striations are flat with steep side slopes.



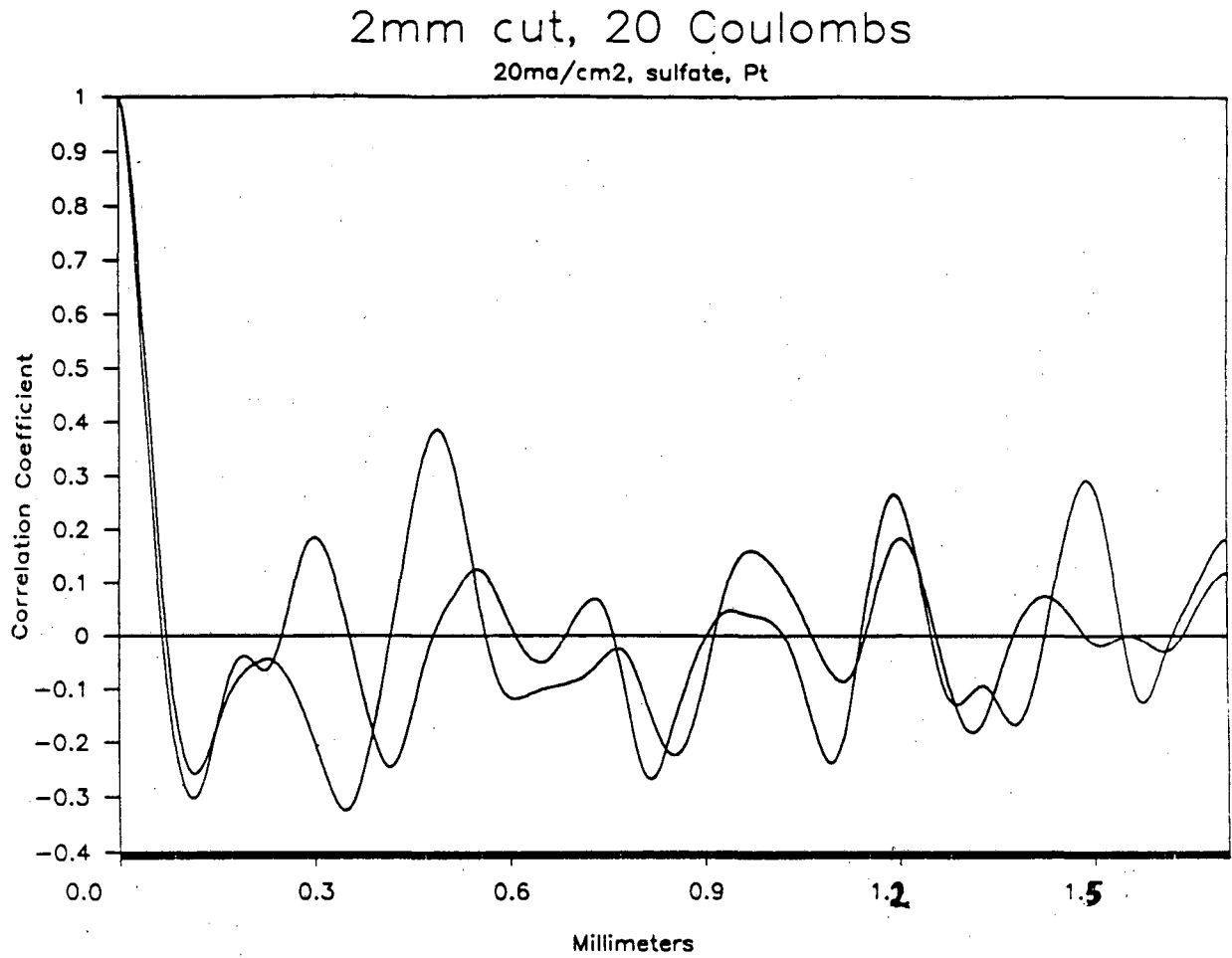


Figure 3.13. Auto-correlation functions from two separate electrodes plated at the same current density, 20 mA/cm<sup>2</sup>, and profiled 2 mm from the leading edge.

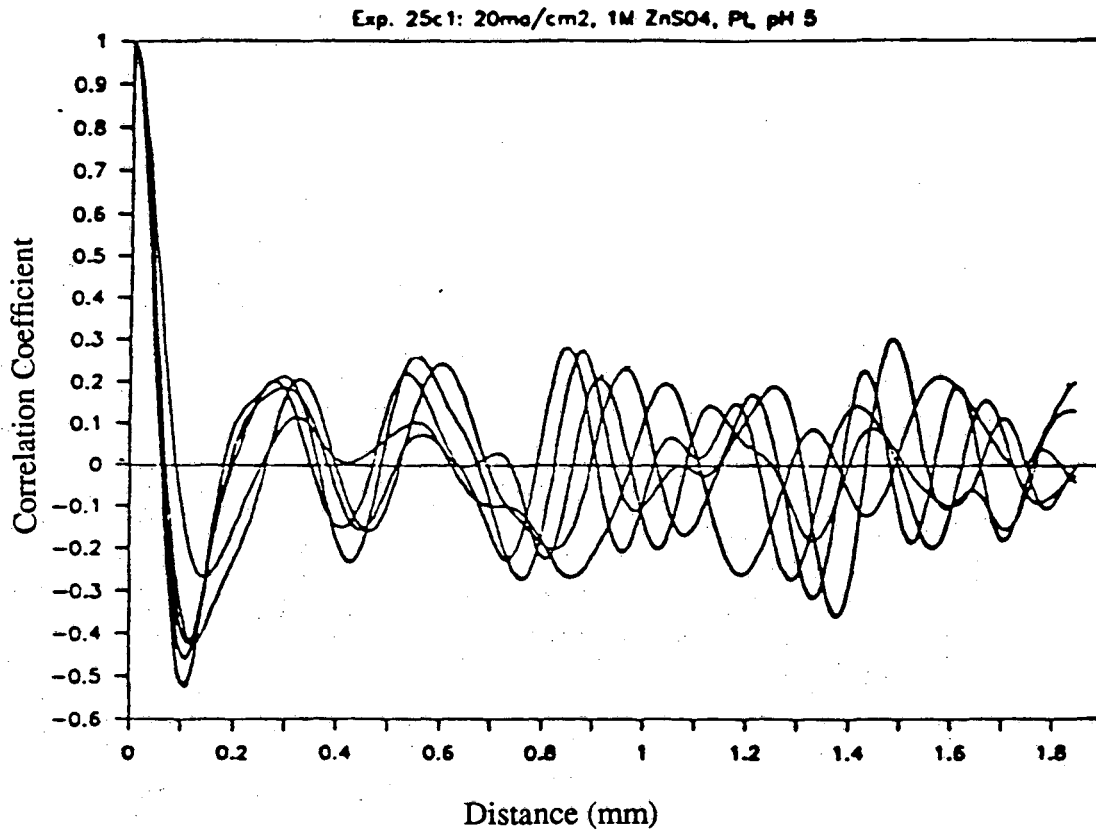


Figure 3.14. Superimposed auto-correlation functions from profiles taken at different distances from the leading edge. A small shift in the dominant mode appears with increasing distance from the leading edge.

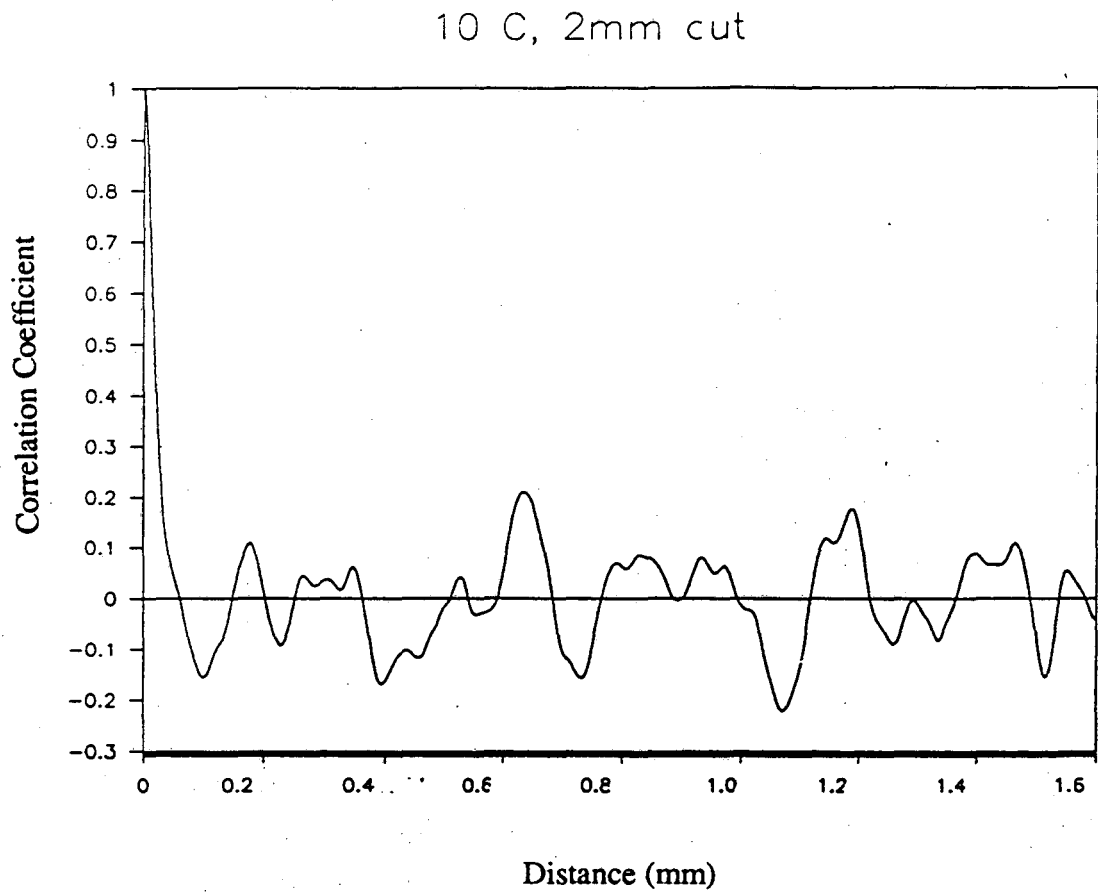


Figure 3.15. Auto-correlation function from a profile taken at 2mm from the leading edge, after 10 Coulombs of deposition at  $20 \text{ mA/cm}^2$ .

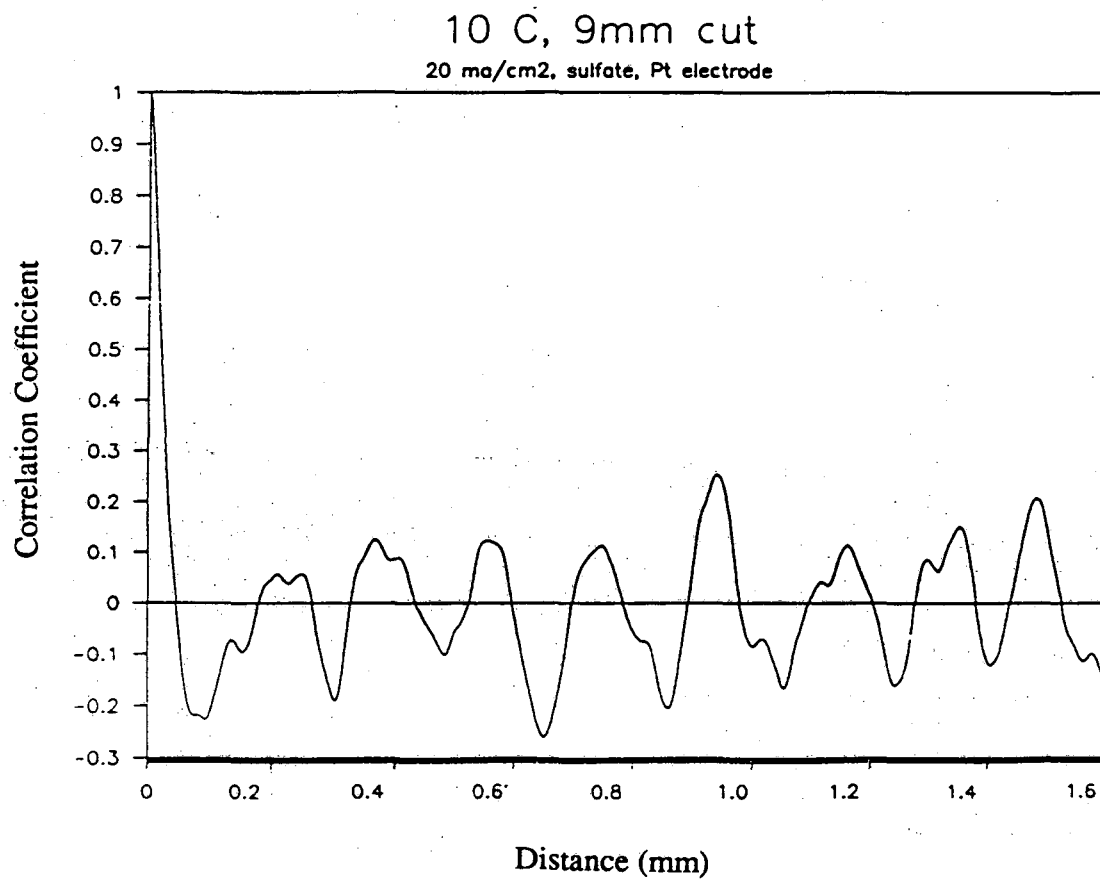
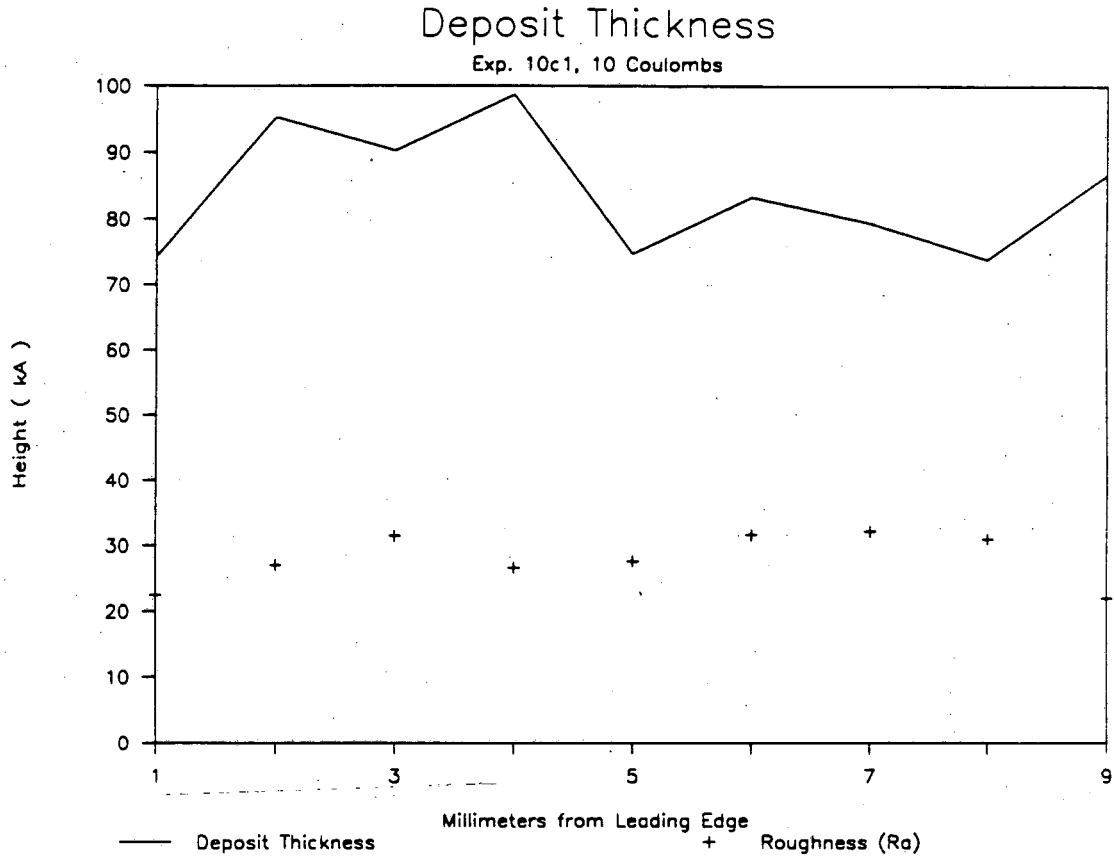
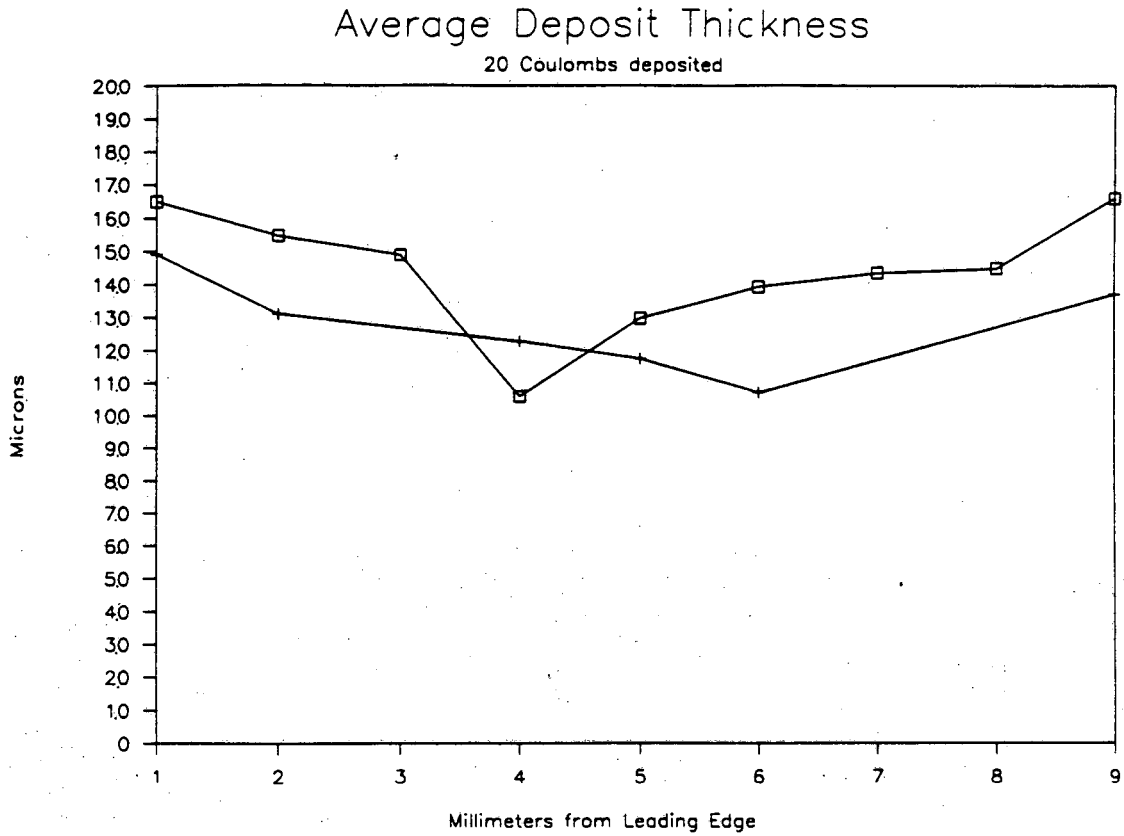


Figure 3.16. Auto-correlation function from a profile taken at 9 mm from the leading edge, after 10 Coulombs of deposition at 20 mA/cm<sup>2</sup>.



XBL 902-364

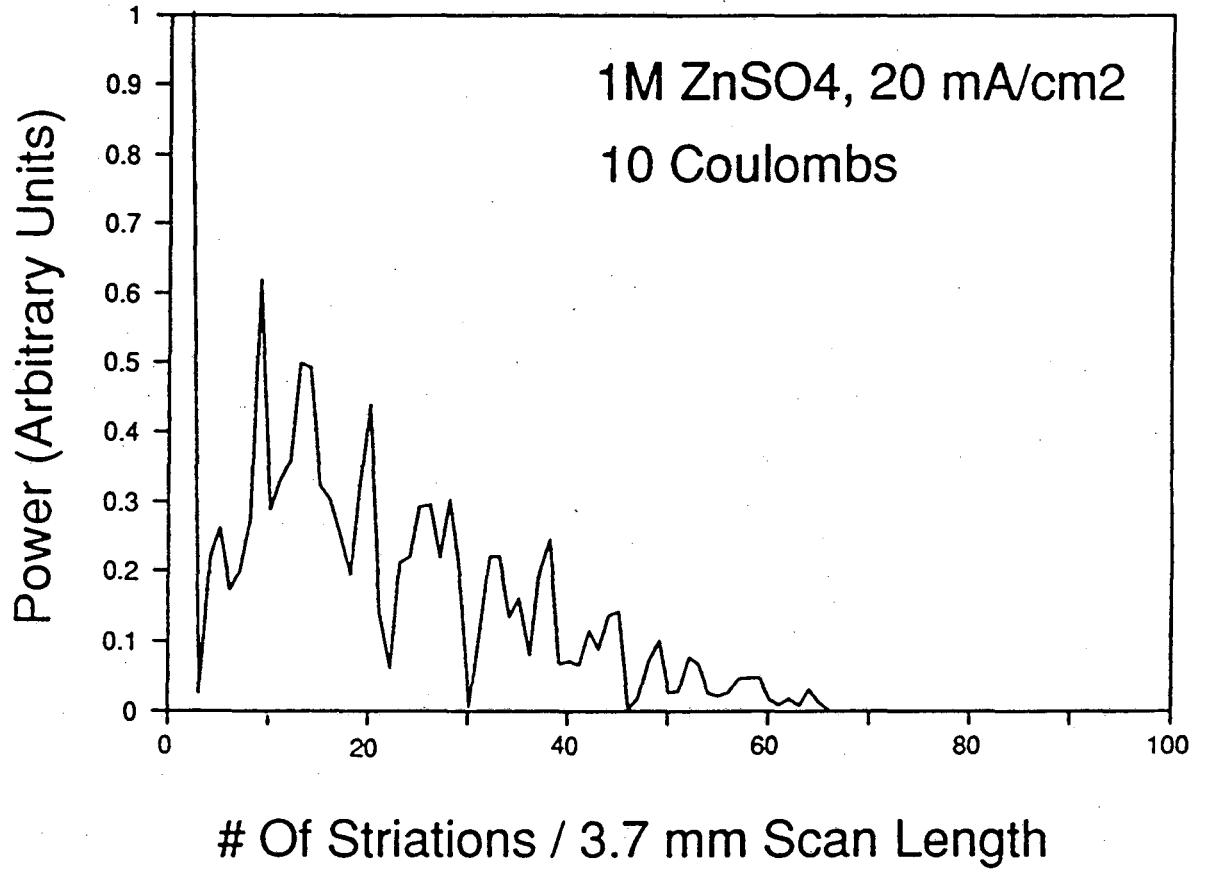
Figure 3.17. Deposit thickness and roughness after the deposition of 10 Coulombs of zinc ( $20 \text{ C/cm}^2$ ).



XBL 902-357

Figure 3.18. Deposit thickness on two separate electrodes after the deposition of 20 Coulombs of zinc ( $40 \text{ C/cm}^2$ ).

# Spectral Power Density



XBL 911-79

Figure 3.19 a) Spectral power density averaged for a total of 27 profiles of three separate electrodes at nine different distances from the leading edge, for a 10 Coulomb zinc deposit (20 mA/cm<sup>2</sup>, ZnSO<sub>4</sub>).

### Spectral Power Density

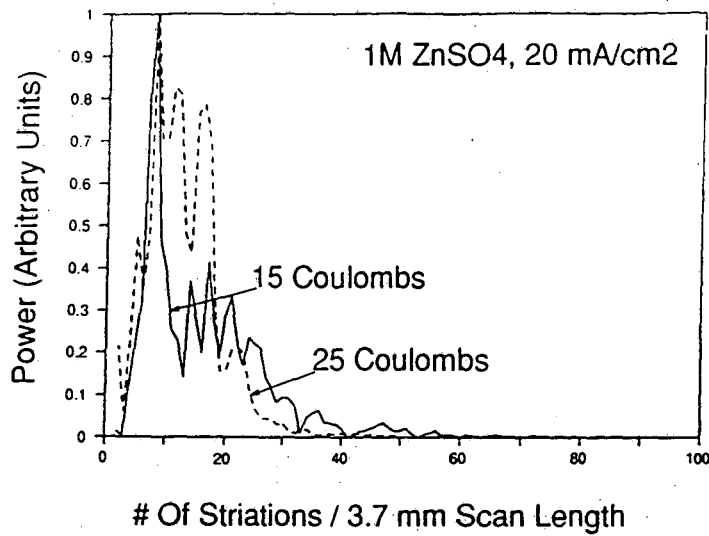


Figure 3.19 b)

XBL 911-78

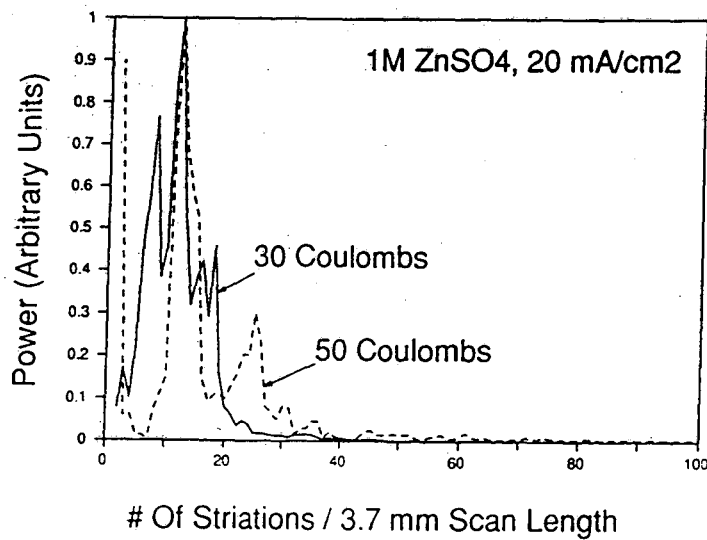


Figure 3.19 c)

XBL 911-77

Figure 3.19 b) and c) Spectral power density averaged for a total of 27 profiles of three separate electrodes at nine different distances from the leading edge, for a 20 - 50 Coulomb zinc deposits (20 mA/cm<sup>2</sup>, ZnSO<sub>4</sub>).



## Spectral Power Density

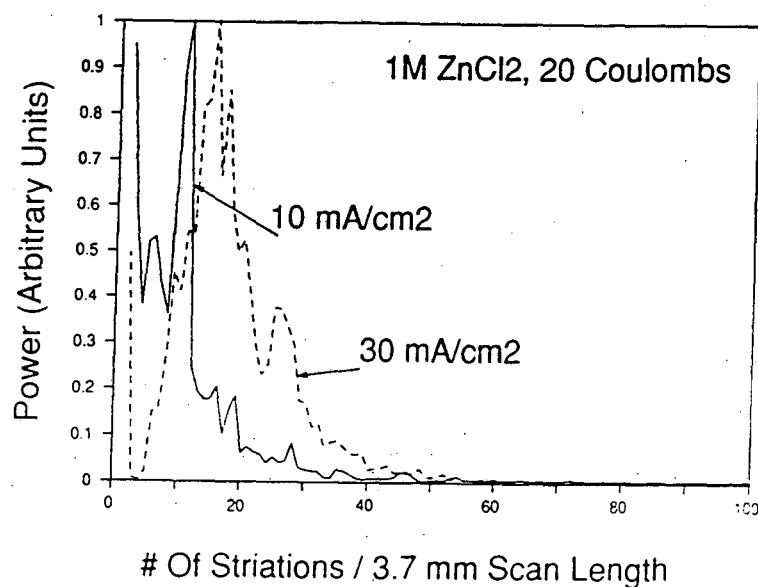
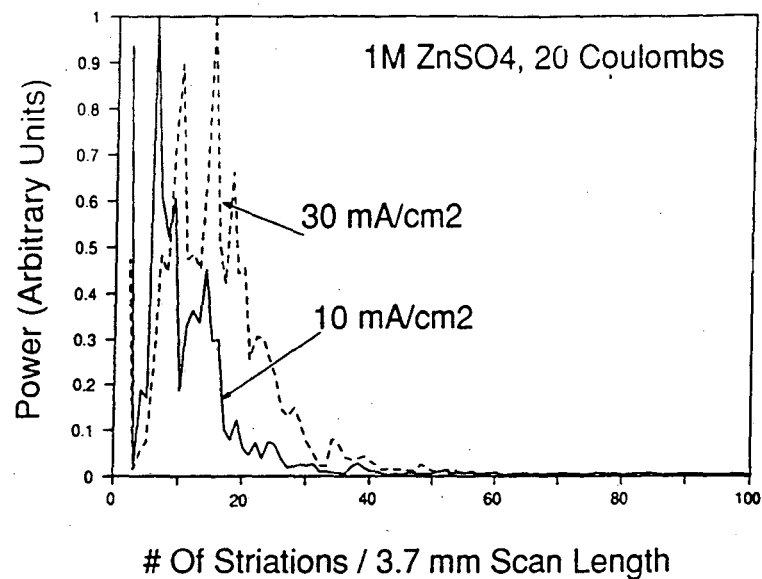


Figure 3.20 a) and b) Spectral power density of deposits plated at 10 mA/cm<sup>2</sup> and 30 mA/cm<sup>2</sup> in a) zinc sulfate and b) zinc chloride solutions.

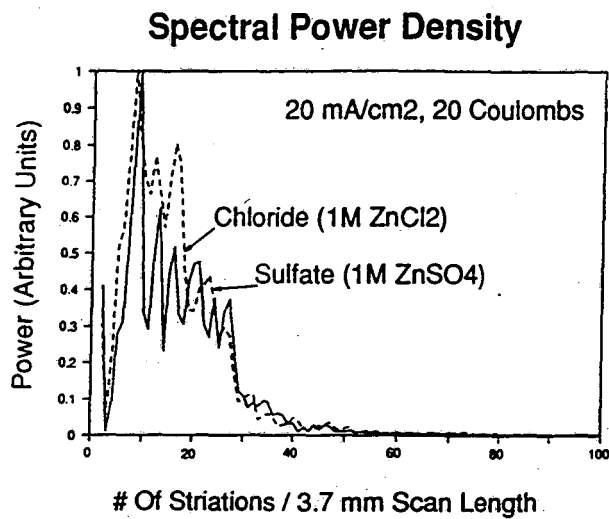


Figure 3.21 a)

XBL 911-72

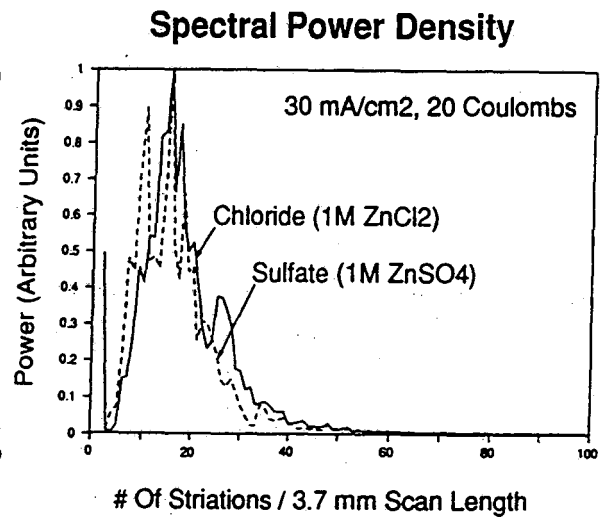


Figure 3.21 b)

XBL 911-73

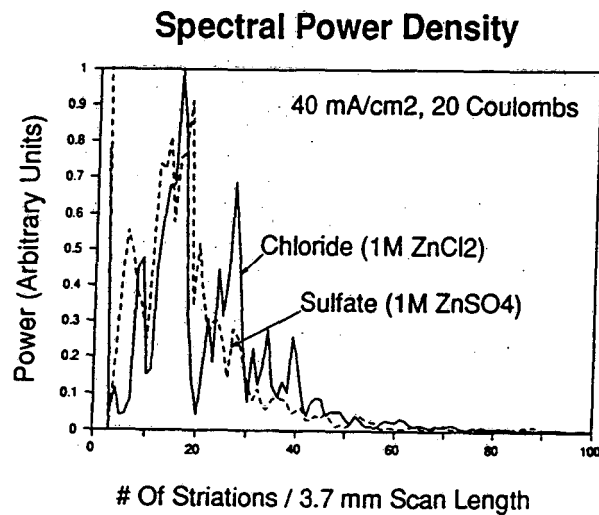
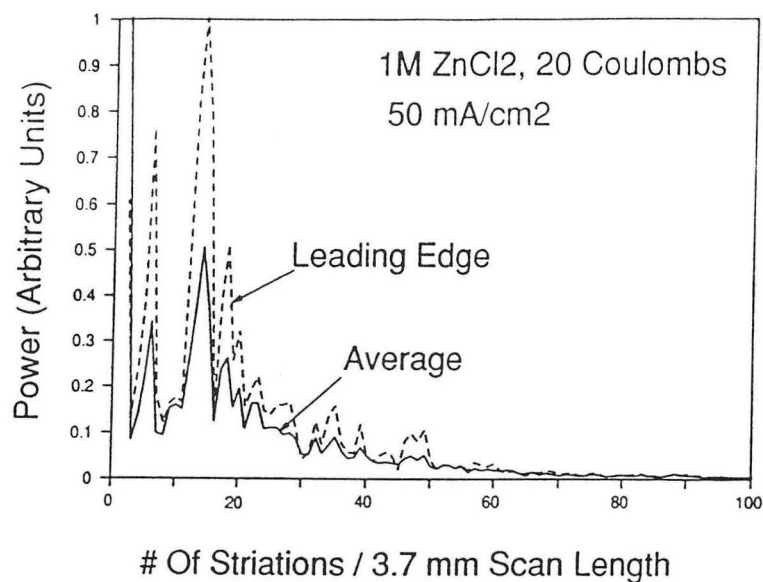


Figure 3.21 c)

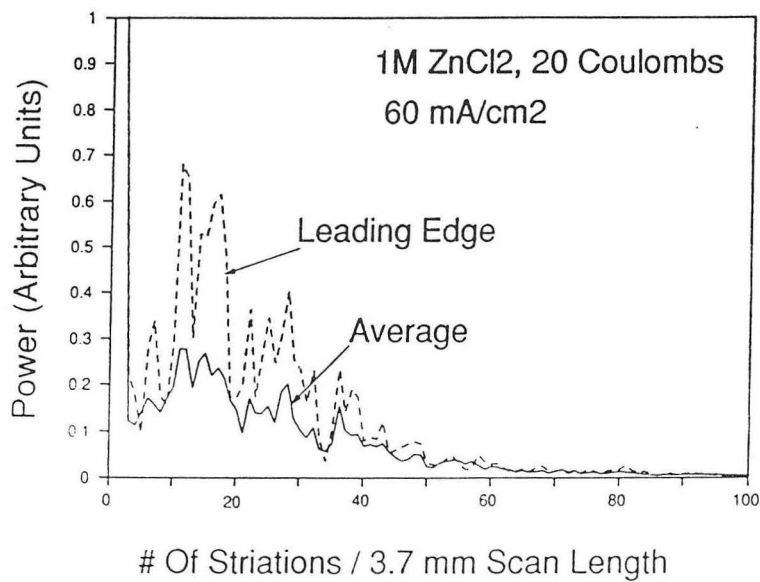
XBL 911-74

Figure 3.21 a), b), and c) A comparison of spectral power densities of zinc profiles on deposits from chloride and sulfate electrolytes.

## Spectral Power Density

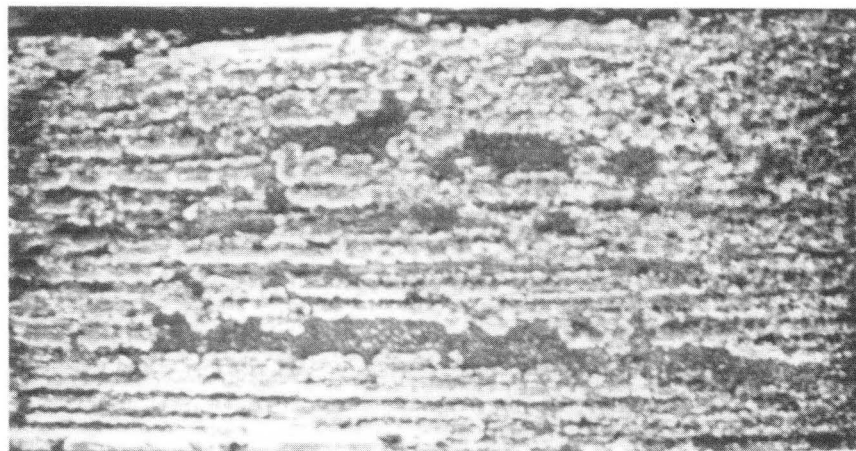


XBL 911-70



XBL 911-71

Figure 3.22 a), b), and c) A comparison of spectral power densities of profiles taken near the leading edge versus the average spectra of all nine profiles for deposits at 50 and 60 mA/cm<sup>2</sup>.



1mm

Fig. 3.23 Striated zinc deposit ( $10 \text{ mA/cm}^2$ ,  $40\text{C/cm}^2$ ) from a well-supported ( $1\text{M ZnCl}_2 + 2\text{M KCl}$ ) solution.

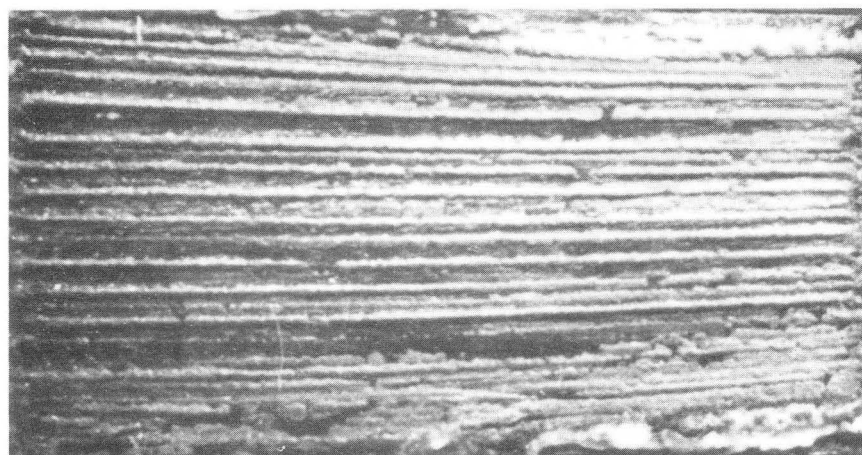
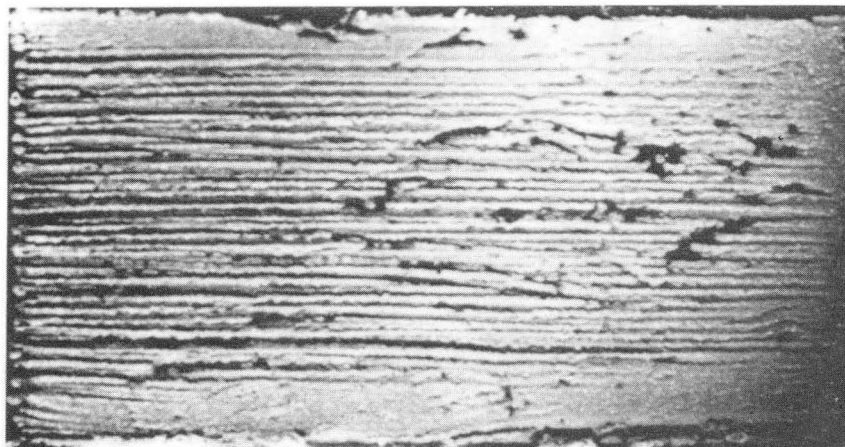


Fig. 3.24 Striated zinc deposit ( $20 \text{ mA/cm}^2$ ,  $40\text{C/cm}^2$ ) from a well-supported ( $1\text{M ZnCl}_2 + 2\text{M KCl}$ ) solution. XBB 906-4911A



1mm

Fig. 3.25 Striated zinc deposit ( $30 \text{ mA/cm}^2$ ,  $40 \text{ C/cm}^2$ ) from a well-supported ( $1 \text{ M ZnCl}_2 + 2 \text{ M KCl}$ ) solution.

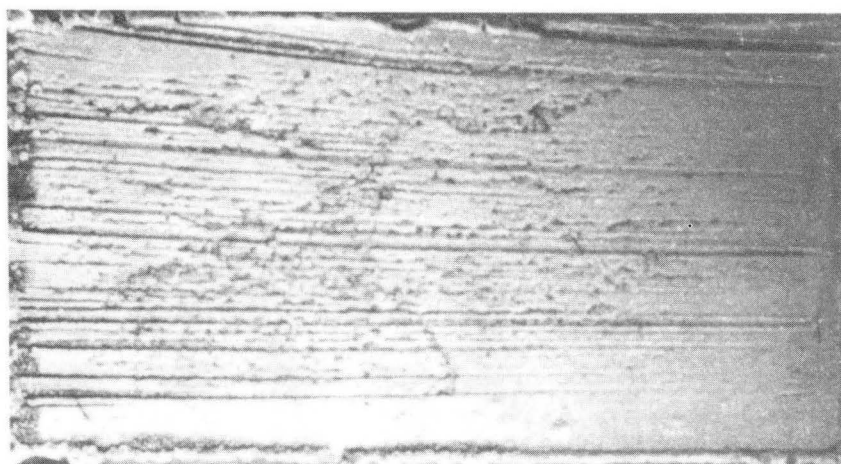


Fig. 3.26 Striated zinc deposit ( $40 \text{ mA/cm}^2$ ,  $40 \text{ C/cm}^2$ ) from a well-supported ( $1 \text{ M ZnCl}_2 + 2 \text{ M KCl}$ ) solution. XBB 906-4909 A

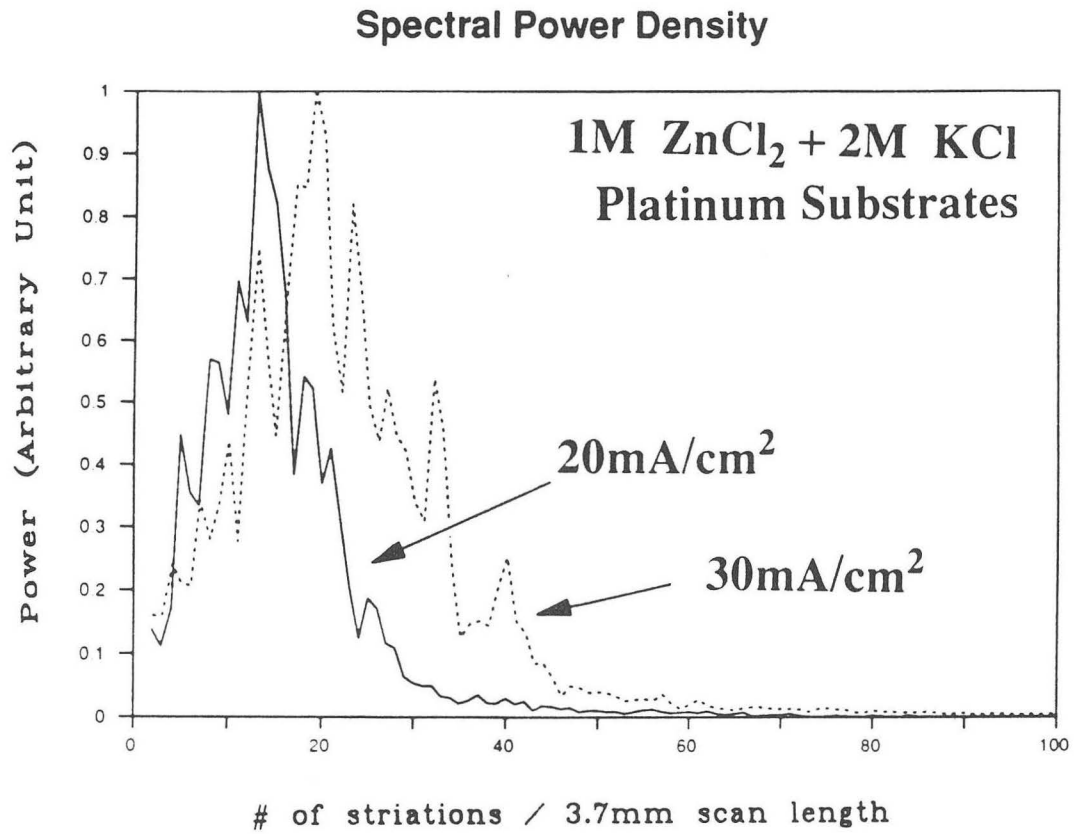


Figure 3.27. Spectral power density of striated zinc deposit profiles.

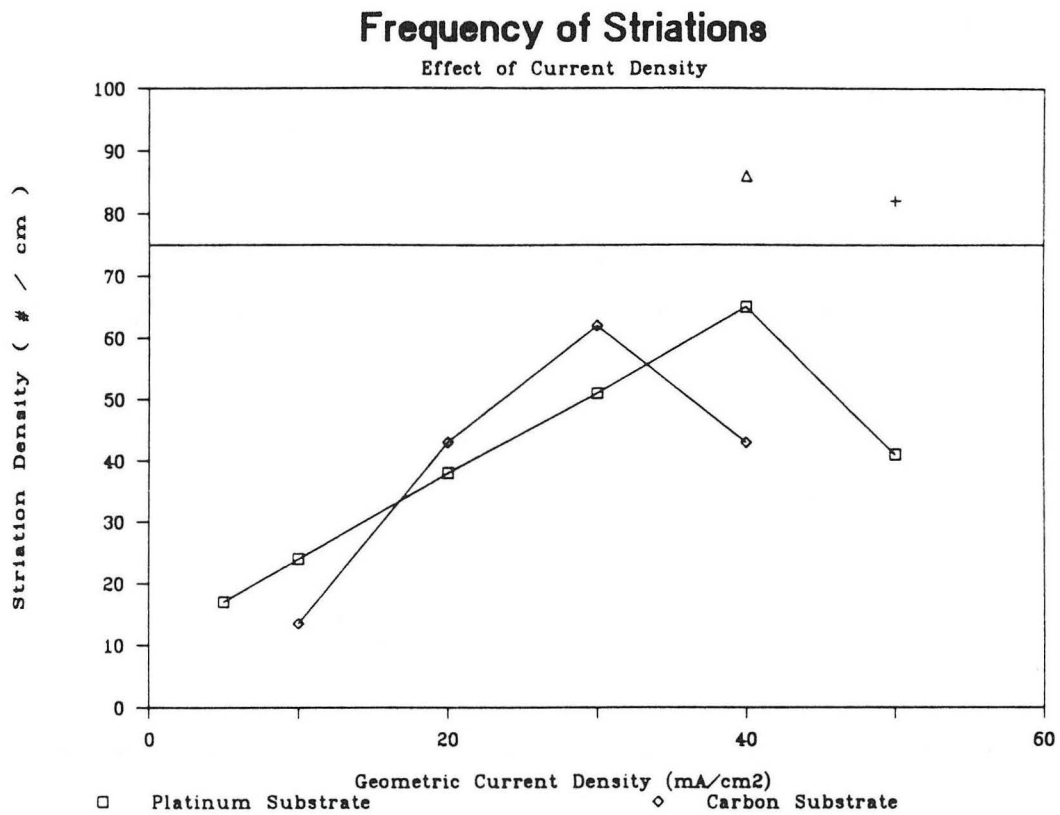
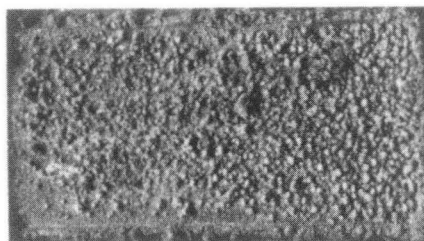


Figure 3.28. Frequency of striations as a function of current density and substrate. Frequency rises with current density until the striae meld; the frequency then falls to half of the expected value.

## MICRO-PATTERNED ELECTRODES

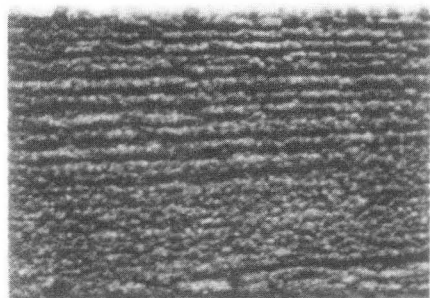
Effect on Zinc Electrodeposits



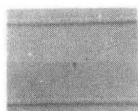
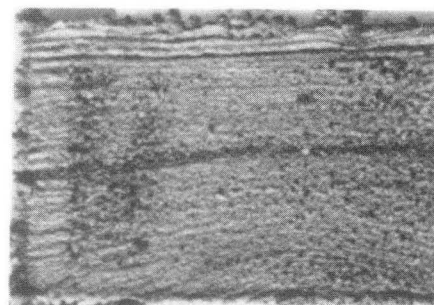
1mm

Unpatterned Control Electrode

Artificial Striae Pattern



Nodular Array Pattern



90 Coulombs

1M  $\text{ZnCl}_2$  and 2M KCl  
 pH = 5.0;  $i = 30 \frac{\text{mA}}{\text{cm}^2}$   
 Re = 2000 (Laminar flow)



Fig. 3.29 The effect of micron-scale patterns on the macro-morphology of zinc electro-deposits. The deposit obtained in a control experiment on a polished platinum surface was nodular, but not striated. At the same conditions, deposits on an MPE show thin and thick striae, depending on the underlying pattern.  
 XBB886-6458B



## Chapter 4 - Analysis of the Causes for the Emergence of Striations

### 4.1 Problem Statement

When zinc is electrodeposited from acid electrolytes in the presence of forced convection, three-dimensional nucleation is followed by the growth of micron-sized nodules. Below a maximum current density, these nodules elongate and form a periodic striated pattern perpendicular to the flow direction. This behavior is perplexing at low deposition rates, since the development of such patterns are usually associated with substantial local depletion of a reacting species. In zinc, counterintuitively, striae appear at current densities below 5-10% of the limiting value, and disappear at higher current densities.

### 4.2 Previous Theories for Striation Emergence

A number of theories have been advanced to explain the genesis of striations. Unfortunately, none of them is able to match the experimental observations satisfactorily. While pattern emergence is a complex phenomenon and may have a combination of causes, some factors may be discounted as primary. To this end, we will first briefly review previously proposed explanations:

#### 4.2.1 Presence of Impurities.

Jaksic [23] and Tsuda [34] both studied the effect of surfactants and inorganic impurities on the formation of striae. Under broad ranges of experimental conditions in ultra-pure solutions, striated deposits developed.

The emergence of striae was delayed, however, when the solution was kept at high purity; in contrast, the addition of hydrogen-promoting impurities accelerated their formation. The addition of hydrogen-inhibiting inorganic adulterants led to a longer initiation time and fewer ridges. The addition of surfactants resulted in a smoother

appearance related to densely-spaced ridges. These observations can be explained by the changes that such impurities induce in zinc nucleation behavior and current efficiency.

#### 4.2.2 Degree of Complexation.

Striations appear both in sulfate solutions, which are non-complexing, and in chloride and bromide solutions, which complex zinc ions to varying degrees, as seen in Fig. 3.10. It has been postulated that complexation hinders the availability of zinc ions for the deposition reaction, so that the actual limiting current is less than in a non-complexed solution. Although this idea has merit, the current densities at which striae appear are typically less than 10% of the measured limiting value, and since striae still occur in sulfate solutions, this effect cannot be important. Fig. 4.1, from McBreen and Cairns [50], shows how zinc ions are distributed among various complexes. Only if equilibration between complexes were slow, and if the deposition reaction occurred preferentially from the  $Zn^{+2}$  ion, would this partitioning have a direct effect on mass-transport. The effect on migration is a weaker one, and in the presence of supporting electrolyte it is negligible. In well-supported electrolytes, striations still appear.

#### 4.2.3 Bubble Wakes.

Selman [56] found that in rotating cylinder systems, zinc striae occur only at conditions where hydrogen gas bubbles also appear, and that bubbles are the initiators of striae. Because of centrifugal forces, bubbles congregate at the electrode surface and interfere with and obscure the deposition process. To study whether striae occur in the absence of significant hydrogen evolution, McVay [31] deposited zinc at conditions of high current efficiency (98% +) in an *in-situ* flow cell. Her time-lapse video of the deposition process shows that nodules elongate and line-up without the presence of any macroscopic flow disturbance or hydrogen bubbles upstream of the nodules themselves.

Both Jaksic [22-24] and the present author have performed experiments at low pH, where bubble coverage is high. Rather than catalyzing striae emergence, bubbles attached to the surface impede the elongation of striae downstream. Figure 4.2 shows how striae bend around bubble imprints and then resume their periodic spacing downstream of the disturbance.

#### 4.2.4 *Edge or Substrate Effects.*

On small electrodes, such as those used in our studies, the effect of edges must be carefully considered. Under some conditions, the number of striae that appear across an electrode is five or fewer, and the non-uniform current distribution at the edge may affect the spacing of striae. The leading edge may also play a significant role in determining striation wavelength.

Faltemier [17] tested the effect of electrode size by depositing zinc in a much larger flow cell, with electrodes that were 20 cm long and 5 cm in across. He observed that at low current densities, striae eventually span the entire electrode surface and have the same period as on smaller electrodes. What his photographs show, however, is that a single striation is unlikely to extend the entire electrode length, rather, the average number stays constant, but individual striae tend to emerge between neighbors and meld back into neighbors over a finite distance [16].

The effect of foreign substrates was also considered, and discounted as a direct cause of striae. Zinc striae appear even when the deposition process occurs on zinc itself, which shows that the emergence of striae is not a foreign substrate effect. Zinc deposition on zinc also includes nodule formation, which is a direct precursor for the appearance of striae. It may be noted, then, that to support reasonable current densities, it is necessary to create 3D nuclei, and these nuclei have a much faster growth rate than on the zinc substrate itself. The rate enhancement may be caused by the greater number of defects on the emerging nodules. If kink and edge sites are present at a larger con-

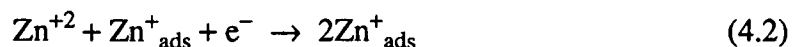
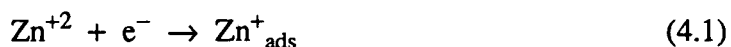
centration than on a polished surface, they may account for the differential rate of growth between nodules and the underlying surface.

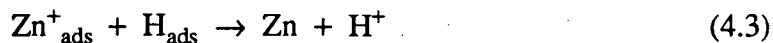
Fig. 3.18 shows the striation frequency on platinum and graphite substrates as a function of the applied current density. While the frequency of striations at a given applied current differ between the two substrate materials, the maximum stable frequency is the same for both. This seems to coincide with the observation that at high current densities the striae meld together before they can form distinct ridges. While different substrates may alter the range of currents over which striae are formed, by changing the nucleation characteristics, they do not directly determine whether striae appear, as long as the zinc nodule density is sufficiently low.

#### 4.2.5 Auto-catalytic Zinc/Hydrogen co-evolution.

According to Epelboin and co-workers [66-69], voltammetry and impedance studies show that zinc deposition is an auto-catalytic reaction. They argue that two-electron transfer is unlikely, and that the reaction sequence must proceed in two consecutive steps. While the intermediate uni-valent zinc species, said to exist as an adsorbate on the surface, has not been detected directly, Epelboin et al. argue that the presence of a backward-bending region in the I-V curve obtained during cyclic voltammetry shows that a catalytic intermediate exists. The negative slope appears after correction for ohmic drop, and covers a region of only two to four millivolts, as seen in Fig. 4.3 from [69]. It occurs only at high zinc ion concentrations.

Epelboin et al. have variously identified the catalytic intermediate in their theory as either the univalent zinc species itself, or an adsorbed hydrogen species. Their proposed reaction sequence involves four separate steps, listed below:





The deposition of zinc in this model must proceed through the prior formation of a uni-valent intermediate which auto-catalyzes the deposition reaction. Adsorbed hydrogen also plays a catalytic role, as an alternative pathway to zinc deposition.

Epelboin et al.'s reaction scheme is quite complicated, and there is no direct evidence to support their claims. Their proposal that a negative resistance region exists during zinc deposition fails to account for the fact that during his experiments, the active area of his deposit may be changing substantially through nucleation and 3-D growth. Smaller kinetic overpotentials would then be expected as a function of time during a galvanostatic experiment. Even with a slowly increasing current density, as in a voltammetric sweep, a small decrease in the kinetic overpotential may be detected in some cases. Since, as noted above, the negative resistance region is about two millivolts wide, a small (less than 4%) error in his ohmic compensation may be the culprit. Thus, his impedance and voltammetry data may be explained by recognizing that the real surface area is growing as deposition proceeds.

#### 4.2.6 Goertler vortices.

Jaksic proposed that striae are caused by Goertler vortices [22]. While vortices occur in a number of flow situations, paired counter-rotating Taylor-Goertler vortices are usually associated only with flow over smoothly-curved surfaces, and not over a bump or set of bumps which are much smaller than the hydrodynamic boundary layer [38a]. Furthermore, if striae appeared as a result of vortices, their frequency would depend on vortex spacing, which, in turn, is a function of the Reynolds number. The apparent lack of correlation in this respect tends to rule out this hypothesis. It is hard to imagine how such vortices would occur not only in laminar, channel flow, but also in rotating disk and rotating cylinder geometries or in a turbulent flow regime.

This proposed explanation also fails to account for what makes zinc a unique material. The appearance of Taylor-Goertler vortices would have to be a general condition of all electrodeposition experiments in laminar flow fields. If so, then the electrodeposition of metals at low fractions of limiting current would often exhibit striations. This is not the case. One must instead focus on the distinctive nature of zinc deposition, on its nucleation and its kinetics, to determine the reasons for the emergence of striations.

Vortices may occur in the wakes of protruding obstructions, but they would be localized to the area immediately behind protrusions which occur in the initial stages of deposition. Vortices have been observed under turbulent conditions, for example, in the wake of small macroscopic objects in a flow cell. Horseshoe vortices appear in air streams [113], at either side of blocks glued to smooth walls in a channel flow cell and extends a long distance downstream. As expected, heat transfer studies show that such vortices significantly promote transport in the wake of protrusions. The conditions in striae experiments are at sufficiently low Reynolds number to discount the possibility that horseshoe vortices occur.

The results of Fischl (discussed in Chapter 1) with 256  $\mu\text{m}$  obstructions at  $\text{Re} = 2000$ , however, show that significant mass-transfer enhancement may still occur as a result of the presence of sub-millimeter flow obstacles. The recirculation in the latter case is probably not of the horseshoe type, and tends to be fairly localized. In any case, on rotating disks, the striae first appear downstream (where the current density is highest), then propagate towards the disk center. Thus, at least for the case of striae on a rotating disk, the effect of horseshoe vortices can be discounted.

None of these theories explains why striae at low deposition rates are unique to zinc, yet appear ubiquitous when zinc is plated from a variety of acidic solutions in a number of different flow geometries. In the next section, the stages of zinc deposition are examined. The remainder of the chapter presents an alternative view, that focuses

on the particular nucleation and kinetic characteristics of zinc in an effort to explain how and why striae develop.

#### *4.3 Stages of Zinc-Deposit Morphological Development*

When the current is stepped to a constant value at the beginning of galvanostatic zinc deposition, the potential overshoots the steady-state value. This "superpolarization" occurs while the surface forms sub-microscopic zinc clusters which have a much higher activity than the flat, polished electrode. The process of charging the double-layer and hydrogen evolution consume a portion of the current, but the majority goes to the formation of these clusters, requiring an additional nucleation overpotential in addition to the kinetic one. At short times, the nuclei that form immediately are dispersed randomly and grow at a diffusion-limited rate. They have a large kinetic advantage over the surrounding surface, which is free of nuclei, and which can only grow by a two-dimensional addition of ad-atoms. This two-dimensional growth dominates at extremely low current densities, when the overpotential is never large enough to create 3D nuclei. The experimental work of Yamashita [79] determined that the exchange current density in this growth regime was very low, less than  $1 \text{ mA/cm}^2$ . Thus, the 3-D sites, which have a  $i_0$  in excess of  $100 \text{ mA/cm}^2$  [48, 49] consume as much current as diffusion will allow. As the potential is high, more nuclei will form. As more of the surface becomes covered with active clusters, the overpotential necessary to maintain the galvanostatically-applied current falls to a steady-state value.

Nucleation proceeds until the overpotential is so small that the probability of new nuclei forming is less than that of dissolving existing nuclei. The value of this "nucleation overpotential" ( $\eta_{\text{nuc}}$ ) has been measured on glassy carbon by McBreen, who reported a value of 40 mV. For large values of  $\eta_{\text{nuc}}$ , the nucleation of zinc is instantaneous, as reported by various authors [51]. The growth centers that eventually emerge from the nuclei form in the first instants of zinc deposition. After the passage of

50 mC, no new growth centers emerge [17].

Photo-micrographs taken by Tsuda [34] show that the size distribution of growth centers is fairly narrow, but that the number and average size varies greatly as the applied current density is increased (Fig. 4.4). This may be shown schematically by Fig. 4.5, where the nodule population is plotted against the mean distance to nearest neighbors; as the current is increased, both the mean distance and the variance decrease. Since essentially all of the growth at these short times occurs on nodules, the rest of the electrode surface contains at most, a thin layer of zinc.

Milchev [110] has shown that in the case of silver nodules, there exists a region of reduced surface overpotential extending up to ten nodule radii. This exclusion region is the result of an ohmic advantage which the taller nodule has over the surrounding flat surface. The nodule also has the added benefit of spherical diffusion, which facilitates mass-transport. The boundary-layer around growing nodules is illustrated in Fig. 4.6. If the nodule is isolated, it will grow fastest. Nodules that are within each others diffusion and ohmic exclusion regions grow more quickly away from one another, but they nevertheless get closer closer and meld with continuing deposition.

When the nodules reach a critical size, approximately 20  $\mu\text{m}$  in height, they begin to elongate in the direction of flow, as shown by McVay [31] and Jaksic [22-24]. They are still not completely aligned, but begin to meld and on a larger scale, show the characteristic spacing that fully emerges after the deposition of 40-50  $\text{C}/\text{cm}^2$ . The relative dimensions of the ohmic exclusion and flow recirculation regions are illustrated in Fig. 4.7. The ohmic region is axisymmetric, while the recirculation is directed in the direction of flow, giving the striae a preferred orientation. It is this time period, between the development of growth centers, and the appearance of fully-developed striae that remains puzzling.



#### 4.4 A Phenomenological Theory of Striation Emergence

Striations in zinc, according to our view, occur at low current densities because of four factors: 1) a moderately high, concentration-dependent exchange current density ( $i_0 = 100 \text{ mA/cm}^2$ ) on nucleated zinc growth centers, 2) a fairly passive non-nucleated background surface ( $i_0 = 1 \text{ mA/cm}^2$ ) where hydrogen evolution is the predominant reaction, 3) the effect of ohmic exclusion near a growing nodule and 4) local fluid recirculation in the wake of nodules. The emerging striation wavelength is thus determined by the nodule density, which is a strong function of the applied current.

While striae occur far from limiting current, it is **not** true that local concentration changes have no importance. Even at low current densities, the deposition potential deviates from the zinc equilibrium potential because of finite kinetics, ohmic drop in the electrolyte, and some depletion of the reactant near the surface. At rates below the exchange current density, the kinetic, and ohmic and concentration overpotentials are proportional to each other. This is called the 'linear' region, since the equations for the individual overpotentials can be linearized as a function of the average current density, as shown in Figure 4.8 and Equation 4.5.

For all reactions,

$$\eta = \eta_s + \eta_{\text{ohm}} + \eta_c \quad (4.5)$$

The total overpotential in the linear region is fairly modest, once the ohmic drop far from the electrode surface is neglected, as in Eq. 4.6.

$$\eta - \bar{\eta}_{\text{ohm}} = \eta_s + \eta_c + \Delta\eta_{\text{ohm}} \quad (4.6)$$

Neglecting ohmic losses far from the electrode surface allows us to define a differential ohmic drop from a chosen reference plane. The electrode surface, or perhaps, a fixed distance away from the electrode equal to the "ohmic boundary layer" may be used. Such a boundary layer can be chosen so that it is much thicker than the surface topology. In this case, the current lines at this imaginary boundary are still perpendicular to

the average surface plane. In our analysis below, the relative ohmic advantage of peaks over valleys will be estimated by this method.

The maximum current density at which striae emerge over the entire electrode after the deposition of 20 microns of deposit is 40 mA/cm<sup>2</sup> based on the original area of the flat, polished electrode. As striations develop into their usual sinusoidal pattern, however, the total macroscopic surface area of the electrode is increased by 10-40% as a sinusoidal profile develops. The actual increase depends on the ratio of striae amplitude to wavelength. This reduces the average current density based on the real area to a maximum of 28.8 mA/cm<sup>2</sup>, above which, striation do not form.

Using the consensus exchange current density from [48] with  $i_0 = 100$  mA/cm<sup>2</sup> at  $[Zn^{+2}] = 1M$ ,  $\alpha = 0.5$ , and  $n = 2$ , and a Butler-Volmer model for the current density, one can calculate the average value of the surface overpotential ( $\eta_s$  in Eq. 4.7), at the conditions where striae form.

$$i_{avg} = i_0 \left(\frac{C}{C_b}\right)^{1.5} \exp\left(\frac{\alpha_c n F \eta_s}{RT}\right) - \exp\left(-\frac{\alpha_a n F \eta_s}{RT}\right) \quad (4.7)$$

Equation 4.7 may be linearized, as seen above, resulting in Eq. 4.7a below:

$$i_{avg} = 2 i_0 \left(\frac{C}{C_b}\right)^{1.5} \frac{(\alpha_c + \alpha_a) n F \eta_s}{RT} \quad (4.7a)$$

From this linearized form, we can calculate a constant differential current per millivolt increase in surface overpotential at a given zinc concentration,

$$\left(\frac{\delta i}{\delta \eta_s}\right)_{C_{Zn} = 1} = 7.82 \text{ mA/mV} \quad (4.7b)$$

For an current density of 28.8 mA/cm<sup>2</sup>, the average surface overpotential is 3.80 mV. In this low current regime, a small change in the local surface overpotential ( $\eta_s$ ) can cause a large **relative change** in the current density. At higher currents, in the Tafel region, a doubling of the local current requires an increase in  $\eta_s$  of 9.64 mV. In the linear region, increases of less than 2.5 mV are needed for the same ratio in current densities. For

example, if the peaks of striae are growing at  $38 \text{ mA/cm}^2$  while the valleys only grow at  $19 \text{ mA/cm}^2$ , then the difference in  $\eta_s$  over the profile is only 2.5 mV. Since this corresponds to the conditions prevailing when striae grow at the highest average current density, this is also the largest deviation in  $\eta_s$  on a striated surface. This calculation overpredicts the difference in  $\eta_s$  since it neglects the roughness due to the microcrystallinity of the deposit.

Small-scale roughness can often increase the real surface area by a factor of two, which would lower the average surface overpotential to 1.78 mV, and the maximum difference in  $\eta_s$  between peaks and valleys to 1.27 mV. Furthermore, the estimate for the exchange current density may be too low, rather than too high. Landau [49] reports that for a growing dendrite, the  $i_0$  measured was  $240 \text{ mA/cm}^2$ , which would also lower the value of the overpotential by a similar ratio. These two effects may be related, however, since microcrystallinity may also increase the apparent exchange current density based on a macroscopic surface area. To stay on the conservative side in our estimates, the effect of microcrystallinity is assumed to be included in the measured value of  $i_0$ . Landau's higher value is not included in the analysis; its use would increase the sensitivity of the zinc deposition reaction to small local variations in concentration and solution conductivity.

The cotemporal evolution of hydrogen gas on the same surface must also be considered. Although the exchange current density of  $\text{H}_2/\text{Zn}$  is very low,  $3.2 \times 10^{-11}$  [36], even at a pH of 5.4 one can calculate that the hydrogen partial current may be as high as  $0.9 \text{ mA/cm}^2$  as shown in Fig. 4.9. This discounts diffusion limitations on the hydrogen ion, however. If these limitations are not significant, as in the leading edge of a channel flow cell, the open-circuit potential lies 0.11 mV anodic of the zinc equilibrium potential under these assumptions. The overpotential reported above must then be corrected by this amount, yielding an average zinc surface overpotential of 3.68 mV.

#### 4.4.1 Estimates of Local Variations in Ohmic and Concentration Overpotential

At 40 mA/cm<sup>2</sup> (based on the geometric area), the difference in thickness of the zinc deposit between the top and bottom of a striation plated from a solution of 1M zinc chloride is a factor of two. This increases to a factor of approximately 5:1 at 15 mA/cm<sup>2</sup>, and below 10 mA/cm<sup>2</sup>, bare substrate can be seen between the ridged zinc deposits. The deposit can be approximated by a sinusoidal wave, with an amplitude of 20 microns (average height = 20 microns), and a wavelength that varies linearly with the average zinc current. Experimentally, the wavelength at 10 mA/cm<sup>2</sup> is 600 microns, while at 40 mA/cm<sup>2</sup> the wavelength is 170 microns.

Data given in Table 4.2 show that in all five cases shown, the difference in surface overpotential between a striation peak and adjoining valley was less than 2.5 mV, even though the range of applied current densities (based on the geometric area) was a factor of eight. Evidently, a key role of the decreasing striation wavelength is to provide additional macroscopic surface area. Combining this with increasing current to the striation valleys keeps the difference in surface overpotential to a value of approximately two millivolts.

At higher current densities, about half of the difference can be attributed to variations in ohmic drop, which is estimated in two ways. a) By assuming that the bottom of the profile is hindered by a amount equal to the resistivity of the solution multiplied by the profile height and the average current density:

$$\Delta\eta_{\text{ohm}} = i_{\text{avg}} l \rho. \quad (4.8)$$

This is an approximate result, and somewhat overestimates the difference in local surface overpotentials. b) The second method is a better approximation: one defines a flat equipotential plane at some distance from the surface, and assuming no change in resistivity as a function of concentration, determines the difference in ohmic drop to the top and bottom of the profile. In the case of primary current distribution solved numerically

by Prentice and Tobias [31], once the ratio of amplitude to wavelength of a sinusoidal profile exceeds 0.15, the valley region has a greatly diminished current density. This numerical result may also be used to estimate the distance at which the potential lines become parallel to the average surface plane, and the current distribution becomes uniform. The thickness of this "ohmic boundary layer" ranges from  $0.4 \lambda$  to  $0.58 \lambda$ , as seen in Table 4.3 and shown schematically in Fig. 4.10. The ohmic drop from this surface to the profile is equal to the resistivity multiplied by the average current along a perpendicular line from the equipotential plane to the surface and the distance along that line. This average current is not equal to the surface average current density, and must be estimated separately.

$$\Delta\eta_{\text{ohm}} = \int_h^{\delta_{\text{ohm}}} i \, dl. \quad (4.9)$$

$$\Delta\eta_{\text{ohm}} \approx (\delta_{\text{ohm}} - h) i_{\text{avg}} \rho. \quad (4.10)$$

If the arithmetic mean between the local and average surface current density is used as an approximation for this value, the ohmic drop to peaks ( $\Delta\eta_{\text{ohm}}^{\text{peak}}$ ) is **larger** than the ohmic drop to valleys at low average current densities, and lower than  $\Delta\eta_{\text{ohm}}^{\text{valley}}$  at higher average current densities, as seen in Table 4.2.

The difference in ohmic drop between the peak and valley is, at most, responsible for only a portion of the difference in surface overpotential between the peak of a growth center and the surrounding valley. The rest must be caused by changes in the local concentration of the reactant. This increases  $\eta_c$  in the valleys and concurrently lowers the exchange current density. Ohmic effects, in any case, could not be the sole cause of the formation of striae, since they do not explain the directionality of striation propagation. There must be an advantage for striae to grow downstream in channel electrodes, and upstream on rotating disks. In both cases, they emerge where the current density is highest, and where there is probably a substantial ohmic advantage

for the growth of peaks, but they propagate based on the presence of enhanced concentration regions.

It may be supposed, based on the work of Fischl [18] and McLarnon [30] that recirculation preceding and trailing emerging nodules replenishes the electrolyte near the electrode surface with solution of bulk concentration. If so, it is possible to calculate what concentration the solution must have at the sides of the nodules to be disadvantaged to the same degree as they are versus the peaks of the striation.

If the entire 2.5 mV differential overpotential were caused by a concentration effect, according to the Nernst equation [37], the valley would be 18% more depleted than the peaks. Since some of the difference in  $\eta$  is accounted for by an ohmic advantage, the valley may be only depleted by, say, 10%. This would mean that the concentration overpotential in the valleys is 1.33 mV larger than at the peaks, but the exchange current density concurrently falls by 15%. If the surface overpotential at the base of striae were between 1 and 2 mV, lowering the concentration would add an additional 0.2-0.3 mV to  $\eta_s$ . The combined effect of the 10% difference in concentrations is approximately 1.6 mV, while the ohmic advantage would contribute the additional 0.9 mV.

This entire analysis does not address one point, however. At times, the apparently bare substrate appears between neighboring striae. This occurs frequently at current densities below 10 mA/cm<sup>2</sup>, but can sometimes happen even at higher deposition rates. If the surface is completely quiescent, ohmic and concentration effects cannot be the culprit. At very small current densities, between 1 and 4 mA/cm<sup>2</sup>, the deposition of zinc galvanostatically is especially difficult, with very thick striae alternating with millimeter-wide patches of apparently passive surface area. This passive region may even extend to the very edge of a channel electrode, where the transport should be maximized, and where ohmic drop is at a minimum. At higher currents, very thick deposits appear at the electrode edge, so that the appearance of passive regions in our

cell is not an artifact. The only explanation that seems plausible for this curious striation-related behavior, is that the concomitant hydrogen evolution (calculated above to be  $0.9 \text{ mA/cm}^2$ ) somehow prevents the development of abundant zinc nuclei. This may occur either through competitive adsorption or through a pH change at the electrode surface. At pH 6, zinc hydroxide is expected to form, and may well precipitate on the surface. It is difficult to investigate this *ex-situ*, since the deposit develops an oxide/hydroxide film when exposed to air.

#### 4.5 Conclusion

The estimates presented allow one to conclude that the emergence of striation occurs in the following manner: As a result of a high exchange current density on zinc growth centers, zinc deposition from acid-halide electrolytes occurs in the linear regime up to a real current density of  $30 \text{ mA/cm}^2$ . It is in this range that striations occur as a result of an increased sensitivity to local values of the surface overpotential. In the linear regime, at an average current density of  $15 \text{ mA/cm}^2$ , a difference in the local surface overpotential of 2 mV will yield thickness ratios of 5:1 between favored and unfavored portions of the surface. In the Tafel region, this would require a difference of over 20 mV in the surface overpotential for an identical thickness ratio. Thus, analyses which previously relied on much lower estimates of the zinc exchange current density were not able to explain its peculiar sensitivity to concentration at conditions far from limiting current.

Contradictory claims can now be resolved. Epelboin's S-shaped voltammetric curves can be explained as a steep current-voltage transient superimposed on a substantial change in the active electrode area. This combination responds in a manner similar to an autocatalytic system. The presence of 3-D growth centers are the actual catalysts, not some proposed univalent zinc species, since the nodules have an exchange current density that is much higher than the underlying substrate. This differential exchange

current density accelerates the deposition reaction as nodules form.

The appearance of passive inter-striae electrode regions at low current densities is left unexplained. It is probably related to competitive hydrogen evolution and a hydrogen-induced pH change which may lead to the precipitation of zinc hydroxide. Although the fraction of the total current used in hydrogen evolution is small, it may be large enough to alter the pH in the recessed valleys, yet small enough not to lead to the generation of bubbles. The poor transport in and out of striation valleys may also cause a change in the local concentration of  $H^+$ .

#### 4.6 Recommendations for Future Work

Although there is evidence to suggest that the appearance of striations is linked to the sensitivity of the deposition reaction to small variations in the local value of the surface overpotential, a more quantitative theoretical model would help confirm this. A rigorous model would involve a three-dimensional simulation, but several approximations may be made which could reduce the inherent complexity and make the problem tractable. The kinetics can be modeled by a linear approximation, which should include, however, a concentration-dependent exchange current density. The real difficulty lies in determining the length scales over which the simulation must be performed. If attention is focused on a single growing nodule, the cooperative behavior between successive nodules more-or-less aligned in the flow direction will be obscured. It is also quite possible that nodules act in concert, creating a much larger ohmic exclusion zone around them. It is otherwise hard to imagine how a spacing of 600 microns occurs at early deposition times, when the nodule radius is on the order of 40 microns. At a distance of 15 radii, the effect of a single nodule must be fairly faint.

The second recommendation relates to future experimental work. It was envisaged that a redesigned micromosaic electrode, described in Appendix B, could be used to determine the local current distribution around growing zinc nodules *in-situ*. As



seen in Part II, a new micromosaic electrode has been manufactured in-house, partially accomplishing this goal. Since development of the required process methodology took longer than expected, the micromosaic was instead used to extend investigations on mass-transport enhancement to multiple gas-bubble columns. Its application to the zinc project seems entirely within the scope of a future research endeavor.

**Table 4.1: Striation Model Parameters and Physical Properties**

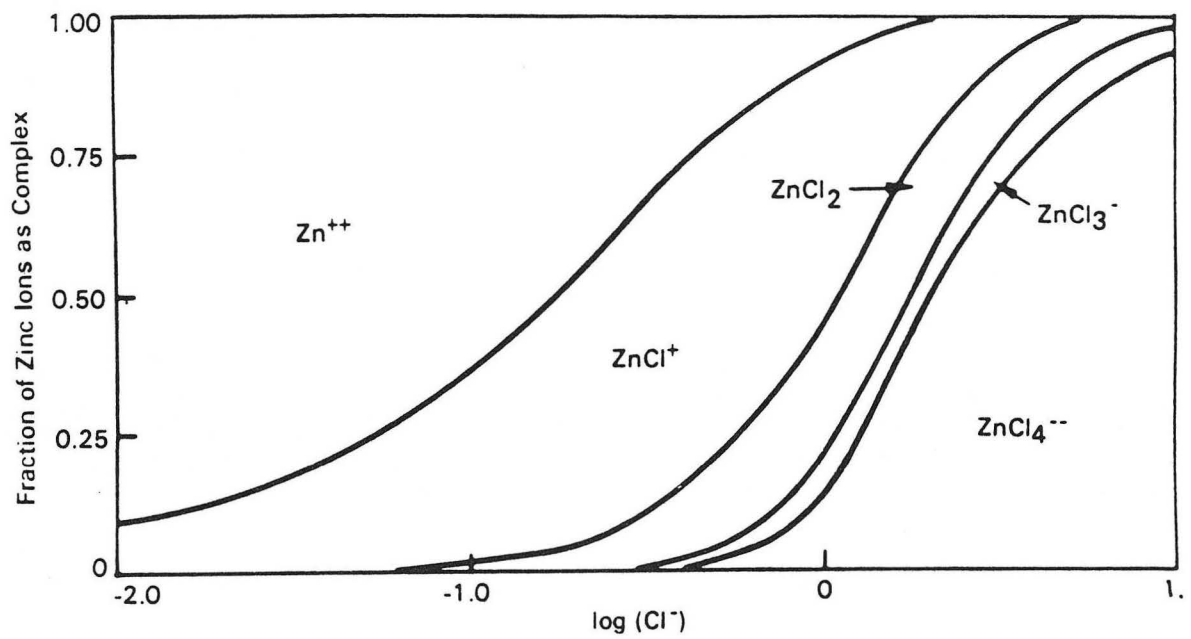
Variable	Value
Striation Amplitude	40 $\mu\text{m}$
$C_b^{\text{Zn}}$	1.00 M
$i_0^{\text{Cb}} \text{Zn}^{++}/\text{Zn}$ (3D)	100.0 $\frac{\text{mA}}{\text{cm}^2}$
$i_0^{\text{Cb}} \text{Zn}^{++}/\text{Zn}$ (2D)	< 1.00 $\frac{\text{mA}}{\text{cm}^2}$
$E_0 - E_{\text{Zn}}$	0.113 mV
$i_{\text{H}_2}$ at $E_0$	0.88 $\frac{\text{mA}}{\text{cm}^2}$
$(d\eta_s/di) \text{Zn}^{++}/\text{Zn}_2$	7.82 mA/mV at $C_b$
$(d\eta_s/di) \text{H}^+/\text{H}_2$	0.04 mA/mV
$\rho \text{ZnCl}_2$	13.4 Ohm-cm
$\rho \text{ZnSO}_4$	33.4 Ohm-cm

Table 4.2: Data for Specific Cases

Variable	Cases			
I (mA)	5	7.5	10	20
$i_{\text{geometric}} \left( \frac{\text{mA}}{\text{cm}^2} \right)$	10	15	20	40
Wavelength ( $\mu\text{m}$ )	600	400	250	170
Amplitude ( $\mu\text{m}$ )	40	40	40	40
Area Factor	1.18	1.22	1.27	1.39
$i_{\text{real}} \left( \frac{\text{mA}}{\text{cm}^2} \right)$	8.47	12.3	15.7	28.8
Thickness Ratio $\left( \frac{i_{\text{peak}}}{i_{\text{valley}}} \right)$	$\infty$	5.0	3.0	2.0
$C_{\text{avg}}/C_b$	0.992	0.988	0.984	0.971
$\eta_s^{\text{Zn}}$ (mV)	0.98	1.48	1.94	3.68
$(d\eta_s/di)_{\text{Zn}}$ (mA/mV)	7.71	7.68	7.66	7.56
$i_0^{\text{avg}} \text{Zn}^{++}/\text{Zn} \left( \frac{\text{mA}}{\text{cm}^2} \right)$	98.8	98.2	97.6	95.7
$i_{\text{H}_2} \left( \frac{\text{mA}}{\text{cm}^2} \right)$	0.92	0.94	0.96	1.03
$i_{\text{Zn}}^{\text{avg}} \left( \frac{\text{mA}}{\text{cm}^2} \right)$	7.5	11.4	14.7	27.8
$i_{\text{Zn}}^{\text{max}} \left( \frac{\text{mA}}{\text{cm}^2} \right)$	15.1	19.0	22.1	37.1
$i_{\text{Zn}}^{\text{min}} \left( \frac{\text{mA}}{\text{cm}^2} \right)$	0	3.8	7.4	18.5
$\Delta \eta_s^{\text{Cl}^-}$ (mV)	0.455	0.66	0.85	1.54
$\Delta \eta_s^{\text{SO}_4^{=}}$ (mV)	1.13	1.65	2.11	3.85

**Table 4.3: Ohmic Boundary-Layer Thickness with Primary Current**

Reduced Amplitude ( $\frac{a}{\lambda}$ )	$\delta_{\text{ohmic}} (\lambda)$
0.068	0.537
0.076	0.531
0.096	0.526
0.106	0.495
0.150	0.400
0.200	0.455
0.250	0.531



XBL 838-11146

Figure 4.1. Degree of zinc ion complexation in zinc chloride solutions from McBreen et al.

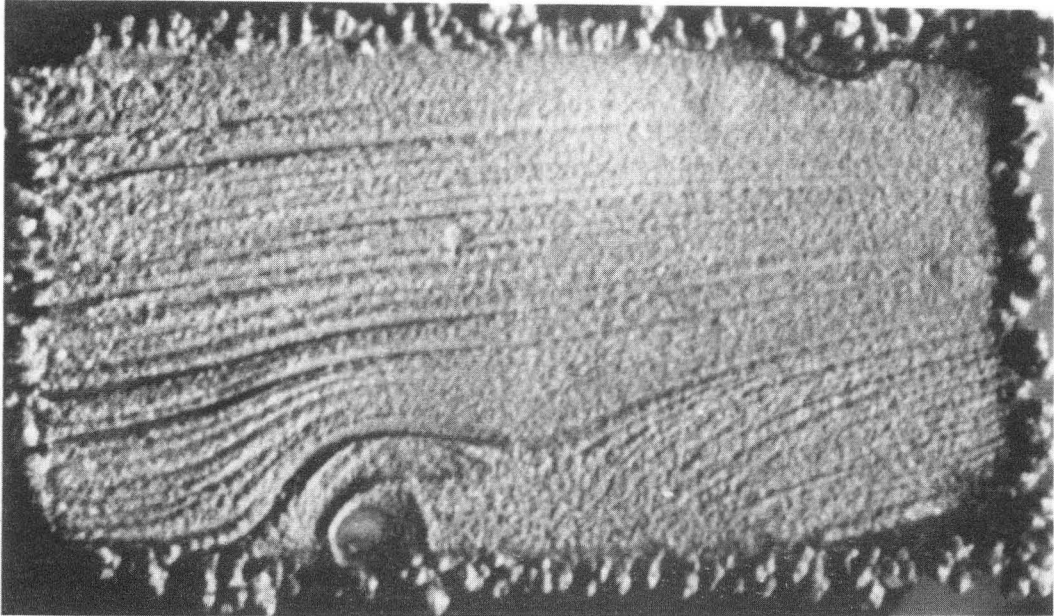


Figure 4.2 Zinc striations growing around an attached hydrogen bubble. The striae originate upstream of the disturbance and follow the flowpath around the obstruction. XBB 886-6459A

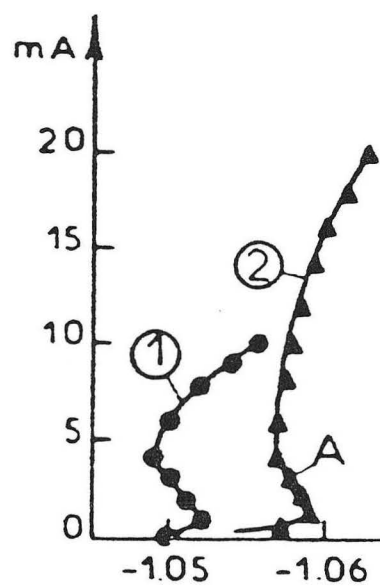
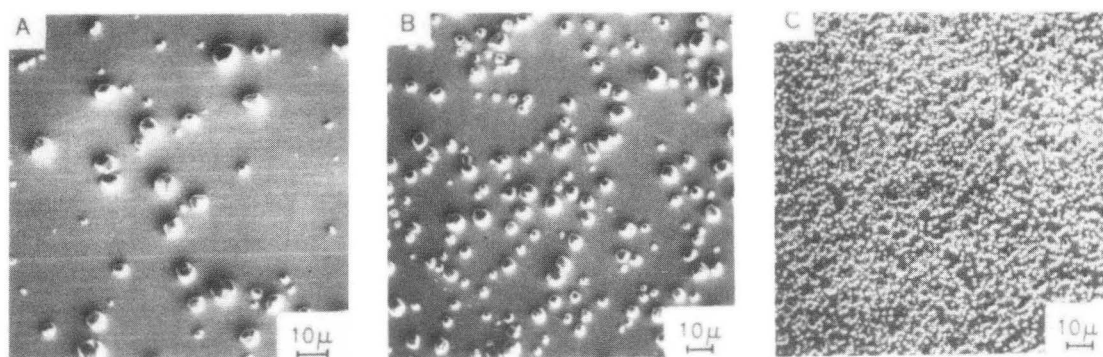


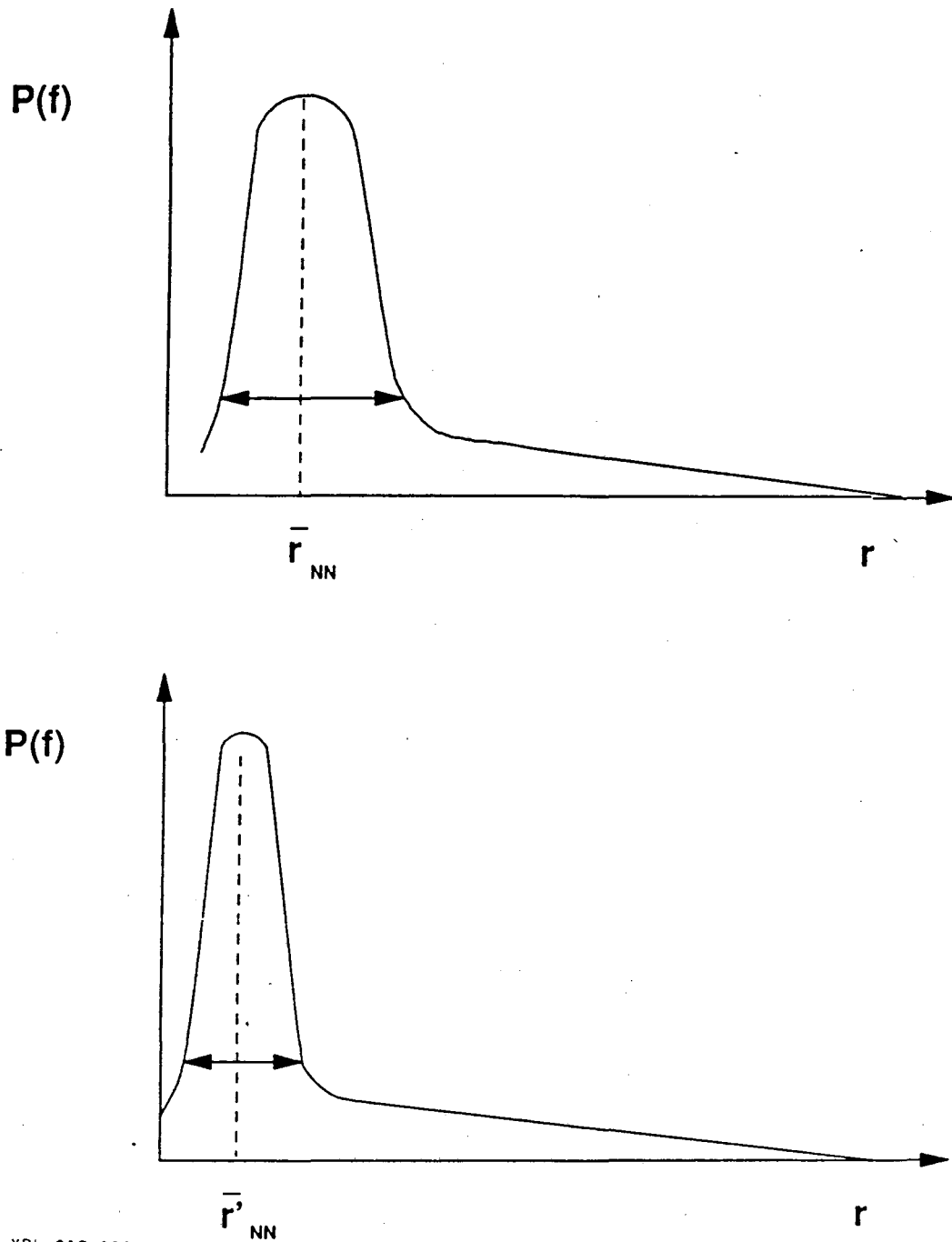
Figure 4.3. Backward-bending "steady-state" current-potential curves, from Epelboin et al. [66]. 3000 rpm, rotating disk electrode. 1) 1.5 M zinc sulfate + 1 M sodium sulfate and 2) 0.72 M zinc chloride + 2.67 M ammonium chloride.



XBB 817-6764B

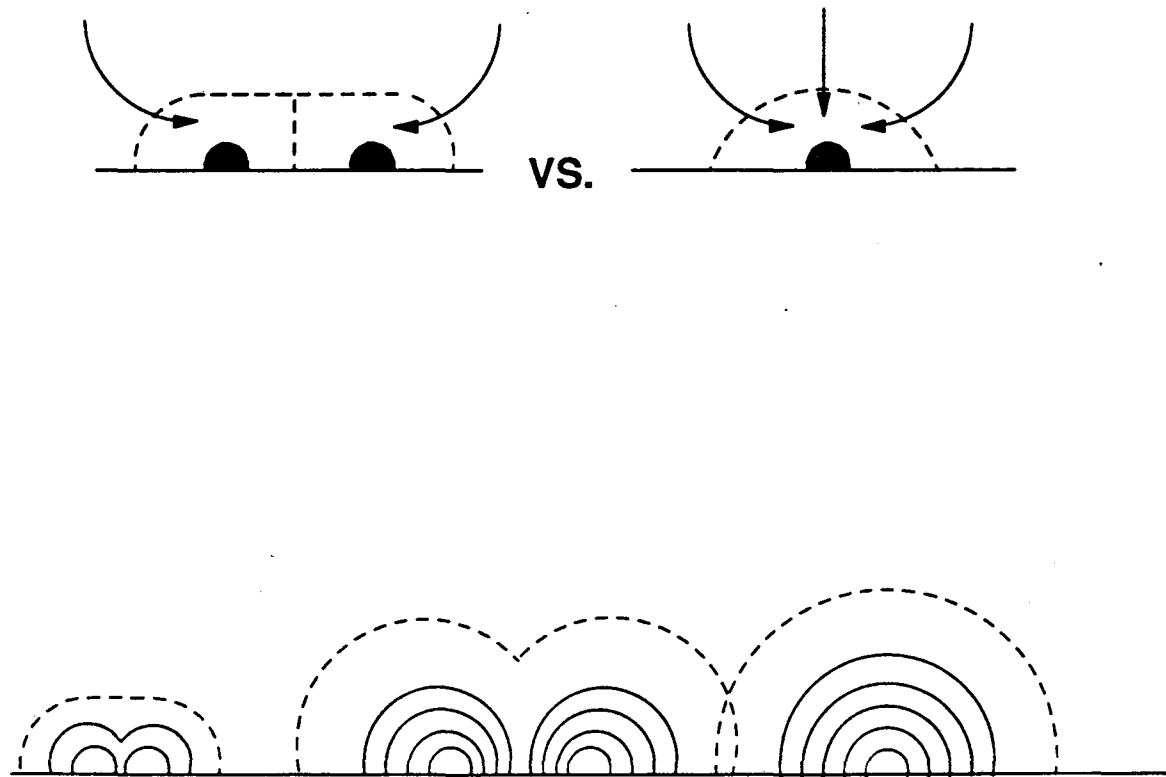
Figure 4.4 Zinc nucleation density after  $900 \text{ mC/cm}^2$  of deposition at three different rates: A)  $10 \text{ mA/cm}^2$ , B)  $30 \text{ mA/cm}^2$ , and C)  $90 \text{ mA/cm}^2$ . Ultrapure 1M zinc chloride (pH 5.2), 800 RPM on a rotating disk. Tsuda and Tobias [34].





XBL 915-1104

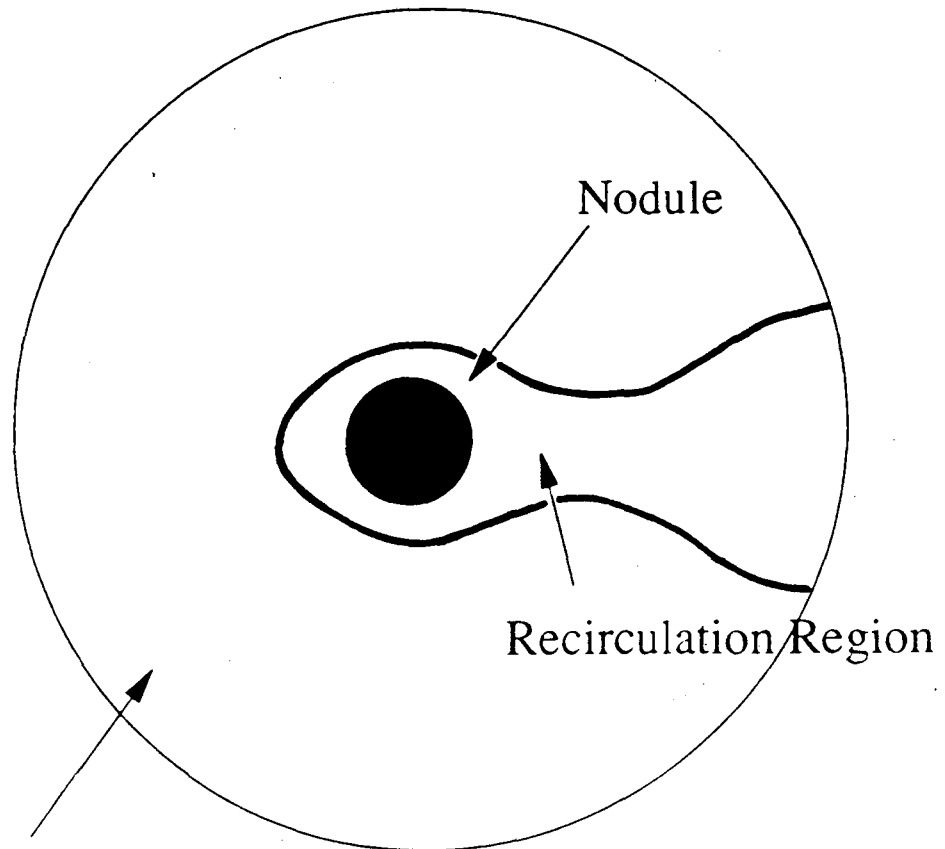
Figure 4.5. Distribution of distances between neighboring nodules. As the nodules become more numerous, the mean and the variance of the separation distance fall.



XBL 915-1105

Figure 4.6. Diffusion-layer around growing nodules.

Exclusion and Enhancement  
in the vicinity of a growing nodule

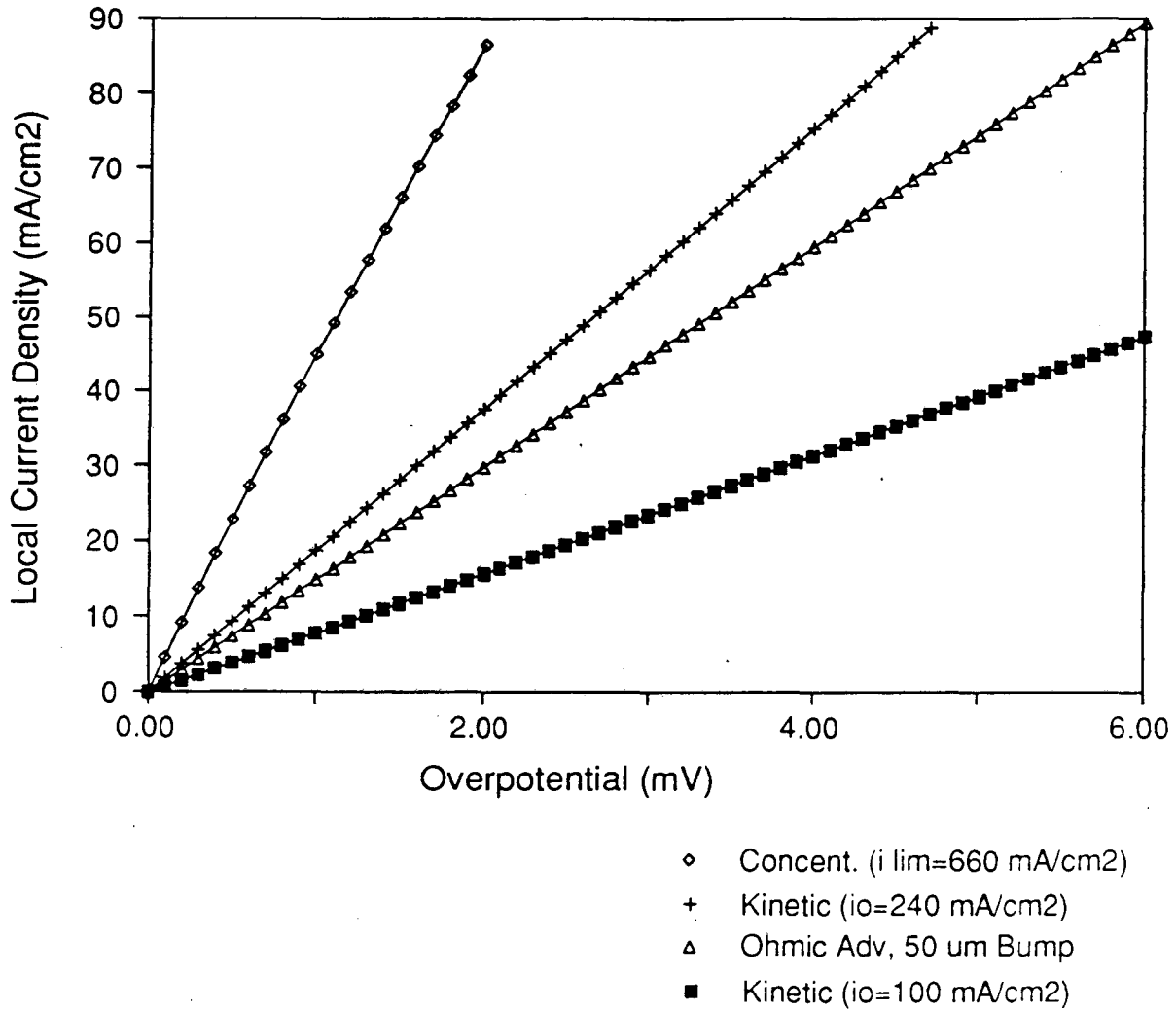


Zone of Ohmic 'Exclusion'  
Milchev (1990)

XBL 9011-3547

Figure 4.7. Ohmic exclusion and flow recirculation zones in the vicinity of a growing zinc nodule, over 20  $\mu\text{m}$  in height.

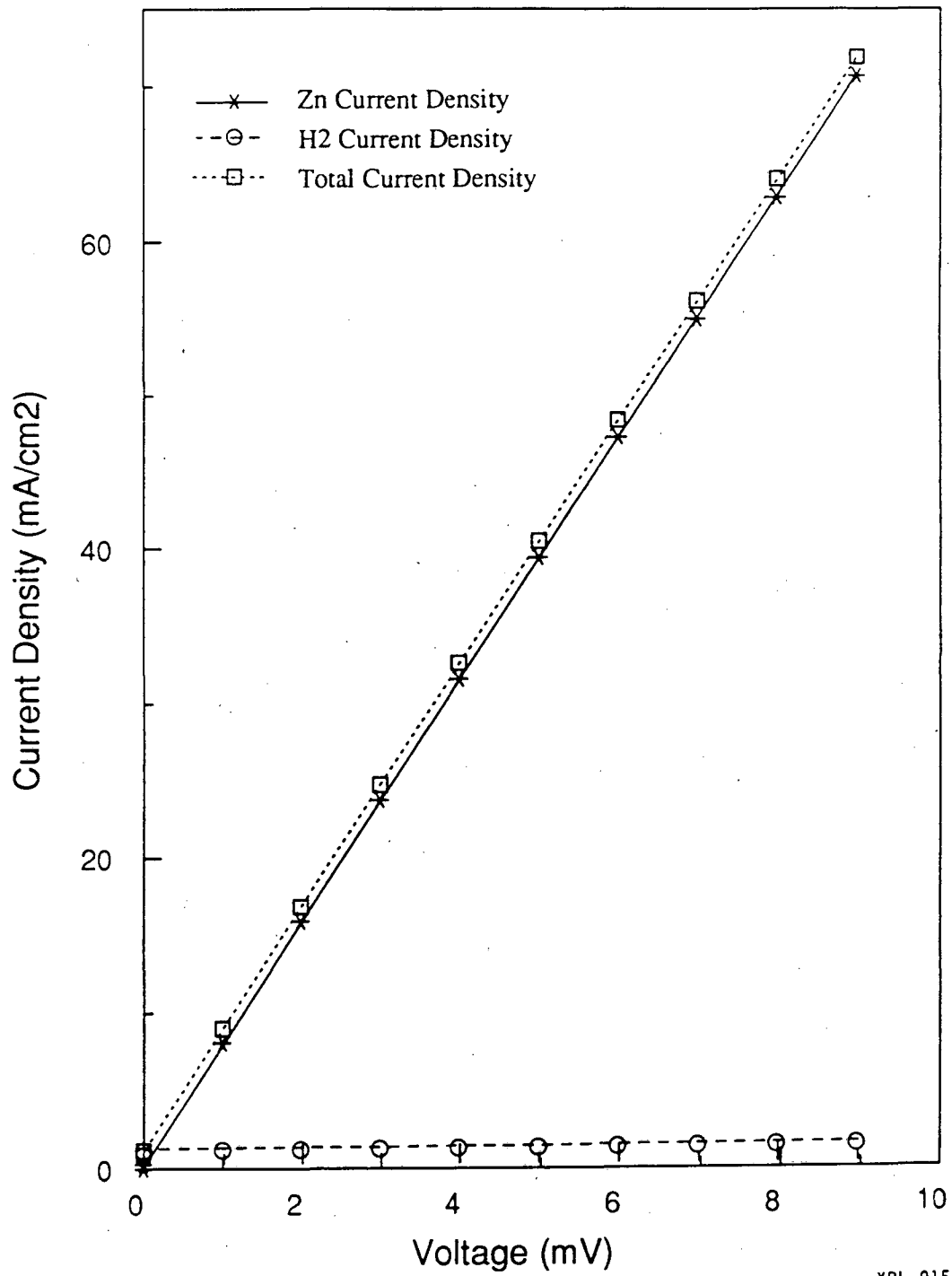
## Cathodic Overpotentials



XBL 919-1100

Figure 4.8. Linear zinc kinetics. Comparison of surface, concentration and ohmic overpotentials.

## Linear Zinc Kinetics



XBL 915-1109

Figure 4.9. Partial hydrogen and zinc currents in the zinc linear kinetic regime.

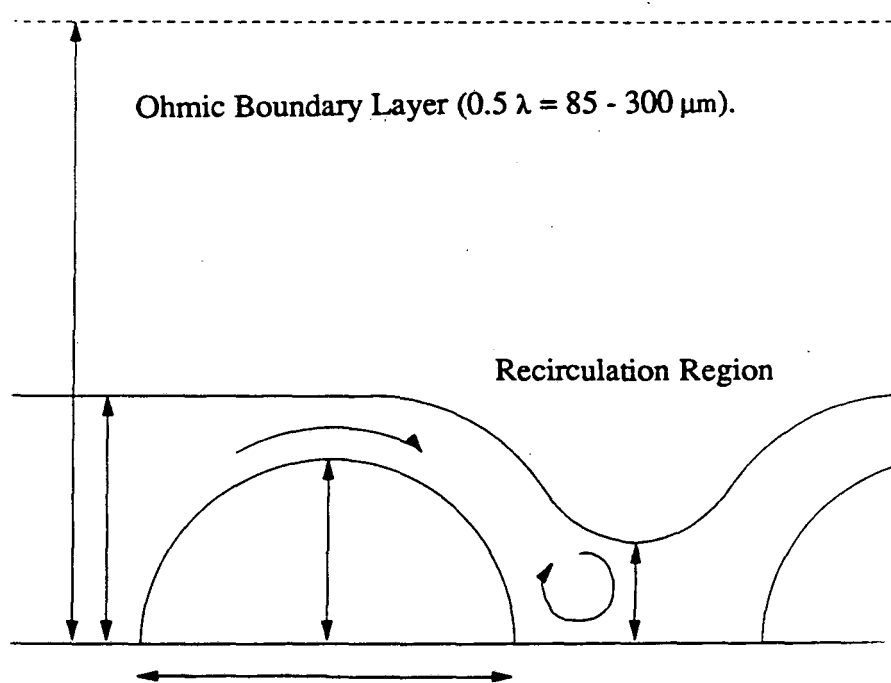


Figure 4.10. Ohmic boundary-layer thickness.

## Part II: Mass-Transport Enhancement by Rising Bubble Curtains

### Chapter 5. Introduction and Literature Review

#### 5.1 Introduction

In many industrial electrochemical processes, mass-transfer to the electrode surface limits the reaction rate. Forced convection is used to promote mass transport, even with the added expense of pumping costs. An economical variant is to use the force of buoyancy to promote mixing. Natural convection alone, however, is rarely sufficient. The addition of electrolytically-generated gas bubbles offers another alternative. The anodic process in chlorate cells, for example, is diffusion-limited and the mass-transfer coefficient is determined by the gas evolution rate [160].

Mixing due to gas evolution can be substantial; Whitney [141] has calculated that even a modest number of bubbles (evolved at a rate of  $130 \text{ mA/cm}^2$ ) can effectively match the diffusion-layer thickness for a bulk flow rate of  $135 \text{ cm/sec}$  in a 1-cm diameter channel. This is equivalent to a Reynolds number of 6700 [143]. Enhancement occurs because bubbles generated on an electrode rise inside of the diffusion boundary layer. Mixing in their wake is extraordinarily efficient in replenishing the region near the electrode surface with reactant. Fouad and Sedahmed [150, 151] compared the power consumed by gas-evolution to the pumping costs required to obtain identical mass-transport rates (Table 5.1). They determined that hydrogen evolution was always more economical, and that the energy savings increased dramatically with gas evolution rates. At the highest rate studied, a 90% power savings could be attained. Bubble mixing also reduces the supersaturation near the electrode surface, which lowers the concentration overpotential and can considerably improve the voltage efficiency.

The addition of a gas-evolving side-reaction is not usually practical, however. Only certain electrochemical systems are compatible with the presence of hydrogen, though some metal deposition reactions, notably that of chromium, are typically performed in the presence of vigorous hydrogen evolution with no adverse effects. In other cases, though, the bubbles cover the electrode surface, and can lead to poor deposit quality. In many instances, bubble curtains create a substantial ohmic resistance and forced convection must still be used to scavenge gas bubbles from the inter-electrode gap. The gases evolved are typically reactive and may back-react on the same electrode as a diffusion-limited reaction.

Gas evolution involves consecutive and simultaneous nucleation, disengagement, and coalescence, in addition to buoyancy-driven motion. To understand the dynamics of this process, it is necessary to separate the different components, and study each in isolation. Work in this laboratory dates back to the 1950's, when Tobias and associates [133, 137, 140] determined the resistivity of gas-electrolyte emulsions and the resistance caused by bubbles rising in the inter-electrode gap. In the 1960's, Cheh [129] studied the growth of non-interacting bubbles in a variety of concentration fields. More recently, Bon, Cettou, Dees [132], Dukovic, Elliott, Putt, Sides, and Whitney [142, 143] examined various issues concerning bubble nucleation, coalescence, and bubble-induced enhancements in mass transport. The reader is referred to their individual theses for specific details [127-141], and to review articles by Vogt and Sides for a broader introduction to the field of electrolytic gas evolution [164, 166].

Mass-transfer enhancement by bubble streams rising near an electrode surface can be quantified by the use of a redox indicator reaction held at a potential where the reduction reaction proceeds at limiting current. By using a micro-mosaic electrode array (MME), which has a characteristic segment length similar in size to the bubble diameter, one is able to measure local mass-transfer coefficients. Dees [130], who designed the original MME, observed the effect on mass-transport of the detachment



and coalescence of bubbles on a horizontal MME, while Whitney [143] examined the effect of an isolated bubble column rising along a vertical MME. In the present work, new, corrosion-resistant MME electrodes are used, equipped with multiple satellite segments for the formation of parallel gas columns. The aim is to examine a case which more realistically model the observed bubble curtains which occur under many electrolysis conditions. The fabrication of the MME is described in detail in Appendix B, and the experimental procedures and results are given in Chapters 6 and 7.

### 5.2 Mass-Transport to Gas-Evolving Electrodes

In 1951, Roald and Beck [160] proposed that the relation

$$k_{\text{MT}} \equiv \left( \frac{\dot{V}_g}{A} \right)^{0.5} \quad (5.1)$$

could be used to correlate the mass-transport coefficient,  $k_{\text{MT}}$ , with the volumetric rate of gas evolution,  $\dot{V}_g$ , normalized by the electrode area. This was confirmed by Ibl and Venczel [155], and a theoretical explanation was given for the square-root dependence. Ibl and Venczel postulated that a penetration model, originally conceived by Stefan, 1878 and similar to one used by Higbie [153] to model the absorption of gas into a liquid, could account for the observed relation. It may be noted that Higbie found that in his case a penetration theory was insufficient to predict the experimental absorption rates [153]. The penetration, or surface-renewal, model postulates that the passage of a gas bubble re-equilibrates the surface reactant concentration with the bulk value, driving up the local mass-transport limited rate. Between bubble passages, the solution is quiescent according to this model, and the transport-controlled current follows the Cottrell equation [35],

$$i(t) = \frac{n_i F D_i C_i^\infty}{(\pi D_i t)^{0.5}} \quad (5.2)$$

The average current density is determined by integrating the current passed between

successive bubbles and dividing by the time. The average diffusion-limited current is proportional to the square-root of the waiting time  $\tau_w$ .

$$i_{\text{avg}} = \frac{2n_iFD_iC_i^\infty}{(\pi D_i \tau_w)^{0.5}} \quad (5.3)$$

It is often assumed that the frequency of bubbles leaving the surface from a given location varies linearly with the gas-evolution current density. This is equivalent to stating that the bubble size is independent of current density, since  $\tau_w$  is proportional to the bubble radius and inversely proportional to the volumetric rate of gas evolution. Changes in the slope of the mass-transfer coefficient versus bubble current have instead been ascribed to changes in the enhancement mechanism, assuming that the bubble size leaving the surface is constant. If the average bubble size changes, it is no longer necessary for the surface-renewal model to predict a 0.5 power dependence of the mass-transfer coefficient on the rate of gas evolution. Therefore, the bubble frequency must be measured independently by photographic or acoustic means. Janssen and Hoogland [158, 159], for example, report that bubble volumes increase at current densities above 30 mA/cm<sup>2</sup> because of coalescence. It should also be noted that *neither the bubble size nor the speed of its ascent enter into the time-averaged current*, since it is assumed that the replenishment of the reactant at the surface is complete and instantaneous.

While often satisfactory in "saving the phenomena", the surface-renewal model is not mechanistically probable in many instances, as admitted by Higbie himself in 1935 [153]. Another hypothesis, proposed by Stefan and Vogt in 1979 [165], leads to the same power dependence. These authors replace Ibl's concept of instantaneous surface-renewal followed by a period of quiescent diffusion [155], with a model that postulates continuous micro-circulation caused by growing gas bubbles. They envision that each bubble creates flows that are localized in nature. Their correlation also predicts a 0.5 dependence on the Reynolds number, but gives mass-transport

coefficients that are a factor of three lower than the surface-renewal model:

$$\text{Sh} = 0.93 \text{ Re}^{0.5} \text{ Sc}^{0.487} \quad (5.4)$$

Figure 5.1 is a plot from Stephen and Vogt [165] which shows that, in general, the rate of enhancement increases as the square root of the gas evolution current. The data are quite numerous, and there are certainly some grouped subsets which seem to follow a different dependence. Vogt explains this by stating that the exact dependence varies with the electrode- and cell-geometry. The disparities are often striking: Alkire and Lu [144] report exponents equal to 0.15 and 0.5 in the same system, over different current density ranges. Even recent work using tracers, such as by Chen and O'Keefe [145], finds it impossible to reconcile their data to either a surface-renewal model or the turbulent natural convection models described below. Fits over a narrow range of current densities may work, but subtle geometric changes yield surprisingly different results.

What is lacking in either of the micro-circulation hypotheses are any distinctions in the flow mechanisms when one varies the orientation of the gas-evolving electrode. Both the surface-renewal model, as discussed by Ibl, and the microconvection model, however, take into account the presence of adhering bubbles on the electrode surface. The second of these theories was explicitly derived for a horizontal electrode, since it envisages a squeeze flow between two growing bubbles as the mechanism for the occurrence of circulatory micro-convection. The data that Stephen and Vogt correlate, however, include results on both horizontal and vertical electrodes; even data on sparged rather than electrolytically generated bubbles. In all cases, the rising gas bubbles are expected to lie inside of the diffusion boundary layer. According to these models, it is the direct, local replenishment of this reactant-poor region that is responsible for the observed increase in mass-transport.

An alternative explanation for the dependence of mass-transport enhancement by rising gas bubbles is the "hydrodynamic" model proposed by Janssen and Hoogland [158], which was presented in a quantitative form by Janssen and Barendrecht [157]. This model is based on earlier studies by Fouad and Ibl [149], Fenech and Tobias [136], and Wragg [167] on laminar and turbulent natural convection. In all of these models, the entire boundary layer is thinned by the presence of macro-convection induced by buoyant flow. The distinction made by Janssen's group is that the flow is created by bubbles rising close to, but perhaps outside of, the mass-transport boundary layer, in direct analogy to Zuber's work on nucleate boiling [168].

Fenech and Tobias [136] examined the limiting current in natural free convection to a horizontal surface, and found that the limiting current scaled as:

$$\text{Sh}' = 0.19(\text{Gr Sc})^{1/3} \quad (5.5)$$

where the Grashof number, Gr, is given by

$$\text{Gr} = \frac{gl^3(\rho_i - \rho_0)}{\rho_i \nu^2} \quad (5.6)$$

In this analysis,  $\rho_i$  refers to the density of the bulk solution while  $\rho_0$  is the density of the solution at the interface. Wragg later redid the analysis, and substituting a different characteristic length scale, nevertheless emerged with the identical correlation, save for a slightly different coefficient:

$$\text{Sh} = 0.16(\text{Gr Sc})^{1/3} \quad (5.7)$$

Ibl and Fouad found experimentally that the limiting current to a **vertical** electrode in turbulent natural convection scaled as the 0.28 power of the Grashof number, while Fouad and Gouda later reported 0.29 as a better fit. All of these exponents are similar to one another, and the use of one-third by Janssen and Hoogland is not surprising. In extending this analysis to bubble-induced hydrodynamic flow, Janssen and Hoogland redefined the densities involved, and the length scale became the bubble radius. They

left the exact coefficient arbitrary, as an adjustable parameter.

Sides ascribes differences in mass-transport theories to the parochialism of national research schools arising separately in Switzerland, Germany, and the Netherlands. To varying degrees, though, both micro-convection and "hydrodynamic" macro-convection are likely to occur during gas evolution. It is the relative degree by which they contribute to mass-transport enhancement that varies from one set of conditions to another. By focusing on the behavior of a single or small set of bubble columns, it may be possible to observe transitions from one regime to another, both spatially and as the gas-evolution rate is changed.

### *5.3 Mass-Transfer Studies with a Micro-mosaic Electrode*

Electrolytically-generated gas bubbles are much smaller than those created in other ways, such as by forced flow through a submerged orifice. Rising hydrogen bubbles generated in an acid solution are usually 60 - 80  $\mu\text{m}$  in diameter, while rising oxygen bubbles in the same low pH solution are generally smaller, approximately 40  $\mu\text{m}$  in size [127, 138, 158]. There is a dependence of size on the applied current, but it is not a reproducible one. Bubble size is generally predicted by arguments that focus on surface tension and contact angle, quantities that do not depend on the dynamics of gas evolution. In practice, however, tiny bubbles on a surface may coalesce before detachment, yielding a more uniform size distribution, not based on the local geometry of the electrode. In order to study the behavior of such small bubbles, it is necessary to use an array of electrodes that have the same dimensions as the bubble. It is also advantageous to use non-interacting columns for the determination of bubble-induced mass-transfer enhancement. Instead of using macroscopic electrodes where the individual volume and surface coverage of bubbles vary greatly and cannot be controlled, a microelectrode with small satellite segments can be used to generate single or multiple bubble streams of precisely-measured size. If the gas column is created at a micro-electrode, it is likely

that the bubbles can be of uniform size, and that scavenging can be avoided. In this manner, changes in mass-transport can be linked directly to the passage of bubbles past the reacting surface, and not to more complicated phenomena such as coalescence. The limiting current on the vertical electrode of a redox couple (measured at a potential where gas evolution does not occur) gives the value of the mass-transfer coefficient. An array of sensor segments can then be used to map out the variation of the enhancement as a function of distance from the rising column. Since each segment has dimensions similar in size to the bubbles themselves, effects that persist over a distance of several bubble diameters can be studied.

Dees and Tobias [131] designed such an array, which was named the micromosaic electrode (MME), shown in Fig. 5.2. The original MME was fabricated by Hewlett-Packard, and later a second set (somewhat modified) was made by Bell Labs. It contained a 10 x 10 array of isolated platinum squares, approximately 100  $\mu\text{m}$  on a side, which were connected to separate current followers, but kept at the same fixed potential. Using the limiting current behavior of a redox reaction as an indicator, Dees was able to measure variations in the mass-transfer coefficient occurring as a result of gas bubble detachment and coalescence.

Whitney and Tobias [143] used the MME to study the effect of single columns of electrolytically-generated gas bubbles on the mass transport to a vertically-oriented electrode. They found that a distinction could be made between bubbles generated on the MME itself, at a satellite segment, and bubbles evolved from a wire a some distance from the micro-mosaic surface. Two competing theories, the surface-renewal and the hydrodynamic models, were directly compared in their ability to correlate the observed mass-transfer enhancement as a function of gas evolution rate and bubble size. For bubbles rising inside the diffusion layer (i.e. generated on a satellite pad on the MME surface itself), the enhancement was local and corresponded to a surface-renewal mechanism, with a corresponding 0.5 power dependence on the gas-evolution rate.

In this case, the bubble moves to a position approximately 60  $\mu\text{m}$  from the vertically-oriented electrode, and rises inside of the diffusion-boundary layer. Whitney determined that there was a region of the surface which was effectively renewed, while the remainder of the MME was unaffected by the passage of the bubble. The width of the renewal path stayed fairly constant with increasing current density but varied with bubble size. Each bubble passing over the MME array disturbed the boundary-layer results in a periodic disturbance in the measured diffusion-limited reaction rate. Whitney's measurements showed such a periodic fluctuation in the observed redox limiting current, which gave further support for the surface-renewal model.

The bubbles evolved at the tip of a wire facing the MME, however, would rise outside of the diffusion boundary layer, and the effect would not be expected to be as localized. Oscillations that were detected were ascribed not to changes in boundary-layer thickness, but rather to periodic occlusion of the electrode by the passing bubbles, resulting in a substantially larger ohmic resistance. For the bubbles rising at a distance, Whitney used a assisted laminar-convection model, where the total mass-transfer coefficient is determined by the cube root of the cubes of the component mass-transfer coefficients. This model was proposed experimentally by Churchill, then supported with scaling arguments by Ruckenstein.

A rising-cylinder model was used to explain the observed dependence of the mass-transfer coefficient on gas-evolution rate. The rising-cylinder theory also predicts a  $1/3$  power dependence, in consonance with earlier hydrodynamic and turbulent natural convection models. This analysis predicts the dependence on gas evolution rate reasonably well, but fails to predict the enhancement distribution over the MME, or the strong variations in enhancement as the cylinder distance was increased.

For the studies on columns generated on the satellite segments, Whitney limited her studies to relatively low current densities, 35 - 160  $\text{mA}/\text{cm}^2$ , corresponding to 3.5 - 16  $\mu\text{A}$ . This was to avoid generating large-scale fluid motion or macro-convection

inside the cell. She grouped the data into two idealized regions, one where surface-renewal enhanced the reaction rate and the other, including the rest of the segmented array, where no effect was presumed to occur. Whitney determined the scale over which a laminar bubble column periodically increased the measured current density and found that it ranged from five to seven bubble diameters, a horizontal distance of approximately 300 - 360  $\mu\text{m}$ . Outside of this region, the current fell to a roughly constant value that was assumed to equal the background free-convection current,  $i_{nc}$  by her nomenclature.

Separate measurement of the free-convection limiting current gave a value that was, in fact, slightly *higher* than the current density to the "unenhanced" region during gas evolution, in three out of five cases. This may have been caused by depletion of the  $\text{Fe}^{+3}$  reactant during experimentation.

For results on the H-P and Bell Lab MMEs (Fig. 5.2), the bubble column is generated at a satellite situated midway between columns five and six, at a distance of 500  $\mu\text{m}$  from the bottom edge of the 10x10 array. Column five in the redesigned MME (Fig. 5.3) is directly underneath the rising bubble stream, which is generated at the same distance from the array as in the older design. The relatively large distance was chosen to minimize variations in measured limiting current caused by the oxidation of dissolved hydrogen. The buffer electrode between the satellite and the array effectively blocks the hydrogen from reaching the sensing matrix. A decrease in redox limiting current is expected with increasing height for the free-convection limiting current. This expected small decrease was not detected experimentally.



Current density A/cm <sup>2</sup>	Applied voltage V	$J_{\text{Fe(CN)}_6^{4-}}$ A/cm <sup>2</sup>	Rate of H <sub>2</sub> evolution cm <sup>3</sup> /cm <sup>2</sup> /s	Power consumed in H <sub>2</sub> evolution W	Velocity of mech. circulation cm/s	Mech. power consumed W
0.0065	2.05	0.006	0.000063	10.2	70	12.6
0.0098	2.20	0.009	0.000100	22.1	138	96
0.0109	2.25	0.010	0.000113	27	164	161
0.0120	2.30	0.011	0.000125	32.4	193	249
0.0133	2.32	0.012	0.000160	37.1	223	386
0.0156	2.40	0.013	0.000325	49.1	255	407
0.0204	2.60	0.014	0.000800	82.6	288	877
0.0225	2.65	0.015	0.000940	96.2	323.5	1243
0.0270	2.80	0.016	0.001380	133.7	360	1738
0.0330	3.05	0.017	0.002000	200	398	2302

Table 5.1 Comparison of power consumption between bubble-induced convection and mechanical stirring. Cell dimensions: 50 cm high, 90 cm wide, 2 cm electrode-separator spacing. Solution composition: 0.2 M K<sub>3</sub>Fe(CN)<sub>6</sub> + 0.2 M K<sub>4</sub>Fe(CN)<sub>6</sub> + 2 N NaOH. Cell voltage: 1.7 V. From Fouad and Sedahmed, [150].

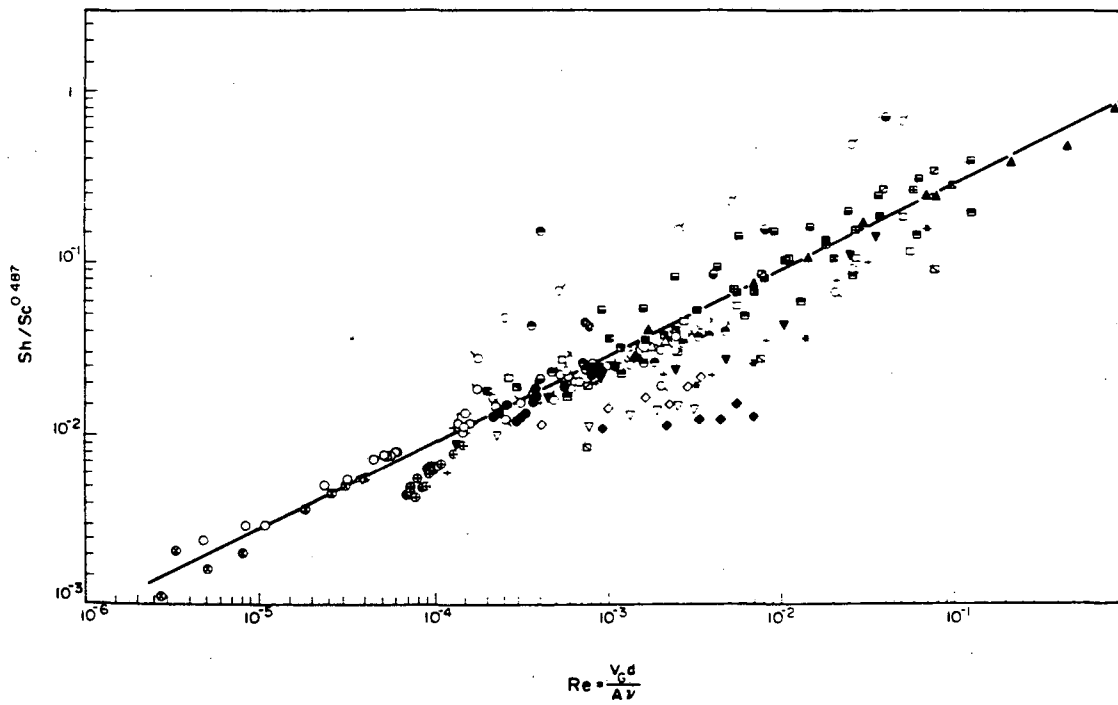


Figure 5.1. Correlation of mass-transport with gas evolution rate from Stephan and Vogt [164].

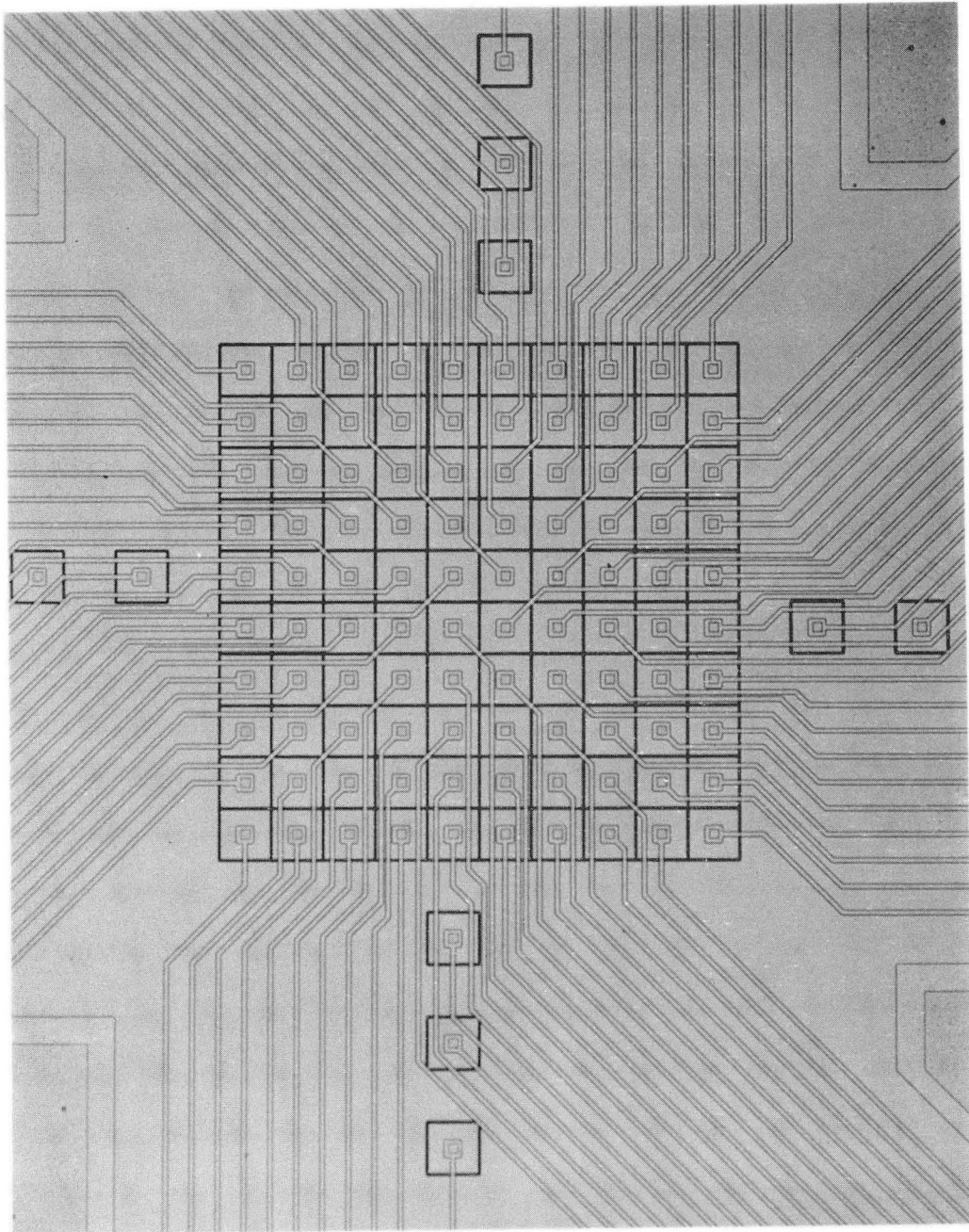


Figure 5.2 Original micro-mosaic electrode designed by Dees and Tobias and fabricated by Hewlett-Packard. Hydrogen bubbles were evolved at the furthest satellite,  $500\ \mu\text{m}$  below the segmented array [146]. XBC 860-8686A

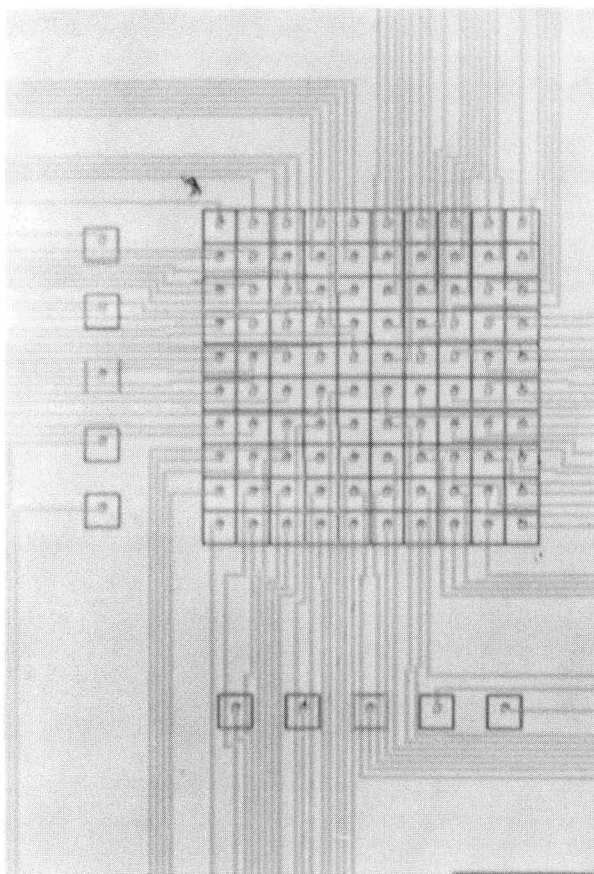


Figure 5.3 Redesigned, corrosion-resistant micro-mosaic electrode fabricated at the U. C. Berkeley microlab by the author. Parallel satellite segments allow the generation of multiple gas columns to simulate a curtain of bubbles rising in the diffusion boundary layer. XBC 911-394A

## Chapter 6 - Experimental Procedures

### 6.1. *Equipment*

#### 6.1.1 *Electrochemical Cell*

Experiments measuring the local mass-transport enhancement to vertical electrodes by multiple gas columns were performed using a redesigned version of a micro-mosaic (MME) electrode developed earlier in this laboratory by Dees [131]. By measuring the change in local limiting current of an indicator reaction (the reduction of  $\text{Fe}^{+3}$  to  $\text{Fe}^{+2}$ ), the magnitude and spatial distribution of convective transport enhancement can be determined. The heart of an MME is a 10 x 10 array of square platinum microelectrodes integrated onto a silicon wafer. Each segment is 96  $\mu\text{m}$  on a side, similar in scale to electrolytically-generated gas bubbles. Appendix B gives a thorough description of the design and fabrication of the redesigned MME, which was built in-house at the UCB microfabrication facility by the author.

A photograph of the electrochemical cell employed, partially-dismantled, is shown in Figure 6.1. On the right stands the clear lucite electrolyte compartment which is positioned over the silicon wafer containing the individual array elements. A schematic diagram of the assembled cell is given in Figure 6.2. At the sides of the electrolyte compartment are two platinum squares which serve as anodes, with electrical connection made at a common lead at the top of the lucite cell. A Luggin capillary connects the cell to the reference electrode compartment, while side openings provide a means of filling the assembled cell with electrolyte. The reference electrode is a mercury/mercurous sulfate electrode, immersed in the same electrolyte as contained in the main cell.

The white semi-circular Teflon attachment seen at the top of the lucite cell in Figure 6.1 below the anode leads, is a micrometer holder. A micrometer, which is not shown, controls the position of a separate platinum wire. The wire is positioned at a distance of 300 - 800 microns from the electrode surface, and can be used to generate a single column of hydrogen gas bubbles [143]. The redesigned MME has satellite segments from where hydrogen can be evolved. In this case, the distance of the rising gas bubbles from the electrode surface is smaller; they rise inside of the diffusion boundary layer.

On the left of Figure 6.1, an MME is shown already placed in its lucite holder, joined to a printed circuit board by underlying zebra connectors. Each aluminum line on the circuit board corresponds to a separate array element, and carries current from that segment, through a junction box and current follower, back to the potentiostat. Four 32-pin connectors mate to the circuit board, and provide a total of 128 available data channels.

Not all of the channels are used, as listed in Table 6.1. Several are reserved to provide power to the surrounding buffer segment, and some are intentionally left blank. The new micromosaic requires fewer connections to the buffer segment, so several of the channels previously used to provide the buffer with current are now either routed to a array element or not used. The changes in configuration required rewiring of the junction box built by Dees [130]. The new wiring is given in Table 6.1, with the affected segments listed with an asterisk. The wiring for the original micro-mosaic electrode is given in Appendix C of [130].

The current from each segment was fed into a current follower with 110 channels, one hundred for the 10 x 10 array and ten for the satellite segments. In this manner, the currents can be monitored simultaneously, with the only time lag being the time necessary for the multiplexer to scan channels sequentially. The current from the much-larger buffer bypasses the sensitive current follower, and passes from the junction

box directly back to the potentiostat. Table 6.2 shows the correspondence between array location and multiplexer channel number for the case when the "B" satellites are underneath the array and the "A" satellites are to the left of the array. Figure B.1 in Appendix B shows the relative position of the satellite segments. The "B" satellites are situated 500  $\mu\text{m}$  away from the array, while the "A" satellites are only 300  $\mu\text{m}$  away, and oriented perpendicular to the "B" group. To use the "A" satellites, the electrode must be rotated 90° counter-clockwise. For most of the experimental runs, hydrogen was evolved from the satellites further away to minimize the back-reaction of hydrogen gas on the MME array. Those segments which were used to generate a bubble column were kept at a more cathodic potential than the buffer and array segments. This potential was called K2, while the potential elsewhere on the cathode was K1. K1 was above the hydrogen-evolution potential, at -300 to -500 mV versus the mercury/mercurous sulfate reference electrode. K1 was chosen to keep the  $\text{Fe}^{+3}/\text{Fe}^{+2}$  reaction at a diffusion-limited rate. K2 was varied until the desired hydrogen or oxygen gas current was obtained. The actual value includes a large ohmic drop which, as explained below, kept the current to each of the satellites the same. For experiments with hydrogen evolution, K2 ranged from -1.2 to -1.95 V versus the reference electrode, while for oxygen evolution, it ranged from +0.4 - +1.5 V. The satellite segments not evolving hydrogen were kept at K1, the same potential as the surrounding buffer and the micromosaic array.

### 6.1.2 Data Acquisition System

The data acquisition system employed in this project was substantially revised from the earlier work of Whitney and Dees [130, 141]. The computer in the original configuration was an HP 9825, and the multiplexer and oscilloscopes used were both compatible with this particular component. The drawbacks in using the old setup were substantial, however, since the HP 9825 employs an outdated programming language,

data cartridges for program storage, and obsolete low-density floppy disks for data storage. Upgrading to an IBM AT-compatible personal computer allowed for the use of standard BASIC programming, immediate storage of much larger amounts of data on a 20MB hard disk (with archiving of data on high-density floppies), and quality graphics using commercial packages such as LOTUS and FREELANCE.

Upgrading did require, however, new hardware interfaces and software. Two 24-bit I/O boards (Metrabyte Model PIO12) provided an interface to the NEFF multiplexer. Random scanning of multiplexer channels and the gain setting were both computer-controlled. The AT computer read individual channel voltages and gain settings, then converted them to the appropriate segment current remotely. All 110 channels could be scanned in approximately 50  $\mu$ seconds. Since the experiments are steady-state, the time between data measurements at neighboring segments is not critical. The actual measured delay was under one  $\mu$ second per segment and was deemed negligible. For all practical purposes, the mass-transport limiting currents were acquired simultaneously.

The gas-evolution potential was set separately from the array potential by use of an RDE3 bi-potentiostat made by Pine Instruments, and an Hewlett-Packard 3325A function generator. Since the Pine potentiostat could not be interfaced directly with the PC, the function generator was used to input a fixed offset voltage to the potentiostat and set the K2 potential at which the hydrogen gas was evolved. The data-acquisition setup is schematically depicted in Figure 6.3, and a photograph of the apparatus connected to the cell is shown in Figure 6.4. The function generator was linked to the PC system by a National Instruments GPIB-PCII interface. The National Instruments board came with a set of BASIC-language programs. Standard Hewlett-Packard commands could be issued in a user-written BASIC program, and by linking with the interface software, the HP programmer could be controlled remotely. For galvanostatic gas evolution, the data acquisition program employed a control loop, whereby the satellite



segment current was read either through a multiplexer channel hooked up to the current output of the potentiostat, or through a Hewlett-Packard model 3455A digital voltmeter. The hydrogen evolution potential was stepped by five millivolts per loop until the desired total current density was attained on the satellite segments. The BASIC and machine-language programs used for data acquisition are listed in Appendix E. Debugging of the control programs was accomplished by the use of a circuit board wired with an array of resistors, each leading to a single multiplexer channel.

### 6.1.3 Electrolyte Solution

The electrolyte consisted of 0.1 M  $\text{H}_2\text{SO}_4$  and 0.05 M  $\text{Fe}_2(\text{SO}_4)_3$ , premixed in quantities of 10 ml. Fresh electrolyte was made for each experiment, since the solution is reduced on exposure to light. The chemicals used for the electrolyte were:

- Baker Ferric Sulfate, n-Hydrate
- Baker Concentrated Sulfuric Acid

### 6.2 Cell Assembly

While the corrosion of micromosaic array elements was essentially eliminated by the electrode redesign, corrosion of the aluminum edge pads by leakage of electrolyte out of the lucite cell compartment was a serious problem. The electrolyte used was a 0.1M  $\text{H}_2\text{SO}_4$  + 0.05 M  $\text{Fe}_2(\text{SO}_4)_3$  solution. The ferric sulfate is a strong oxidizing agent, and dissolves aluminum on contact. The edge pads and the large current-carrying lines were fabricated out of aluminum in order to take advantage of its high conductivity. Covering the edge pad with platinum did not forestall corrosion over the relatively large area pads since the electrolyte could seep under the sides of the pad. It was necessary, therefore, to insure that none of the electrolyte leaked out of the cell, and that after an experiment the cell was triple-rinsed with distilled water before disassembly. The lucite compartment was sealed with a gasket tightened by four

screws at the corners of the wafer area. The gasket seemed to be chemically-resistant to the electrolyte, but curiously, had poorer sealing properties when the acidic solution was placed in the cell than when distilled water was in the cell. To prevent leaks contacting the edge pads, a barrier of silicone and teflon tape was created outside of the cell compartment. In the event of leaks, the electrolyte flowed around the barrier and avoided contacting the pads.

Filling of the reference electrode compartment was also difficult, since the cell had to remain in the vertical orientation. This meant that the reference compartment was directly in front of the cell and obscured the view of the Luggin capillary. The Luggin tip sometimes became blocked by small gas bubbles. This was a catastrophic event since the potential was controlled by the reference electrode. After cutoff, the MME was covered by bubbles as the potentiostat sent the potential to an extreme value of 2 Volts. Some segments were damaged as a result. Filling the cell through the Luggin capillary from the reference compartment became the accepted practice to avoid trapped bubbles.

### 6.3 *Experimental Procedure*

After the electrode has been placed in its holder, the circuit board is laid over it, and the lucite cell is screwed into place. The cell is filled as described above, through the Luggin capillary. First, distilled water is used to test whether the gasket is sealing properly, then the water is drained and replaced by electrolyte. The circuit board on the assembled cell is then mated to the four 32-pin connectors, and placed in its vertical holder where it is held in place by clamps.

The experiment is started by setting both K1 and K2 to a potential in the limiting current region for the  $\text{Fe}^{+++}/\text{Fe}^{++}$  reaction. Control of the satellite potential and data acquisition is then computer-controlled as described above. Selection of hydrogen-evolving satellites is done manually by means of a series of switches. Uniform current

densities were obtained on each of the satellites by linking each in series to a 11.5 K $\Omega$  resistor and a 10-turn 100K potentiometer. Use of a uniform external resistor did not by itself guarantee equivalence in the bubble current to each satellite. It appears that the kinetics of the satellites varies, and that one must use a different ohmic drop to each gas-evolving segment in order to assure the same current to each. Once the potentiometers have been adjusted and K2 potential is set to the desired value, switching segments on and off changes the total hydrogen current, but not the partial current to each segment that is left on.

#### *6.4 Electrical Testing of the in-house MME*

There are three ways in which information from the MME array can be lost or degraded. The first is through the existence of defects, such as broken lines caused by dust and misfabrication during the processing sequence. In this case, information from that particular array segment is lost, and the current to adjoining elements is skewed by the resultant inhomogeneity in mass-transport over the non-polarized portion of the mosaic. Such "still-born" segments average about 10 out of the 100 in the array. There is little that can practically be done to eliminate this type of loss. Other failures are less damaging, however.

Many segments may also be lost through corrosion as described in Appendix B. Even silicon nitride films provide only a temporary barrier to the oxidation of the underlying aluminum layer. The first new micromosaic used in our experiments (#4 from Batch 1), lost approximately 1/3 of all active segments still alive, after every 24 hours in solution. While better than the Hewlett-Packard electrodes, this performance was poorer than old electrodes fabricated by Bell Laboratories. Bell Labs also used titanium and silicon nitride as the intermediate layers between the buried aluminum wires and the overlying electrode. They then encapsulated the entire wafer with a polyimide film, leaving only the center and the buffer pads exposed.

As a result, it was determined that a polymer film over the insulation layer would help protect the MME from accelerated corrosion. Polyimide has a serious drawback, however: it tends to lose adhesion and peel off. It is also difficult to spin and pattern, and requires a long 300 ° C baking process to fully imidize. In contrast, positive photoresist, such as Shipley 1400J, is much better suited for patterning, needs shorter baking times, and provides the same protective qualities as polyimide. It does not peel off, but after soaking in electrolyte for three days, there was a slight color change. Thus, the rest of the new MMEs used in our runs were patterned with resist before use and hardbaked for 45 minutes. Hardbaking is required to drive out solvents, which may otherwise contaminate the solution, and form a film on the platinum electrode surface. Such a film was observed after overnight cathodic polarization of an MME with a poorly-baked resist layer. After following this procedure, MME wafer #5 suffered only three corroded segments in three days of continuous experimentation. The losses occurred in large gaps in the photoresist film; none occurred because of electrolyte seepage through the polymer film itself.

The third cause of degraded information from the MME array was through shorts between neighboring lines. The Faradaic current in this case is overwhelmed by a purely electronic current caused by the impedance mismatch between the separate current followers attached to the two wires. Each current follower attempts to measure the current through the wire, but in doing so, draws current from the other current to voltage converter connected to the same circuit through the short. These non-Faradaic currents may be conveniently detected before the MME is actually used by running all 120 current followers simultaneously before the electrode is immersed in the electrolyte. Any currents that appear are caused by shorts, and each pair of shorted elements may also be identified. One channel will have the exact current as its shorted counterpart, but with opposite sign. Since the current is really flowing in a closed loop, the net current must be zero. By disconnecting one of the two current followers, the other will

measure the sum of the Faradaic currents going to both segments during the experiment. This is preferable to disconnecting both elements, in that the current to neighboring, isolated elements is not distorted. Since column averages are used in our experiments, the row position of each segment need not be known, only which column it belongs to. Thus, several of the doubled-up segments were used without modification.

<b>Table 6.1: Mapping Electrode Segments to Multiplexer Channel</b>				
<b>Mapping by Connector Position (Connector I)</b>				
<b>Connector</b>	<b>Electrode</b>	<b>Junction Box #</b>	<b>Multiplex Ch.</b>	<b>Datary #</b>
I-2,I-3,I-4 *	(3,7)	(12,8)	71	hex 46
I-5	(2,7)	(12,10)	128	hex 7F
I-6	(1,7)	(11,10)	127	hex 7E
I-7	(5,6)	(10,10)	126	hex 7D
I-8	(4,6)	(9,10)	125	hex 7C
I-9	(3,6)	(8,10)	124	hex 7B
I-10	(1,6)	(7,10)	123	hex 7A
I-11	(2,6)	(6,10)	122	hex 79
I-12 *	Blank	disconnected		-
I-13 *	Blank	disconnected		-
I-14 *	Blank	disconnected		-
I-15 *	Blank	disconnected		-
I-Center	Buffer	-		-
I-19	(1,5)	(1,10)	117	hex 74
I-20	(2,5)	(11,9)	116	hex 73
I-21	(3,5)	(10,10)	115	hex 72
I-22	(4,5)	(9,9)	114	hex 71
I-23	(1,4)	(8,9)	113	hex 70
I-24	(2,4)	(12,9)	72	hex 47
I-25	(3,4)	(6,9)	111	hex 6E
I-26	(1,3)	(5,9)	110	hex 6D
I-27	(2,3)	(4,9)	109	hex 6C
I-28	(1,2)	(3,9)	108	hex 6B
I-29	(1,1)	(2,9)	107	hex 6A
I-30	(A1)	(1,9)	106	hex 69
I-31	(2,2)	(11,8)	105	hex 68
I-32	(2,1)	(10,8)	104	hex 67
I-33	(3,3)	(9,8)	103	hex 66
I-34	(3,2)	(8,8)	102	hex 65
I-35	(3,1)	(7,8)	101	hex 64

**Table 6.1: Mapping Electrode Segments to Multiplexer Channel Numbers**

<b>Mapping by Connector Position (Connector II)</b>				
<b>Connector</b>	<b>Electrode</b>	<b>Junction Box #</b>	<b>Multiplexer Ch.</b>	<b>Datary #</b>
II-2,II-3,II-4 *	(9,10)	(12,6)	69	hex 44
II-5	(8,9)	(11,5)	64	hex 3F
II-6	(8,10)	(10,5)	63	hex 3E
II-7	(7,7)	(9,5)	62	hex 3D
II-8	(7,8)	(8,5)	61	hex 3C
II-9	(7,9)	(7,5)	60	hex 3B
II-10	(7,10)	(6,5)	59	hex 3A
II-11	(6,6)	(5,5)	58	hex 39
II-12	(6,7)	(4,5)	57	hex 38
II-13	(6,8)	(3,5)	56	hex 37
II-14	(6,10)	(2,5)	55	hex 36
II-15	(6,9)	(12,3)	6	hex 05
II-Center	Buffer	-		
II-19	(5,9)	(11,4)	53	hex 34
II-20 *	(5,10)	(12,2)	7	hex 06
II-21	(5,8)	(9,4)	51	hex 32
II-22	(5,7)	(8,4)	50	hex 31
II-23	(4,10)	(7,4)	49	hex 30
II-24	(4,9)	(6,4)	48	hex 2F
II-25	(4,8)	(5,4)	47	hex 2E
II-26	(3,10)	(4,4)	46	hex 2D
II-27	(3,9)	(3,4)	45	hex 2C
II-28	(2,10)	(2,4)	44	hex 2B
II-29	(1,10)	(1,4)	43	hex 2A
II-30	(2,9)	(11,3)	42	hex 29
II-31	(1,9)	(10,3)	41	hex 28
II-32	(3,8)	(9,3)	40	hex 27
II-33	(2,8)	(8,3)	39	hex 26
II-34	(1,8)	(7,3)	38	hex 25
II-35	(4,7)	(6,3)	37	hex 24

**Table 6.1: Mapping Electrode Segments to Multiplexer Channel Numbers**

<b>Mapping by Connector Position (Connector III)</b>				
<b>Connector</b>	<b>Electrode Segment</b>	<b>Junction Box #</b>	<b>Multiplexer Channel</b>	
III-2,III-3,III-4 *	(10,3)	(12,5)	8	hex 07
III-5	(7,4)	(5,3)	36	hex 23
III-6	(8,4)	(4,3)	35	hex 22
III-7	(B2)	(3,3)	34	hex 21
III-8	(9,4)	(2,3)	33	hex 20
III-9	(10,4)	(1,3)	32	hex 1F
III-10	(6,5)	(11,2)	31	hex 1E
III-11	(7,5)	(10,2)	30	hex 1D
III-12	(8,5)	(9,2)	29	hex 1C
III-13	(10,5)	(8,2)	28	hex 1B
III-14	Blank	-	27	hex 1A
III-15	Blank	Disconnected	-	
III-Center	Buffer	-	-	
III-19	(9,5)	(5,2)	25	hex 18
III-20	(B3)	(4,2)	24	hex 17
III-21	(9,6)	(3,2)	23	hex 16
III-22	(10,6)	(2,2)	22	hex 15
III-23	(8,6)	(1,2)	21	hex 14
III-24	(7,6)	(12,1)	20	hex 13
III-25	(10,7)	(11,1)	19	hex 12
III-26	(B5)	(10,1)	18	hex 11
III-27	(B4)	(9,1)	17	hex 10
III-28	(9,7)	(8,1)	16	hex 0F
III-29	(8,7)	(7,1)	15	hex 0E
III-30	(10,8)	(6,1)	14	hex 0D
III-31	(9,8)	(5,1)	13	hex 0C
III-32	(10,9)	(4,1)	12	hex 0B
III-33	(10,10)	(3,1)	11	hex 0A
III-34	(9,9)	(2,1)	10	hex 09
III-35	(8,8)	(1,1)	9	hex 08



**Table 6.1: Mapping Electrode Segments to Multiplexer Channel Numbers**

<b>Mapping by Connector Position (Connector IV)</b>				
<b>Connector</b>	<b>Electrode Segment</b>	<b>Junction Box #</b>	<b>Multiplexer Channel</b>	
IV-2,IV-3,IV-4 *	(4,4)	(12,7)	70	hex 45
IV-5	(4,3)	(6,8)	100	hex 64
IV-6	(A2)	(5,8)	99	hex 63
IV-7	(4,2)	(4,8)	98	hex 62
IV-8	(4,1)	(3,8)	97	hex 61
IV-9	(5,5)	(2,8)	96	hex 60
IV-10	(5,4)	(1,8)	95	hex 5F
IV-11	(5,3)	(11,7)	94	hex 5E
IV-12	(5,1)	(10,7)	93	hex 5D
IV-13	(5,2)	(9,7)	92	hex 5C
IV-14	(A3)	(8,7)	91	hex 5B
IV-15	(6,2)	(7,7)	90	hex 5A
IV-Center	Buffer	-	-	
IV-19	(6,1)	(6,7)	89	hex 59
IV-20	(6,3)	(5,7)	88	hex 58
IV-21	(6,4)	(4,7)	87	hex 57
IV-22	(7,1)	(3,7)	86	hex 56
IV-23	(7,2)	(2,7)	85	hex 55
IV-24	(A4)	(1,7)	84	hex 54
IV-25	(A5)	(11,6)	83	hex 53
IV-26	(7,3)	(10,6)	82	hex 52
IV-27	(8,1)	(9,6)	81	hex 51
IV-28	(8,2)	(8,6)	80	hex 50
IV-29	(9,1)	(7,6)	79	hex 4F
IV-30	(10,1)	(6,6)	78	hex 4E
IV-31	(9,2)	(5,6)	77	hex 4D
IV-32	(B1)	(4,6)	76	hex 4C
IV-33	(10,2)	(3,6)	75	hex 4B
IV-34	(8,3)	(2,6)	74	hex 4A
IV-35	(9,3)	(1,6)	73	hex 49

Table 6.2: Multiplexer Channel Numbers for Individual Segments

Electrode Array Location										
Col.→ Row↓	1	2	3	4	5	6	7	8	9	10
1	107 <sup>(1,1)</sup>	108 <sup>(1,2)</sup>	110 <sup>(1,3)</sup>	113 <sup>(1,4)</sup>	117 <sup>(1,5)</sup>	123 <sup>(1,6)</sup>	127 <sup>(1,7)</sup>	38 <sup>(1,8)</sup>	41 <sup>(1,9)</sup>	43 <sup>(1,10)</sup>
2	104 <sup>(2,1)</sup>	105 <sup>(2,2)</sup>	109 <sup>(2,3)</sup>	72 <sup>(2,4)</sup>	116 <sup>(2,5)</sup>	122 <sup>(2,6)</sup>	128 <sup>(2,7)</sup>	39 <sup>(2,8)</sup>	42 <sup>(2,9)</sup>	44 <sup>(2,10)</sup>
3	101 <sup>(3,1)</sup>	102 <sup>(3,2)</sup>	103 <sup>(3,3)</sup>	111 <sup>(3,4)</sup>	115 <sup>(3,5)</sup>	124 <sup>(3,6)</sup>	71 <sup>(3,7)</sup>	40 <sup>(3,8)</sup>	45 <sup>(3,9)</sup>	46 <sup>(3,10)</sup>
4	97 <sup>(4,1)</sup>	98 <sup>(4,2)</sup>	100 <sup>(4,3)</sup>	70 <sup>(4,4)</sup>	114 <sup>(4,5)</sup>	125 <sup>(4,6)</sup>	37 <sup>(4,7)</sup>	47 <sup>(4,8)</sup>	48 <sup>(4,9)</sup>	49 <sup>(4,10)</sup>
5	92 <sup>(5,1)</sup>	93 <sup>(5,2)</sup>	94 <sup>(5,3)</sup>	95 <sup>(5,4)</sup>	96 <sup>(5,5)</sup>	126 <sup>(5,6)</sup>	50 <sup>(5,7)</sup>	51 <sup>(5,8)</sup>	53 <sup>(5,9)</sup>	5 <sup>(5,10)</sup>
6	89 <sup>(6,1)</sup>	90 <sup>(6,2)</sup>	88 <sup>(6,3)</sup>	87 <sup>(6,4)</sup>	31 <sup>(6,5)</sup>	58 <sup>(6,6)</sup>	57 <sup>(6,7)</sup>	56 <sup>(6,8)</sup>	6 <sup>(6,9)</sup>	55 <sup>(6,10)</sup>
7	86 <sup>(7,1)</sup>	85 <sup>(7,2)</sup>	82 <sup>(7,3)</sup>	36 <sup>(7,4)</sup>	30 <sup>(7,5)</sup>	20 <sup>(7,6)</sup>	62 <sup>(7,7)</sup>	61 <sup>(7,8)</sup>	60 <sup>(7,9)</sup>	59 <sup>(7,10)</sup>
8	81 <sup>(8,1)</sup>	80 <sup>(8,2)</sup>	74 <sup>(8,3)</sup>	35 <sup>(8,4)</sup>	29 <sup>(8,5)</sup>	21 <sup>(8,6)</sup>	15 <sup>(8,7)</sup>	9 <sup>(8,8)</sup>	64 <sup>(8,9)</sup>	63 <sup>(8,10)</sup>
9	79 <sup>(9,1)</sup>	77 <sup>(9,2)</sup>	73 <sup>(9,3)</sup>	33 <sup>(9,4)</sup>	25 <sup>(9,5)</sup>	23 <sup>(9,6)</sup>	16 <sup>(9,7)</sup>	13 <sup>(9,8)</sup>	10 <sup>(9,9)</sup>	69 <sup>(9,10)</sup>
10	78 <sup>(10,1)</sup>	75 <sup>(10,2)</sup>	8 <sup>(10,3)</sup>	32 <sup>(10,4)</sup>	28 <sup>(10,5)</sup>	22 <sup>(10,6)</sup>	19 <sup>(10,7)</sup>	14 <sup>(10,8)</sup>	12 <sup>(10,9)</sup>	11 <sup>(10,10)</sup>

106 <sup>(A1)</sup>	—	99 <sup>(A2)</sup>	—	91 <sup>(A3)</sup>	—	84 <sup>(A4)</sup>	—	83 <sup>(A5)</sup>
---------------------	---	--------------------	---	--------------------	---	--------------------	---	--------------------

76 <sup>(B1)</sup>	—	34 <sup>(B2)</sup>	—	24 <sup>(B3)</sup>	—	17 <sup>(B4)</sup>	—	18 <sup>(B5)</sup>
--------------------	---	--------------------	---	--------------------	---	--------------------	---	--------------------

Multiplexer channels #27 and 52 are blank. The "A" satellites are 300  $\mu\text{m}$  from the array, and the "B" satellites are 500  $\mu\text{m}$  from the array. In the nomenclature used, "B" satellites are directly below the array, and the "A" satellites are to the left. A 90° counter-clockwise turn allows use of the "A" satellites. The electrode numbering would then change (i.e. (1,10)=(1,1), etc.).

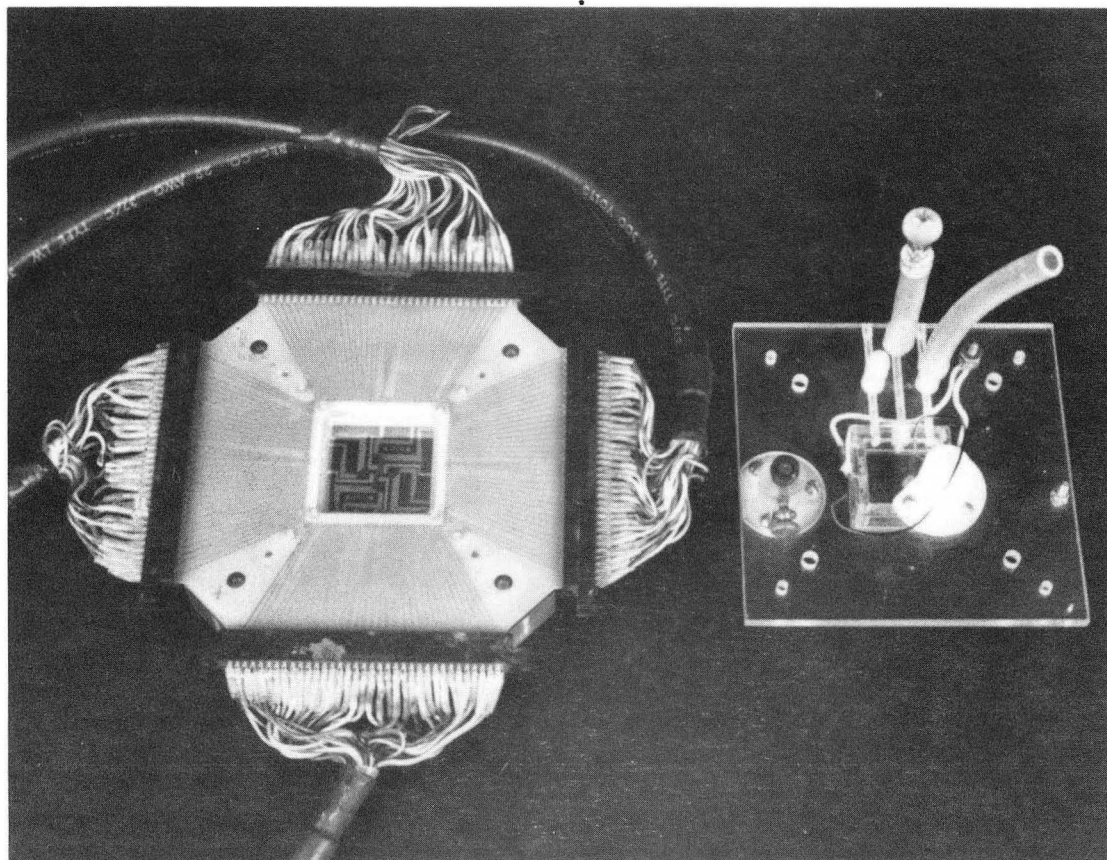
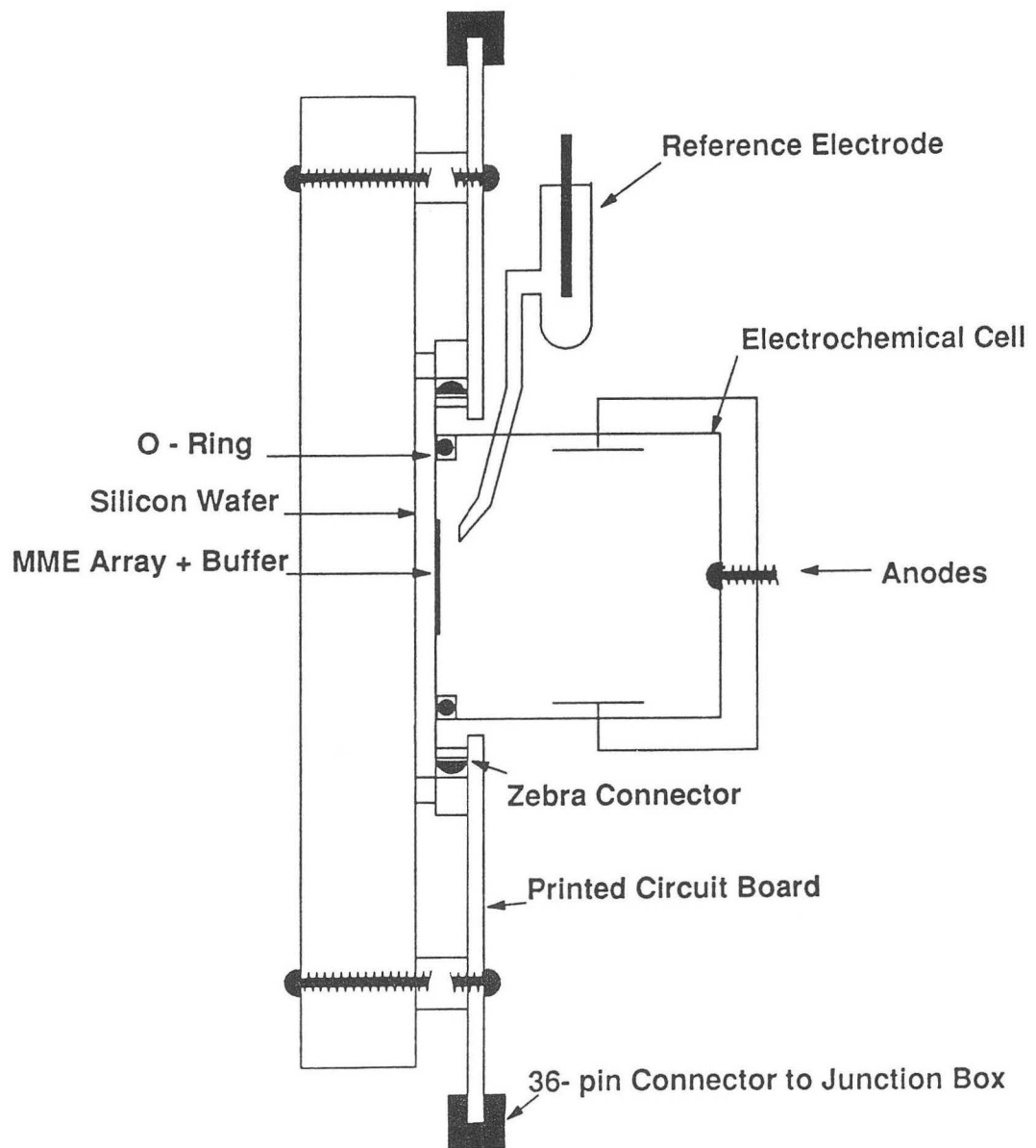
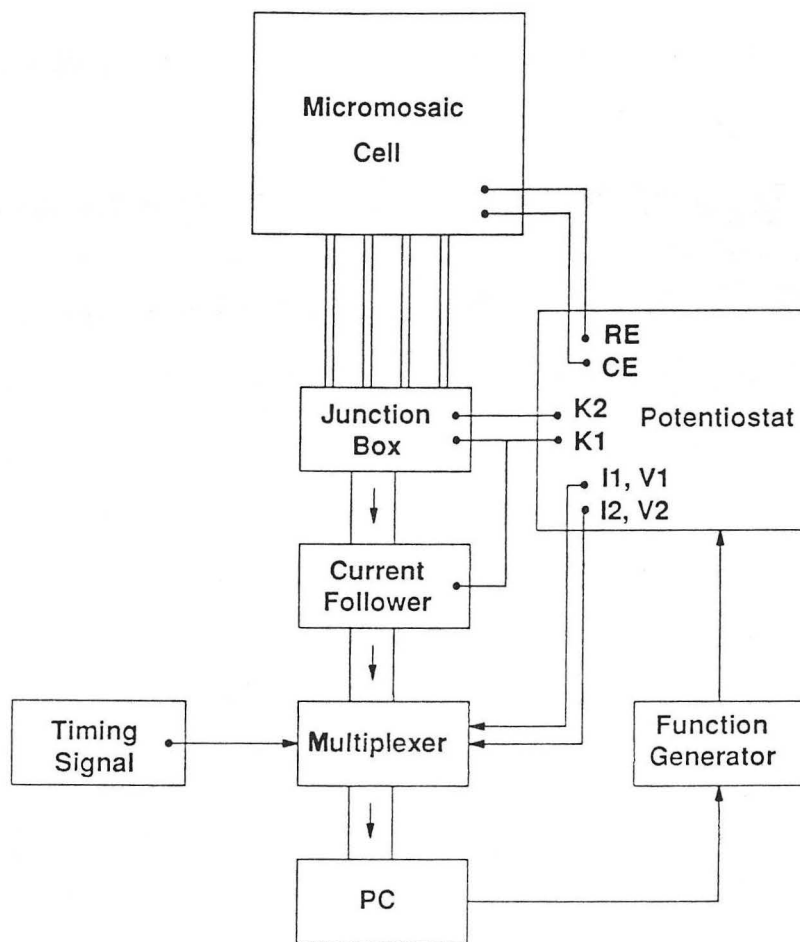


Figure 6.1 Partially-disassembled cell for studies on electrolytic gas evolution with a micro-mosaic electrode. The MME is shown in its casing, attached to four 32-pin connectors which lead to the data-acquisition system. CBB 912-957A



XBL 915-1101

Figure 6.2. Electrochemical cell for gas-evolution experiments.



XRL 915 1102

Figure 6.3. Schematic diagram of data acquisition system for the micro-mosaic gas-evolution experiments.

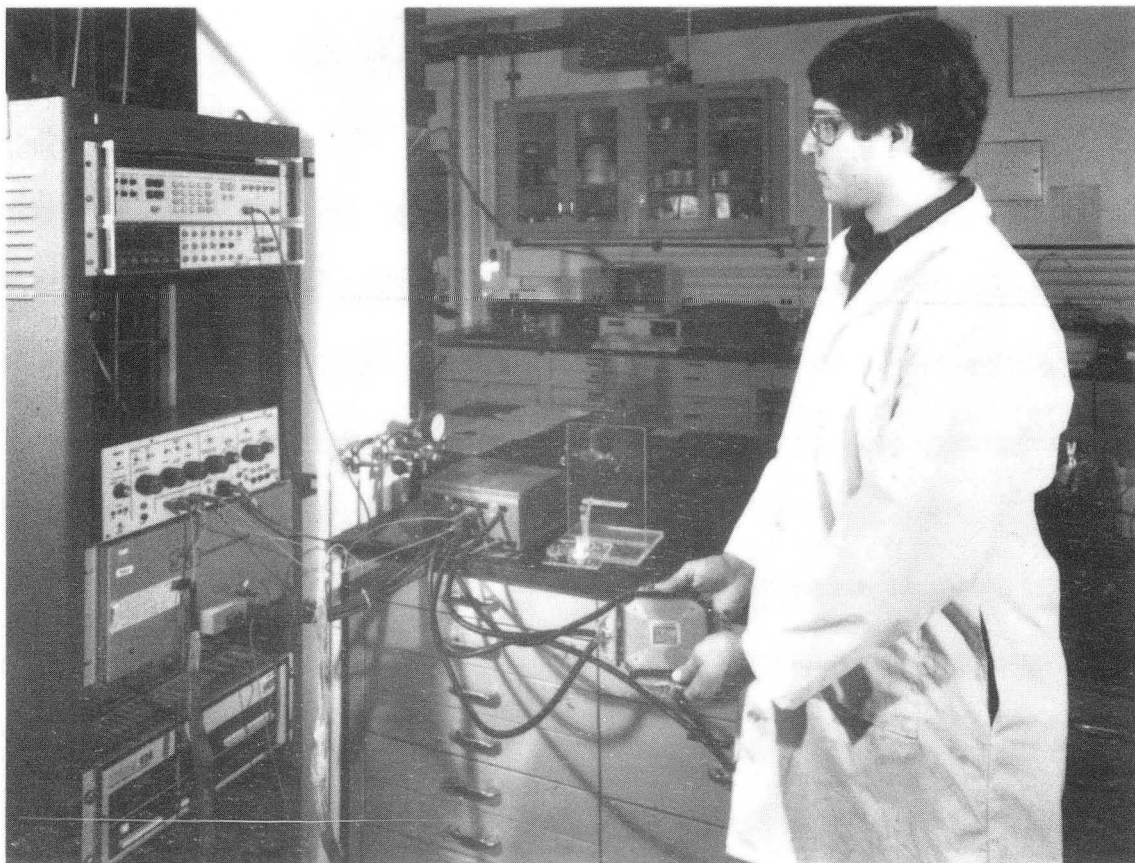
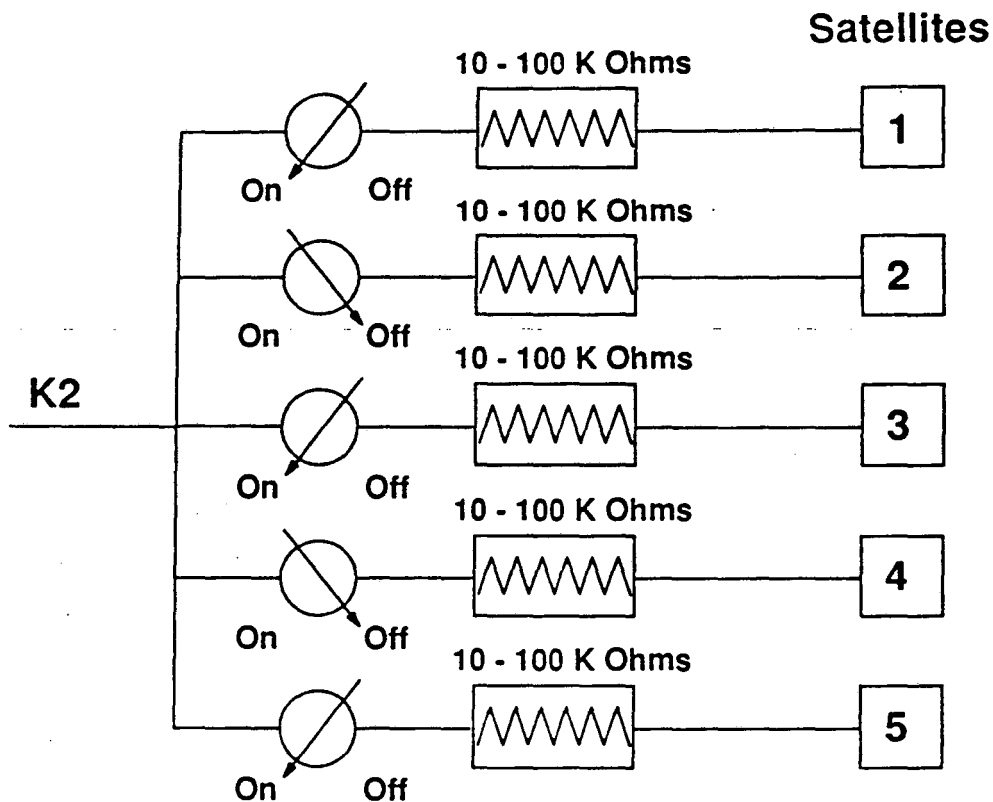


Figure 6.4 Experimental apparatus for studies on bubble-induced mass-transport enhancement. CBB 912-959A



XBL 915-1103

Figure 6.5. Schematic diagram of the potentiometers used to control the current to the satellite segments. Each segment has a variable resistor to match the satellite's impedance with the other gas-evolving segments. Once the current flow to each of the electrodes is the same at a given potential K2, the number of columns can be varied by use of the toggle switch. In the diagram, three columns of gas, on satellites 1, 3, and 5, are being evolved.

## Chapter 7 - Mass-Transport to Vertical Electrodes

### 7.1 Single Hydrogen Bubble Columns

Experiments were performed on single and multiple hydrogen gas columns to determine their effect on the mass-transport of a transport-limited reaction to a vertical electrode. Limiting currents for the reduction of  $\text{Fe}^{+3}$  were gathered over a broad range of practical gas-evolution rates, from  $35 \text{ mA/cm}^2$  up to  $1 \text{ A/cm}^2$ . The results for a single hydrogen bubble column are presented first, while data on parallel hydrogen and oxygen gas streams are discussed below.

Figure 7.1 shows results for a single hydrogen bubble column evolved from a Hewlett-Packard electrode identical to those used in previous work by Whitney and Tobias. Fig. 7.2 gives results from experiments on a gold MME of the original design, built by Bell Labs, while data from experiments with the new, redesigned micromosaic are shown in Fig. 7.2a.

The data obtained with the HP electrode purposely cover the range of bubble current densities used by Whitney, to test whether the present experiments match her results. The ratio in relative local and far-field current densities in the presence low-current a single bubble stream is used as the basis for comparison. Local enhancement is taken to be the ratio of the bubble-enhanced transport-limited current density to the background value in the absence of rising bubbles ( $i_l^*/i_l$ ), measured directly under the passing bubble stream. The far-field current is the average for the same ratio, measured at columns 1, 2, 9 and 10 (those that lie at least  $400 \mu\text{m}$  to the side of the bubble path). At  $35 \text{ mA/cm}^2$ , Whitney obtained a ratio between the two regions of 1.32, compared to a ratio of 1.96 in our experiments. At higher current densities, the results are less disparate. The earlier work reported a relative enhancement ratio of 2.01 at  $160 \text{ mA/cm}^2$ , while the present results give a ratio of 2.25 at  $140 \text{ mA/cm}^2$  and 2.28 at  $250 \text{ mA/cm}^2$ .



The discrepancy in peak and relative enhancements between the two studies may have several causes. Concurrent chromium corrosion on the HP micromosaics skews the observed enhancement ratios, but deviations are more likely because of the effect of secondary variables such as the bubble frequency and size, both of which may have been different between our runs and Whitney's. It is likely that the bubbles generated on satellite segments do not capture all of the hydrogen evolved. Total capture was assumed by Whitney and Dees in their studies. As a result, the current density alone may not determine the level of observed enhancement.

While segments on the HP MME failed after extensive corrosion, flickering and bipolar behavior were also observed before the appearance of an open circuit. Corrosion was not significant in experiments with either the Bell or in-house MMEs, although non-working segments caused by fabrication flaws or non-adhesion still were present. The exact location of non-working and bipolar segments alters the average enhancement of the mass-transfer coefficient for each of the individual segments. Errors introduced by non-working segments are minimized by presenting the data as column averages, so that the effect of a single non-working segment is less pronounced.

Our results on the HP and Bell electrodes were qualitatively similar to each other in terms of the breadth of the central enhancement region, but the value of the peak enhancement was off by a substantial margin. At  $11 \mu\text{A}$  ( $110 \text{ mA/cm}^2$ ) on the HP electrodes, for example, the peak value of  $i_1^*/i_1$  was 3.17, while it was only 2.55 for the Bell experiments. On the new MME, runs at such low bubble currents were not performed, owing to the lack of uniformity between the sizes of successive bubbles.

On the gold (Bell Labs) micro-mosaics, the peak enhancement also goes through a maximum then declines slightly at the highest gas-evolution rate,  $100 \mu\text{A}$  ( $1 \text{ A/cm}^2$ ). While this phenomenon occurred at much higher hydrogen current densities than studied previously, it was still unexpected that an increase in gas-evolution rate would lower, rather than raise the mass-transfer coefficient directly behind the rising

bubble stream. It is unlikely that ohmic drop in the vicinity of the bubble would have created the diminished enhancement, since varying the potential at which the limiting current was measured did not change the data. What is evident is that the overall enhancement at  $1 \text{ A/cm}^2$  still rises to the side of the passing bubble, so that the renewal path is broader. This implies that the bubbles forming the stream are larger at  $1 \text{ A/cm}^2$ , though perhaps their passage over the electrode is less frequent.

Although not emphasized in her discussion, Whitney [141] reported that the enhancement ratio actually falls between runs at  $9 \mu\text{A}$  ( $90 \text{ mA/cm}^2$ ) and those at  $16 \mu\text{A}$  ( $160 \text{ mA/cm}^2$ ). There was a large concurrent increase in the reported bubble diameter as well, precisely between these two cases. At lower bubble currents, the diameter ranged from 45 - 60 microns, then jumped to 78 microns for the  $16 \mu\text{A}$  experiment. It may be surprising to find that a larger bubble would have less of an effect than a smaller one, since Stokes' Law predicts that the velocity of a rising sphere scales as the square of the radius. The bigger bubble rises faster, but as the increase in gas-evolution current is not proportional to the larger size, the bubble frequency falls between the two cases. It is likely that the higher frequency of the low-current case results in the larger enhancements to the column directly beneath the rising stream, both in Whitney's data and our own at  $1 \text{ A/cm}^2$  on the Bell electrodes.

This is precisely what is predicted by surface renewal models, which show that the redox mass-transfer coefficient should vary as the square root of the bubble frequency. Only when bubble size stays constant, can the frequency dependence be replaced by a gas-evolution rate dependence. In order to test the hypothesis that the frequency, not the size of bubbles determined the observed peak enhancement, microphotographs (Fig. 7.3) of the bubble streams were taken for experiments with the new MME.

The hydrogen bubble volumes were then compared to the those expected from a mass-balance using a hard-sphere Stokes' value as the velocity of the rising bubbles ([35a]). Janssen and Hoogland [158] observed that the speed with which bubbles rise past a vertical electrode does not stay constant with increasing height. Rather, there is an acceleration caused by convective currents. While the Stokes' Law velocity for a 50  $\mu\text{m}$  bubble is 0.56 cm/s, Janssen and Hoogland reported velocities four times as large. It was not possible to determine the velocity of our streams independently, since high speed motion pictures were not taken, but for a mass balance and the observed distance between bubbles, it may be estimated that the stream is traveling close to the Stokes' velocity (within a factor of 25%), and no acceleration is observed in Figure 7.3. Acceleration would result in an increase in distance between successive bubbles towards the top of the photographs.

The micro-photographs reveal that the bubble diameter is not constant as a function of current density, which is consistent with the experimental work of Bon [127] and Putt [138], who report that the bubble size increases with the volumetric rate of gas evolution until a constant maximum size is reached at very high current densities (2  $\text{A}/\text{cm}^2$  and higher). On an ideal surface, the size of a detaching bubble is uniquely determined by its surface tension and contact angle. On real electrodes, especially microelectrodes with sharp corners, the proximity of sites for gas evolution is closer than the spacing of marginally stable bubbles. In this event, coalescence on the surface will precede detachment. At higher currents, the coalescence events are very numerous, leading to substantially larger bubbles emerging before detachment. Thus, the size of detaching bubbles is determined by the dynamics of the nucleation and the growth of small bubbles, rather than by purely thermodynamic considerations. This accounts for the variation in bubble size with increasing current density.

Figure 7.4 shows the measured hydrogen bubble size as a function of gas-evolution rate. Comparison is made between the size measured from microphotographs to the size calculated from a mass-balance, assuming that Stokes' law holds and that the microelectrodes have a 100% capture efficiency for the generation of bubbles from the evolved hydrogen. At low current densities, this condition is severely violated, since a substantial supersaturation is necessary at the electrode surface before gas bubbles nucleate. This means that a substantial fraction of the hydrogen generated is used to maintain this supersaturation, as some of the dissolved hydrogen diffuses away from the gas-evolving satellite. This fraction becomes less significant at higher current densities, and near-total capture of the generated hydrogen in evolved bubbles can be assumed. This corresponds with our measurements; a slight negative deviation from the calculated value of the bubble diameter is found experimentally for bubbles generated at current densities below  $200 \text{ mA/cm}^2$ . The capture efficiency at the lowest current density ( $35 \text{ mA/cm}^2$ ) is  $51\% \pm 11\%$ . The large margin of error at low current densities is a reflection of the difficulty of accurately measuring the diameter of the very small ( $< 35 \text{ }\mu\text{m}$  diameter) rising bubbles from enlargements of micro-photographs.

Fig. 7.5 shows a logarithmic plot of the bubble-volume data versus gas-evolution rate. Linear regression gives a best-fit with an exponent of 0.367, with a correlation coefficient,  $r^2$ , of 0.993. The volume, which is proportional to the cube of the diameter, scales as the 1.1 power with the gas evolution rate; that is, an approximately linear dependence. This indicates that in our experiments, the frequency, not the bubble size, is the variable which stays roughly constant. Figure 7.6 gives estimates for the frequency, calculated from the distance between successive bubbles, for a large range of hydrogen currents. While the gas-evolution current was increased by a factor of 20, the frequency increased by less than a factor of two, and above  $25 \text{ }\mu\text{A}$ , seems to have stayed fairly constant. If the frequency doubles, the enhancement is expected to increase by a factor of 1.42, since the mass-transport coefficient is proportional to the

square root of the bubble frequency.

The enhancement ratio plotted in Fig. 7.7 on a logarithmic scale, rises less quickly above  $20 \mu\text{A}$  than at lower currents. This corresponds precisely to the current density where the capture efficiency becomes very close to one, and where the frequency of the bubbles no longer rises substantially. Thus, above this value, the contribution from surface-renewal mechanisms to the measured mass-transfer coefficient should be constant. It is not surprising, then, to find that the peak enhancement is only a weak function of gas-evolution rate. In the case of the Bell MME experiments, a small fall in the bubble frequency may cause the enhancement to diminish directly underneath the rising bubble stream at the highest reported current density.

Since the enhancement to the side of the center-line of the gas stream continues to rise, albeit slowly, at higher gas volumes, an additional mechanism must also be at work to provide more efficient mass-transport to the vertical electrode. At these high current densities, it is likely that macroscopic hydrodynamic flows will contribute to the background natural convection. The drag exerted by the rising bubbles forces the fluid in the cell to rise, and creates a cell-wide recirculating pattern that reinforces the natural convective flow caused by density variations near the electrode surface.

The unexpected lowering of background limiting currents in the presence of rising bubble streams seen in Whitney's results was not observed. A modest *enhancement* of the limiting current was measured over the entire segmented electrode under all experimental conditions, even at current densities lower than those used in the earlier study. This may help elucidate how the enhancement of mass-transport varies with distance to the sides of rising gas columns. Directly underneath and in close proximity to the rising stream, surface-renewal is the dominant mechanism. Further away, the enhancement is weaker but more uniform, probably resulting from an assisting macroscopic convective flow. This suggests that an analysis using the hydrodynamic models presented above in Chapter 5, made be useful in correlating the data.

Based on turbulent natural convection models, Janssen and Barendrecht obtain the following dependence of the mass-transport coefficient on the diameter and gas fraction of the bubbles, as in Eq. 5.7:

$$\text{Sh} \equiv \frac{kd_{\text{bub}}}{D_i} = 0.16 \left( \frac{12\rho_l}{\rho_l - \rho_g} \right) \left( \frac{vd_{\text{bub}}}{D_i} \right)^{1/3} \quad (7.1)$$

This is very identical to the analogous model proposed by Zuber [168] for heat transfer at a horizontal electrode during nucleate boiling. By incorporating a dependence of  $r_{\text{bub}}$  on the current density,

$$r_{\text{bub}} \propto (i_{\text{bub}})^{0.367} \quad (7.2)$$

we transform 7.1 into 7.3:

$$i_l^{\text{red}} \propto (i_{\text{bub}})^{0.09} * \epsilon^{0.33} \quad (7.3)$$

Experimentally, from our measurements for outlying segment columns (i.e. columns 1-3 and 8-10), the mass-transport increases as a function of the gas current density with an exponent ranging from 0.12 to 0.17, with a correlation coefficient,  $r^2$ , of 0.97-0.99+, as seen in Fig. 7.7. While somewhat higher than predicted by the revised hydrodynamic model, better agreement is obtained after the effect of changing bubble size is included in the analysis. The effect of the gas fraction may be one reason for the discrepancy, since (7.1) was derived for a small gas fraction.

The exponent in the correlation is also sensitive to the addition rule used for determining the relative contributions of background natural convection, bubble-assisted laminar flows, and surface-renewal by local turbulent mixing. Using Churchill's sum of cubes [146] approach as discussed in Chapter 5, for combining the hydrodynamic contribution with background leads to the low power dependence reported. Previous researchers have not subtracted out background at all [158], or have followed Beck's proposed linear summation [160]. Therefore, although Alkire and Lu [144] also obtained a 0.15 dependence, it was after a linear subtraction of the back-

ground natural convection. If we followed Beck's convention, the exponent would range from 0.25 to 0.32, similar to the ranges reported for turbulent natural convection by Fouad and Ibl [149].

The surface-renewal contribution is not of the same form as an assisting laminar flow, so the proper addition rule to be employed remains undecided. It seems likely that the presence of a bubble-induced laminar fluid flow provides the surface renewal mechanism with an appropriate background diffusion layer thickness, which is periodically thinned with a frequency equal to the time between successive bubbles passing the surface. If so, the contribution of the surface-renewal must be linearly, not cubically, summed with the contributions of the two laminar flow mechanisms. The total mass-transfer coefficient will then be

$$k_{\text{tot}} = k_{\text{sr}} + (k_{\text{nc}}^3 + k_{\text{hyd}}^3)^{1/3} \quad (7.4)$$

This hypothesis can be tested with experiments on multiple columns. In situations where surface-renewal is the dominant enhancement mode, linear superposition of single-column enhancement should predict the effect of multiple columns if Eq. 7.5 holds.

Finally, as stated above, the actual velocity of the bubbles is only important in so far as the frequency is determined by the spacing between bubbles divided by their velocity. At higher bubble currents, the velocity of the rising stream may add linearly to the Stokes' velocity, so that frequencies calculated in Fig. 7.6 may be too conservative at the upper gas-evolution rates. Thus, the divergence between the predicted power dependence from the 'hydrodynamic' model and that obtained experimentally may be caused by higher frequencies than would be expected with bubbles rising in a quiescent fluid.

## 7.2 Multiple Hydrogen Bubble Columns

While single-column data was useful in identifying the mechanisms of enhancement, it is nevertheless far removed from situations normally encountered in electrochemical systems. Curtains of bubbles rising lamarily over a vertical electrode are ubiquitous, and studies on parallel columns allow us to more closely approximate them. Our experiments measured the effect of distance between adjacent gas streams as well as the effect of the total number of columns. The most extensive set of runs was done with two columns, but data was also obtained on the effect of three and five parallel, non-interacting streams. Experiments with more than two columns give a more complete picture regarding the cooperative effect of columns. At some point, cell-scale recirculating flow created by the bubbles will become the dominant enhancement method, and experiments with three and five columns can determine these effects.

The generation of multiple columns required careful matching of the impedance of each micromosaic satellite to obtain the same current density at each one. Both the resistances and the catalytic activity of each of the electrodes were different. The difference in overpotential for hydrogen generation had to be compensated by use of trim potentiometers on each of the satellites, as explained in Chapter 6.

Figure 7.8 shows two columns rising from adjacent segments. The microphotographs differ only in the type of lighting used. The placement and angle of the fiber-optic illumination greatly changes the contrast between the vertical electrode and the bubble. In the top micro-photo, the bubbles are dark circles, which approach each other as they rise. The resulting enhancement, Fig. 7.9, is stronger and broader than for a single column. Fig. 7.10 shows a comparison between the enhancement for single columns at 25 and 50  $\mu\text{A}$ , and for two columns, with 25  $\mu\text{A}$  evolved on each. When comparing the overall enhancement for the same total hydrogen gas-evolution, **creating two parallel columns with smaller bubbles gives higher peak and far-field enhancement than a single stream.**



Towards the periphery, the hydrodynamic effect is the dominant enhancement mechanism, while close to the streams, surface-renewal provides the larger contribution to the mass-transfer coefficient. While both effects are promoted by the presence of the more-numerous smaller bubbles, the surface-renewal model explicitly states that the frequency of bubble passage, not the size of the bubble, determines the local enhancement. It should be remembered that the volume of a sphere is proportional to the cube of the diameter, while the velocity of a rising bubbles is proportional to the square. **Thus, for equivalent volumes of gas, the smaller-width stream of bubbles will pass an electrode more frequently, even if its velocity is lower.**

The results for columns spaced only 200  $\mu\text{m}$  apart show only one enhancement peak, so that the columns act as if they were one. This is so, even if the bubbles do not travel side by side. Rather, they try to space themselves so that the bubbles in one column are exactly out-of-phase with their nearest neighbor, doubling their frequency relative to the case with a single bubble stream. The phase-locking behavior is probably a result of entrainment, whereby the resistance to buoyant motion is minimized if the aggregate column width is narrowed. The narrowest column is created when the bubbles stay  $180^\circ$  out of phase.

At larger separations, the bubbles no longer tend to entrain one another. They rise vertically along the centerline between adjacent micromosaic segments, directly above the satellites from where they were generated, as seen in the micro-photographs in Fig. 7.11. The enhancement for the 400  $\mu\text{m}$  separation between adjacent columns shows a double peak at low current densities, which becomes a wider single envelope at higher bubble currents (Fig. 7.12). The results for this pair of satellites is the least symmetric of all the experiments done, probably caused by a small ( $< 5\%$ ) difference in gas-evolution rates between the two streams. In spite of this, there is a remarkable pattern that develops when a second column of gas bubbles is turned on, on one side of the center stream. As Fig. 7.13 shows, segments on the other side of the center bubble

stream remain completely unperturbed by the presence or absence of additional gas columns. The effect of gas streams B1 and B2 is negligible on columns 6 - 10. If peak enhancement were caused by macroscopic flows, this would not be likely. Rather, localized turbulent mixing is shielded by the presence of the central bubble stream.

The penalty for increasing the bubble separation from 200 to 400  $\mu\text{m}$  is also very modest. The peak enhancement is equally high in both cases, but is spread out over a larger width for the wider separation. The closer separation is clearly less optimal if the enhancement ratios are averaged over the entire micromosaic. Increasing the separation further (Fig. 7.12), to 800  $\mu\text{m}$ , creates a smaller enhancement between the bubble columns. The peak enhancement ratio also falls from 3.6 using streams B1+B2 and B1+B3, to 3.2 for experiments with B1+B5, as seen in Fig. 7.14. Thus, the optimal spacing of gas streams for maximal uniform enhancement lies between 400 and 800  $\mu\text{m}$  separation for bubbles that are approximately 80 microns in diameter. Since the surface-renewal effect has been shown by Whitney to extend for 5-7 bubble diameters, an optimal spacing of approximately 400-560  $\mu\text{m}$  would have been expected.

Figure 7.15 shows micro-photographs of three parallel bubble columns. Entrainment is noticeable when the streams are 200  $\mu\text{m}$  apart; the bubbles in neighboring streams are locked out-of-phase with respect to one another and the width of the composite stream is contracted. Superposition of enhancement can be tested by plotting the results as in Fig. 7.16. Here we see that three bunched gas streams do not have a wider effect than expected by superposition. The results for B3 match those for B1+B2+B3 for columns 6-10. In fact, the fit is amazingly reproducible. The results for the B3 case alone, were taken several hours earlier than for the combined case. The slight deviation (<5%) between the two can be accounted for by the small (9%) difference in the current densities used. As seen in earlier examples, the enhancement ratio is only a weak function of gas-evolution rate, but a strong function of the position of the gas stream. When the three columns are spaced widely apart (Fig. 7.17), the effect of

column B1 is again matched perfectly, for the same reasons as given above for B3. If superposition holds, then the data from parallel columns can be predicted by data from single columns, as long as entrainment does not distort the behavior of the component streams. Section 7.7 below shows the results of such a model for both the hydrogen and oxygen bubble experiments.

With the use of three, more widely-spaced columns (Fig. 7.18), surface-renewal is supplemented by strong cell-wide flows. This is seen both by the stronger and flatter enhancement profiles, and by experimental data taken after the bubble columns were shut off. If surface-renewal were acting exclusively, the enhancements for micromosaic columns 1-4 would coincide between the experiments with B1+B2+B3 versus B1-B5. They do not, and five gas streams yields a significantly higher enhancement, especially at currents below 100  $\mu\text{m}$  per column.

The "abklingen" or decay experiment consists of measuring the limiting current for the reduction of  $\text{Fe}^{++}$  to  $\text{Fe}^{+++}$  on the micromosaic after the bubble evolution is stopped. Before shut-off, three columns of gas were used. Their individual gas-evolution rates were fairly modest; 16  $\mu\text{A}$  per column. Fig. 7.19 plots the decay of the average current density on the micromosaic versus time. It takes up to 1-2 minutes until the limiting current falls back to the background level. This suggests that for multiple bubble columns, the thinning of the boundary layer by assisted laminar convection is the primary method of enhancement.

The experiments with five bubble columns continue the trend observed in the earlier runs. The photos (Fig. 7.20) show possible entrainment, with the bubbles moving out-of-phase with their nearest neighbor, greater enhancement than equivalent-volume runs with fewer columns is shown in Fig. 7.21, with a broad uniform enhancement over the entire micromosaic. The only difference from data with fewer bubble streams is that there does not appear to be the same degree of monotonic increase as the bubble current density is increased. While the average enhancement always rises, some

mosaic columns show a greater relative increase than others.

### *7.3 Oxygen Bubble Columns at Low pH*

A second set of experiments was conducted with oxygen bubbles generated in the same low pH (0.5 M H<sub>2</sub>SO<sub>4</sub>) solution. It has been reported that oxygen bubbles are smaller than hydrogen bubbles in acid electrolytes [138]; and our micro-photographs confirm this. Rather than obtaining a single bubble at each satellite, oxygen forms a tightly grouped stream which is composed of several smaller bubbles entraining each other. With hydrogen, all coalescence occurred on the satellite segment prior to detachment, and the bubbles formed were fairly large in size. For oxygen, a distribution of bubble sizes emerges from the satellite, and over a short vertical distance the larger bubbles scavenge their slower-moving neighbors. The scavenging is over before the stream passes the micromosaic, where the mass-transport measurements are made.

Figure 7.22 shows two micro-photographs of an oxygen stream rising over the micromosaic, at 25 and 100  $\mu$ A. A careful examination shows that below the micromosaic, the bubble size is considerably smaller than towards the top, showing signs of bubble scavenging. The stream width is also larger than with the single-bubble hydrogen columns, and the expectation is that the mass-transport enhancement generated by oxygen bubbles will also have a broader impact.

Fig. 7.23 shows such a comparison of enhancements induced by the two different gases for identical single 25  $\mu$ A streams. It should be remembered that an equivalent volume of oxygen consumes twice as much charge as hydrogen, so that this comparison is not of streams with equivalent volumes. The far-field enhancements between these two cases are, however, nearly identical, with the background hydrodynamically-induced enhancement ratio ranging from 1.45 - 1.55 versus the background natural-convection limiting current. This allows one to make a direct comparison of the strength and extent of the surface-renewal effect between the two bubble

varieties.

As noted above, smaller bubbles were shown to be more effective at enhancing transport when two, parallel 25  $\mu\text{A}$  hydrogen streams were compared to a single 50  $\mu\text{A}$  hydrogen bubble stream. The frequency of the smaller bubbles was double, and their surface area was also increased. This consequently increased the total drag on the surrounding fluid, which induced a commensurately larger hydrodynamic effect.

As expected from a surface-renewal model, the oxygen stream's peak enhancement is higher, but the peak width is a bit narrower. The oxygen stream has much smaller, more closely spaced bubbles. The ratio of enhancements should equal the square root of the ratio of frequencies,

$$\frac{i_{\max}/i_{\min}^{\text{hyd}}}{i_{\max}/i_{\min}^{\text{oxy}}} = \frac{v_{\text{H}_2}}{v_{\text{O}_2}} \quad (7.5)$$

Since the peak enhancement is 40% larger for the 25  $\mu\text{A}$  oxygen stream, the surface-renewal predicts that the frequency of the oxygen column must be nearly twice as high. From interpolation between Fig. 7.3c and 7.3d, the distance between hydrogen bubbles rising in a single stream is 180  $\mu\text{m}$ , while their radius is 68  $\mu\text{m}$ . Over the micromosaic, at any instant, there are approximately six hydrogen bubbles. Fig. 7.22 show, however, that the oxygen bubbles are much more numerous (thirty cover the segmented array), and that their diameters range from 10 to 45  $\mu\text{m}$ . The distance between nearest neighbors in the oxygen stream is only about 50  $\mu\text{m}$ . What is difficult to determine is the velocity of the rising street of oxygen bubbles. Stokes' law would give a large range of velocities for the individual bubbles, and would not account for the fact that the small bubbles rise much more quickly because of entrainment. The entrainment in this case is much more pronounced than with two parallel hydrogen streams, which had a fairly mono-disperse bubble size.

When a statistical analysis is done, and both curves are fitted to Gaussians, the centerline (midway between columns 5 and 6) and the background enhancement stay constant between the two cases. What varies is the half-width of the surface-renewal region which increases from 117  $\mu\text{m}$  for oxygen bubbles to 174  $\mu\text{m}$  for hydrogen. The data from the Gaussian analysis is given in Fig. 7.24 and Table 7.1 underneath the figure.

The average diameter of hydrogen bubbles generated at 25  $\mu\text{A}$  is given in Fig. 7.4 as 68  $\mu\text{m}$ . The full width of renewal path is expected to be 325 - 450  $\mu\text{m}$  by Whitney's analysis. Replacement of Whitney's assumption that the renewal is uniform within the path with a Gaussian approximation of the renewal's effect leads to a best fit of 348  $\mu\text{m}$  for the full width, in excellent agreement with her previous estimates.

The oxygen bubbles are also smaller than the hydrogen bubbles, but the width of the stream is larger because, on average, between one and two oxygen bubbles travel side-by-side as they rise. If the average oxygen bubble is 35  $\mu\text{m}$  (from Fig. 7.20), its renewal path should be approximately 175-245  $\mu\text{m}$  wide. The width of the stream is 100  $\mu\text{m}$  wide, so that the bubble position may vary by 65  $\mu\text{m}$  and remain within the stream. Adding 65  $\mu\text{m}$  to the renewal path of a single bubble, yields the renewal path of the oxygen stream as 240-305  $\mu\text{m}$ . The gaussian analysis yields 234  $\mu\text{m}$  which is in fair agreement with these estimates.

The only caveat is that the data points are not numerous enough to conclude with certainty that the renewal path between the two cases is statistically different. Since data was gathered at only ten columns, the fit is good but the margins of error are fairly broad, as seen in Table 7.1. Data with a refined mesh (i.e. a higher-resolution mosaic array) would be necessary to confirm our findings. Such an array would be difficult to fabricate, since the current lines must be thinner than the segment size, yet wide enough to prevent substantial ohmic drop.

### 7.6 Parallel Oxygen Bubble Streams

The results for multiple oxygen bubble columns show that the enhancement is indeed more localized and stronger than for the hydrogen gas data. Even when neighboring satellites (B2 and B3) are used to generate side-by-side gas streams (a 200  $\mu\text{m}$  separation distance), at low current densities one obtains a bimodal enhancement and even at high gas-evolution rates, the single enhancement peak exhibits the presence of a shoulder, as in Fig. 7.25. The micro-photographs in Fig. 7.26 show that oxygen neighboring streams do not seem to entrain one another, as in the case of two neighboring hydrogen columns. This lack of entrainment indicates that the columns act separately, rather than cooperatively. Linear superposition should account for their combined enhancements. As Fig. 7.24 illustrates, oxygen streams at low current densities have very small bubbles, so their renewal path is not expected to extend far. Further separation yields a more distinct separation between enhancement peaks, as seen in Fig. 7.27. As with earlier experiments using hydrogen bubbles, segments to the right of stream B3 are not affected at all by the use of either stream B1 or B2.

The final set of experiments used three oxygen bubble columns. In the case of hydrogen bubbles, this produced a relatively flat enhancement profile, with the average level of enhancement much improved over the two-column case. This is not seen in the case of oxygen bubble streams separated by 400  $\mu\text{m}$ . The streams act quite independently, and no unexpectedly large enhancement caused by cell-scale flow was observed. Fig. 7.28 shows microphotographs of the columns and Fig. 7.29 gives the enhancement ratios as a function of current density. Three peaks are evident, and they are relatively similar in height to the results for B3 alone, and B1 and B3 combined.

### 7.7 A Linear-Shielding Model

In the previous sections, we have seen that the enhancement of mass-transport can be separated into contributions from surface-renewal mechanisms and bubble-enhanced turbulent natural convection. A question remains: Can the enhancements for multiple columns be predicted on the basis of single stream data?

A linear summation of the enhancements is shown in Fig. 7.30, and for segments to the side of the individual streams, the match is poor. This is because each column effectively shields the effect of the other column from influencing farther regions of the micromosaic. The data in columns 1-3, and 6-10 is much better matched by the single stream results shown below the composite data. What is surprising is that shifting the B3 data to the left by 200  $\mu\text{m}$  (to simulate a stream at B2) does a remarkably good job of predicting the B2 result. Thus, linear superposition between columns and acknowledgement of shielding to the far side of columns should provide the best fit to the multiple-column data set. Fig. 7.31 gives the composite model, and the agreement is nearly exact. Fig. 7.32 compares the linear summation rule with the sum-of-cube (Ruckenstein and Churchill) rule, and a sum-of-squares rule. The best fit is clearly given by our simple linear/shielding model.

Predictions for data B1 and B3 is shown in Fig. 7.33 and the match is not quite as good. For three columns, however, our model is extremely accurate, as in Fig. 7.34. All three peaks are well-matched, as well as the strength of the troughs. The model is premised on the idea that the strong observed enhancement is local in nature, not the result of an assisting laminar flow, and that the effect can be thwarted by the presence of an obstruction such as a neighboring column. It is in consonance with the basic principles of a surface-renewal model, in both its length scale and in its logical summation rules.



The model is not limited to the oxygen evolution experiments, as seen in Fig. 7.35 and 7.36. The mass-transport enhancement caused by the rise of parallel hydrogen columns can also be well predicted, although with less accuracy than with the oxygen columns, which have a narrower renewal path. What is interesting to note is that the linear model matches the upward indentation in the enhancement ratio at column 5, for the experiment with streams B1 and B5. This is an unintuitive result since there is no gas stream rising at this position, and the higher enhancement is clearly the result of superposition.

The linear-shielding model should not be expected to work as when either of two occurrences manifest themselves: 1) when entrainment occurs between neighboring bubble streams, or 2) when hydrodynamic flows differ between the single and multiple stream experiments (i.e. at high current densities for three and five parallel hydrogen gas streams). As expected, the model's predictions are poorer in these cases.

## *7.6 Conclusions*

It is remarkable that in the gas-evolution literature to date, little distinction has been made between mass-transport enhancement to vertical and horizontal surfaces, and that the surface-renewal and hydrodynamic models are claimed to be valid in both cases. While the exponent of the dependence in mass-transfer correlations may fortuitously agree, there is no justification for supposing that the enhancement mechanisms in the two cases are identical. The presence of coalescing bubbles on horizontal gas-evolving surfaces and the scavenging of small bubbles by larger ones over vertical electrodes also introduce unnecessary complexities into a credible analysis. By studying the mass-transport effect of parallel non-interacting bubble columns, a simple approximation to the gas curtains found in industrial systems was simulated, without the accompanying uncertainties introduced by the combined effects of coalescence, scavenging, and the consequently unpredictable distribution of bubble volumes.

It was shown that the enhancement of the mass-transfer limited current of an indicator ion on a vertical electrode is increased by rising gas streams, and rises as a weak function of the gas-evolution rate. The peak enhancement rises in almost direct proportion to the far-field enhancement, showing that it is the result of a general, rather than local improvement in the mass-transfer coefficient. This suggests that a 'hydrodynamic' model should account for the increase, but does not explain the higher constant enhancements in the vicinity of a single stream.

By measuring the size of generated bubbles, and calculating their dependence on gas current, it was determined that the time between bubble passages over the mosaic does not vary by more than a factor of two, even if the gas-evolution rate is increased 20-fold. Since the enhancement predicted by surface-renewal models is solely a function of the bubble frequency, it seems likely that contributions from periodic renewal would not be a function of gas volume. Thus, the total mass-transfer coefficient would be expected to include contributions from background natural convection, local surface-renewal, and more global assisted laminar flow generated by the rising bubbles. The surface-renewal effect was postulated to sum linearly in addition to the other mass-transfer mechanisms, and also to be linearly superimposable. This last point was tested by modeling the behavior of both multiple hydrogen and oxygen bubble streams as superimposed and shifted single gas columns. The match obtained was excellent.

Testing of the surface-renewal theory was also accomplished by comparing enhancements from equivalent volume single and double hydrogen gas columns. The enhancement obtained from two columns, separated by 200  $\mu\text{m}$ , was significantly higher than for a single column with the same gas volume. This indicates that the size of bubbles is important in two ways: 1) smaller bubbles that are more frequent than larger bubbles of equivalent volume by a factor of  $r_{\text{large}}/r_{\text{small}}$ , and 2) an equivalent volume of small bubbles will have a higher drag on the surrounding fluid causing the

far-field hydrodynamic enhancement to rise as well.

According to Whitney's data, the renewal path for a penetration model should be between 5 and 7 bubble diameters. After correction for the width of the oxygen stream (which is more than two diameters wide), our data comparing hydrogen and oxygen bubble streams agree with her estimates. The surface renewal theory predicted, accurately, that the oxygen stream would cause a larger peak enhancement, but be confined to a width only  $2/3$  as wide. Modeling of the enhancement as a gaussian distribution gives precisely this result for the relative width of the two enhancements (hydrogen vs. oxygen). What was not known *a priori* was that the integrated total enhancement between the cases would be nearly identical even though the volume of the oxygen bubbles was only half as much as for the hydrogen stream. Sharper, narrower enhancement regions with oxygen streams give (within 5%) the same integrated increase in mass-transport as an equivalent hydrogen columns, whose frequency is lower but size larger. It is possible that the smaller oxygen bubbles also rise closer to the electrode surface, and this may compensate partially for their smaller total gas volume.

The degree of precision in our data is attributable to the use of single and non-interacting parallel gas columns, in conjunction with a redesigned corrosion-resistant micromosaic array. The speed of acquisition and spatial resolution of the data make this experimental system ideal for studies of micro-scale mass-transfer enhancement.

<b>Table 7.1: Parameters of the Gaussian Fit</b>		
<b>Variable</b>	<b>Oxygen bubbles</b>	<b>Hydrogen bubbles</b>
Column Centerline (#)	5.51	5.69
Full-width at half-maximum	242 $\mu\text{m}$	348 $\mu\text{m}$
Far-field Enhancement (baseline)	1.50	1.46
Integral Enhancement	6.41	6.76

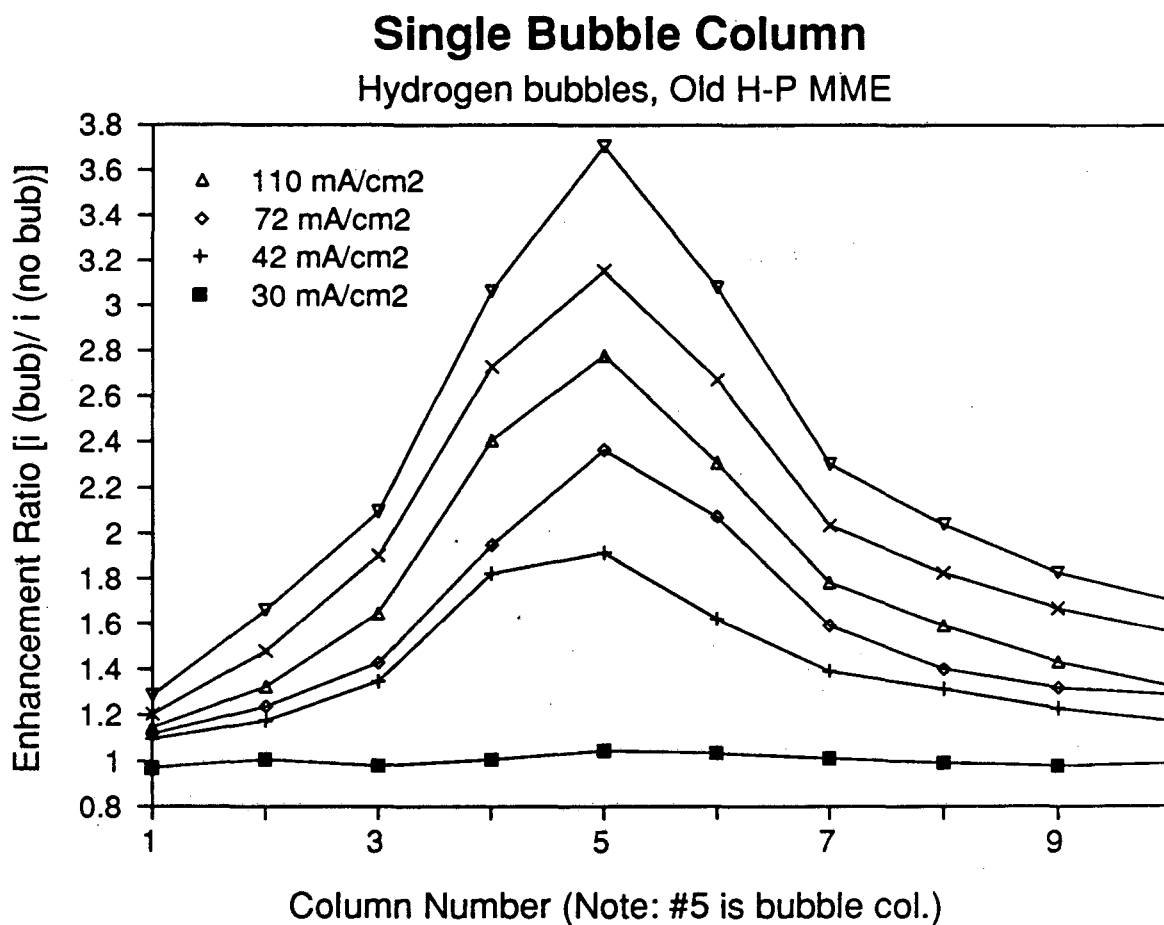
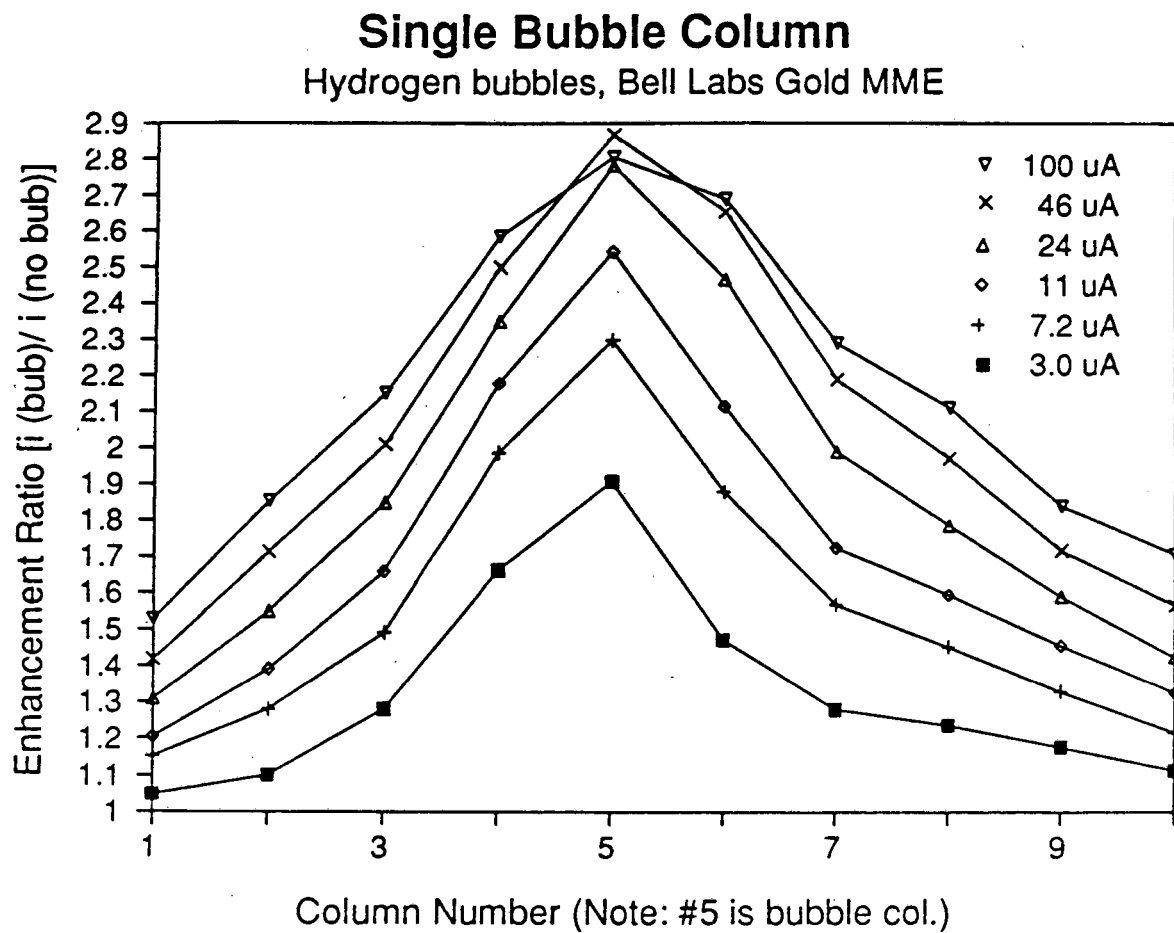
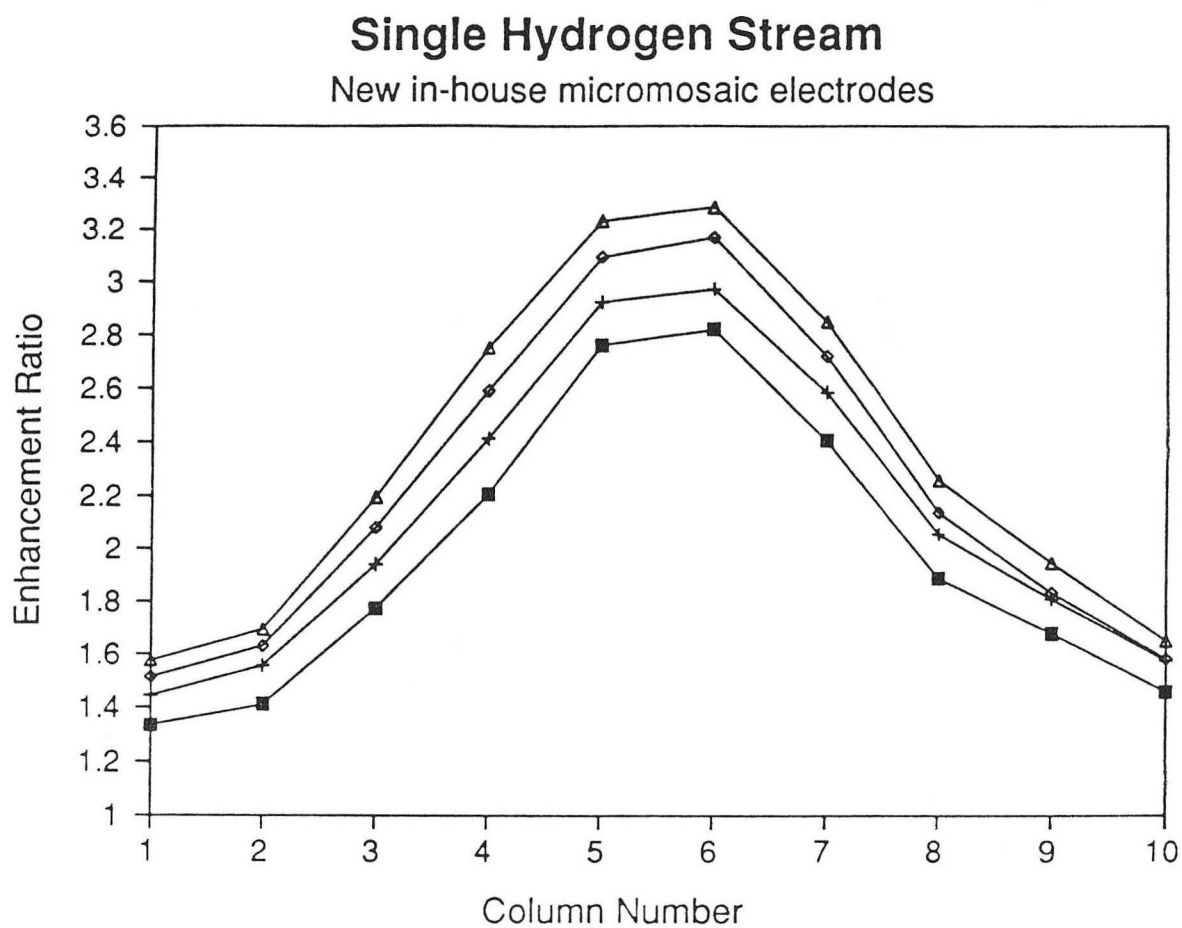


Figure 7.1.  $\text{Fe}^{+3}$  reduction limiting current at a vertical H-P micromosaic electrode in the presence of a single, rising stream of hydrogen bubbles plotted as a ratio versus the natural-convection background value (in the absence of bubbles). Each column is 100  $\mu\text{m}$  wide, and the bubbles rise past column five.



XRI 915-1110

Figure 7.2a. The limiting current for  $\text{Fe}^{+3}$  reduction on a vertical, gold micromosaic electrode in the presence of a single, rising stream of hydrogen bubbles plotted as a ratio versus the natural-convection background value (in the absence of bubbles). Each column is  $100 \mu\text{m}$  wide, and the bubbles rise past column five.



XBL 915-1112

Fig. 7.2b Mass-transport enhancement to a vertical, re-designed micro-mosaic electrode caused by a single rising hydrogen bubble stream.

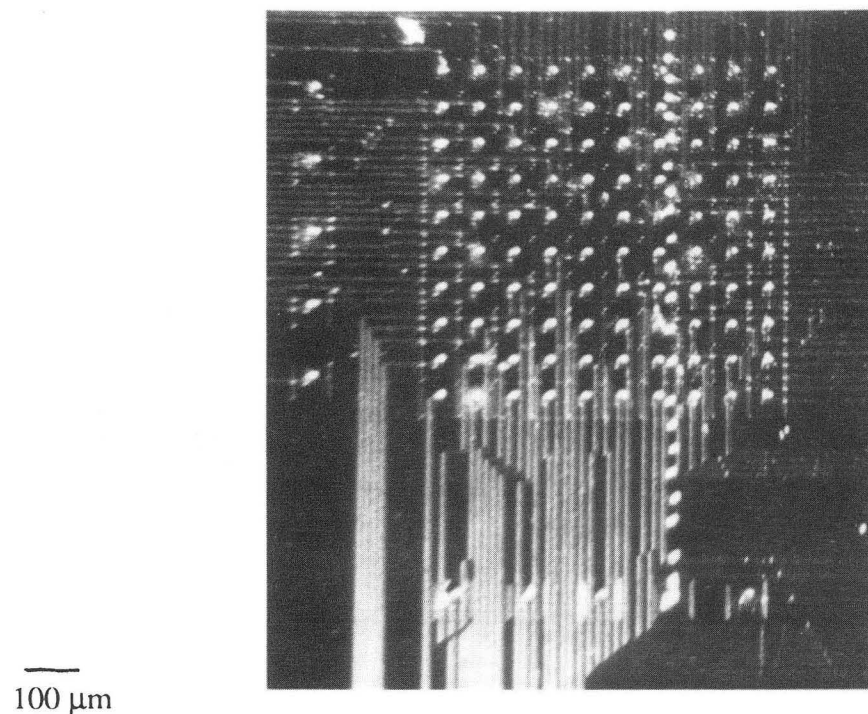


Fig. 7.3 a) Single  $4 \text{ mA/cm}^2$  stream of hydrogen bubbles generated at an MME satellite.

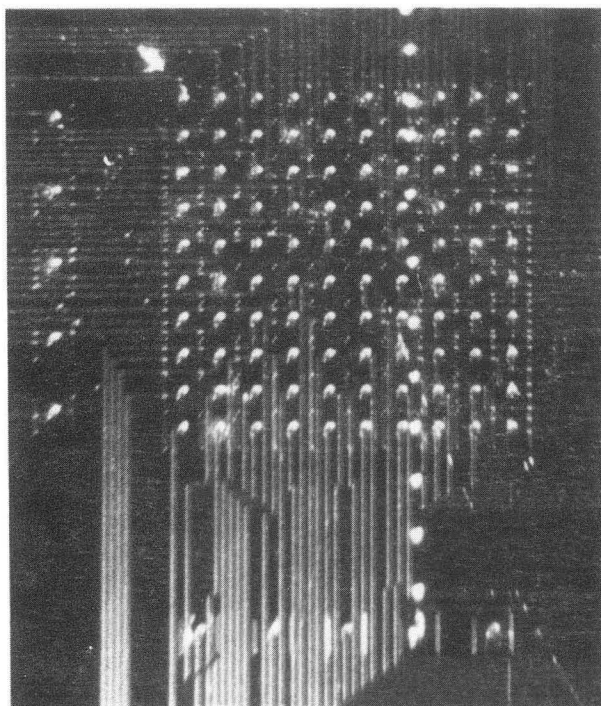


Fig. 7.3 b) Single  $10 \text{ mA/cm}^2$  stream of hydrogen bubbles generated at an MME satellite. XBB 915-3730 A



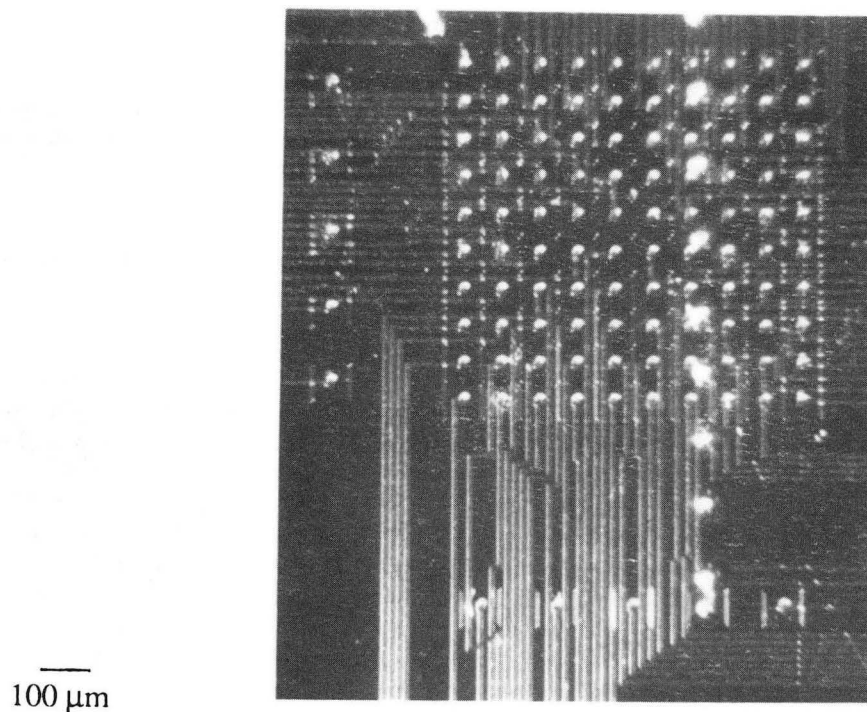


Fig. 7.3 c) Single  $20 \text{ mA/cm}^2$  stream of hydrogen bubbles generated at an MME satellite.

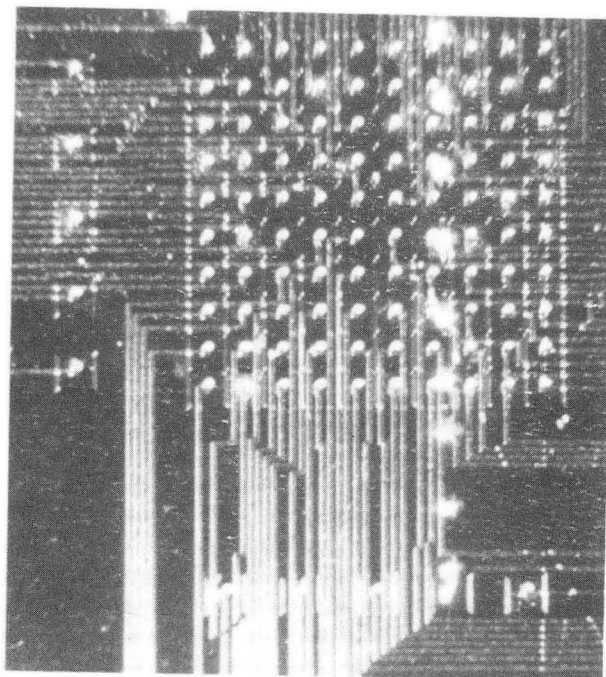


Fig. 7.3 d) Single  $30 \text{ mA/cm}^2$  stream of hydrogen bubbles generated at an MME satellite. XBB 915-3733 A

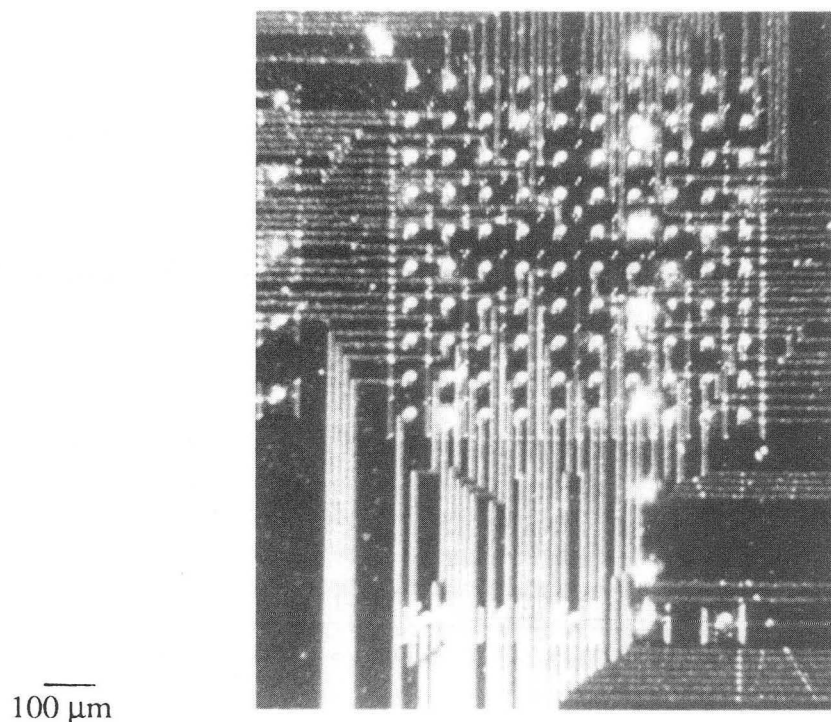


Fig. 7.3 e) Single 50 mA/cm<sup>2</sup> stream of hydrogen bubbles generated at an MME satellite.

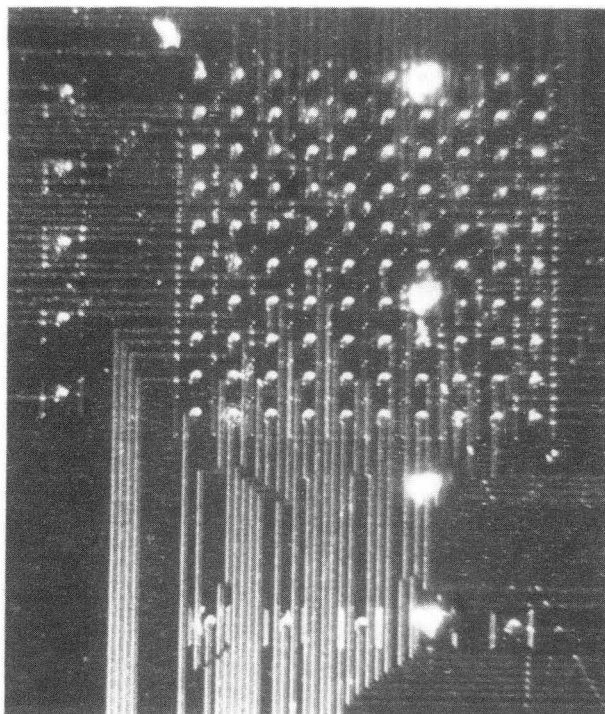


Fig. 7.3 f) Single 100 mA/cm<sup>2</sup> stream of hydrogen bubbles generated at an MME satellite. XBB 915-3737A

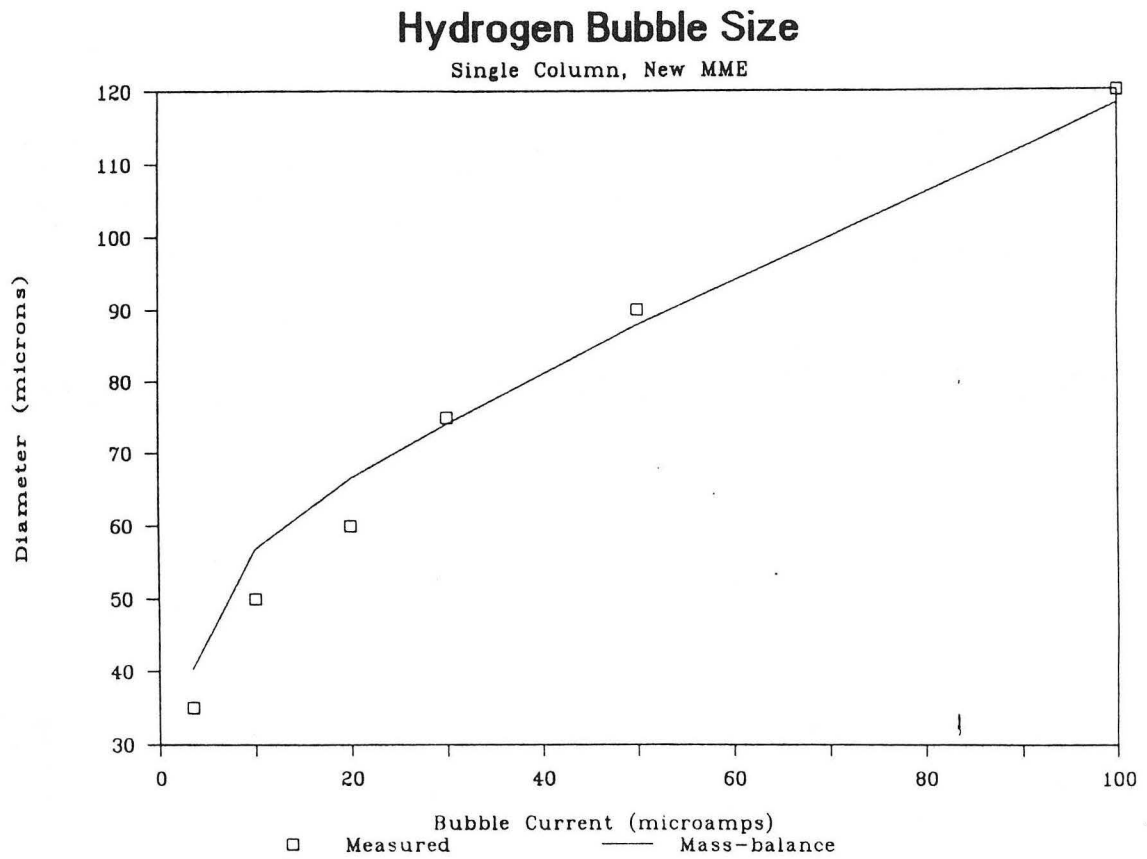


Fig. 7.4 Hydrogen bubble size measured from photographs and calculated from a mass-balance, using Stokes' law for a hard-sphere.

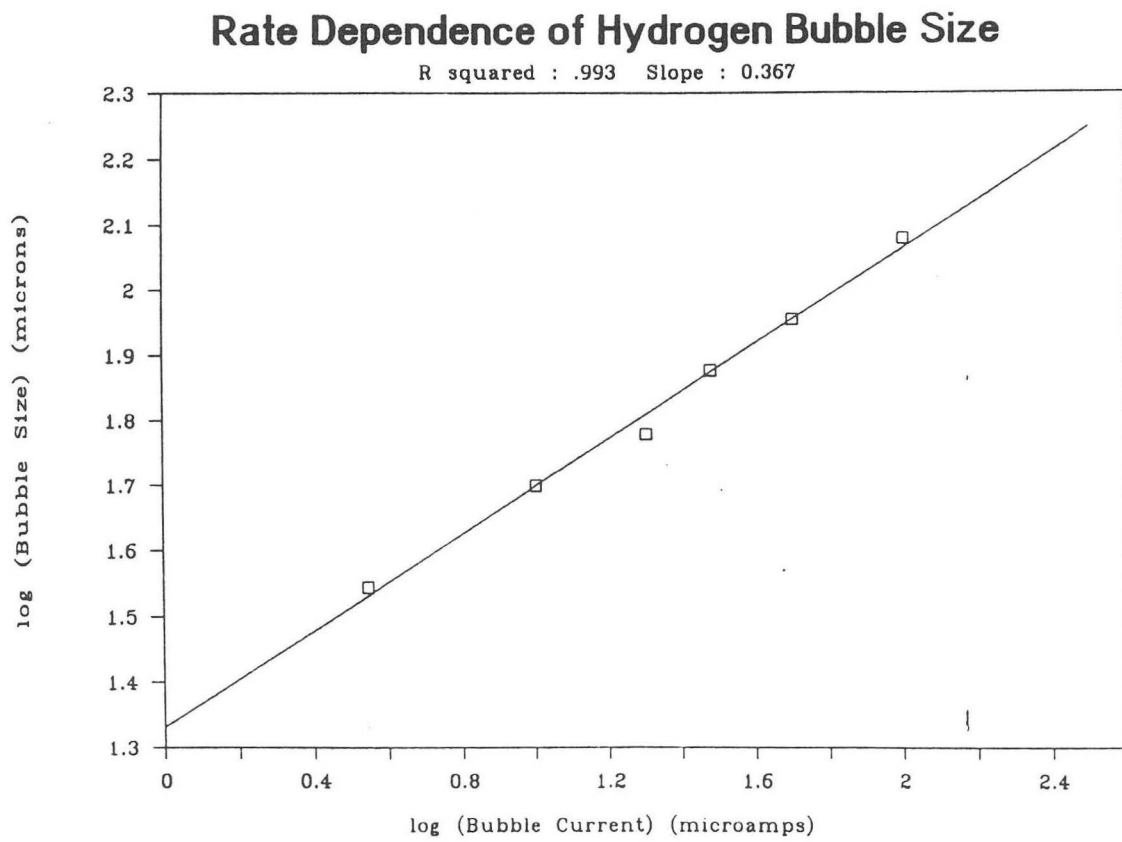


Fig. 7.5 Linear regression of hydrogen bubble size versus gas evolution rate.

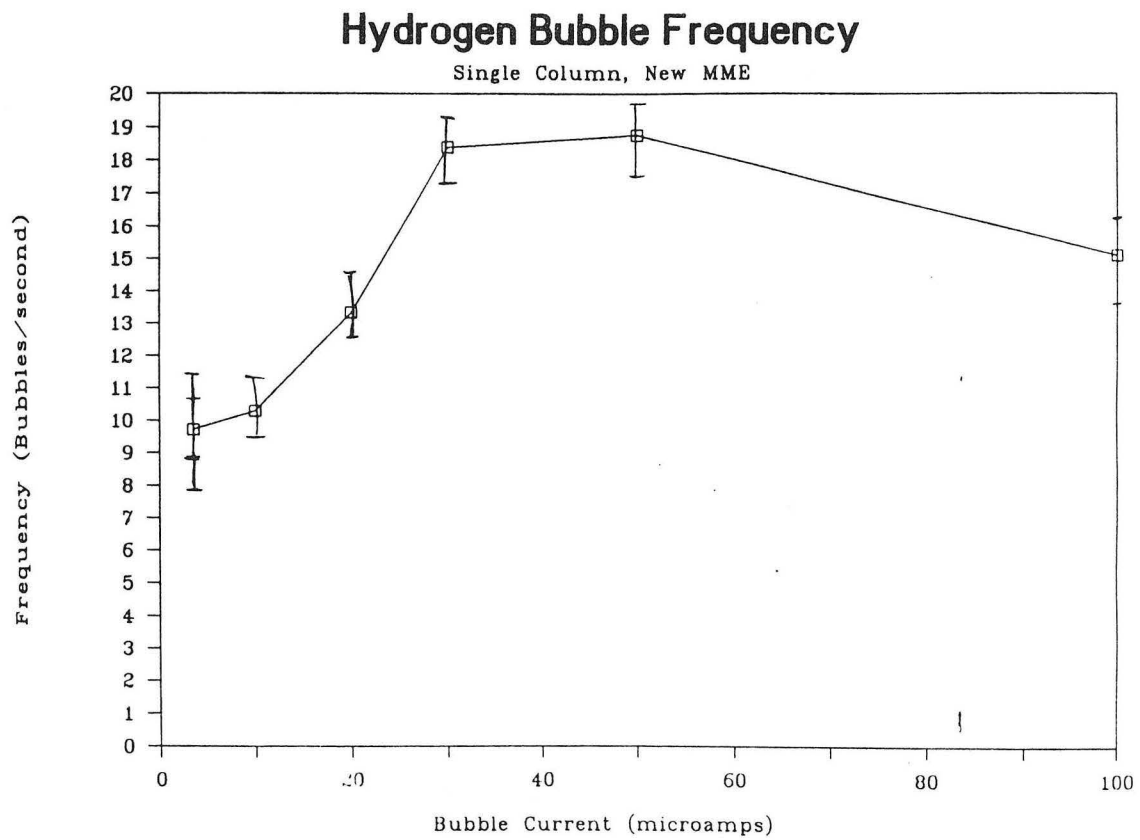


Fig. 7.6 Frequency of hydrogen bubbles passing the micro-mosaic array.

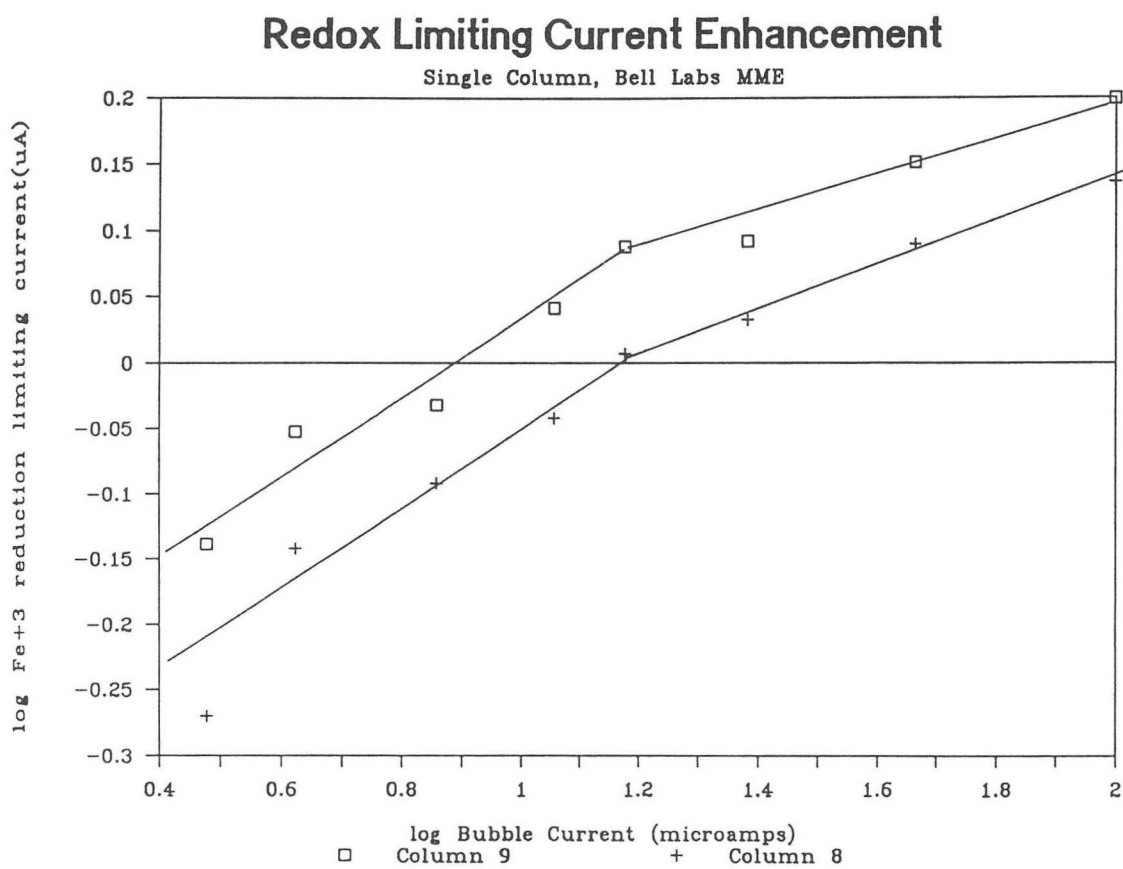
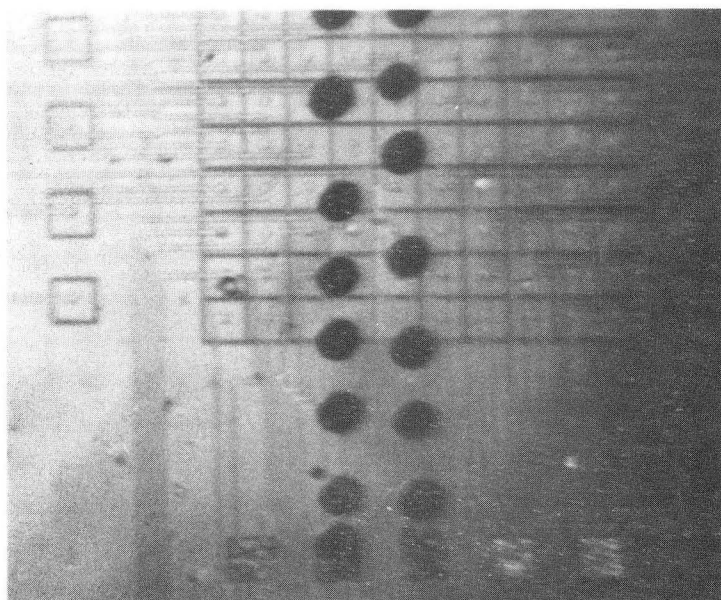
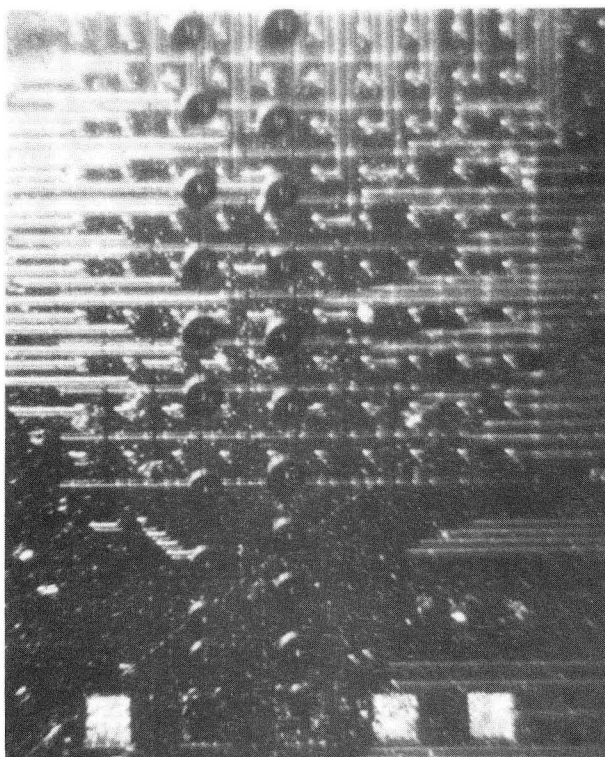


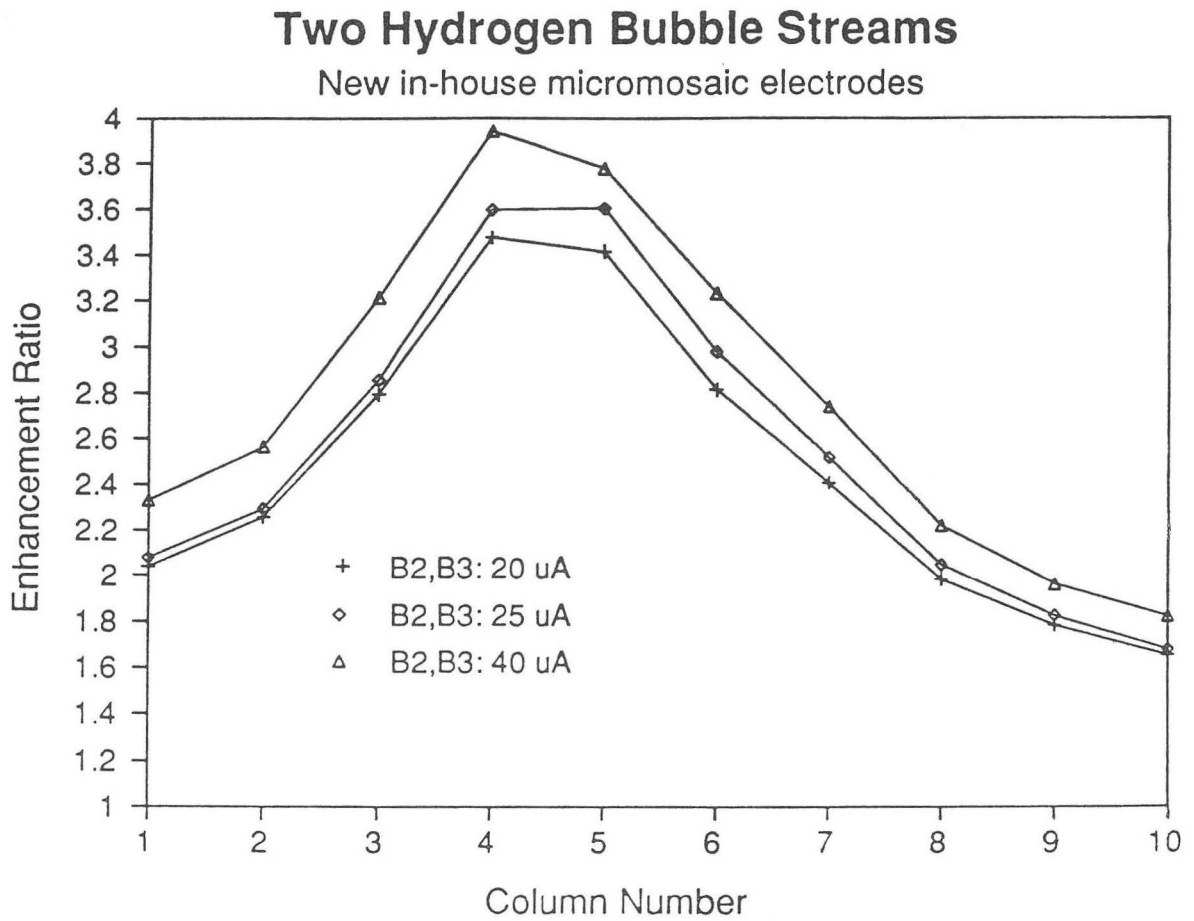
Fig. 7.7 Linear regression for the enhancement ratio versus the gas evolution rate on the Bell Labs micro-mosaic. Single hydrogen stream.



100  $\mu\text{m}$

Fig. 7.8 Micro-photograph of two parallel hydrogen bubble streams, 50  $\text{mA}/\text{cm}^2$ . The difference between the photos is caused by the angle of illumination. The bubbles are attracted to each other by entrainment, and minimize drag by forming a narrower column.

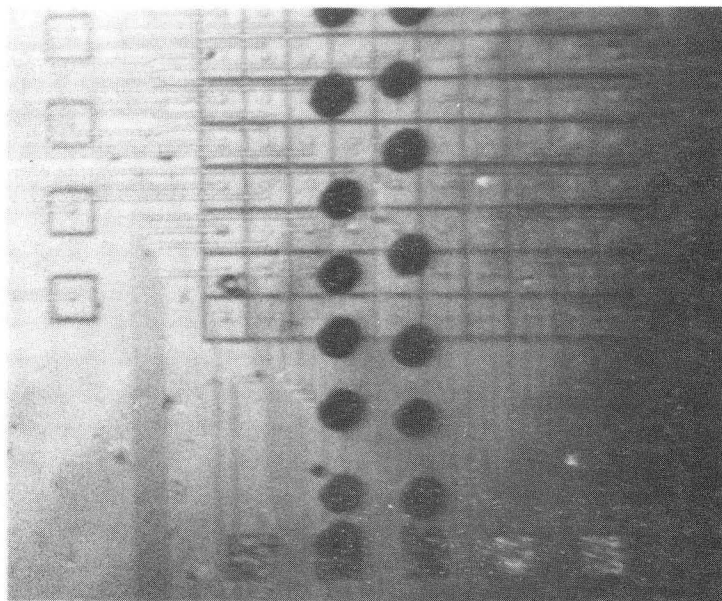
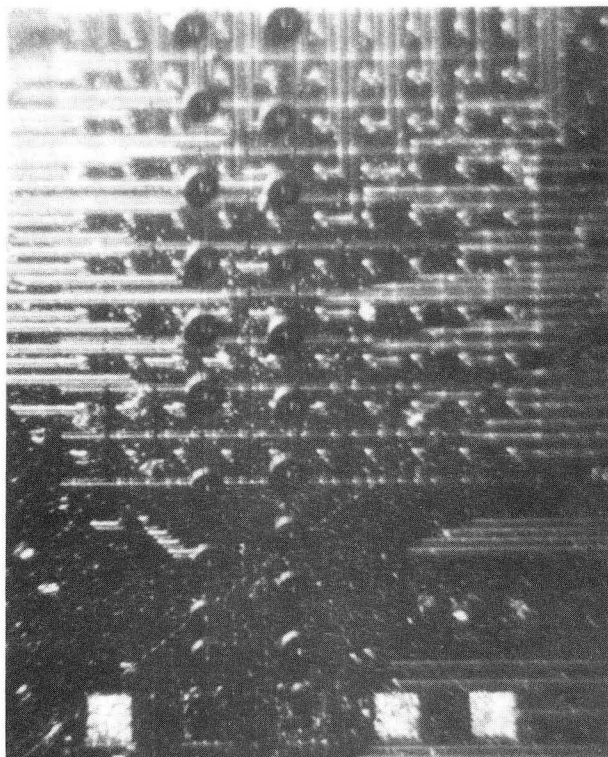
XBB 916-4167A



XBL 915-1115

Fig. 7.9 Ratio of mass-transfer coefficients: two parallel hydrogen columns, 200  $\mu$ m apart, versus background natural-convection. The two bubble columns are rising between columns 3 + 4 and 5 + 6.

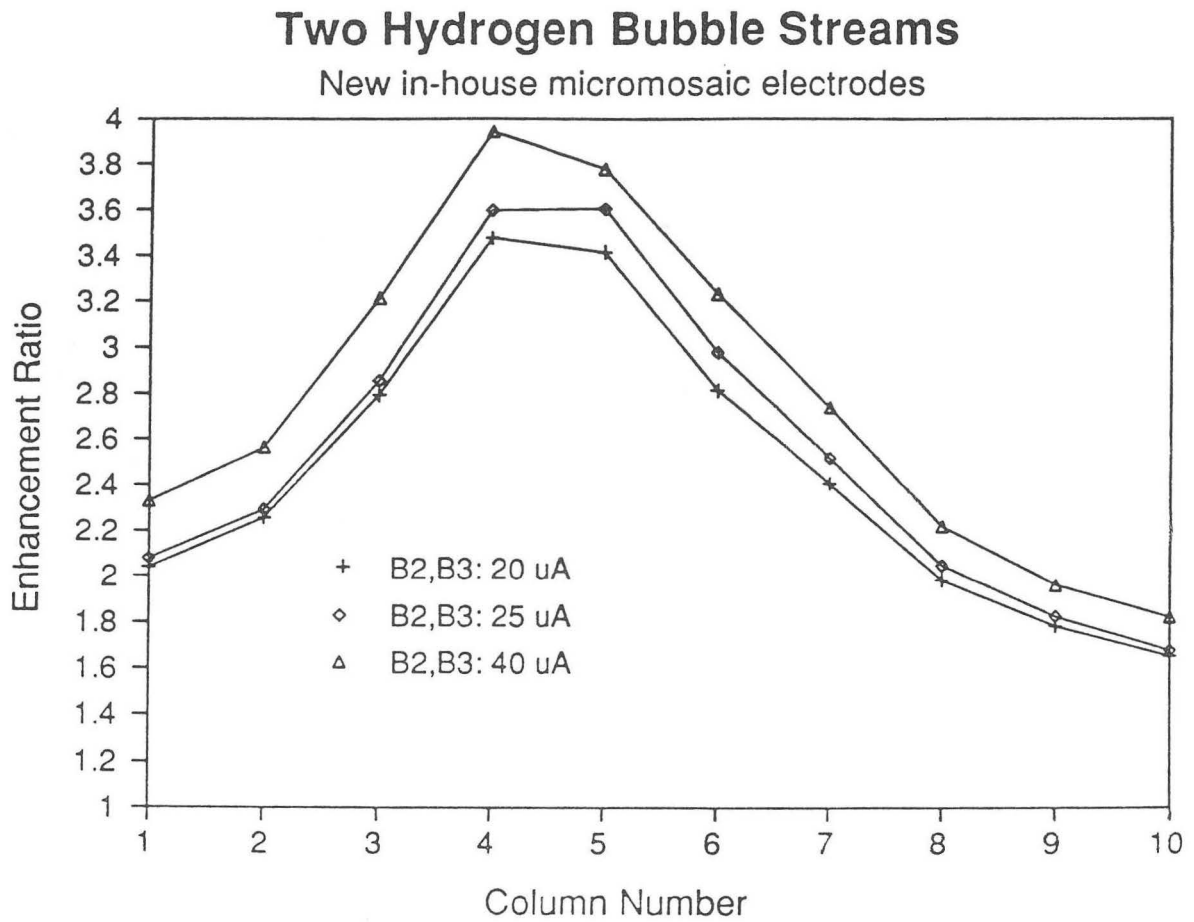




—  
100  $\mu\text{m}$

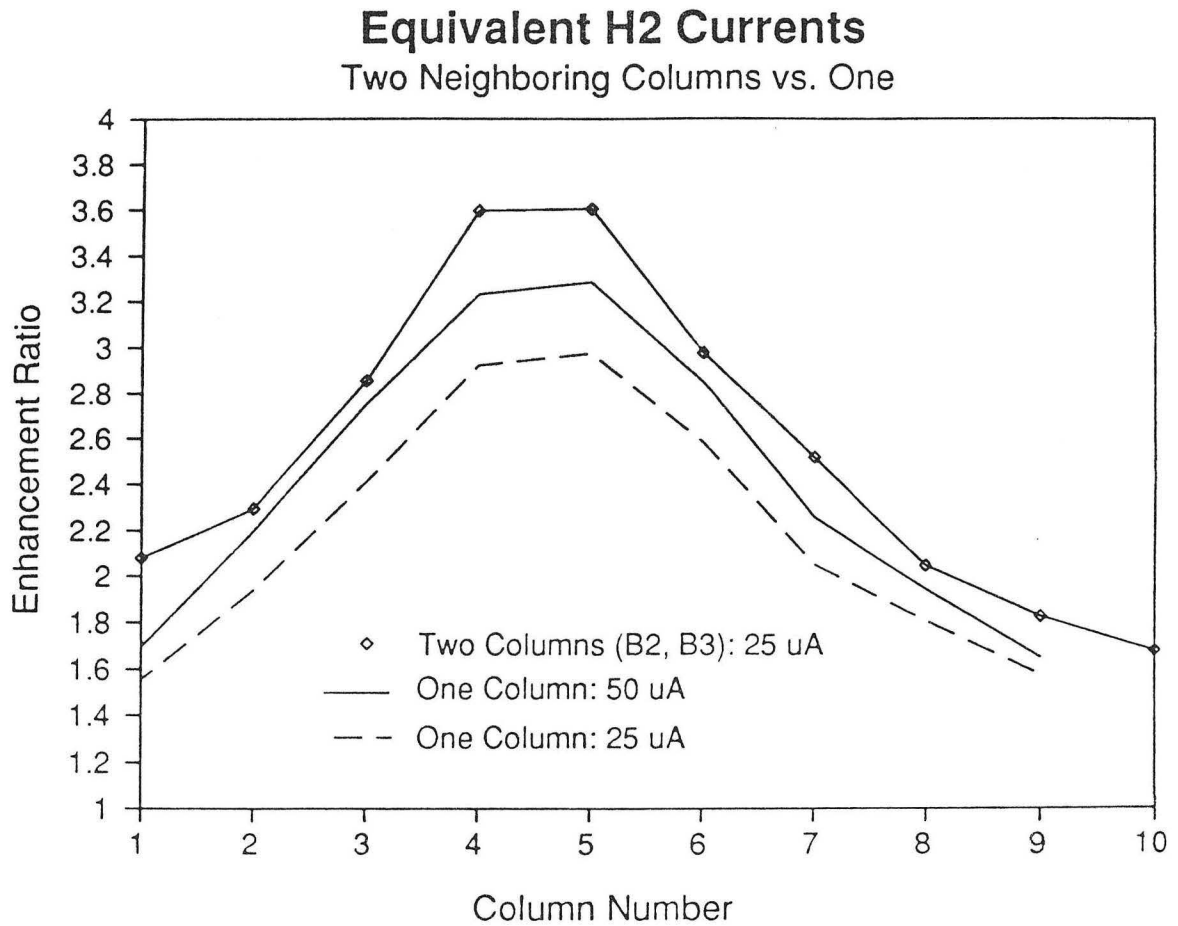
Fig. 7.8 Micro-photograph of two parallel hydrogen bubble streams, 50  $\text{mA}/\text{cm}^2$ . The difference between the photos is caused by the angle of illumination. The bubbles are attracted to each other by entrainment, and minimize drag by forming a narrower column.

XBB 916-4167A



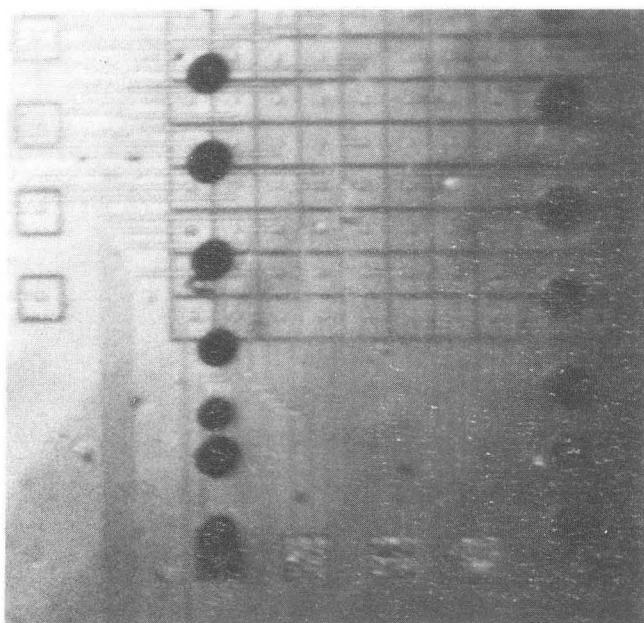
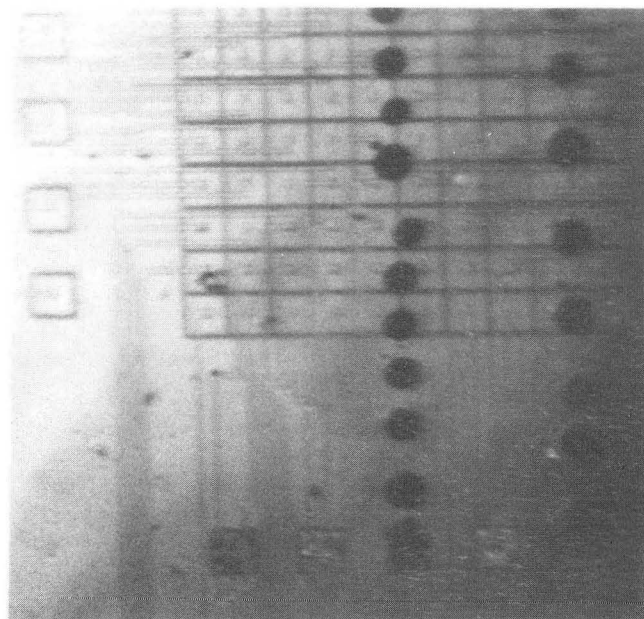
XBL 915-1115

Fig. 7.9 Ratio of mass-transfer coefficients: two parallel hydrogen columns, 200  $\mu\text{m}$  apart, versus background natural-convection. The two bubble columns are rising between columns 3 + 4 and 5 + 6.



XBL 915-1114

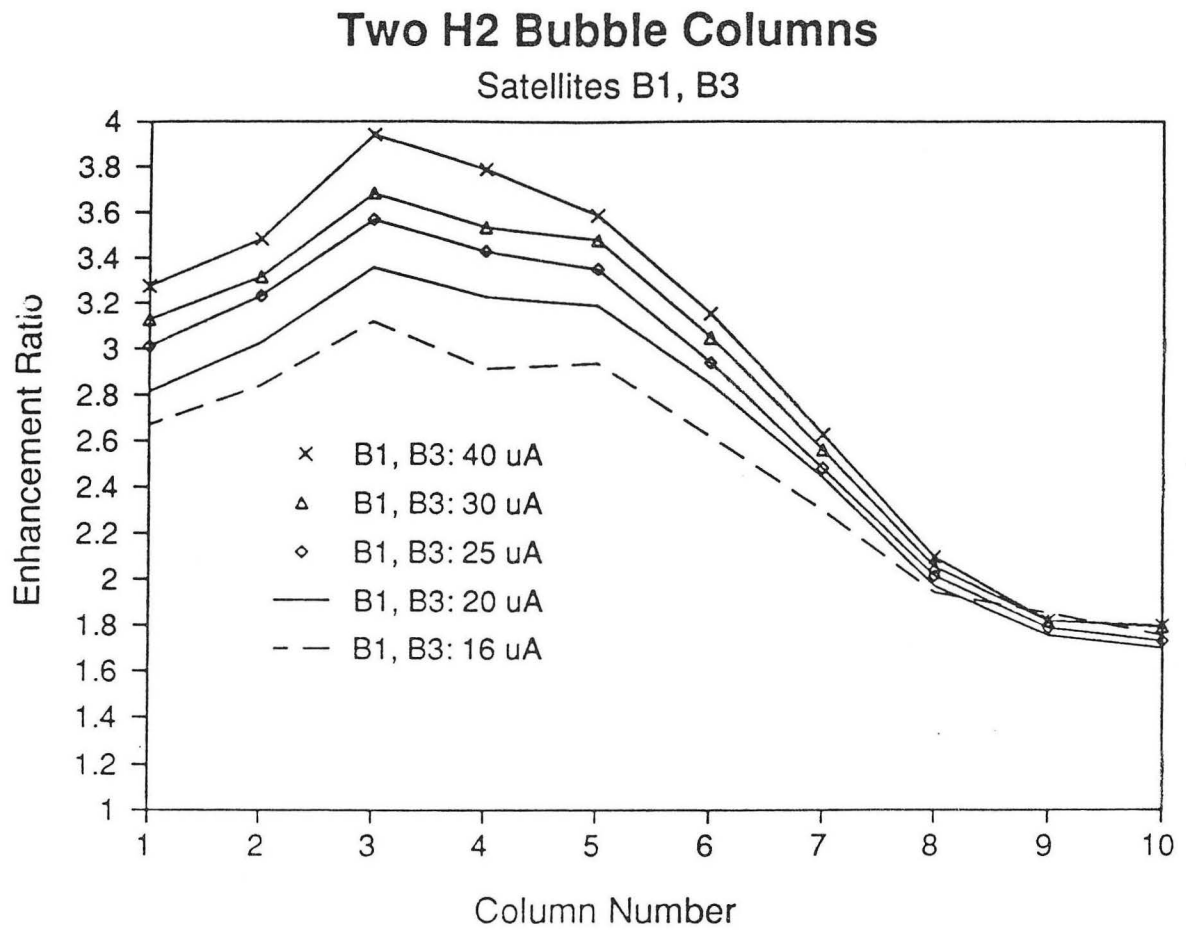
Fig. 7.10 Mass-transfer enhancement ratios. Effect of two parallel hydrogen columns, 200  $\mu$ m apart, compared to the effect of a single column. The two columns are each generating 25  $\mu$ A of hydrogen gas.



—  
100  $\mu\text{m}$

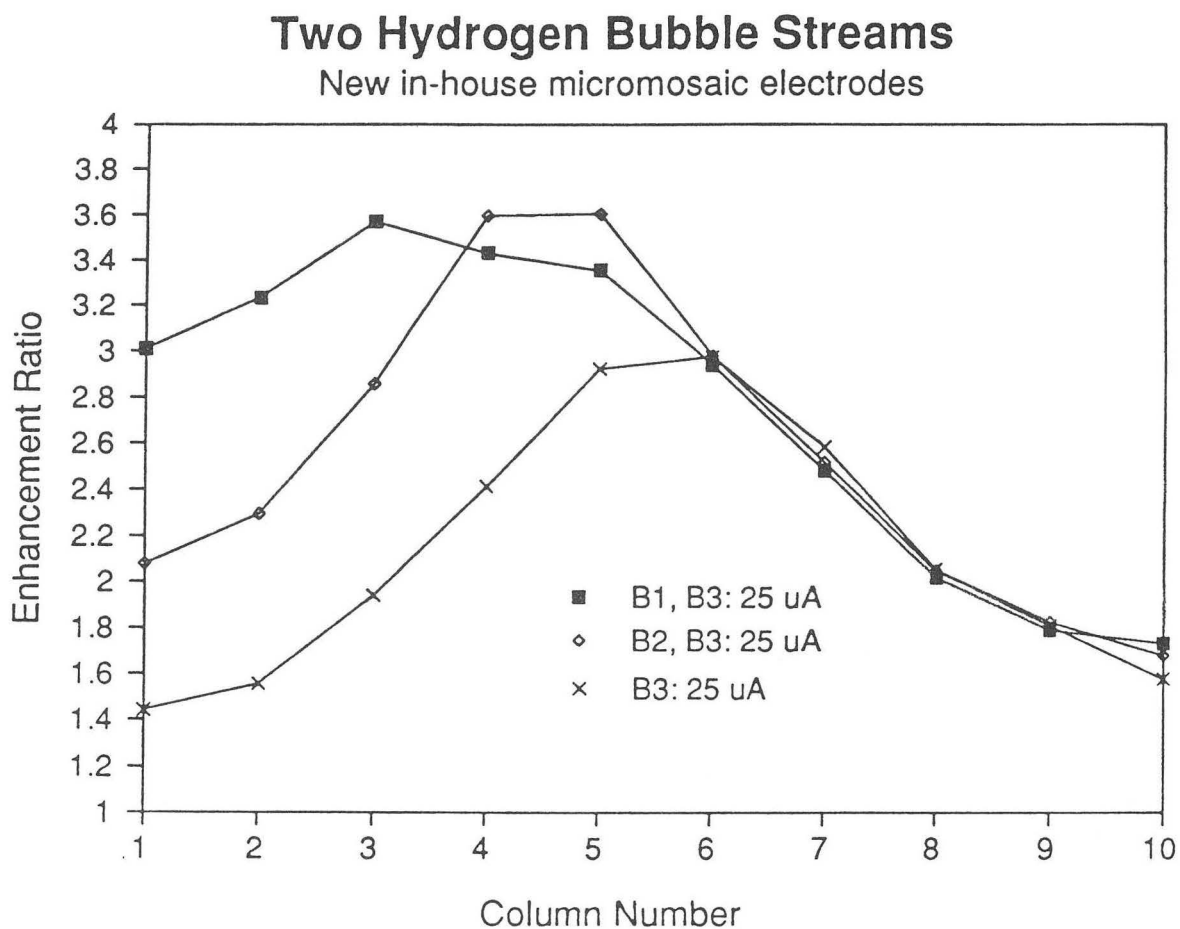
Fig. 7.11 Micro-photograph of two parallel hydrogen bubble streams, 50  $\text{mA}/\text{cm}^2$ . The streams are 400  $\mu\text{m}$  (top) and 800  $\mu\text{m}$  (bottom) apart. No entrainment is seen.

XBB 916-4190A



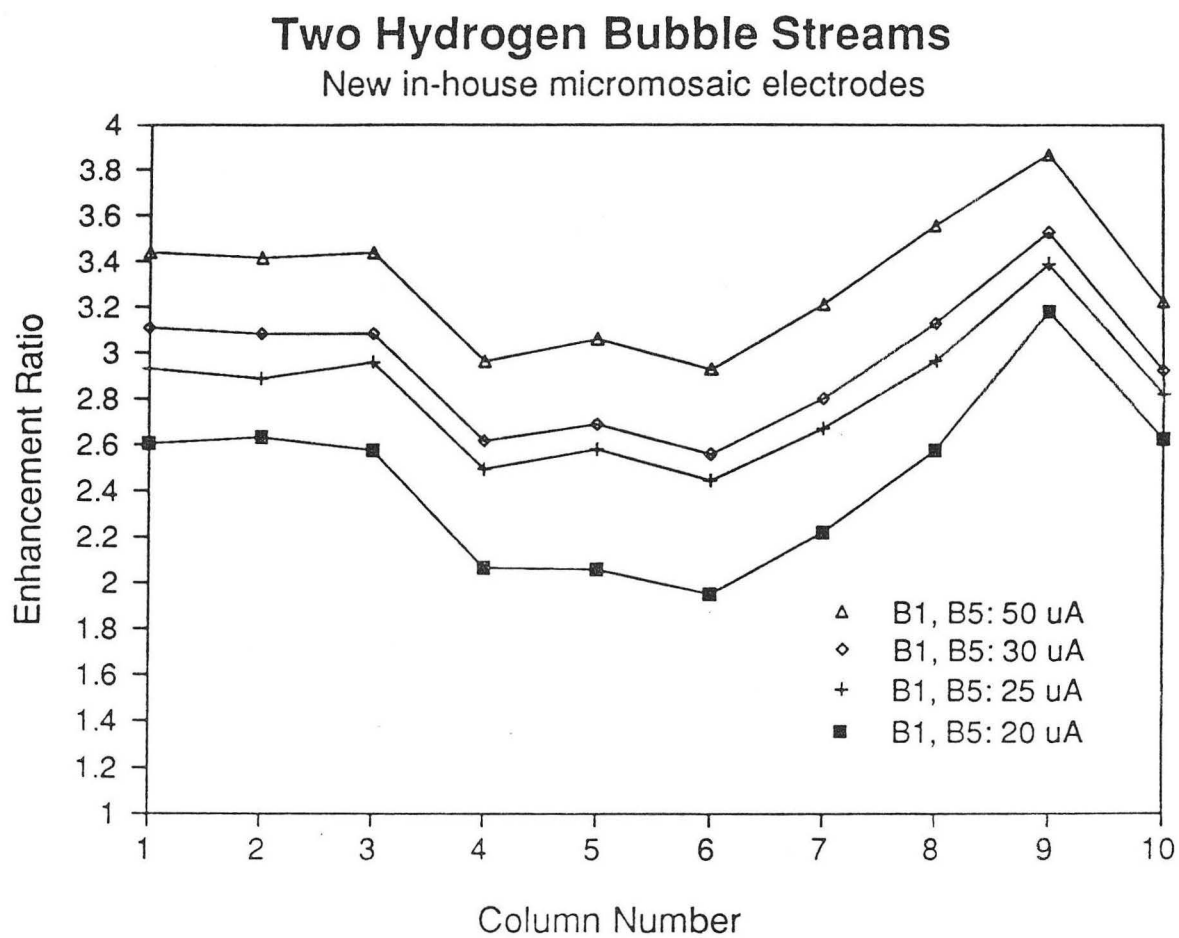
XBL 915-1113

Fig. 7.12 Mass-transfer enhancement ratios. Effect of two parallel hydrogen columns, 400  $\mu\text{m}$  apart.



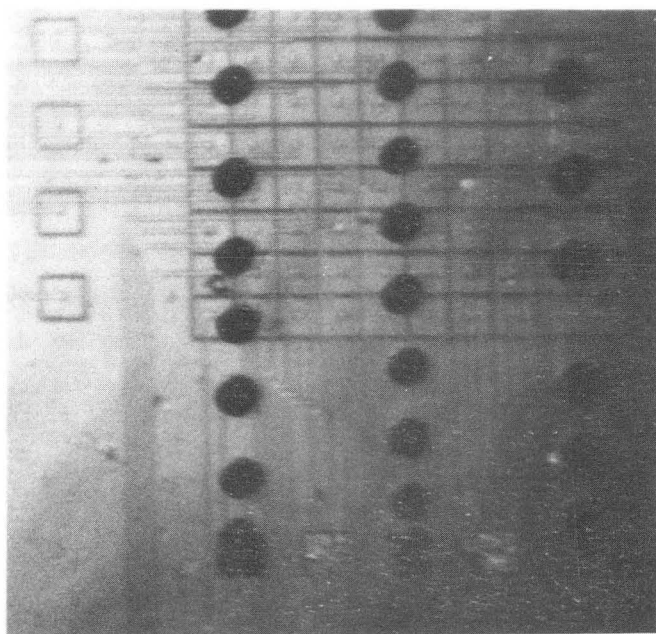
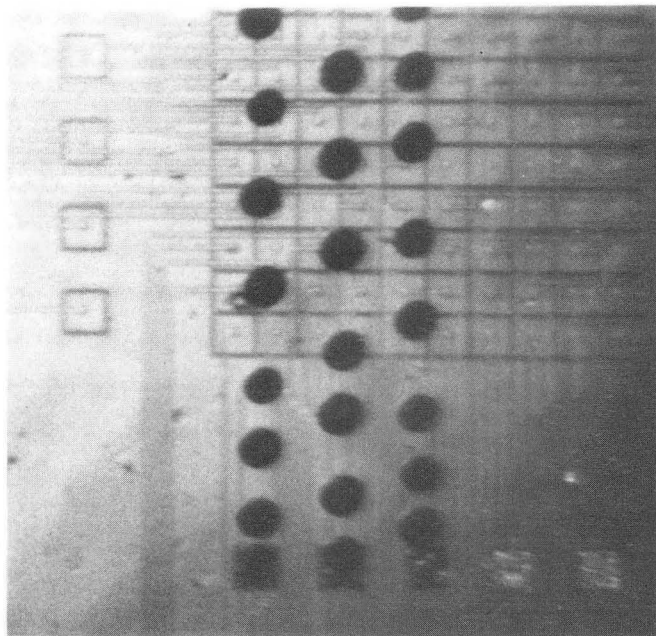
XBL 915-1116

Fig. 7.13 Comparison of mass-transfer enhancement ratios. Effect of two parallel hydrogen columns, spaced 200 and 400  $\mu\text{m}$  apart, versus the effect of a single column of rising bubbles. The effect on mass-transport of additional columns of gas is confined to the region to one side of a neighboring column. The neighboring column acts as a shield; micro-mosaic segments on the other side of the center gas stream do not benefit from the generation of bubbles at sites B1 or B2.



XBL 915-1117

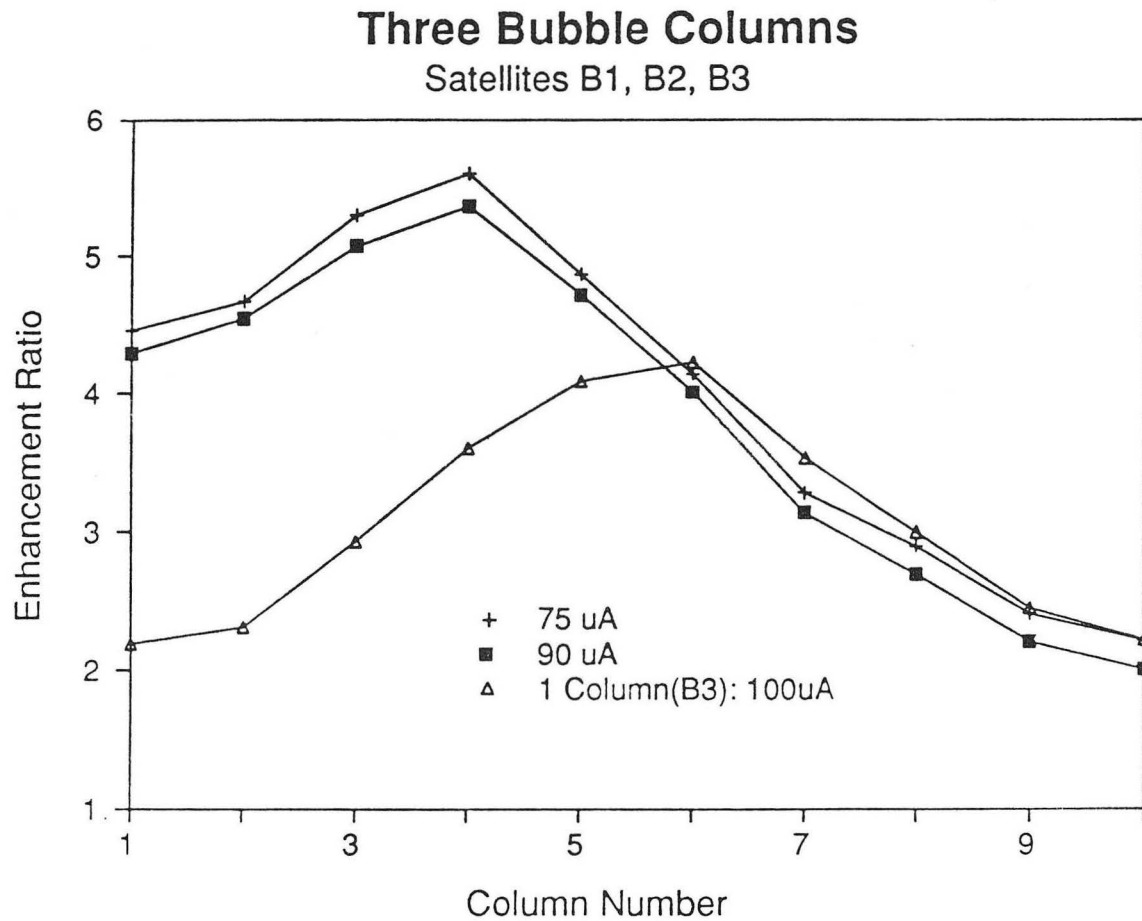
Fig. 7.14 Mass-transfer enhancement ratios. Effect of two rising hydrogen streams spaced 800  $\mu\text{m}$  apart.



100 μm

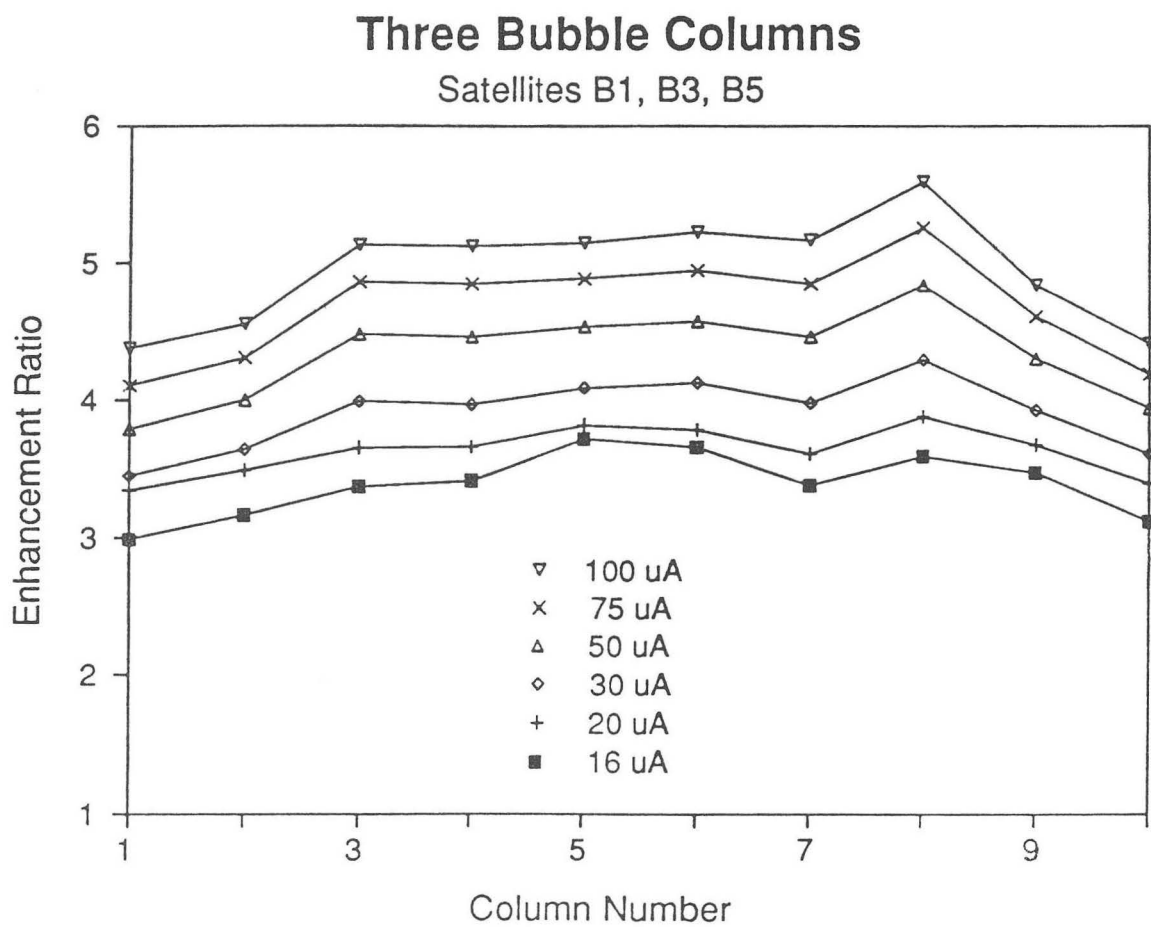
Fig. 7.15 Micro-photograph of three parallel hydrogen bubble streams, 50 mA/cm<sup>2</sup>. The streams are 200 μm (top) and 400 μm (bottom) apart. Entrainment is noticeable in the slight narrowing of the space between the center and right column in the top photo. At a larger separation, no entrainment is observed. XBB 916-4192A





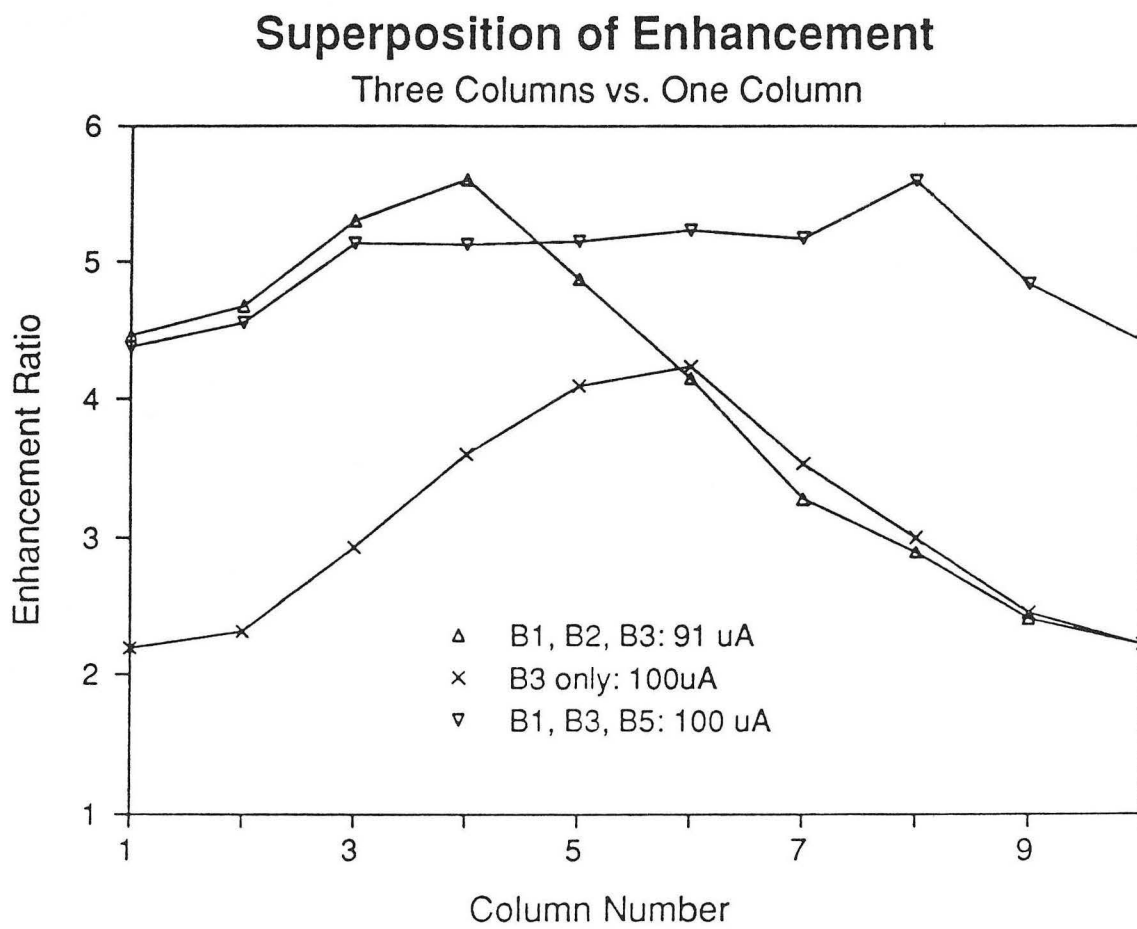
XBL 915-1120

Fig. 7.16 Mass-transfer enhancement ratios. Effect of three rising columns of hydrogen gas bubbles, spaced  $200 \mu\text{m}$  apart, compared to the effect of a single column of bubbles.



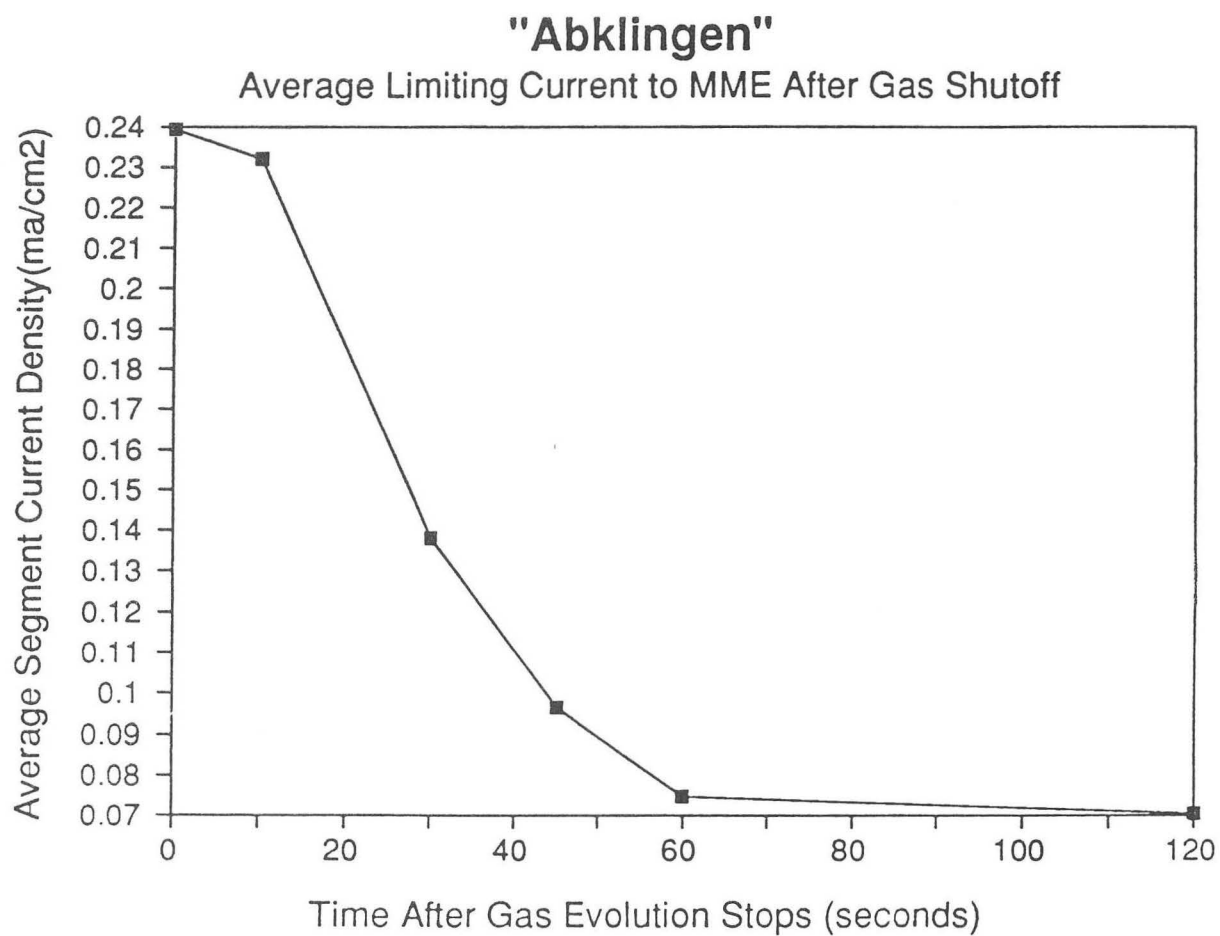
XBL 915-1118

Fig. 7.17 Mass-transfer enhancement ratios. Effect of three rising columns of hydrogen gas bubbles, spaced  $400 \mu\text{m}$  apart.



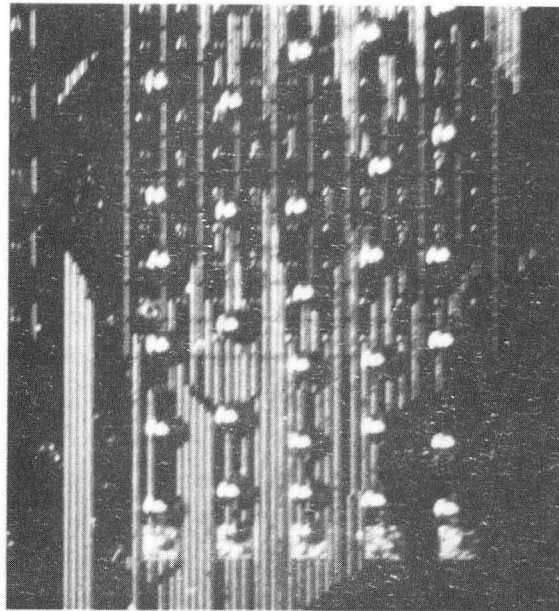
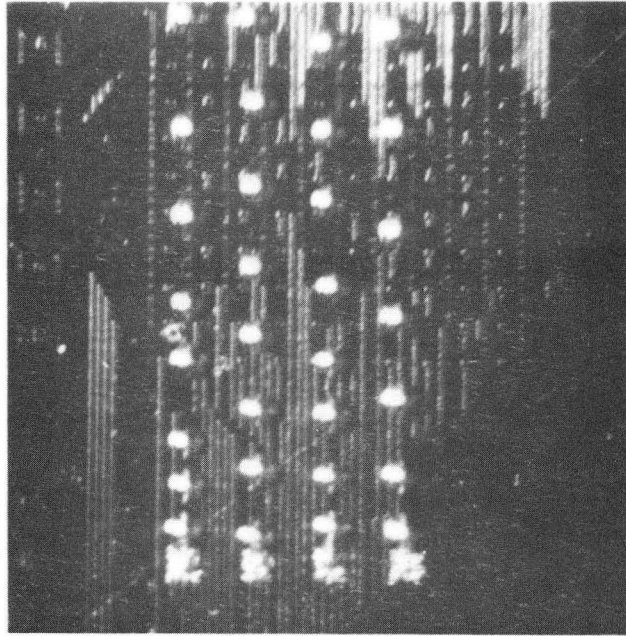
XBL 915-1119

Fig. 7.18 Comparison of enhancement ratios. Intermediate bubble columns shield the far-field effect of neighboring bubble streams.



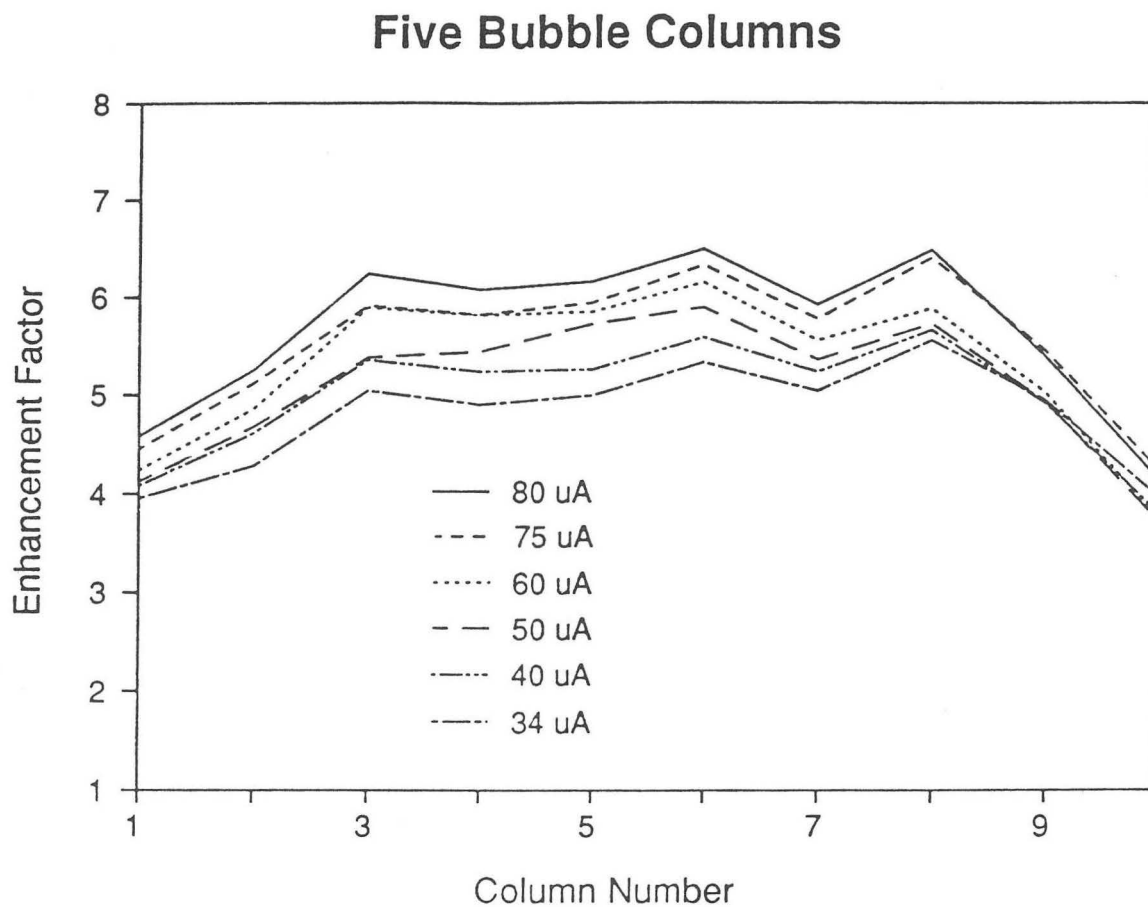
XBL 915-1122

Fig. 7.19 Decay of limiting current on the micromosaic array to the background value caused by natural convection. In excess of a minute is required for the mass-transport rate to relax; this implies the presence of substantial cell-wide flows induced by the rising curtain of gas bubbles. The gas evolution rate was  $16 \mu\text{a}$  for each of three parallel columns.



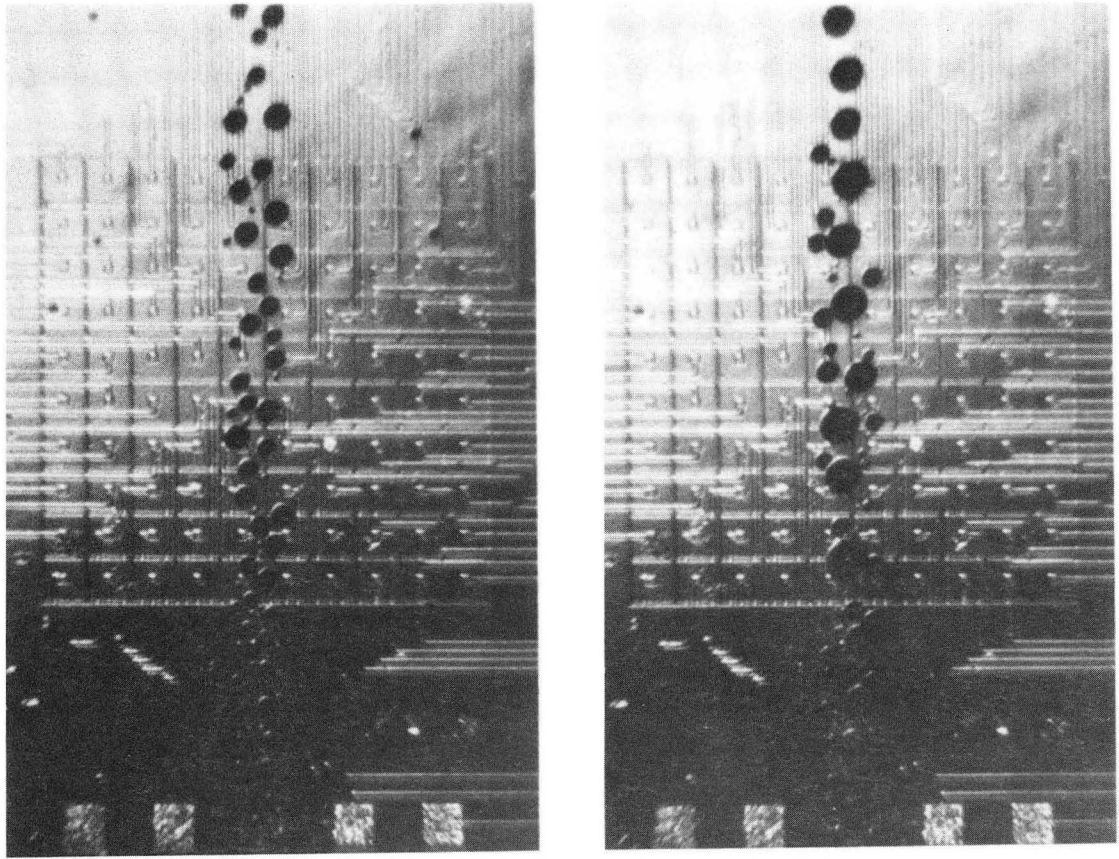
—  
100  $\mu\text{m}$

Fig. 7.22 Micro-photograph of four and five parallel hydrogen bubble streams. The streams are 200  $\mu\text{m}$  apart. Narrowing of the distance between streams is not very noticeable, perhaps because of the strong cell-wide flows that occur in the presence of a wide curtain of rising bubbles. XBB 915-3745A



XBL 915-1123

Fig. 7.21. Enhancement to mass-transport caused by a curtain of five, closely-spaced, parallel hydrogen bubble columns. The peak enhancement is a factor of six higher than the natural-convection limiting current.



25 mA/cm<sup>2</sup>

50 mA/cm<sup>2</sup>

Fig. 7.22 Streams of oxygen bubbles generated at a single satellite segment. The bubble diameters are not mono-disperse and the rising column is significantly wider than a single bubble. XBB 916-4206A

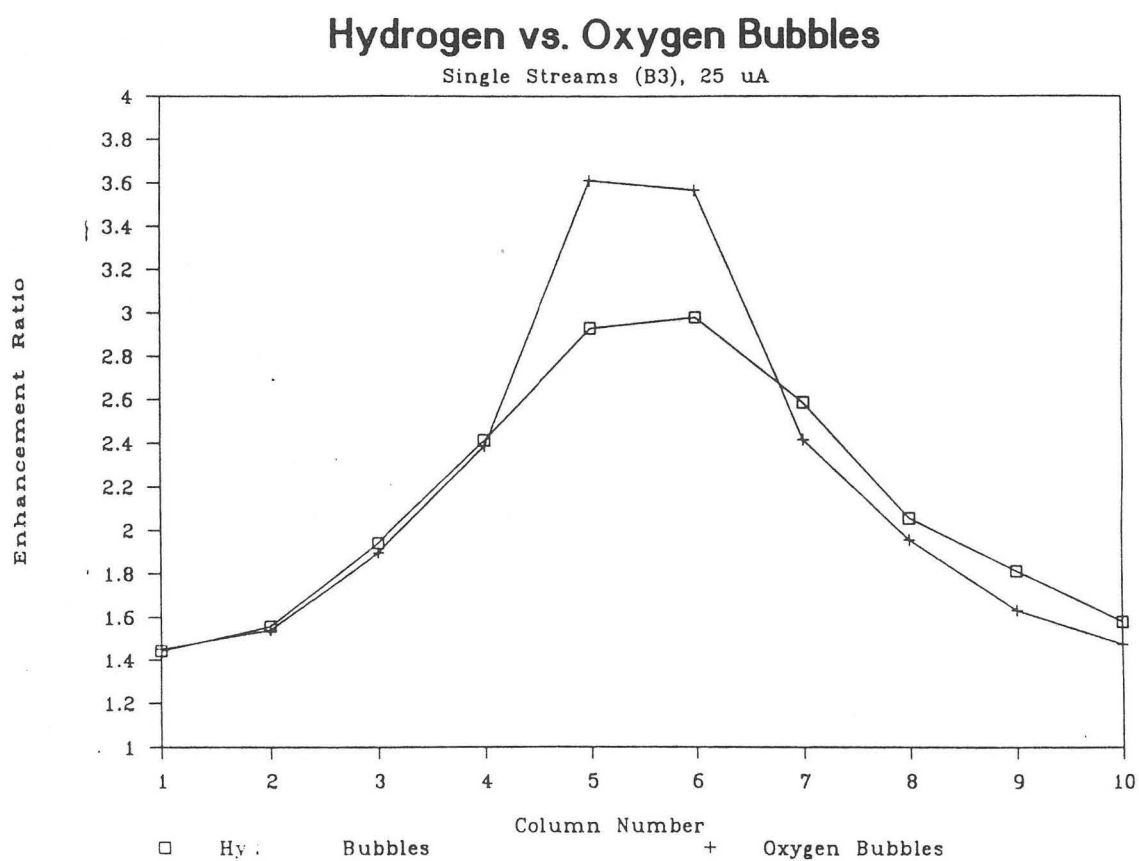


Fig. 7.23. The effect of hydrogen and oxygen bubble streams evolved from a single satellite segment, 25  $\mu$ A. The volumetric rate of the oxygen stream is half that of the hydrogen column.



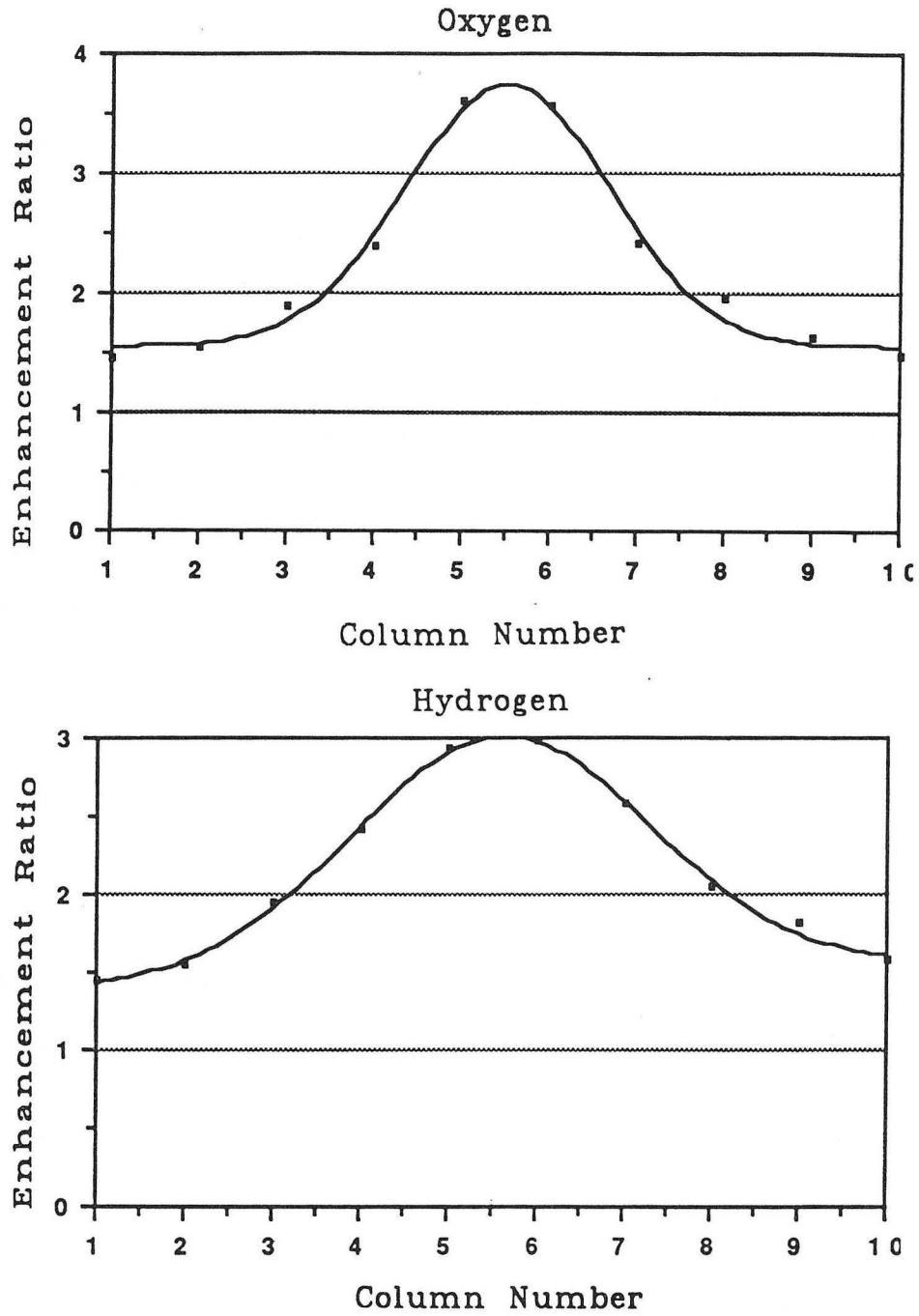
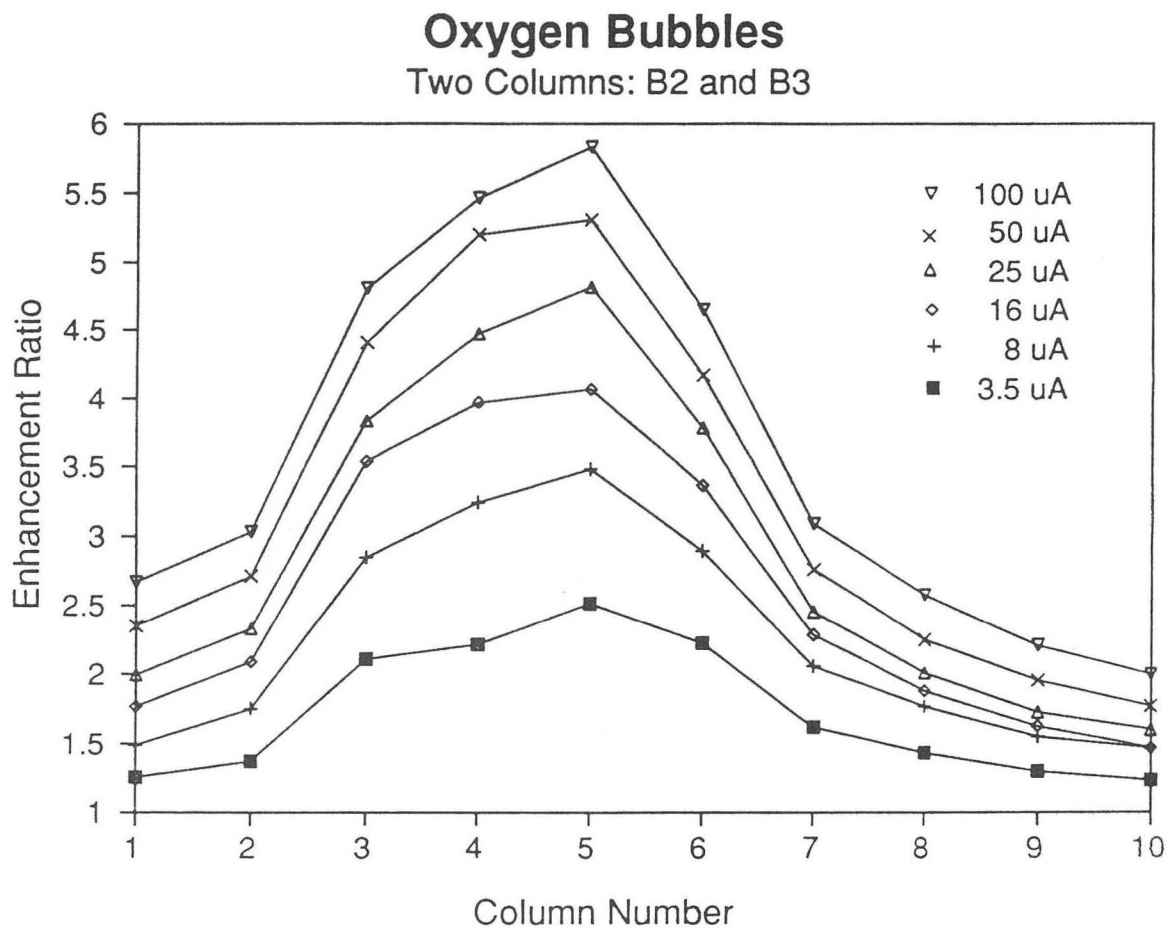


Fig. 7.24. Data from fig. 7.23 modeled as gaussians.



XBL 915-1124

Fig. 7.25. Mass-transfer enhancement caused by two parallel oxygen bubble streams, spaced  $200 \mu\text{m}$  apart.

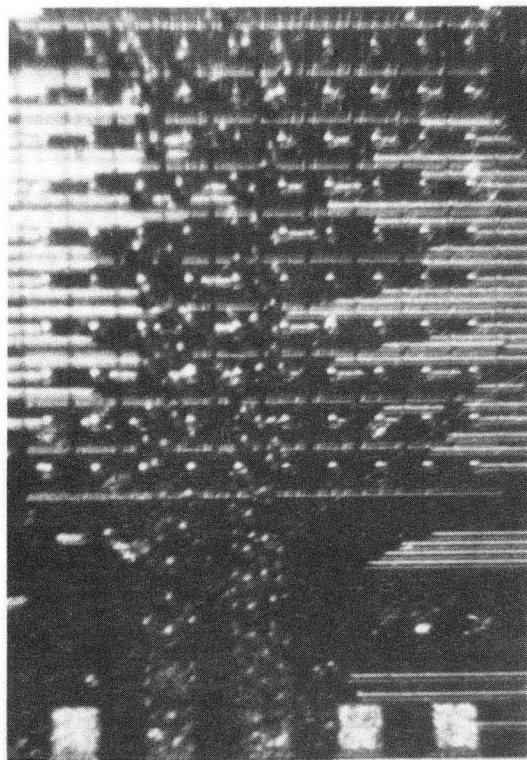
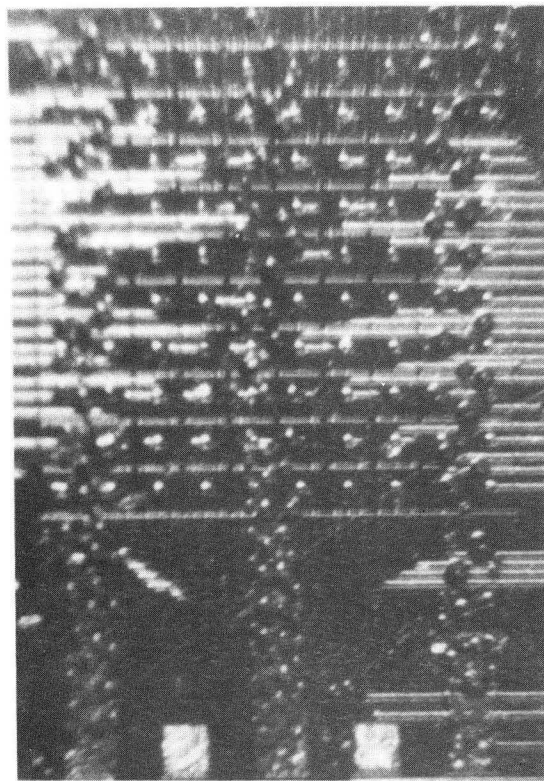
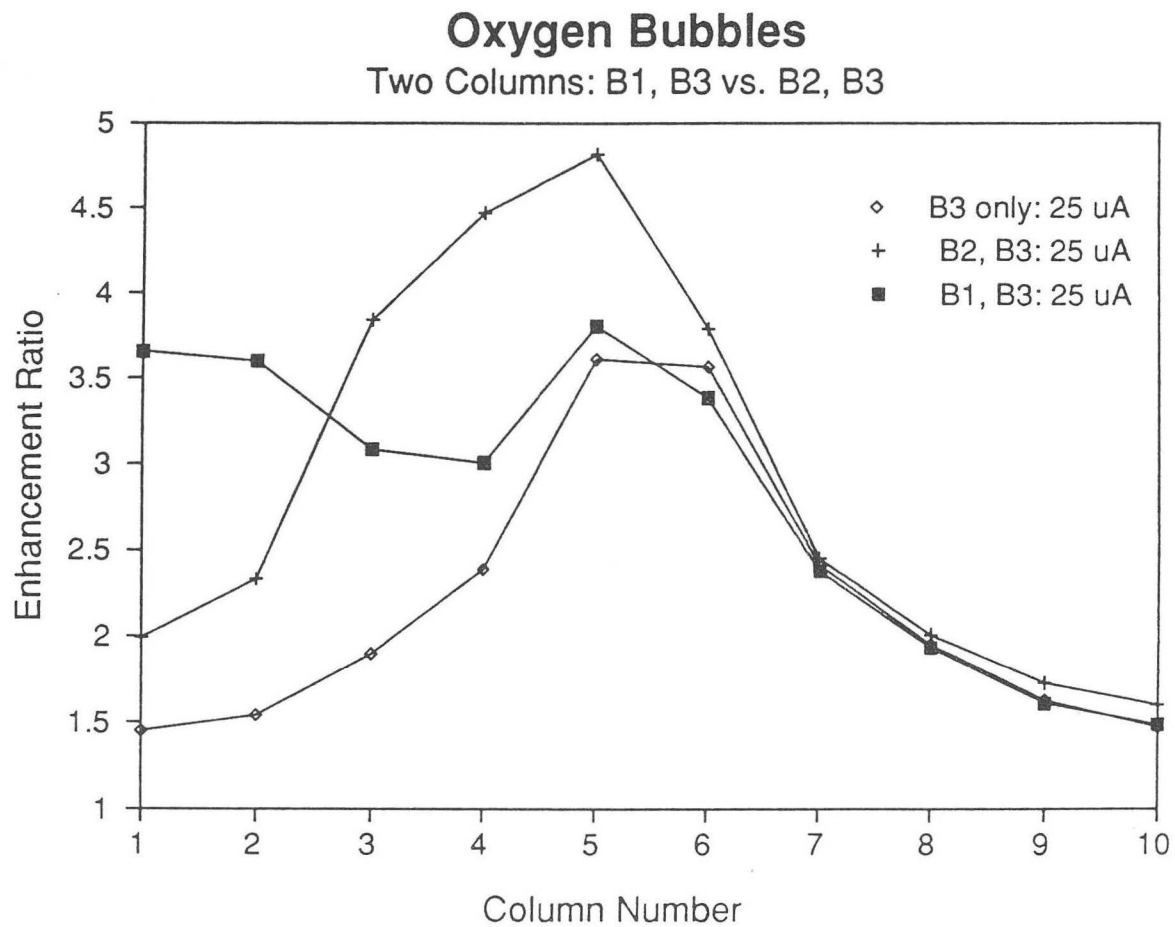
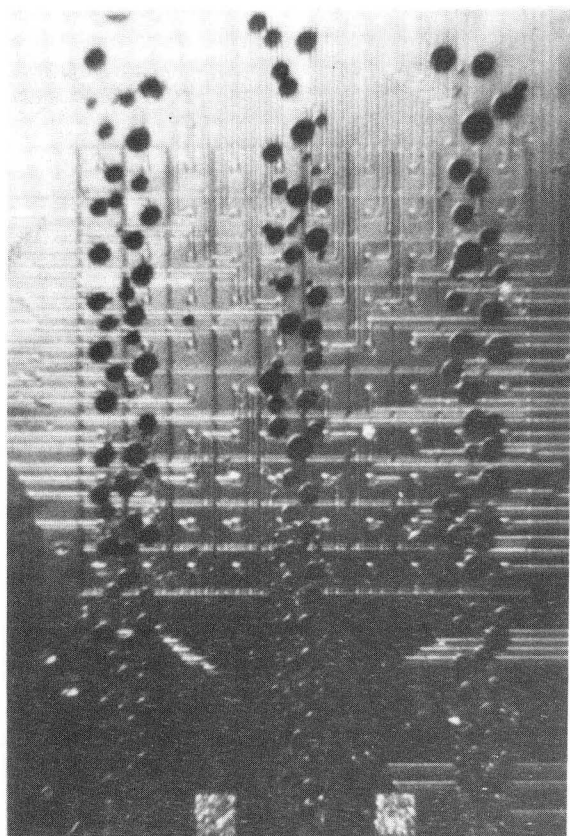
Two O<sub>2</sub>StreamsThree O<sub>2</sub> streams

Fig. 7.26 Streams of oxygen bubbles generated at a low current density, 20 mA/cm<sup>2</sup>. The detaching bubbles are very fine (10 - 20 μm in diameter), but are scavenged and agglomerate before over the segmented array. XBB 916-4196A

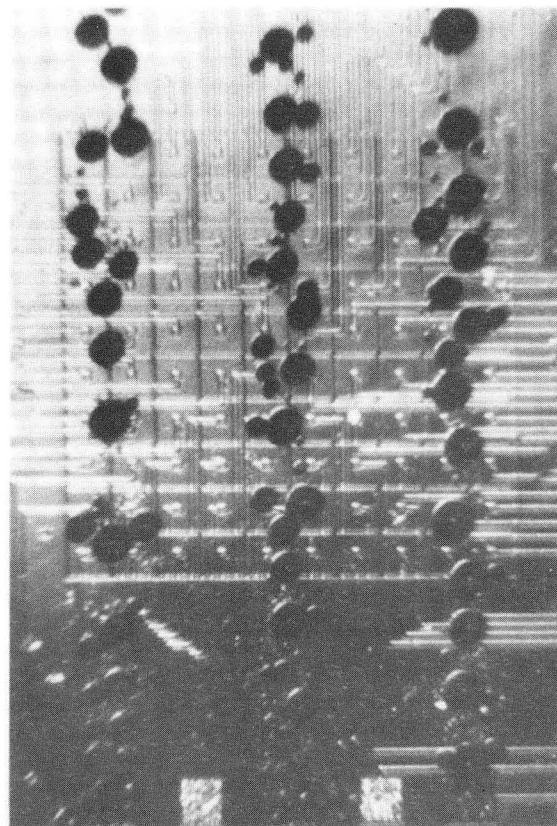


XBL 915-1128

Fig. 7.27. Comparison of mass-transfer enhancements caused by two parallel oxygen bubble streams, spaced 200 and 400  $\mu$ m apart, with the effect of a single rising column of bubbles.

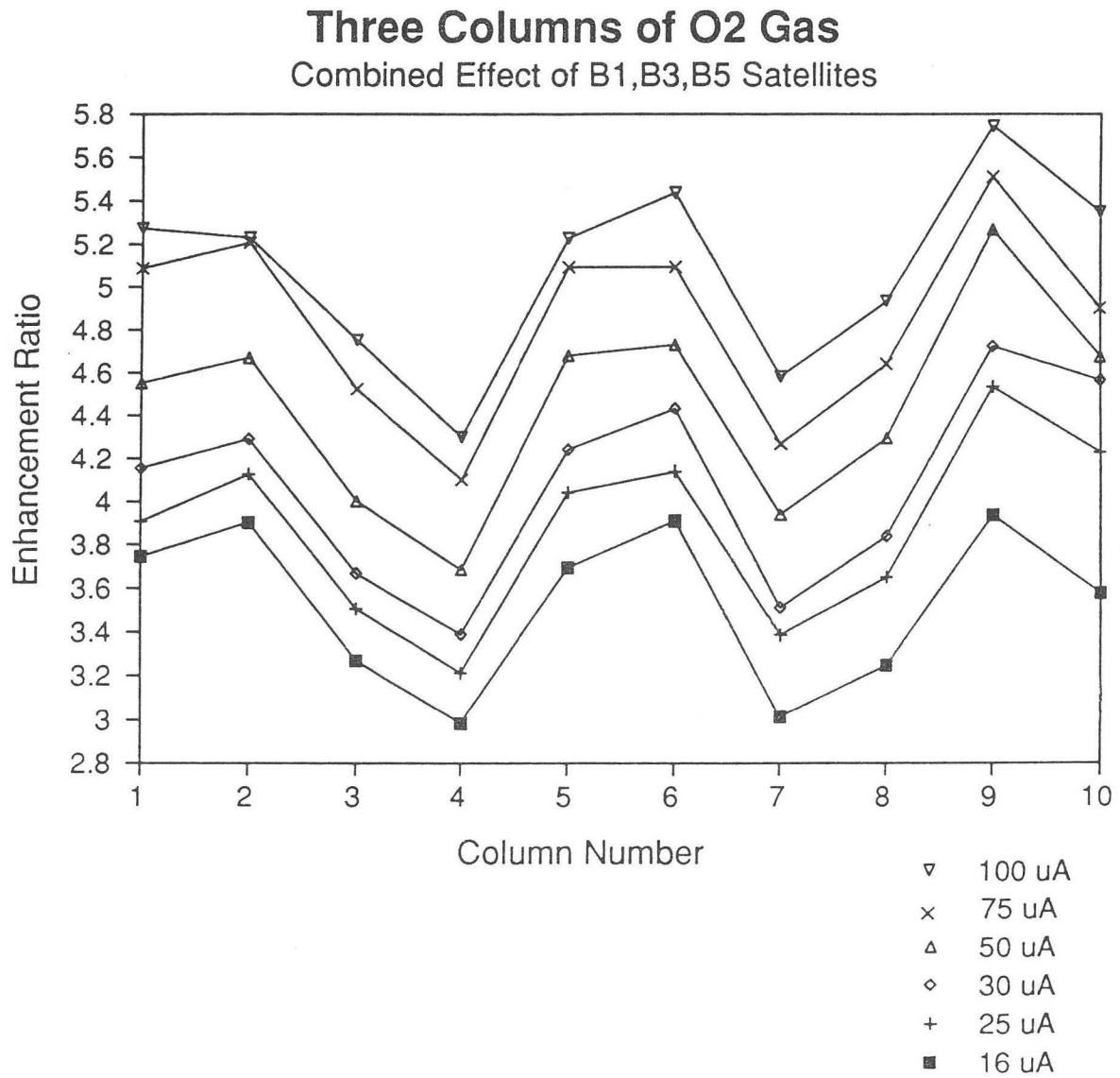


25 mA/cm<sup>2</sup> per stream



100 mA/cm<sup>2</sup> per stream

Fig. 7.28 Three parallel streams of oxygen bubbles. XBB 916-4207A



XBL 915-1129

Fig. 7.29. Mass-transfer enhancement caused by three parallel oxygen bubble streams, spaced 400  $\mu\text{m}$  apart.

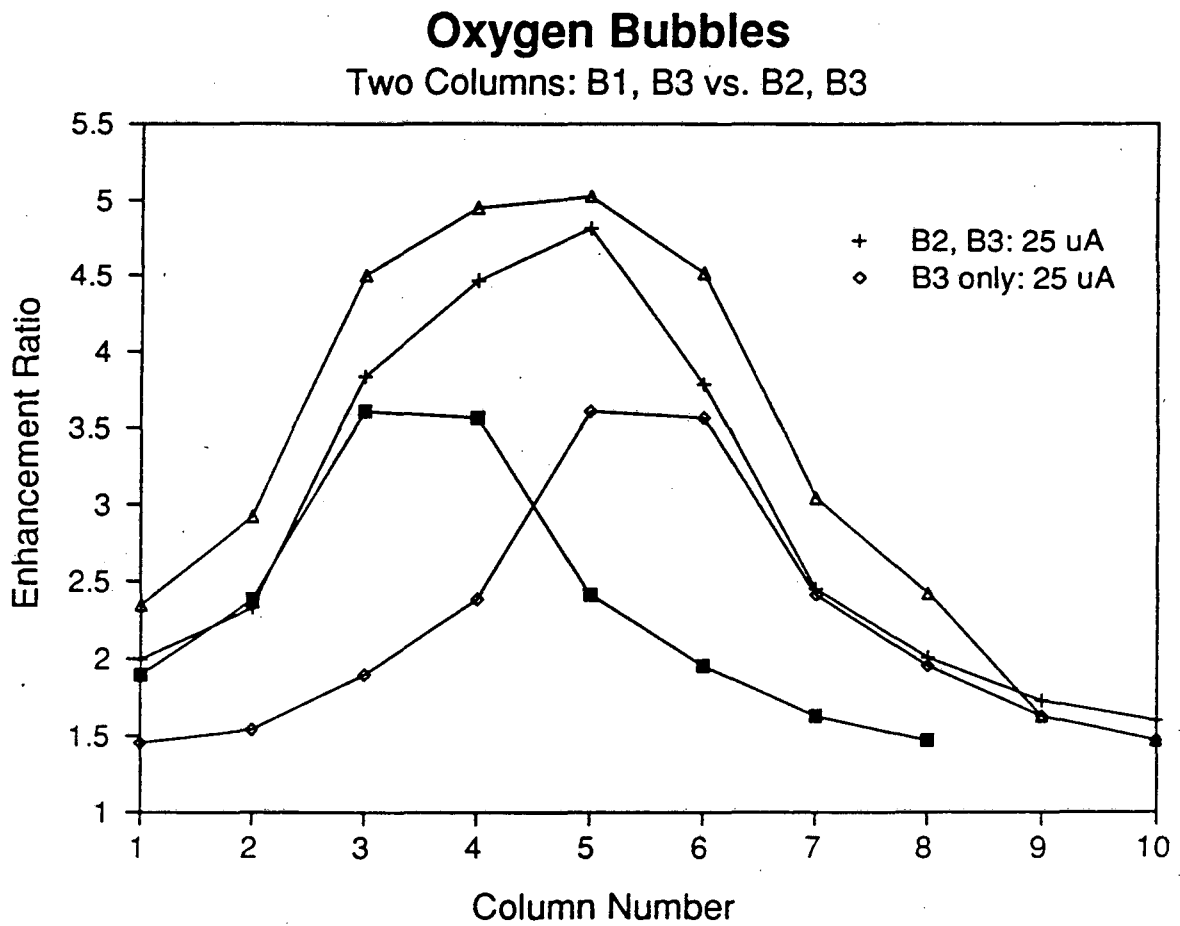
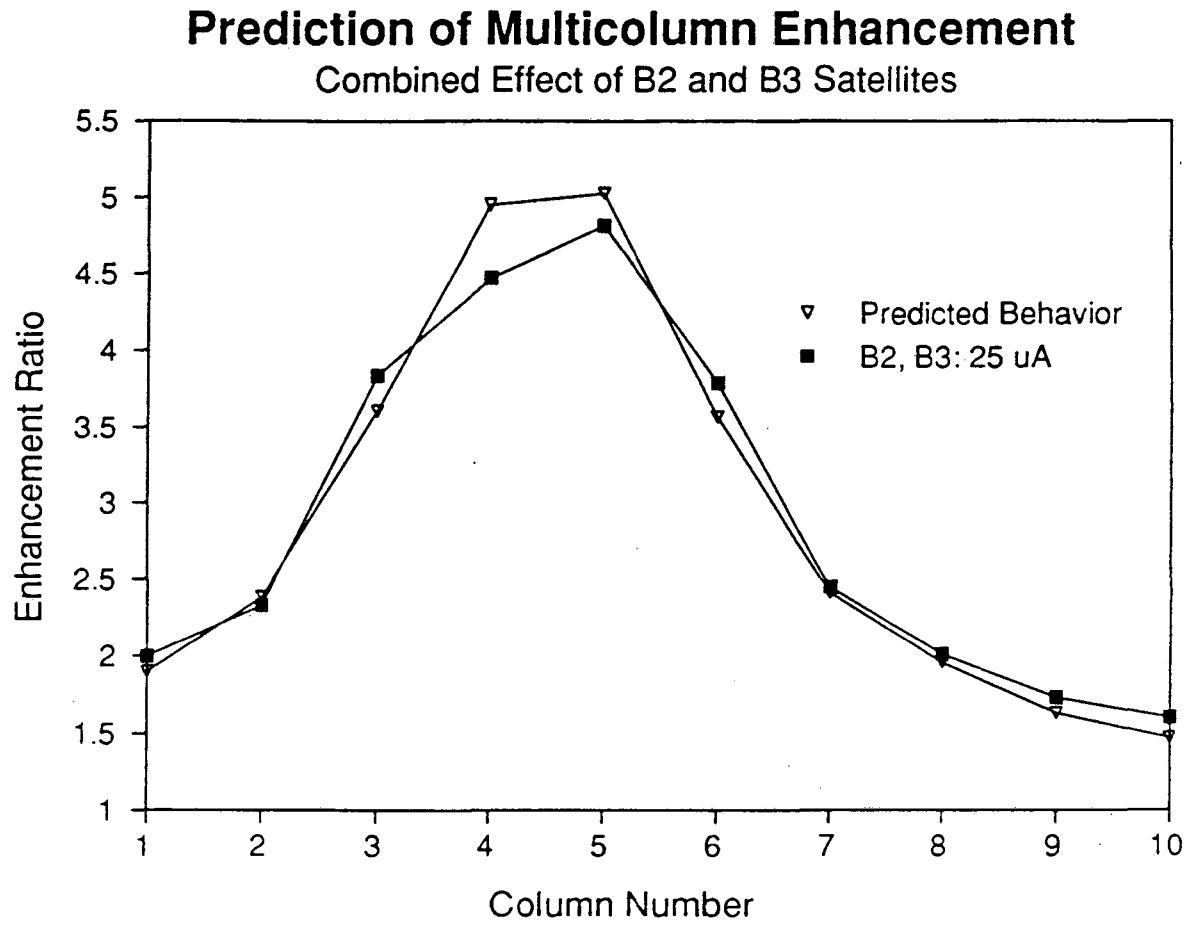


Fig. 7.30. Linear summation of single-bubble enhancements overpredicts the measured limiting current in the presence of two columns, especially in the far-field.

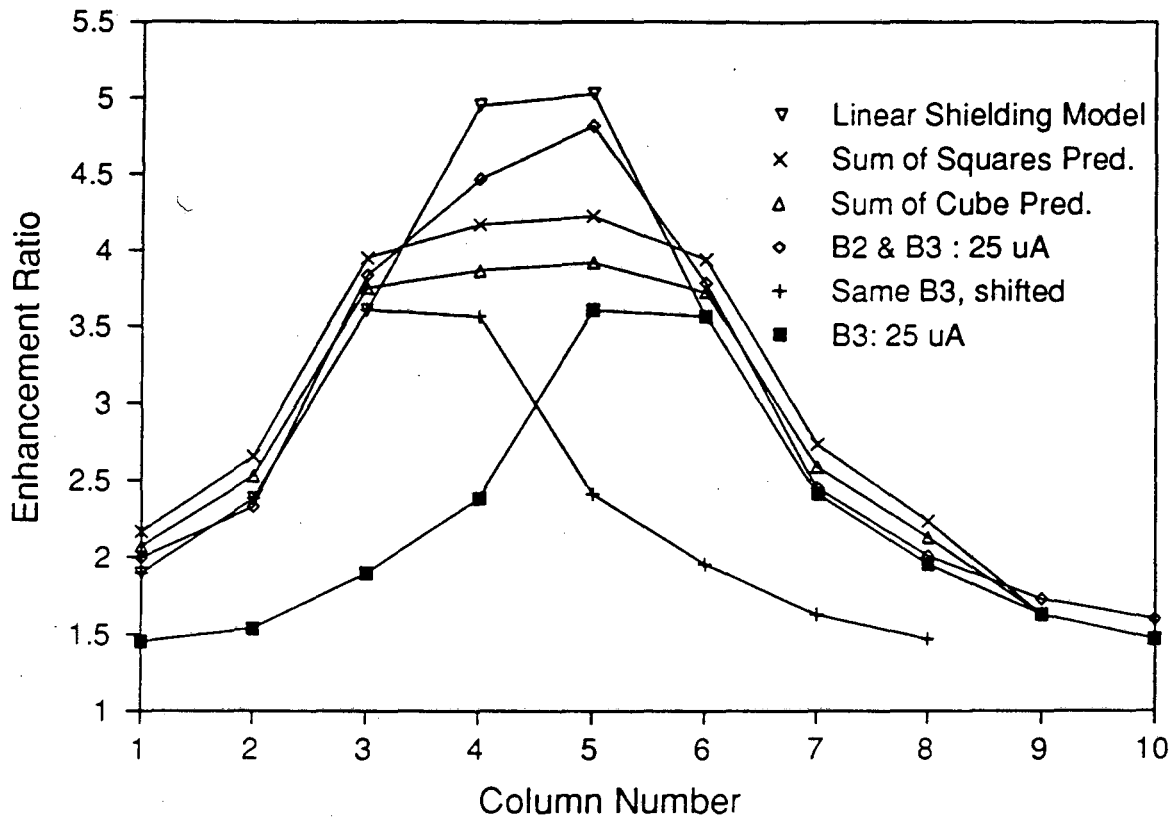


XBL 915-1125

Fig. 7.31. Linear summation of single-bubble enhancements between columns combined with shielding towards the periphery.

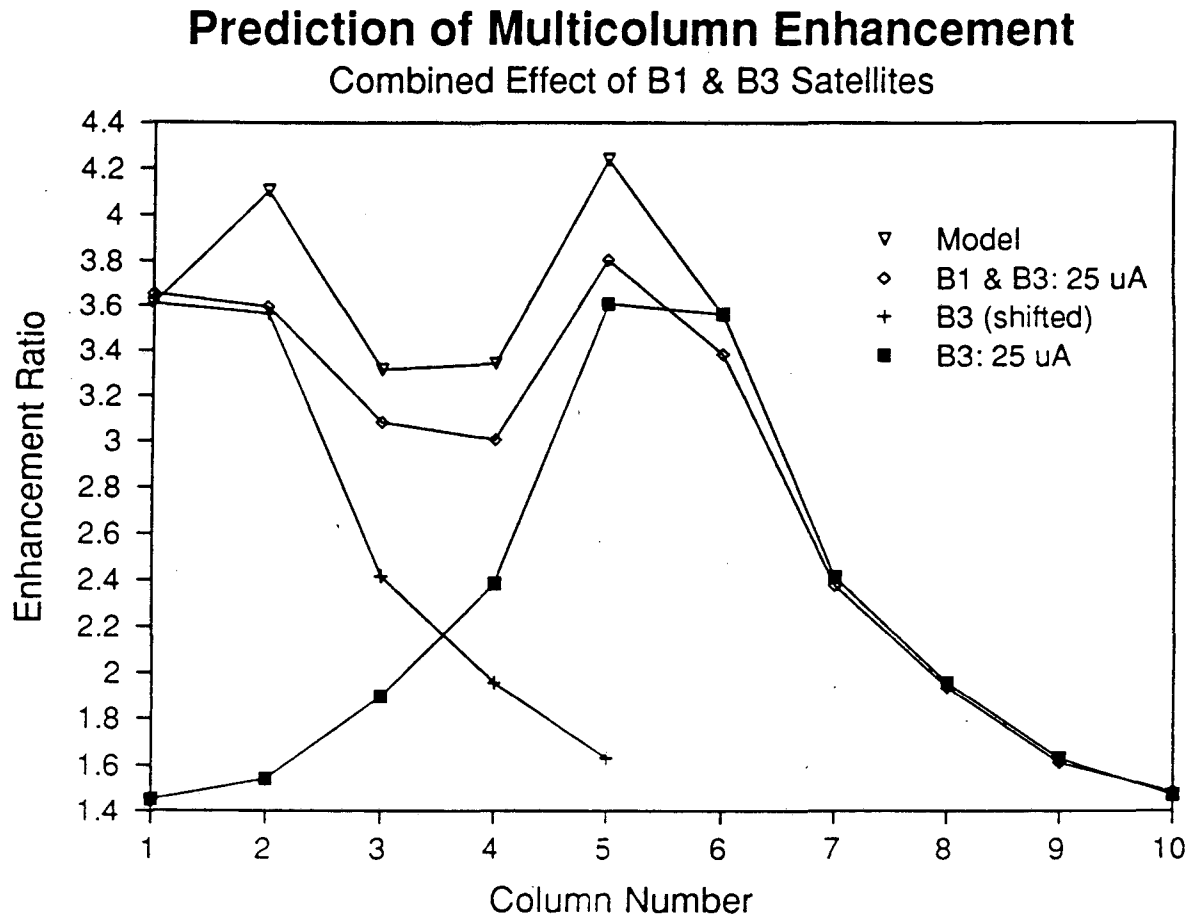


## Prediction of Multicolumn Enhancement Combined Effect of B2 and B3 Satellites



XBL 915-1126

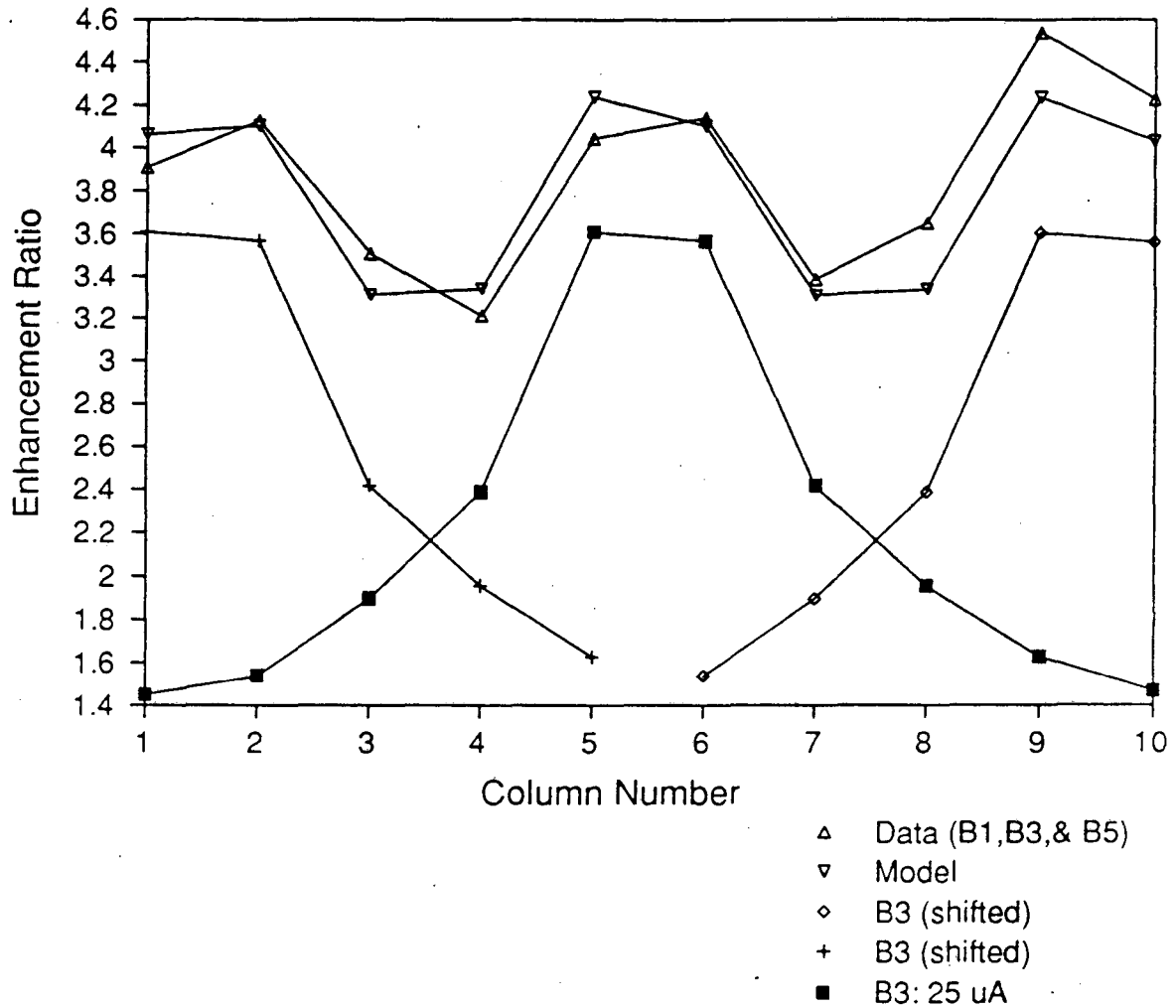
Fig. 7.32. Comparison of alternative addition rules: Prediction of the combined multi-column effect on mass-transport by linear, quadratic, and cubic summation of single-bubble enhancements.



XBL 915-1127

Fig. 7.33. Prediction of the combined effect of two oxygen bubble streams (B1 and B3) on mass-transport by a linear-shielding model.

## Prediction of Multicolumn Enhancement Combined Effect of B1,B3,B5 Satellites



XBL 915-1139

Fig. 7.34. Prediction of the combined effect of three oxygen bubble streams (B1, B3, and B5) on mass-transport by a linear-shielding model and single-column data (on B3).

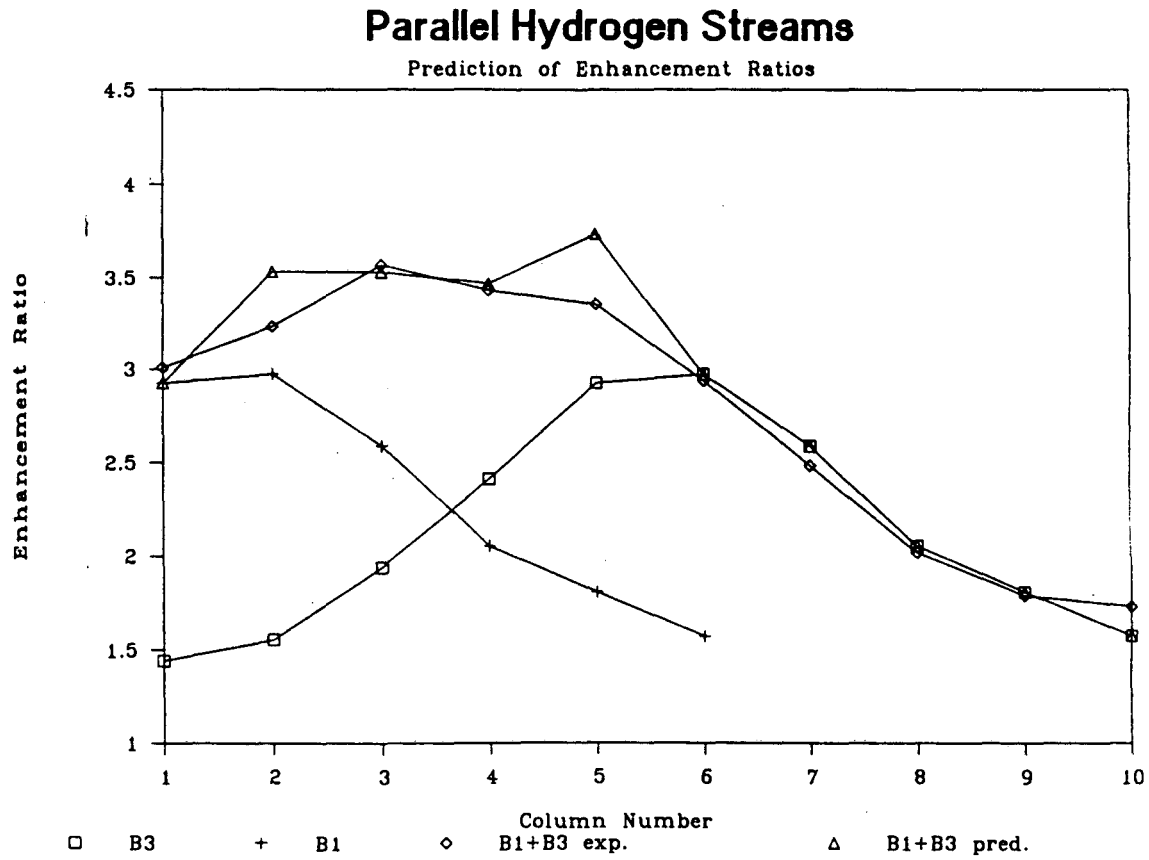


Fig. 7.35. Prediction of the combined effect of two hydrogen bubble streams (B1 and B3) on mass-transport by a linear-shielding model and single-column data (on B3).

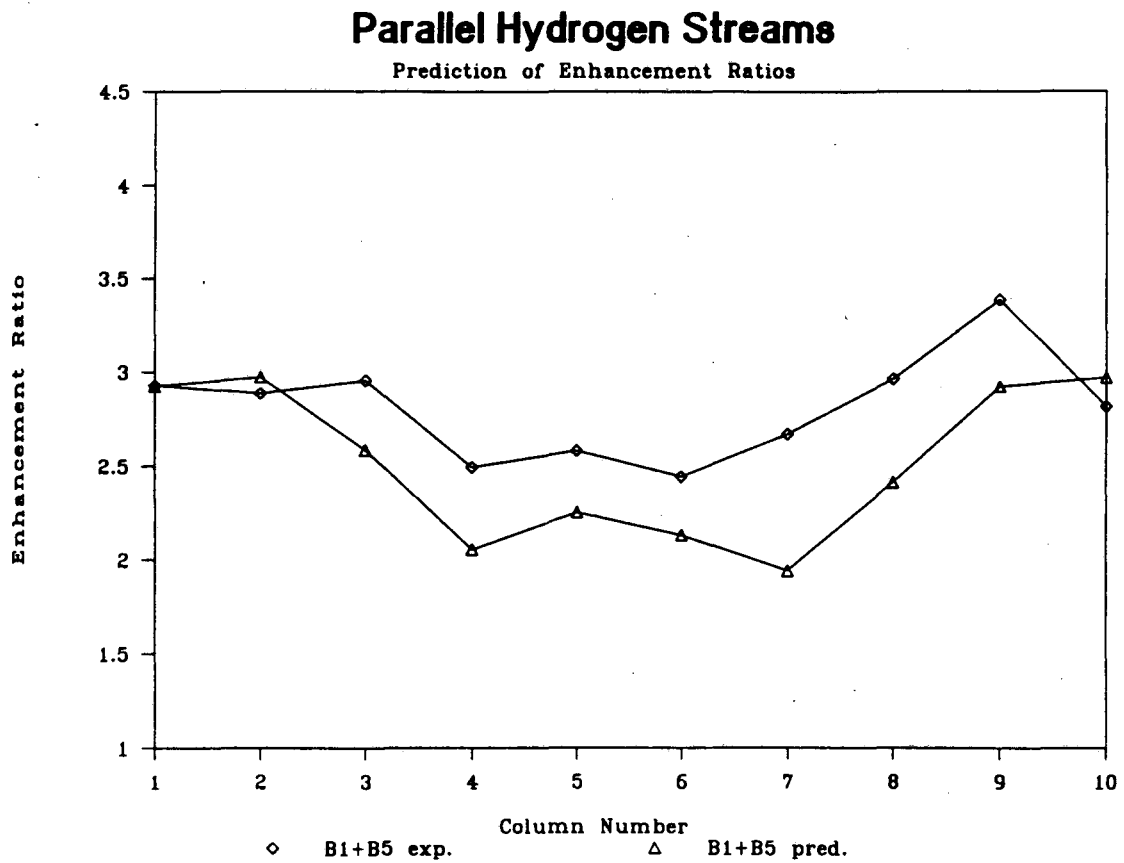


Fig. 7.36. Prediction of the combined effect of two hydrogen bubble streams (B1 and B5) on mass-transport by a linear-shielding model and single-column data (on B3). The inflection at column five, where no bubble stream is passing, is predicted by the model.

## Nomenclature

### Roman Letters

$A$	area ( $cm^2$ )
$C$	concentration ( <i>moles/l</i> )
$C_b$	concentration in the bulk ( <i>moles/l</i> )
$D$	diffusion coefficient ( $cm^2/s$ )
$E$	equilibrium electrode potential ( <i>volts</i> )
$E^o$	equilibrium electrode potential at standard conditions ( <i>volts</i> )
$F$	Faraday's constant (96,487 C/eq)
$Gr$	Grashof number
$i$	current density based on the initial geometric area ( $mA/cm^2$ )
$i_{avg}$	average current density over the real surface area
$i_l$	limiting current density ( $mA/cm^2$ )
$I$	total current ( <i>Amps</i> )
$l$	characteristic height of striae ( <i>cm</i> )
$n$	number of electrons transferred
$R$	Universal Gas Constant
$Re$	Reynolds number
$Sc$	Schmidt number
$T$	temperature ( $^{\circ}C$ )
$v$	velocity ( $cm/s$ )

### Greek Letters

$\alpha$	symmetry factor in Butler-Volmer Equation (taken to be 0.5)
$\eta$	total overpotential
$\eta_s$	surface or kinetic overpotential
$\eta_c$	concentration overpotential
$\Delta\eta_{ohm}$	differential ohmic drop from ohmic boundary layer
$\kappa$	ionic conductivity ( $ohm^{-1}cm^{-1}$ )
$\lambda$	striation wavelength
$\mu$	viscosity ( $g/cm-s$ )
$\pi$	3.14159....
$\rho_o$	density ( $g/cm^3$ ) in the bulk.
$\rho_i$	density ( $g/cm^3$ ) in the gas column.

**Superscripts**

' property in recirculation region (Chap. 4)

**Subscripts**

*b* bulk phase

*s* surface

## References

### Zinc-Halide Battery Development

- [1] Bellows, R. et al. **Development of a Circulating Zinc-Bromine Battery - Phase III**, Sandia National Laboratory, June, 1987.
- [2] Bolsstad, J. J. and R. C. Miles. *Development of the Zinc/Bromine Battery at Johnson Controls, Inc.*, Proc. 24th Intersociety Energy Conversion Engineering Conference (IECEC-89), 1311.
- [3] Carr, P. et al. **Development of the Zinc Chloride Battery for Utility Applications**, EPRI Report EM-3136, June, 1983
- [4] Dow, H. H. *A Zinc-Bromide Storage Battery*, Trans. Electrochem. Soc., **1** (1902), 129.
- [4a] Pearce, J. E., Letters Patent No. 356,261 (1887),  $ZnCl_2$  battery patent.
- [4b] Bradley, U.S. Patents No. 312,802 (1885) and No. 409,448 (1889),  $ZnBr_2$  battery patents.
- [5] Fujii, T. et al. *4MW Zinc/Bromine Battery for Electric Power Storage*, Proc. 24th Intersociety Energy Conversion Engineering Conference, (IECEC-89), 1319.
- [6] Grimes, P. et al. **Zinc-Bromine Electric Vehicle Battery Development**, Final Report, Sandia National Laboratory, June, 1987.
- [7] Jorne, J. *Flow Batteries*, Am. Scientist, **71** (1983), 507.



- [8] Leo, A. *Status of Zinc-Bromine Battery Development at Energy Research Corporation*, Proc. 24th Intersociety Energy Conversion Engineering Conference (IECEC-89), IEEE (1989), 1303.
- [9] McBreen, J. *Rechargeable Zinc Batteries*, *J. Electroanal. Chem.*, **68** (1984), 415.
- [10] Misawa, Y. *Demonstration Test of a 60 KW-Class Zinc/Chlorine Battery as a Power Storage System*, Proc. 24th Intersociety Energy Conversion Engineering Conference, (IECEC-89), 1325.
- [11] Nakayama, T. et al. *The Current Status of Development of Advanced Battery Electric Energy Storage Systems in Japan*, Proc. 24th Intersociety Energy Conversion Engineering Conference, (IECEC-89), 1297.
- [12] Savinell, R. F. and H. S. Burney, Jr. *Report of the Electrolytic Industries for the Year 1989*, *J. Electrochem. Soc.*, **137** (1990), 485C.
- [13] Wranglen, G. *Dendrites and Growth Layers in the Electrocrystallization of Metals*, *Electrochimica Acta*, **2** (1960), 130.

#### **Work at Berkeley - Zinc Striations and Related Topics**

- [14] Anderson, R. and C. W. Tobias. **Studies on Zinc Nodules Electrodeposited from Acid Electrolytes**, MS Thesis (UC Berkeley), LBL Report 18646, Dec. 1984.
- [15] Carlson, E. J. **Electrodeposition Around Protruding Surface Imperfections in Turbulent Flow**, MS thesis (UC Berkeley), LBL Report 3175, Jan. 1975.

- [16] Faltemier, J. L., M. M. Jaksic, T. Tsuda, and C. W. Tobias. **An Inventory of Photographs of Zinc Electrodeposited from Acid Electrolytes**, LBL Report 16601, Sept., 1983.
- [17] Faltemier, J. L. and C. W. Tobias. **The Effect of Hydrodynamic Flow on the Morphology of Electrodeposited Zinc**, PhD Thesis (UC Berkeley), LBL Report 16485, Aug. 1983.
- [18] Fischl, D. S., K. J. Hanson, R. H. Muller and C. W. Tobias. *Mass Transfer Enhancement By Small Flow Obstacles in Electrochemical Cells*, **Chemical Engineering Communication**, 38 (1985), 191.
- [19] Fischl, D. S., R. H. Muller and C. W. Tobias, **Effects of Small Flow Obstacles on the Limiting Current and Pressure Drop in a Square Duct**, M.S. Thesis (UC Berkeley), LBL Report 16422, August, 1983.
- [20] Hanson, K. J. **Interferometric Study of Mass-Transfer Enhancement by Turbulence Promoters**, M.S. Thesis (UC Berkeley), LBL Report 9038, April, 1979.
- [21] Hauser, A. K. **The Corrosion of a Zinc Rotating Disk in One Molar Hydrochloric Acid**, M.S. Thesis (UC Berkeley), LBL Report 17461, April, 1984.
- [22] Jaksic, M. M. *Impurity Effects on the Macromorphology of Electrodeposited Zinc, Part I*, **Surface Technology**, 24 (1985), 193.
- [23] **Ibid.** Part II, **Surface Technology**, 28 (1986), 113.
- [24] **Ibid.** Part III, **Surface Technology**, 29 (1986), 95.

- [25] Jaksic, M. M. *Hydrodynamic Effects of Surfactants on the Macromorphology of Electrodeposited Zinc and Flow Visualization*, **J. Electroanal. Chem.**, **242** (1988), 21.
- [26] Jaksic, M. M. *Hydrodynamic Effects on the Macromorphology of Electrodeposited Zinc and Flow Visualization*, **J. Electroanal. Chem.**, **249** (1988), 35.
- [27] Ibid. **J. Electroanal. Chem.**, **249** (1988), 63.
- [28] Jiricny, V., H. Choi, and J. W. Evans. *Zinc Electrodeposit Morphology under Conditions of Fluctuating Current Density*, **J. App. Electrochem.**, **17** (1987), 91.
- [29] McLarnon, F., Muller, R. H. and C. W. Tobias. *Interferometric Observation of Turbulent Mass Transfer in Channel Flow*, **J. Electrochem. Soc.**, **122** (1975),
- [30] McVay, L., R. H. Muller, and C. W. Tobias. **Studies of Macromorphology and Current Efficiency of Zinc Electrodeposited from Flowing Chloride Electrolytes**, M.S. Thesis (UC Berkeley), LBL Report 21492, May, 1986.
- [31] McVay, L., R. H. Muller, and C. W. Tobias. *Application of Video Microscopy to In-situ Studies of Electrodeposition*, **J. Electrochem. Soc.**, **136** (1989), 3384.
- [32] Prentice, G. A. and C. W. Tobias, *Deposition and Dissolution on Sinusoidal Electrodes*, **J. Electrochem. Soc.**, **129** (1982), 316.
- [33] Sutija, D. P., R. H. Muller, and C. W. Tobias. **Development of a Micropatterned Electrode for Studies of Zinc Electrodeposition**, M.S. Thesis (UC Berkeley), LBL Report 22576, December, 1986.

- [34] Tsuda, T. and C. W. Tobias. **The Effect of Lead Ions on the Morphology of Electrodeposited Zinc**, MS Thesis (UC Berkeley), LBL Report 13057, Sept. 1981.

#### **Electrochemical Texts and Reference Books**

- [35] Bard, A. J. and L. R. Faulkner, **Electrochemical Methods** (New York: Wiley, 1980).
- [35a] Batchelor, G. K. **An Introduction to Fluid Dynamics** (Cambridge: Cambridge University Press, 1967).
- [36] Dobos, D. **Electrochemical Data** (Amsterdam: Elsevier, 1975).
- [37] Newman, J. **Electrochemical Systems** (Englewood Cliffs, N.J.: Prentice-Hall, 1974).
- [38] Pourbaix, M. **Atlas of Electrochemical Equilibria in Aqueous Solutions**, second edition (Houston: NACE, 1974).
- [38a] Schlichting, H. **Boundary-Layer Theory**, seventh edition, (New York: McGraw-Hill, 1979).

#### **The Rotating Disk**

- [39] Cochran, W. G., *The Flow due to a Rotating Disk*, **Proc. Cambridge Phil. Soc.**, **30** (1934), 365.

- [40] Levich, V. G. **Physicochemical Hydrodynamics**. (Englewood Cliffs, N.J.: Prentice-Hall, 1962).
- [41] Riddiford, A. C. *The Rotating Disk System* in **Advances in Electrochem. and Electrochem. Eng.**, P. Delahay and C. W. Tobias, eds. (New York: Interscience, 1966), 47.
- [42] Von Karman, T. **Z. angew. Math. Mechanik**, **1** (1921), 233.

#### **Studies on Dendrites and Zinc Morphology in Acid Electrolytes**

- [43] Hill, M. R. H. and G. T. Rogers, *Polyethylene Glycol in Copper Electrodeposition onto a Rotating Disk Electrode*, **J. Electroanal. Chem.**, **86**, (1978), 179.
- [44] Hill, M. R. H. and G. T. Rogers, *The Cause of Spirals on Electrodeposits Formed on a Rotating Disk Electrode* **J. Electroanal. Chem.**, **96**, (1979), 87.
- [45] Johnson, G. R. and D. R. Turner, *The Effect of Some Addition Agents on the Kinetics of Copper Electrodeposition from a Sulfate Solution. II. Rotating Disk Experiments* **J. Electrochem. Soc.**, **109**, (1962), 918.
- [46] Jorne, J. and D. Labelle, *Combined Natural and Forced Convection in a Horizontal Flow Channel*, **Chemical Eng. Comm.**, **38** (1985), 347.
- [47] Kralik, D. and J. Jorne, *Hydrogen Evolution and Zinc Nodular Growth in the Zinc-Chloride Battery*, **J. Electrochem. Soc.**, **127** (1980), 2335.
- [48] Landau, U. et al. **Zinc Electrodeposition and Dendritic Growth from Zinc Halide Electrolytes**, EPRI Report EM-2393, May, 1982.

- [49] Landau, U. and J. H. Shyu. **Roughness Evolution and Dendritic Growth in Zinc Electrodeposition from Halide Electrolytes**, EPRI Report EM-2937, March, 1983.
- [50] McBreen, J. and E. Cairns, **The Zinc Electrode** in Adv. in Electrochemistry and Electrochemical Engineering, H. Gerischer and C. W. Tobias, ed., 11 (New York: John Wiley and Sons, 1978), 273.
- [51] McBreen, J. and E. Gannon, *Electrodeposition of Zinc on Glassy Carbon from  $ZnCl_2$  and  $ZnBr_2$  Electrolytes*, **J. Electrochem. Soc.**, **130** (1983), 1667.
- [52] McBreen, J. and E. Gannon. **Zinc Electrode Morphology in Acid Electrolytes**, Brookhaven National Lab, Annual Report, April, 1983.
- [53] Oren, Y. and U. Landau, *Growth of Zinc Dendrites in Acidic Zinc Chloride Solution*, **Electrochimica Acta**, **27** (1982), 739.
- [54] Rogers, G. T. and K. J. Taylor, *Effect of Small Protrusions on Mass Transport to a Rotating-Disk Electrode*, **Nature**, **200** (1963), 1062.
- [55] Rogers, G. T. and K. J. Taylor, *A Rotating Disc Electrode Study of the electrodeposition of zinc from alkaline zincate solutions*, **J. Electroanal. Chem.**, **167** (1984), 251.
- [56] Selman, J. R. and W. C. Hsie. **Dendritic Zinc Deposition From Flowing Acidic Solution**, LBL Reports 4512010 and 4534910, July, 1986.
- [57] Selman, J. R. and Y. P. Lin. **Investigation of Dendritic Zinc Deposition in Flow Batteries**, LBL Technology Base Research Project, August, 1989.

- [58] Yee, K. E. and J. Jorne, *Striated Zinc Electrodeposition at Rotating Disk and Hemisphere Electrodes*, **J. Electrochem. Soc.**, **137** (1990), 2403.
- [59] Yee, K. E. **Striated Zinc Electrodeposition at Rotating and Planar Electrodes**, Ph.D. Thesis, Wayne State University, Detroit, Michigan, 1986.

#### **Kinetics and Mechanisms of the Zn/Zn<sup>++</sup> electrode reaction**

- [60] Beshore, A. C. *et al.*, *Nucleation and Growth of Zinc Electrodeposited from Acidic Zinc Solutions*, **J. App. Electrochem.**, **17** (1987), 765.
- [61] Breivik, T. R. and T. Hurlen, *Ion Activities and Zinc Electrode Reactions in Calcium Chloride Solutions*, **Acta Chem. Scand. A** , **32** (1978), 799.
- [62] Brodd, R. J. and V. E. Leger. **Zinc** in Encyclopedia of the Electrochemistry of the Elements, **V-1**, A. J. Bard, ed. (New York: Marcel Dekker, 1976).
- [63] Cachet, C. and R. Wiart, *Kinetics of Zinc Dissolution in Chloride Electrolytes*, **J. Electroanal. Chem.**, **111** (1980), 235.
- [64] Cachet, C. and R. Wiart, *Reaction Mechanisms for Zinc Dissolution in Chloride Electrolytes*, **J. Electroanal. Chem.**, **129** (1981), 103.
- [65] Eriksrud, E., *Effect of Halides and Alkali Cations on the Zn(Hg)/Zn(II) Electrode Reactions* , **J. Electroanal. Chem.** , **76** (1977), 27.
- [66] Epelboin, I., M. Ksouri, and R. Wiart, *On a Model for the Electrocrystallization of Zinc Involving an Autocatalytic Step*, **J. Electrochem. Soc.**, **122** (1975), 1206.

- [67] Epelboin, I., M. Ksouri, and R. Wiart, *Intermediaries adsorbed and electrocrystallization*, **J. Electroanal. Chem.**, **65** (1975), 373.
- [68] Epelboin, I., M. Ksouri, and R. Wiart, *Kinetics of Zinc Electrocrystallization Correlated With Deposit Morphology*, **Faraday Symp. Chem. Soc.**, **12** (1977), 115.
- [69] Epelboin, I., *et al.*, *A Study of the Elementary Steps of Electron-Transfer During the Electrocrystallization of Zinc*, **Electrochimica Acta**, **20** (1975), 603.
- [70] Gaiser, L. and K. E. Heusler, *Die Kinetik der Zink-elektrode in Zinkperchloratlosungen*, **Electrochimica Acta**, **15** (1970), 161.
- [71] Hurlen, T. and E. Eriksrud, *Kinetics of the Zn(Hg) / Zn (II) Electrode in Acid Chloride Solution*, **J. Electroanal. Chem.**, **45** (1973), 405.
- [72] Hurlen, T. and E. Eriksrud, *Single-Ion Activities and Zn / Zn(II) Reactions in Alkali Chloride Solutions* , **J. Electroanal. Chem.**, **63** (1975), 157.
- [73] Hurlen, T. and K. Fischer, *Kinetics of Zn / Zn (II) Reactions in Acidified Solutions of Potassium Chloride* , **J. Electroanal. Chem.**, **61** (1975), 165.
- [74] Jorne, J., J. T. Kim, and D. Kralik, *The Zinc-Chlorine Battery: Half-cell Overpotential Measurements* , **J. App. Electrochem.**, **9** (1979), 573.
- [75] Kim, J. T. and J. Jorne, *The Kinetics and Mass Transfer of Zinc Electrode in Acidic Zinc-Chloride Solution*, **J. Electrochem. Soc.**, **127** (1980), 8.
- [76] Sanchez Cruz, M., F. Alonso, and J. M. Palacios, *The effect of the concentration of TBACl on the electrodeposition of zinc from chloride and perchlorate electrolytes* , **J. App. Electrochem.**, **20** (1990), 611.



- [77] Scott, A. C., R. M. Pitbaldo, G. W. Barton and A. R. Ault, *Experimental determination of the factors affecting zinc electrowinning efficiency* , **J. App. Electrochem.**, **18** (1988), 120.
- [78] Sierra Alcazar, H. B., and J. A. Harrison, *The Rate of Zinc Deposition at Zinc Amalgam and Zinc Metal* , **Electrochimica Acta**, **22** (1977), 627.
- [79] Yamashita, T., *Electro-deposition and Electro-dissolution of Zinc in the Vicinity of Equilibrium Potential in Aqueous Zinc Sulfate Solutions*, **J. Electroanal. Chem.**, **106** (1980), 95.
- [80] Wark, I. W. *The Electrodeposition of Zinc from Acidified Zinc Sulphate Solution*, **J. App. Electrochem.**, **9** (1979), 721.

#### **Zinc-Halide Complex Formation and Transport Properties**

- [81] Agnew, A. and R. Paterson. *Transport in Aqueous Solutions of Group IIB Metal Salts at 298.15 K (Part 6)* , **J.C.S. Faraday Trans.**, **74** (1978), 2896.
- [82] Albright, J. and D. Miller, *Mutual Diffusion Coefficients of Aqueous ZnSO<sub>4</sub> at 25°C*, **J. Sol. Chem.**, **4** (1975), 809.
- [83] Egan, D. M. and J. R. Partington, *Transport Numbers of Zinc Halides* , **J. Am. Chem. Soc.** , **67** (1945), 191.
- [84] Harris, A. C. and H. N. Parton, *The Transport Numbers of Zinc Chloride from EMF Measurements* , **Trans. Faraday Soc.** , **36** (1940), 1139.
- [85] Miller, D. G., A. W. Ting, and J. A. Rard, *Mutual Diffusion Coefficients of Various ZnCl<sub>2</sub> (0.5M)-KCl-H<sub>2</sub>O Mixtures at 298.15 K by Raleigh Inter-*

*ferometry*, **J. Electrochem. Soc.** , **135** (1988), 896.

- [86] Parton, H. N. and J. W. Mitchell, *The Activity Coefficients and Transport Numbers of Zinc Bromide at 25 ° C from EMF Measurements*, **Trans. Faraday Soc.** , **35** (1930), 758.
- [87] Rard, J. A. and D. G. Miller, *Ternary Mutual Diffusion Coefficients of ZnCl<sub>2</sub>-KCL-H<sub>2</sub>O at 25°C by Rayleigh Interferometry*, **J. Sol. Chem.** , **19** (1990), 129.
- [88] Skou, E., T. Jacobsen, W. Van der Hoeven, and S. Atlung, *On the Zinc-Chloride Complex Formation* , **Electrochimica Acta** , **22** (1977), 169.
- [89] Thomas, B. K. and D. J. Fray, *The Conductivity of Aqueous Zinc Chloride Solutions*, **J. App. Electrochem.** , **12** (1982),1.

### **Morphological Stability Analysis**

- [90] Aogaki, R. *Image Analysis of Morphological Instability in Galvanostatic Electrocrystallization*, **J. Electrochem. Soc.** Parts I and II, **129** (1982),2442.
- [91] Aogaki, R. and T. Makino, *Morphological Instability in Nonsteady Galvanostatic Electrodeposition* **J. Electrochem. Soc.**, Parts I and II, **131** (1984), 40.
- [92] Mullins, W. W. and R. F. Sekerka, *Morphological Stability of a Particle Growing by Diffusion or Heat Flow*, **J. App. Physics** , **34** (1963), 323.
- [93] Sekerka, R. F., *A Stability Function for Explicit Evaluation of the Mullins-Sekerka Interface Stability Criterion*, **J. App. Physics** , **36** (1965), 264.

### Nucleation Theory

- [94] Abyaneh, M. Y., *Formulation of Current-Time Transients Due to Nucleation and Coalescence of Spherical-Cap Growth Forms*, **J. Electroanal. Chem.**, **209** (1986), 1.
- [95] Abyaneh, M. Y. and M. Fleischmann, *The Electrocrystallisation of Nickel, Part I and II* **J. Electroanal. Chem.**, **119** (1981), 187 and 196. Also in **Trans. Inst. Metal Fin.**, **58** (1980), 91.
- [96] Avrami, M., *Kinetics of Phase Change. I. General Theory*, **J. Chem. Phys.**, **7** (1939), 1103.
- [97] **Ibid.** *II. Transformation-Time Relations for Random Distribution of Nuclei* **J. Chem. Phys.**, **8** (1940), 212.
- [98] **Ibid.** *III. Granulation, Phase Change, and Microstructure*, **J. Chem. Phys.**, **9** (1941), 177.
- [99] Budevski, E., et al., **Electrochimica Acta**, **11** (1966), 1697.
- [100] Budevski, E. B., *Deposition and Dissolution of Metals and Alloys. Part A: Electrocrystallization*, Chapter 7 in B. E. Conway et al., eds., **Comprehensive Treatise of Electrochemistry**, **7**, 1983.
- [101] Burton, W. K., N. Cabrera, and F. C. Frank, **Nature**, **163** (1949), 398.
- [102] Damjanovic, A. and J.O'M. Bockris, *The Kinetics of the Electrodeposition and Dissolution of Metal Monolayers as a Function of Dislocation Density*, **J. Electrochem. Soc.**, **110**(1963), 1035.

- [103] Deutscher, R. L. and S. Fletcher, *Nucleation on Active Sites, Part IV and V*. **J. Electroanal. Chem.**, **239** (1988), 17 and **277** (1990), 1.
- [104] Fleischmann, M. and H. R. Thirsk, *Metal Deposition and Electrocrystallization*, Chapter 3 in J. O'M. Bockris, ed., **Modern Aspects of Electrochemistry**, **X** (1963), 123.
- [105] Fletcher, S. and T. Lwin, *A General Probabilistic Model of Electrochemical Nucleation*, **Electrochimica Acta**, **28** (1983), 237.
- [106] Fletcher, S., *Nucleation on Active Sites Part II*. **J. Electroanal. Chem.**, **164** (1984).
- [107] Gunawardena, G., J. Hills and I. Montenegro, *Potentiostatic Studies of Electrochemical Nucleation*, **Electrochimica Acta**, **23** (1978), 693.
- [108] Kaischew, R. and I. N. Stranski, **Z. Physik. Chem.**, **B26** (1934), 317.
- [109] Milchev, A. *Ohmic Drop and Zones of Reduced Overpotential During the Growth of Small Clusters*, **J. App. Electrochem.**, **20** (1990), 307.
- [110] Milchev, A. and V. Tsakova, *Theory of Progressive Nucleation and Growth Accounting for the Ohmic Drop in the Electrolyte, I*. **J. App. Electrochem.**, **20** (1990), 301.
- [111] Volmer, M. and A. Weber, **Z. physik Chem.**, **119** (1926), 277.

### **Fluid Flow and Turbulent Eddies in the Wake of 3D Nodules**

- [112] Focke, W. W., *On the Mechanism of Transfer Enhancement by Eddy Promoters*, **Electrochimica Acta**, **28** (1983), 1137.
- [113] Mason, P. J. and B. R. Morton, *Trailing Vortices in the Wakes of Surface-Mounted Obstacles*, **J. Fluid Mech.**, **175** (1987), 247.
- [114] Ralph, M. E. and T. J. Pedley, *Flow in a Channel with a Moving Indentation*, **J. Fluid Mech.**, **190** (1988), 87.

### Statistical Methods

- [115] Bracewell, R. N., *Numerical Transforms*, **Science**, **248** (1990), 697.
- [116] Dagnall, H. **Exploring Surface Texture** (Leicester: Rank Taylor Hobson, 1986).
- [117] Lange, F. H. **Correlation Techniques** (Princeton: Van Nostrand, 1967).
- [118] Press, W. H. et al. **Numerical Recipes: The Art of Scientific Computing** (Cambridge: Cambridge University Press, 1986).
- [119] Tolstov, G. P. **Fourier Series** (New York: Dover Publications, 1962).
- [120] Young, R. D. and E. C. Teague, *Measurement and Characterization of Surface Finish*, in R. Sand, ed. **Properties of Electrodeposits: Their Measurement and Significance** (Princeton: Electrochemical Soc., 1975), p.22.

## Microfabrication

- [121] Duva, R. *Pulse Plating: The Pros and Cons of Practical Application, Finishing Highlights*, (Jan-Feb. 1979).
- [122] Engelhard Corp., *Brochure on the Engelhard Acid Gold Process*.
- [123] *Kic Tutorial*, Microfabrication Laboratory, U.C. Berkeley.
- [124] **Microfabrication Laboratory Handbook**, University of California, Berkeley.
- [125] Wolf, S. and R. N. Tauber. **Silicon Processing for the VLSI Era** (Sunset Beach, Ca: Lattice Press, 1986).
- [126] Schuegraf, K. K. **Handbook of Thin-Film Deposition Processes and Techniques** (San Francisco: Noyes Publications, 1989).

## Electrolytic Gas Evolution - Research in the Tobias group

- [127] Bon, C. K. **Supersaturation at Gas-Evolving Electrodes**, M.S. Thesis (U.C. Berkeley), UCRL Report 19612, Sept. 1970.
- [128] Cettou, P. and C.W. Tobias, **The First Generation of Bubbles at Gas Evolving Electrodes**, LBL Report 13632, Dec. 1981.
- [129] Cheh, H. Y. **On the Mechanism of Electrolytic Gas Evolution**, Ph.D. Thesis (U.C. Berkeley), Feb. 1967.

- [130] Dees, D. W. **Mass Transfer at Gas-Evolving Electrode Surfaces in Electrolysis**, Ph.D. (U.C. Berkeley), LBL Report 16176, September, 1983.
- [131] Dees, D. W. and C. W. Tobias, *Experimental Studies of Free-Convection Mass Transfer to a Horizontal Surface with a Micro-mosaic Electrode*, **J. Electrochem. Soc.**, **134** (1987), 369.
- [132] Dees, D. W. and C. W. Tobias, *Mass Transfer at Gas Evolving Surfaces: A Microscopic Study*, **J. Electrochem. Soc.**, **134** (1987), 1702.
- [133] DelaRue, R. E. and C. W. Tobias *On the Conductivity of Dispersions*, **J. Electrochem. Soc.**, **106** (1959), 827.
- [134] Dukovic, J. O. **Studies on Current Distribution in Electrochemical Cells**, Ph.D. Thesis (U.C. Berkeley), LBL Report 22084, Aug. 1986.
- [135] Elliott, Steven and C. W. Tobias. Unpublished Results.
- [136] Fenech, E. J. and C. W. Tobias, *Mass Transfer by Free Convection at Horizontal Electrodes*, **Electrochimica Acta**, **2** (1960), 311.
- [137] Meredith, R. E. and C. W. Tobias *Conductivities in Emulsions*, **J. Electrochem. Soc.**, **108** (1961), 286.
- [138] Putt, R. **Studies of the Events Occuring at Gas-Evolving Electrodes**, M.S. Thesis (U.C. Berkeley), LBL Report 3989, Oct. 1975.
- [139] Sides, P. J., **Bubble Dynamics at Gas-evolving Electrodes**, Ph.D. Thesis (U.C. Berkeley), LBL Report 11849, 1981.

- [140] Tobias, C. W., *Effect of Gas Evolution on Current Distribution and Ohmic Resistance in Electrolyzers*, **J. Electrochem. Soc.**, **106** (1959), 833.
- [141] Whitney, G., **Microscale Resolution of Interfacial Mass-Transfer Rates in Electrode Processes**, Ph.D. Thesis (U. C. Berkeley), LBL Report 23596, June, 1987.
- [142] Whitney, G. and C. W. Tobias, *The Onset of Buoyancy-induced Convection at a Micro-mosaic Electrode*, **J. Electroanal. Chem.**, **229** (1987), 429.
- [143] Whitney, G. and C. W. Tobias, *Mass-Transfer Effects of Bubble Streams Rising near Vertical Electrodes*, **AICHE J.**, **34** (1988), 1981.

#### **Mass-Transfer to Gas-Evolving Electrodes**

- [144] Alkire, R. and P-Y. Lu, *Effect of Hydrogen Evolution on Current Distribution During Electrodeposition at Vertical Electrodes*, **J. Electrochem. Soc.**, **126** (1979), 2118.
- [145] Chen, S. F. and T. J. O'Keefe, *Enhanced Mass-Transfer in Electrogalvanizing Systems by Hydrogen Evolution*, **Electrochimica Acta**, **33** (1988), 789.
- [146] Churchill, S. W., *A Comprehensive Correlating Equation for Laminar, Assisting, Forced and Free Convection*, **AICHE J.**, **23** (1977), 10.
- [147] Economou, D. J. and R. C. Alkire, *Two-Phase Mass Transfer in Channel Electrolyzers with Gas-Liquid Flow*, **J. Electrochem. Soc.**, **132** (1985), 601.
- [148] Fouad, M. D. and Gouda, *Natural Convection Mass Transfer at Vertical Electrodes*, **Electrochimica Acta**, **9** (1964), 1071.



- [149] Fouad, M. D. and N. Ibl, *Natural Convection Mass Transfer at Vertical Electrodes under Turbulent Flow Conditions*, **Electrochimica Acta**, **3** (1960), 233.
- [150] Fouad, M. D. and G. H. Sedahmed, *The Effect of Gas Evolution on the Rate of Mass Transfer at Vertical Electrodes*, **Electrochimica Acta**, **17** (1972), 665.
- [151] Fouad, M. D. and G. H. Sedahmed, *Mass-Transfer at Horizontal Gas-Evolving Electrodes*, **Electrochimica Acta**, **18** (1973), 55.
- [152] Gijssbers, H. F. M. and L. J. J. Janssen, *Distribution of Mass-Transfer over a 0.5-m-tall Hydrogen-evolving Electrode*, **J. App. Electrochem.**, **19** (1989), 637.
- [153] Higbie, R., *The Rate of Absorption of a Pure Gas into a Still Liquid During Short Times of Exposure*, **Trans. AICHE**, **31** (1935), 365.
- [154] Ibl, N. and R. H. Muller, *Studies of Natural Convection at Vertical Electrodes*, **J. Electrochem. Soc.**, **105** (1958), 346.
- [155] Ibl, N. and J. Venczel, *Untersuchung des Stofftransports an Gasentwickelnden Elektroden*, **Metalloberfläche**, **24** (1970), 366.
- [156] Janssen, L. J. J., *Mass Transfer at Gas-Evolving Electrodes*, **Electrochimica Acta**, **23** (1978), 81.
- [157] Janssen, L. J. J. and E. Barendrecht, *The Effect of Electrolytic Gas Evolution on Mass Transfer at Electrodes*, **Electrochimica Acta**, **24** (1979), 693.
- [158] Janssen, L. J. J. and J. G. Hoogland, *The Effect of Electrolytically Evolved Gas Bubbles on the Thickness of the Diffusion Layer*, **Electrochimica Acta**, **15** (1970), 1013.

- [159] **Ibid.** Part II, *Electrochimica Acta*, **18** (1973), 543.
- [160] Roald, B. and W. Beck, *The Dissolution of Magnesium in Hydrochloric Acid*, **J. Electrochem. Soc.**, **98** (1951), 277.
- [161] Rousar, I., V. Cezner, et al. *Transfer of Mass or Heat to an Electrode in the Region of Hydrogen Evolution, I. and II.*, *Electrochimica Acta*, **20** (1975), 289 and 294.
- [162] Ruckenstein, E. and Rajagopalan, R., *A Simple Algebraic Method for Obtaining the Heat or Mass Transfer Coefficients under Mixed Convection*, **Chem. Eng. Comm.**, **4** (1980), 15.
- [163] Shah, A. and J. Jorne, *Mass-Transfer under Bubble-Induced Convection in a Vertical Electrochemical Cell*, **J. Electrochem. Soc.**, **136** (1989), 144.
- [164] Sides, P. J. Phenomena and Effects of Electrolytic Gas Evolution, **Modern Aspects of Electrochemistry**, **18** (1986), 303.
- [165] Stephan, K. and H. Vogt, *A Model for Correlating Mass-Transfer Data at Gas-Evolving Electrodes*, *Electrochimica Acta*, **24** (1979), 11.
- [166] Vogt, H., *Gas-evolving Electrodes*, **Comprehensive Treatise of Electrochemistry**, **6** (1983), 445.
- [167] Wragg, A. A. *Free Convection Mass Transfer at Horizontal Electrodes*, *Electrochimica Acta*, **13** (1968), 2159.
- [168] Zuber, N., *Nucleate Boiling. The Region of Isolated Bubbles and the Similarity with Natural Convection*, **Int. J. Heat Mass Transf.**, **6** (1963), 53.

## Appendices

## Appendix A - Fabrication of the Microprofiled Electrode

### A.1. Mask Design and Process Sequence

The design of the Micro-profiled Electrode (MPE) was accomplished as a master's project by the present author; various process and layout considerations are discussed in detail in [32]. The description in this appendix will focus on the adopted fabrication steps used in our work, shown in Fig. A.1.

The MPE consists of two layers. The first is the underlying substrate, which is a polished copper square. The copper is 5.0 mm thick and 6.0 cm on a side. The polishing was done with successively finer grades of sandpaper, then, with the use of a special jig, it was continued on nylon embedded with 6  $\mu\text{m}$  and 1  $\mu\text{m}$  diamond paste and a Buehler lubricant. The polishing yielded a surface with a peak-to-peak roughness ranging from 0.15 to 0.30  $\mu\text{m}$ , and no scratches deeper than 2  $\mu\text{m}$ .

After polishing, the copper was degreased and dipped in concentrated sulfuric acid to remove any oxides. Rinsing under clean room conditions prepared the substrate for the second process step, evaporation of a  $\mu\text{m}$ -thick layer of gold on the active side. The gold was evaporated in a Veeco 401 evaporator.

The second layer of the MPE is the one which contains micron-sized surface features. The nodules and artificial striae are created through a combination of micro-photolithography and pulse-plating of gold in the holes in the photoresist. Figure A.2 shows the whole mask layout, where each of the 32 electrodes has a distinct pattern. The gray regions represent areas with high nodule density, with a separation of 40  $\mu\text{m}$ . This is not resolved on the computer plot, so that a gray area appears in the figure.

The original process sequence envisioned using a process called lift-off to define the nodule layer. In lift-off, after the photoresist is exposed and developed, a second metal layer is evaporated. Where the photoresist has been removed the metal contacts the substrate, while the remainder deposits on the polymer. The resist is then removed

with acetone, and the metal not adhering to the substrate is supposed to flake off, leaving behind the desired pattern. The first attempts to use evaporation as a means to prepare the noded surface met with no success. The MPE, as originally conceived, was to be made of platinum, but the evaporation of this high melting-point metal proved to be an obstacle. The platinum formed a eutectic with the tungsten boats which are heated during the process. The boats melted before any appreciable amount of platinum was evaporated.

As a consequence, gold was chosen as the preferred substrate material. It has a low melting point, and has the added advantage that, unlike platinum, it does not enhance the hydrogen co-evolution rate substantially. Zinc forms an under-potential deposition layer on gold and also forms an alloy. The surface, therefore, is covered by zinc before bulk deposition begins. In spite of gold's manifest advantages, lift-off was also not successful for the desired 2.0  $\mu\text{m}$  film thickness. The gold was too malleable and peeled off, detaching the bumps after dissolution of the photoresist layer.

#### *A.2. Pulse-plating*

As an alternative to evaporation, pulse-plating of gold was employed to obtain the desired nodules. One considerable advantage is the ability to modify the shape of the deposited bump by varying the current distribution over the exposed substrate. Dry processes may have left nodules which were far from hemispherical, with sharp edges which would distort the current distribution during experiments on zinc striation emergence.

A gold-covered copper square was again used as the underlying substrate, spun with a 5- $\mu\text{m}$  thick photoresist and patterned photolithographically. The gold-covered copper was then immersed in a proprietary Engelhard gold cyanide acid-process electrolyte, which has a solution pH of five [122]. A pulsed current of 100  $\mu\text{sec}$ . on-time and 1 msec. off-time was used. Most of the 30 mA total current flowed to the exposed

backside of the copper square, but the current density was uniform on both sides [121]. For a thickness of 2.5  $\mu\text{m}$ , forty-two minutes of deposition time was required. The morphology of the resulting nodule was quite hemispherical, although somewhat rough on the sub-micron scale. It is important to cathodically polarize the copper before immersion, since a cementation reaction exchanging copper and gold may occur otherwise. In one run, the electrolyte changed color as copper was dissolved. The temperature of the bath was 45 °C.

After plating, the resist was removed from the substrate, SEM photos of the surface taken, independent width measurements made on a Vickers optical microscope, and then the electrode was coated with a protective layer of resist prior to dicing [124]. Fig. A.3 and A.4 show photographs of the finished MPE electrodes.

### *A.3. Electrodissolution Machining*

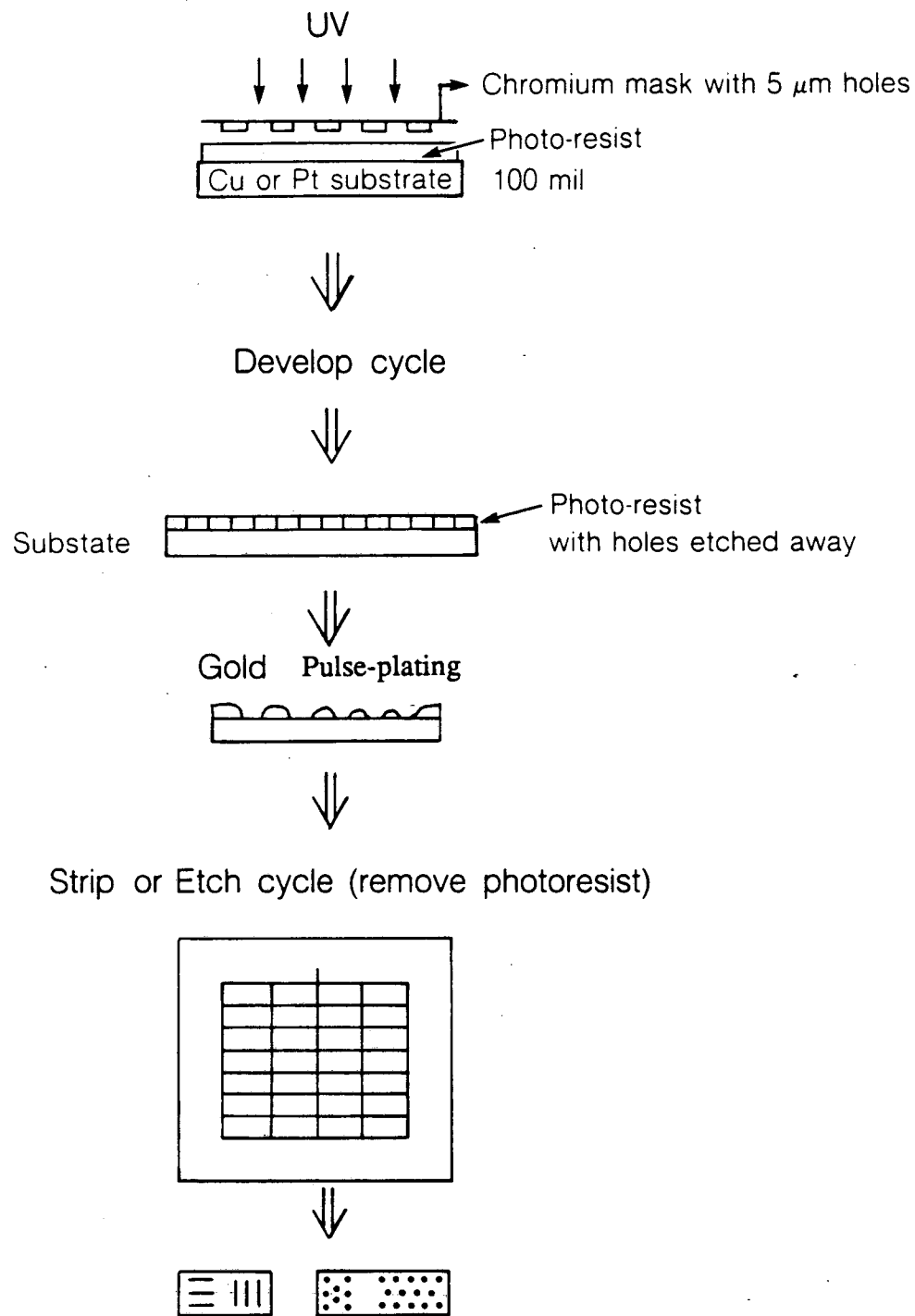
A variety of techniques were explored to dice the individual profiled electrodes, including a variety of saws, as well as dissolution machining. The saws suffer from the disadvantage that they either have difficulty in cutting the 5mm-thick copper plate, or would have left a burr and other defects on the surface. An attempt at careful sawing left an erratically wide street, with the electrodes non-uniform in size and somewhat skewed in shape. The final alternative was to use spark erosion machining where large current pulses are passed between a thin wire and the substrate. The cost of this process was considerably higher than that of alternatives, but no burrs were evident on the sectioned electrodes and the street was even and equal in size to the design specifications. The spark erosion machining was done with the EDM machine in the Lawrence Berkeley Laboratories (LBL) machine shop by the shop staff.

The LBL machine shop also built the replaceable Teflon holders which housed the MPE substrates. A brass core is surrounded by a Teflon plug with a hole in the top for insertion of the MPE. Contact is made by silver epoxy injected into the small

opening to the side of the MPE.

#### *A.4. Reusability*

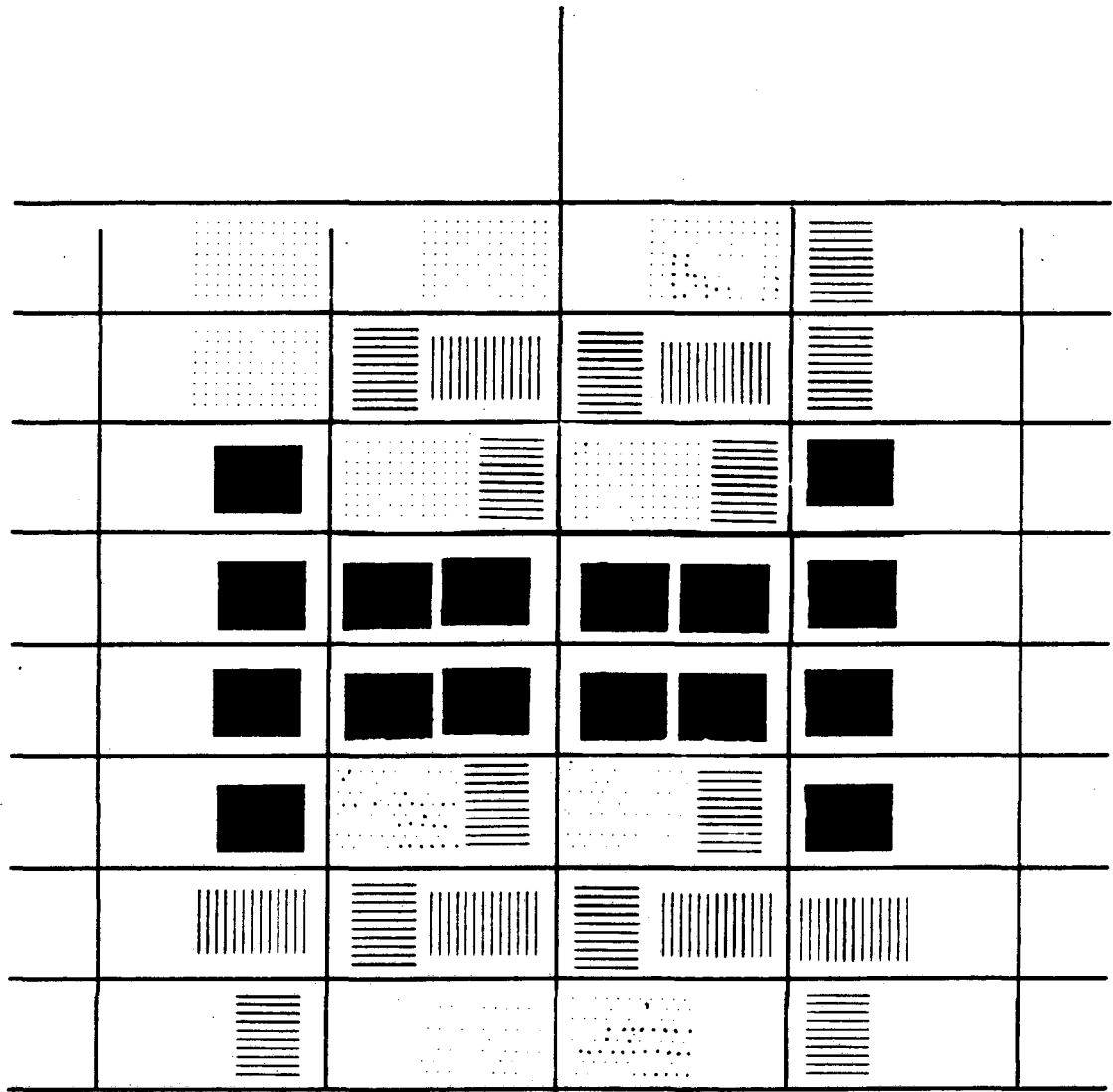
It was originally conceived that the MPE would prove to be a permanent surface on which to carry out studies of the zinc deposition process. This proved not to be the case. Substantial alloying occurs between the zinc deposit and the gold substrate, as well as between the gold layer and the underlying copper. Upon dissolution, either by anodization or by immersion in 1M sulfuric acid, the profiled pattern is often severely damaged and the surface is pock-marked. Adequate adhesion between the gold and copper is rarely maintained after dissolution of the zinc deposit. As a result, these substrates were not reused.



XBL 869-11683

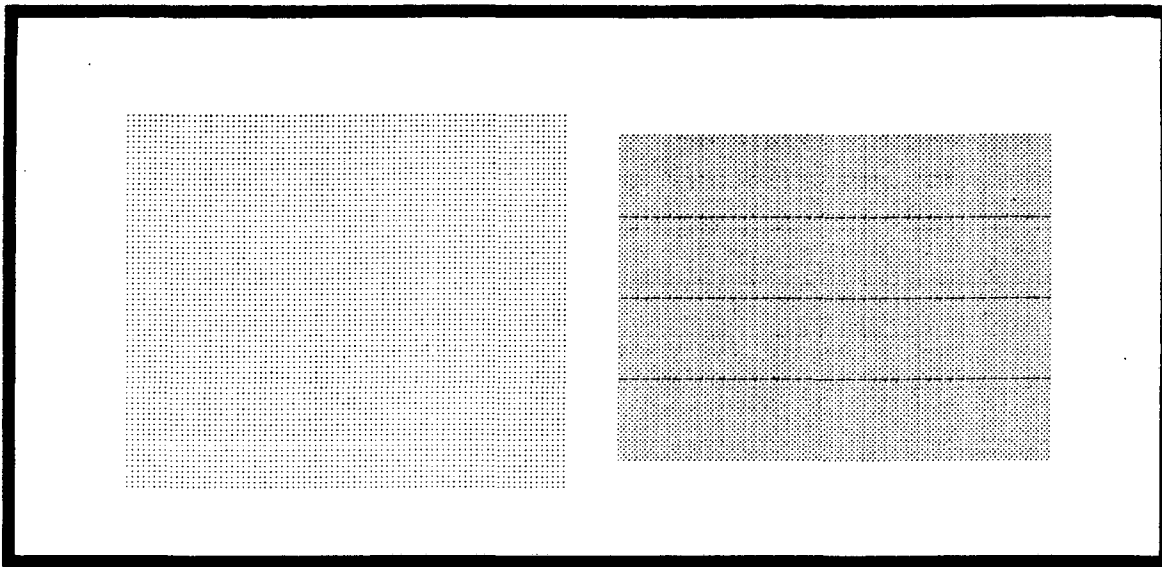
Figure A.1. Fabrication sequence for the micro-patterned electrode (MPE).





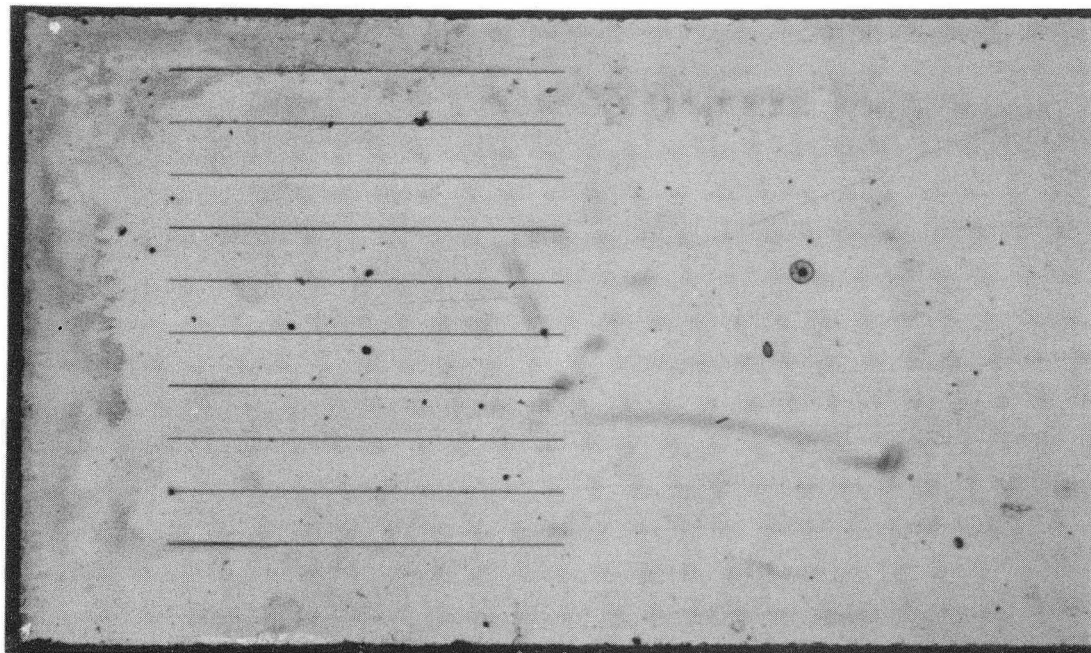
XBL 8611-4777

Figure A.2. Mask layout for the micro-patterned electrode. There are 32 dies, with eight separate patterns. The dark squares are regions with tightly-packed arrays.



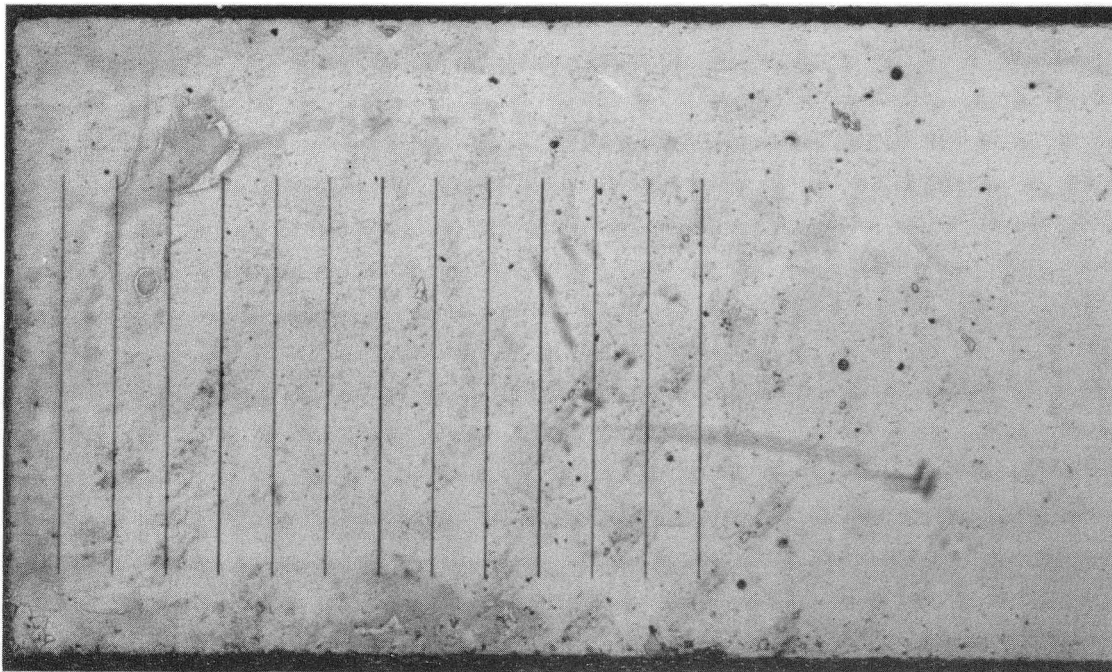
XBL 868-3205

Figure A.3. Mask layout for a single micro-patterned electrode with a set of densely-packed arrays, one is square-pitched; the other is triangular-pitched.



1mm

Ridges aligned with flow



1mm

Ridges perpendicular to flow

Fig. A.4 Micro-profiled electrodes with artificial ridges aligned with and perpendicular to the flow direction. The ridges are 3  $\mu\text{m}$  tall, and 20  $\mu\text{m}$  wide, spaced 250  $\mu\text{m}$  apart. CBB909-7760A

## Appendix B: The Fabrication of a Redesigned Micro-mosaic Electrode

### B.1. *The Redesigned Mask Set*

The experiments described in Part II required the design of a new micro-mosaic electrode (MME) which can resist corrosion in acidic media and has additional satellite electrodes allowing the evolution of multiple bubble columns parallel to each other. Similar to the earlier design by Dees [144], the redesigned micromosaic electrode consists of a square 10 x 10 array of platinum microelectrodes 98 microns on a side, surrounded by a 25 mm<sup>2</sup> platinum buffer segment, integrated on a silicon wafer. The buffer region also contains embedded, but electrically isolated, satellite segments from which bubbles may be evolved. To supply current to the individual segments, an underlying aluminum layer is patterned so that each electrode is connected to its own individual edge pad. The aluminum is then coated with a dielectric material, over which the platinum segments are fabricated in the center of the silicon wafer. Contact is made between the two layers by a small via into which titanium is deposited.

The redesign involved substantial changes in the fabrication sequence. All processing for the new mosaic was carried out by the author in the Microfabrication Laboratory at U.C. Berkeley, a class 100 clean room facility. The original micro-mosaic, fabricated by Hewlett-Packard and Bell Labs [144], was hampered by the use of chromium interlayers and SiO<sub>2</sub> as a passivating layer over the aluminum. The SiO<sub>2</sub> layer was apparently permeable to the electrolyte, which led to corrosion of both the chromium and the underlying Al wire layer [144,158]. The original masks were not suitable for re-use, since they lacked alignment marks and depended on an outdated process involving negative photoresists which are substantially less dependable than the positive resists used in Microlab. The old masks also had two flaws which caused two stillborn (open) segments per micromosaic. The differences between the old and new designs are summarized in Table B.1.

The new mask set has six separate masks, consisting of two aluminum layer masks, one contact mask, two buffer and pad masks, and one milling mask for electrode definition. The masks were laid out using .xkic on a Sun workstation, an interactive graphics program for mask-making [123]. The geometries had to be changed, since the pattern generator used in Microlab has difficulty with non-"manhattan" features (manhattan geometries are those which have only right angles) [124]. Fig. B-1 shows the layout when the masks are superimposed on each other. The bottom layer which connects the large edge pads on the periphery to the central region is most clearly seen. This layer is fairly coarse, with the line width equal to 50 microns. Fig. B-2 through B-4 show details of the center region. Fig. B-2 shows the second mask which connects the coarse aluminum lines to the underside of the individual elements of the micro-electrode array. Fig. B-3 shows the rest of the central masks, including the buffer, the contacts, and the milling-line mask. Fig. B-4 illustrates the vias (small dark squares) that provide electrical contact between the underlying aluminum layer and the overlying platinum segments.

## *B.2. Process Sequence*

The processing used standard silicon technology to create a corrosion-resistant multi-level structure. The minimum feature size was 4 microns, which is fairly conservative [125]. Contact printing was used since the size of the entire die was well outside the limits allowed by reduction exposure. A combination of sputtering, low-temperature plasma-enhanced chemical vapor deposition (CVD), reactive ion etching (RIE), and liftoff were used during fabrication. The entire sequence given in Table B.2 consists of forty-four process steps, and uses six separate lithographic masks.

While many of the process steps are standard, fabrication of this multi-layered structure requires a large number of individual stages, each with a probability of catastrophic (irreparable) failure. If the probability that a wafer is damaged, improperly

processed, or breaks at any step is just 1%, the yield after 44 steps will be 64% of the original total. If the probability of catastrophic failure is 3%, then the yield falls to 26%. Our yields were five out of twenty-two wafers (23%) for our first batch, and a much improved eleven out of twenty-four (46%) for our second batch. Approximately one-third of the losses occurred during the lift-off process, while another 20% of the wafers were broken by malfunction of the automatic lithographic equipment, beyond the direct control of the operator. The other half of the losses were caused by inaccurate processing, dropped wafers, and during process development involving especially the first batch.

The rest of this section will describe parts of the process that were non-standard and involved optimization or development by the author. Results of corrosion tests and resistivity measurements are also given. A more thorough process guide is the Micro-lab manual [124], which details each piece of equipment individually, or a textbook such as Wolf and Tauber [125]. Table B.3 gives a list of the equipment used to build the in-house MME, and a synopsis of the various equipment functions.

### B.2.1 *Insulating Underlayers and Aluminum Line Definition*

P-type silicon wafers, four inches (10.16 cm) in diameter with <100>-orientation, were used as substrates for the electrode fabrication sequence. To insure that no current passes through the semiconducting silicon during experimentation, two thick insulating films were first grown on the wafer surfaces in Tylan furnaces by CVD. The first film, 1 $\mu$ m-thick SiO<sub>2</sub> was formed using a standard steam oxidation recipe, SWETOXB. Silicon nitride (Si<sub>3</sub>N<sub>4</sub>) was then grown on top of the oxide layer as a second passivating film; a choice made primarily because of its superior moisture resistance. The process was done using the SNITC recipe, which grows a nitride film at 800 °C. It requires almost three hours of furnace time, plus an additional hour for the slow ramp-up to the desired temperature. These two CVD processes are standard, but

are among the most costly steps in the fabrication sequence; processing in a batch of 24 wafers reduces the per-wafer cost significantly. The yield is about 95%: some wafers crack as a result of the heating and cooling, which induces stress.

The next steps involve micro-photolithography using Masks 1 & 2 to define the aluminum wire layer which conducts current from the external bonding pads to the micromosaic elements. The first aluminum layer is created subtractively, by wet etching a continuous sputtered film in warm (50 °C) phosphoric acid. Sputtering is done in a CPA assembly where trays containing nine wafers are carried on a track, and passed under a target which is being continually sputtered at a constant rate. The deposition thickness is adjusted by changing the track speed; the deposition constant in the micro-lab system is calibrated weekly, and averages  $83,000 \text{ ( \AA of Al * } \frac{\text{cm}}{\text{min}} \text{ track speed)}$ . The sputtered aluminum film is partially covered with a patterned photoresist layer. Photoresists are photo-active, acid-resistant polymers, and are used in lithography to transfer an image from a mask onto the substrate wafer. Areas that are to remain intact, with no etching of the underlying aluminum, are protected by the resist. After wet etching, the photoresist is easily removed with acetone, and the wafer is then rinsed in distilled water until the resistivity of the water is over 10 M $\Omega$ .

The second layer is formed additively by a process known as "lift-off." The mask with fine aluminum wires is precisely aligned to the coarse layer after a new photoresist layer has been spun on the wafer. The process is facilitated by alignment marks (open crosses inside large boxes) in the upper right and lower left portions of the mask. Fig. B.5 shows the alignment mark both before and after addition of the second aluminum layer. The top photo (Fig. B.5a) shows an unused alignment cross, while the next two show precise alignment and the maximum tolerated misalignment, respectively. The small misalignment in the third cross leads to the placement of connecting boxes at the edge of the underlying coarse aluminum line, as seen in Fig. B.5d.

After alignment, the wafer is exposed and developed in the usual manner, leaving holes in the photoresist where the fine lines should go. Aluminum is then sputtered over the patterned photoresist. Where the photo-active polymer was removed, the sputtered film adheres to the substrate, while elsewhere it lands on top of the photoresist. When the resist is dissolved in acetone, the non-adherent aluminum flakes off, or may be peeled off as a non-adherent film. Unfortunately, when the thickness of the sputtered film is larger than 25% of the resist height, bridging may occur between the aluminum adhering to the substrate, and that lying on top of the polymer. If that is the case, after the photoresist is dissolved in acetone, the aluminum film stays behind, especially in the gap between two thin lines.

The best method to avoid bridging involves use of chlorobenzene as a resist hardener before the exposure process. Dipping the entire wafer in chlorobenzene changes the degree of polymer cross-linking in a region near the surface, but does not change its characteristics at some distance from the surface. Greater cross-linking decreases the resist sensitivity to light, and means that a ledge near the surface is formed at the edge between the exposed and unexposed regions after development. This overhanging ledge prevents bridging, but the addition of the chlorobenzene step adds complexity to the process sequence. Each wafer must be individually dipped in petri dishes placed in a laminar-flow hood, and care must be taken to prevent inhalation of the volatile, carcinogenic organic compound. The main advantage of using 4" wafers is their compatibility with the automatic lithographic equipment such as the Eaton resist dispenser and the MTI omnichuck. This time-saving advantage is eliminated when manual processing is used instead. Manual processing also introduces inhomogeneities in the individual behavior of electrodes, since bake times, resist thicknesses, and development times are no longer standardized as carefully.



Care must also be taken to prevent heating the photoresist to temperatures above 150 °C (some operators feel that Shipley 1400J has a greater temperature resistance than KTI resist, although no difference was discerned in our work). If the polymer temperature exceeds this value, as may occur during sputtering or exposure to high-energy plasmas, acetone will no longer act as a solvent. In this case, aluminum adhering to this recalcitrant photoresist will not "lift-off." One should deposit only a portion of the desired 5000 Å aluminum layer thickness in each pass, since the photoresist cannot cool off in the evacuated sputtering chamber. Cooling is accomplished most efficiently by venting a side load-lock to atmospheric pressure.

If only a portion of the photoresist becomes acetone-insoluble, a film remains on the electrode surface after lift-off. This film can be removed by plasma-ashing: exposing the carbon-rich photoresist to a low-power (80 watt) oxygen plasma at **high** partial pressure for fifteen minutes. The carbon is volatilized as CO<sub>2</sub>, and the surface is thereby cleaned.

Figure B.6 shows micro-photographs of the fine aluminum layer at different magnifications. Figure B.6A is an overview of the central region showing the 110 separate Al lines, while Figure B.6B illustrates the closest approach (~6 μm) between adjacent lines (10 μm wide). Several imperfections may appear: exogenous defects such as dust or endogenous ones such as mask or layout errors. The two types are seen in top and bottom of Figure B.7, respectively. While dust particles are usually not a problem in the Class 100 clean room facilities at the Microlab, the MME suffers from a disadvantage relative to most chip designs. While a typical wafer has forty dies on it, our wafers have only a single pattern, and the entire pattern must be error-free for the MME to work properly. The MME is 5 cm across, and the line-lengths are also 5 cm or longer, so that a dust particle landing on any portion of this line will cut the connection between periphery and the segmented electrode. If a single segment does not pass current, data is lost on the inoperable array element, and the local concentration field at

the electrode surface is altered. The reactant concentration at a working MME electrode held at a potential in the limiting current regime is close to zero, but is increased over a non-operating micro-electrode. As a consequence, the eight adjoining segments also collect more current than they otherwise would and the current distribution on the MME becomes distorted. If the MME loses more than 10% of its individual segments, the array is essentially useless. The mask errors on the redesigned masks are comparatively trivial, since they do not lead to the creation of open segments. Small indentations, such as those seen in Fig. B.7, may change the line width slightly, but the measured resistivity difference caused is insignificant.

Visual inspection usually can determine whether electrical contact is adequate. Scratches and other defects (i.e. misalignment, bad liftoff, and bridging between neighboring lines) can all be seen under low-power magnification. Resistivity testing, the results of which are given in Table B.4 for a typical wafer, was delayed until after the platinum overlayer was created. The buffer segment and edge pads make suitable contacts for the resistivity probes; contacting the probes directly to the thin aluminum layer results in heavy damage.

At this point, the wafers can no longer be processed in a large batch, because of the space limitations in the thin-film vacuum apparatuses necessary for the growth and etching of the barrier film on top of the aluminum layers. In retrospect, it may be appropriate to cut the wafers down to the size of the electrode at this point in the process, since this increases the number that can be processed simultaneously in the CVD and RIE chambers from four to seven. The advantages of automatic lithographic processing are lost, but this is compensated by the fact that the alignment of Mask 4, the contact holes through the nitride barrier, is more easily accomplished on the smaller, diced wafers. The dicing was actually done after the Ti sputtering step, however.

After lift-off of the aluminum, a visual inspection or triage determined those wafers that merited further treatment. They were passed on to the plasma-CVD step, while the rest were used for testing, process development, or were recycled by etch-back of the Al film. A curious problem occurs after etch-back, however: the original pattern of the MME aluminum lines becomes imprinted in the  $\text{Si}_3\text{N}_4$  layer, as the warm 50 °C phosphoric acid is also a weak  $\text{Si}_3\text{N}_4$  etchant. This "ghost" pattern is an interference color difference caused by the variable thickness of the underlying  $\text{Si}_3\text{N}_4$ . Performance is not affected by the appearance of this "ghost" pattern.

### B.2.2 Plasma-Enhanced CVD of $\text{Si}_3\text{N}_4$ and Corrosion Testing

The most important difference in the process sequence between the redesigned micromosaic and the original version consisted of replacing the  $\text{SiO}_2$  insulator with plasma-deposited  $\text{Si}_3\text{N}_4$ . The original  $\text{SiO}_2$  film was porous to electrolyte, and both Dees and Whitney reported serious corrosion problems in the aluminum current-carrying layers. In contrast,  $\text{Si}_3\text{N}_4$  films are impermeable to aqueous solutions if the structure of the film is continuous. This is usually the case for standard, high-temperature CVD processes, but in our case, the aluminum already on our wafer would melt at those conditions. In the presence of non-refractive metals, plasmas are used to selectively energize the vapor phase without heating up the substrate. Free radicals and ionized species form in the plasma and react on the surface, forming a solid phase. As a result, the substrate is heated to only 300 °C, but the film often contains incorporated voids known as "pinholes."

A second problem is that plasma-enhanced CVD is often mass-transport sensitive, so that the deposition rate in the reactor varies by up to 50% with radial and angular position, relative to the gas inlet. Ammonia ( $\text{NH}_3$ ) and silane ( $\text{SiH}_4$ ) are decomposed in the 100W plasma with a 4:1 stoichiometric excess of ammonia to assure complete reaction of the silane, and prevent its venting to the atmosphere (silane is

pyrophoric). A  $1000 \text{ \AA}$  film can be grown in five minutes with mass flow rates of 40 sccm and 10 sccm for ammonia and silane, respectively. To eliminate pinholes that traverse the entire passivating layer, the film is deposited in four stages, each fifteen minutes long. The system is vented between passes, and the position of the wafers in the reactor is changed and they are rotated  $90^\circ$ . After four 15-minute depositions, the passive layer thickness is at least  $1.2 \text{ \mu m}$ , with a variation of less than 10% over the wafer.

The introduction of a multiple-pass deposition sequence virtually eliminated corrosion of the buried aluminum in a hot ( $80^\circ \text{C}$ ) phosphoric acid bath. The most sensitive area for corrosion is at the location of the largest step-height on the wafer. This occurs at the juncture between the first and second Al layers, as illustrated in the schematic cross-section shown in Figure B.8. The thickness of the two aluminum layers on top of each other ranges from  $1.0\text{-}1.1 \text{ \mu m}$ .

Corrosion tests were performed on  $\text{Si}_3\text{N}_4$  films of various thicknesses, to investigate their protective properties. If the film growth were conformal (kinetically-limited by the available surface) and independent of the local composition on the surface (i.e. if  $\text{Si}_3\text{N}_4$  grew on aluminum as fast as on silicon), a thin  $\text{Si}_3\text{N}_4$  layer would be sufficient to protect even topologies with large steps. On the other hand, if the deposition did not cover steps well, a thickness equal to the aluminum height would be needed as a barrier.

For comparison, an unprotected  $0.5 \text{ \mu m}$  Al film was etched in 10-15 seconds. The corrosion tests on the protected films lasted 30 minutes, by comparison. In 30 minutes, silicon nitride will also etch slightly, but not more than  $100\text{-}500 \text{ \AA}$  will be dissolved [126]. This allowed us to determine if any spots were protected only by a very thin layer of nitride, especially below pinholes. Figure B.9 shows the results, a dramatic decrease in corrosion with increasing barrier film thickness. At top, a single  $3000 \text{ \AA}$   $\text{Si}_3\text{N}_4$  layer with pinholes protects the large Al line, but the thin Al wire is completely

dissolved by the acid; only the interference colors of the underlying nitride are visible. A corrosion-front on the edges of the large Al line are visible, as well as circular corrosion spots originating at a sub-micron sized pinhole. Under these conditions, pinholes most often nucleated at the edge between the aluminum lines and the substrate. The middle photo shows the results with a doubly-coated nitride barrier. Tiny pinholes are evident as black dots, but since they do not cross layers (they occur randomly in each, and do not line-up), no corrosion is evident in their vicinity. At the  $1.0\mu\text{m}$  step, corrosion still occurs, cutting the fine Al line and creating an open circuit. The  $6000\text{ \AA}$  nitride film is not conformal enough to cover this step. In the bottom photo, a completely protected step is shown. Four layers ( $3000\text{ \AA}$  each,  $1.2\mu\text{m}$  total) of  $\text{Si}_3\text{N}_4$  were deposited in separate passes over the aluminum layer. Further tests in ferri/ferro sulfate solutions with  $0.5\text{M H}_2\text{SO}_4$  show only a little line degradation after a 24-hour immersion at room temperature. The new MME is thus found to be much more stable than its predecessor.

### B.2.3 Reactive-Ion Etching of $\text{Si}_3\text{N}_4$ Protective Film

The next challenge was to develop an etching technique which would allow patterning of the nitride film but leave the underlying aluminum unaffected. Wet etching of nitride ( $150\text{ }^\circ\text{C}$  phosphoric acid, for example) will completely dissolve the aluminum lines. Reactive-ion etching in a plasma chamber was used as a "dry" alternative. Most dry methods do not have selectivity for nitride over silicon, and only a moderate selectivity for nitride over silicon oxide [126]. In our case, this was not a concern, but serves as an explanation why the microlab did not have a standard nitride RIE process.

The development process used an  $\text{SF}_6$  plasma, a gas available in the general plasma etching system, the Plasmatherm. Etch rates at various powers, 40-100 Watts, and chamber pressures, 50-150 mtorr, were determined by profiling the wafers after a timed exposure to the reactive-ion plasma. As seen in Figure B.10, taken after a five

minute etch at 70 Watts and 60 mtorr, an average of 8000 Å of nitride has been etched, but the etch rate close to the edges is substantially higher. The bottom of the etch trench is also fairly rough, although once the aluminum layer is reached, no further chemical etching occurs. The conditions shown in this figure were chosen to do all subsequent etching, since the rate was slow and uniform enough to determine the required etch time over the entire wafer. Three two-minute runs, with rotation of the wafer between etch cycles, were used as the standard etch for a 1.2 μm plasma-deposited Si<sub>3</sub>N<sub>4</sub> layer.

Etch rate increases quickly with increasing power, and becomes substantially more non-uniform depending on position in the plasma reactor. At 100 Watts, the nitride barrier is etched in much less than a minute, and the underlying aluminum is damaged by physical ion bombardment for the remainder of the etch cycle. Such physical damage was eliminated by increasing the pressure, thereby lowering the mean free path of the ions, and by decreasing the power of the plasma. Fig. B.11 shows the etched profiles of the small center contacts. The lip to the sides of the contact shows the nitride layer covering the step between the bare wafer and the thin aluminum lines. In the center of the line, a contact is etched and the profiles show that all trenches are of uniform depth. The nitride film, in this case, was 0.9-1.0 μm thick.

#### B.2.4 Pt/Ti Sputtering and Milling

The final steps in the fabrication involve the deposition of the metal electrode overlayers, titanium (for adhesion and corrosion protection) and platinum (the active electrode material). Titanium was selected as a via-filling material since it did not corrode in our preliminary testing, where we dipped wafers with patterned metal films in our oxidizing electrolyte. Figure B.12 shows the mask used to pattern the deposited metal films.

Titanium and platinum were both deposited using lift-off, but the process was much simpler than for the fine Al layer. The metal thickness for this step is only 2000 Å and the feature on Mask 5 is a single, large central square. The titanium was deposited in the same CPA assembly as the Al layer, but the platinum was done separately. The CPA does not have a platinum target, since it would have to be several inches wide, and would therefore be prohibitively expensive. A general sputtering system, the Randex, has a wider range of available targets, including platinum, but the deposition area is much smaller in size, requiring individual processing of each wafer.

After Ti and Pt deposition, individual segments are defined by argon ion-milling through a patterned resist layer, using the standard method described in the microlab manual [124]. The milling time should not exceed twenty minutes, or else the photoresist will become insoluble in acetone. Photoresist ashing is helpful in removing the rest of the resist layer. Figure B.13 shows the final electrode cross-section, the top layer being the Pt/Ti film, although substitution of the Pt with another noble metal such as gold is possible. Figure B.14 shows a photograph of a completed mosaic segment.

### B.3 *Summary and Process Alternatives*

A process for fabricating corrosion-resistant micro-mosaic electrodes in the UCB microlab was developed. New positive-resist masks, an improved passivation and via layers, and redesigned geometry characterize the in-house electrode.

Two modifications in the process may improve the performance even more: replacement of the aluminum layer with a new sputtered copper film (a recent improvement in microlab's technology base makes this possible), and replacement of the two wire layer with a single mask. In hindsight, there is no reason why the entire wire layer cannot be deposited in a single step. Contact printing in the mask copier is sufficiently free of vibrations to allow the printing of fine 20 μm lines. This would eliminate the complicated Al lift-off step, and probably improve yields by at least 50 %.

<b>Table B.1: In-house Micromosaic Project</b>		
<b>Differences between Electrode Designs</b>		
<b>Features</b>	<b>Old Electrode</b>	<b>In-House Electrode</b>
<i>Mask Layout</i>		
1	Negative Photoresist	Positive Photoresist
2	No Alignment Marks	Standard Alignment Crosses
3	2 Stillborn Segments	No Mask Flaws
4	Non-Manhattan Geometry	Only Right Angles
5	Thinner Outer Lines	Thick Outer Lines
<i>Processing</i>		
6	3000Angstrom Al Lines	5000Angstrom Al Lines
7	SiO <sub>2</sub> Passivation Layer	Si <sub>3</sub> N <sub>4</sub> Passivation Layer
8	Chromium Adhesion Layer	Titanium Adhesion Layer
9	Single Satellite Segment	5 Parallel Satellite Segments

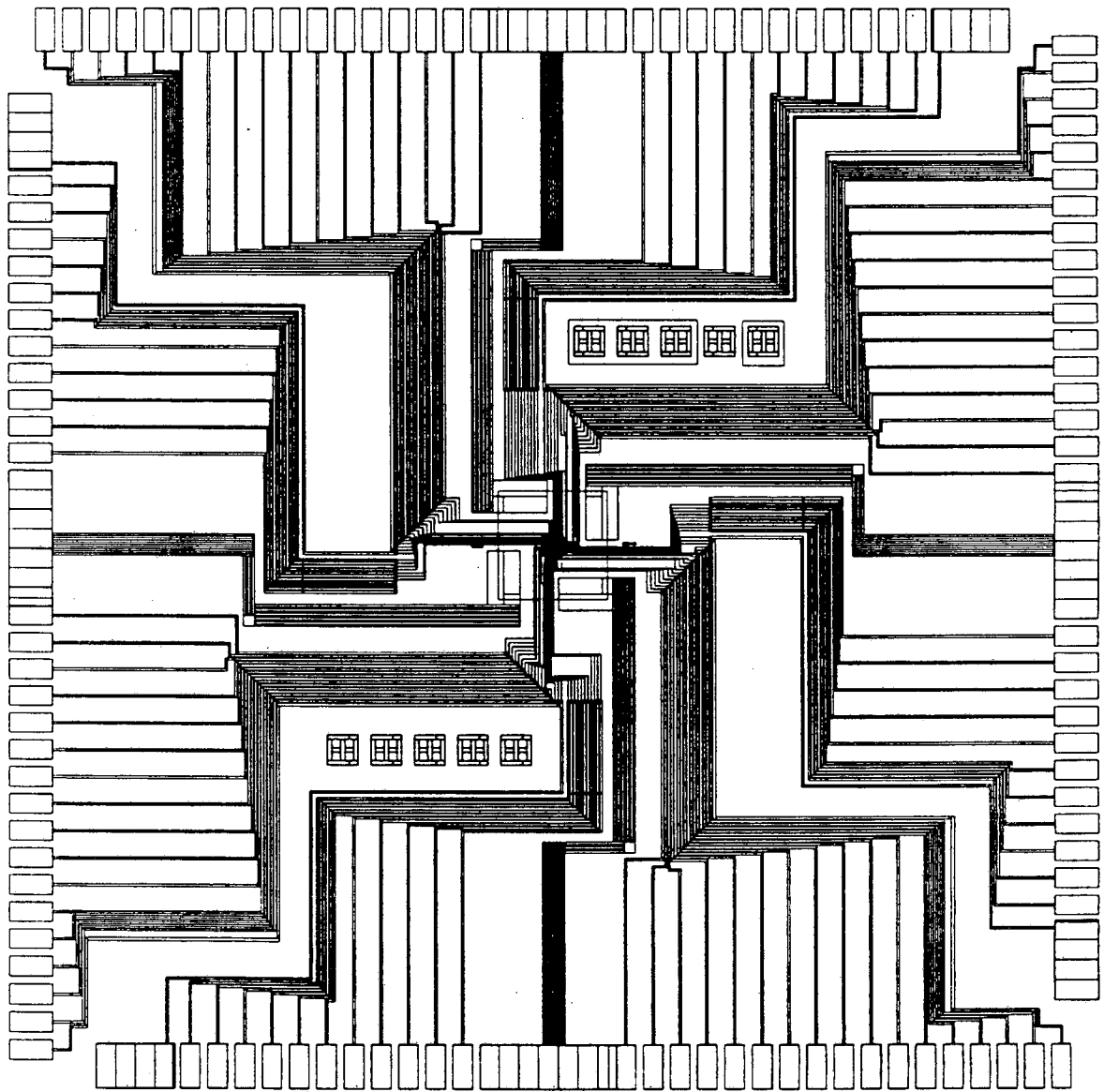


Table B.2: In-house Micromosaic Project	
Process Sequence	
Step	Description
1	Obtain clean <100>-orientation Silicon test wafers.
2	Grow 1 $\mu\text{m}$ of $\text{SiO}_2$ by wet oxidation (SWETOXB) in Tylan furnaces.
3	Grow 8000 Angstroms of thermal $\text{Si}_3\text{N}_4$ (SNITC) in Tylan furnaces.
<i>Mask I.</i>	
4	Sputter aluminum in CPA sputterer, 5000 Angstrom thickness.
5	Lithography; Spin standard KTI on Eaton photoresist dispenser.
6	Use Mask Copier to expose far field (large Al line definition).
7	Develop in MTI omnichuck, program 1; standard KTI develop.
8	Etch the Aluminum in Phosphoric Acid at 50 °C.
9	Remove photoresist in the MTI.
<i>Mask II.</i>	
10	Lithography; Use Shipley 1400J photoresist, spin on Eaton.
11	Bake in oven at 90 °C for five to ten minutes.
12	Dip in chloro-benzene for resist under-cutting.
13	Expose in Kasper contact printer for 6 seconds.
14	Develop by hand with undiluted Microposit developer for 40 seconds.
15	Sputter second 5500 Angstrom Al layer in CPA (Use three passes).
16	Liftoff Procedure:
	a. Carve lines in far field with a razor blade.
	b. Soak wafers in Acetone overnight.
	c. Use ultrasonic agitation to break micro-ridges.
	d. If absolutely necessary, gently use q-tip to remove recalcitrant Al.
	e. Rinse with distilled water and blow dry.
	f. Plasma-ash remaining photoresist in Technics-C (300W, 10 minutes).
17	Triage!! Determine which wafers warrant further processing.
18	Chemical Vapor Deposition of $\text{Si}_3\text{N}_4$ in Technics-B.
	3 passes of 4000 Angstroms $\text{Si}_3\text{N}_4$ each are required to prevent pinholes.

Table B.2: In-house Micromosaic Project	
Process Sequence	
Step	Description
<i>Mask III. (Large Contacts)</i>	
19	Two-step Lithography; Spin KTI photoresist on Eaton.
20	Expose Mask III in Mask copier for 90 seconds on Chrome settings.
21	Develop in MTI for <i>half-time (25 seconds)</i> using Run 40.
22	Check under microscope to see if pattern cleared.
<i>Mask IV. (Small Contacts)</i>	
23	Do not put wafer in white light, align and expose mask IV on Kasper.
24	Use MTI to re-develop wafer, use normal develop run.
25	Hardbake at 120 °C for 20 minutes.
26	Etch Si <sub>3</sub> N <sub>4</sub> layer in Plasmatherm. Text has process parameters.
27	Remove remaining photoresist with Acetone.
28	Use Alpha-step 2000 to measure step heights.
<i>Mask V. (Center Buffer)</i>	
29	Dice the electrode into a square with the Tempress saw.
	This reduces wafer size, and allows simultaneous processing of two wafers in the limited area of the Randex and Ion Mill.
30	Standard Lithography; Spin KTI with Eaton.
31	Expose on Kasper using Mask V
32	Develop in MTI
33	Sputter 2000 Angstroms of Titanium in the CPA
34	Remove photoresist in ultrasonic agitator.
35-37	Repeat 30 - 32 with the same mask.
38	Sputter 2000 Angstroms of Platinum in the Randex.
39	Remove resist and test line resistance with a I-V probe.
<i>Mask VI. (Segment Definition)</i>	
40-42	Repeat 30 - 32 with mask VI.
43	Ion mill trenches between segments.
44	Remove resist, recoat, and expose pads and active area (Mask III). END!.

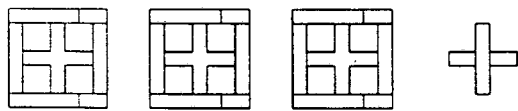
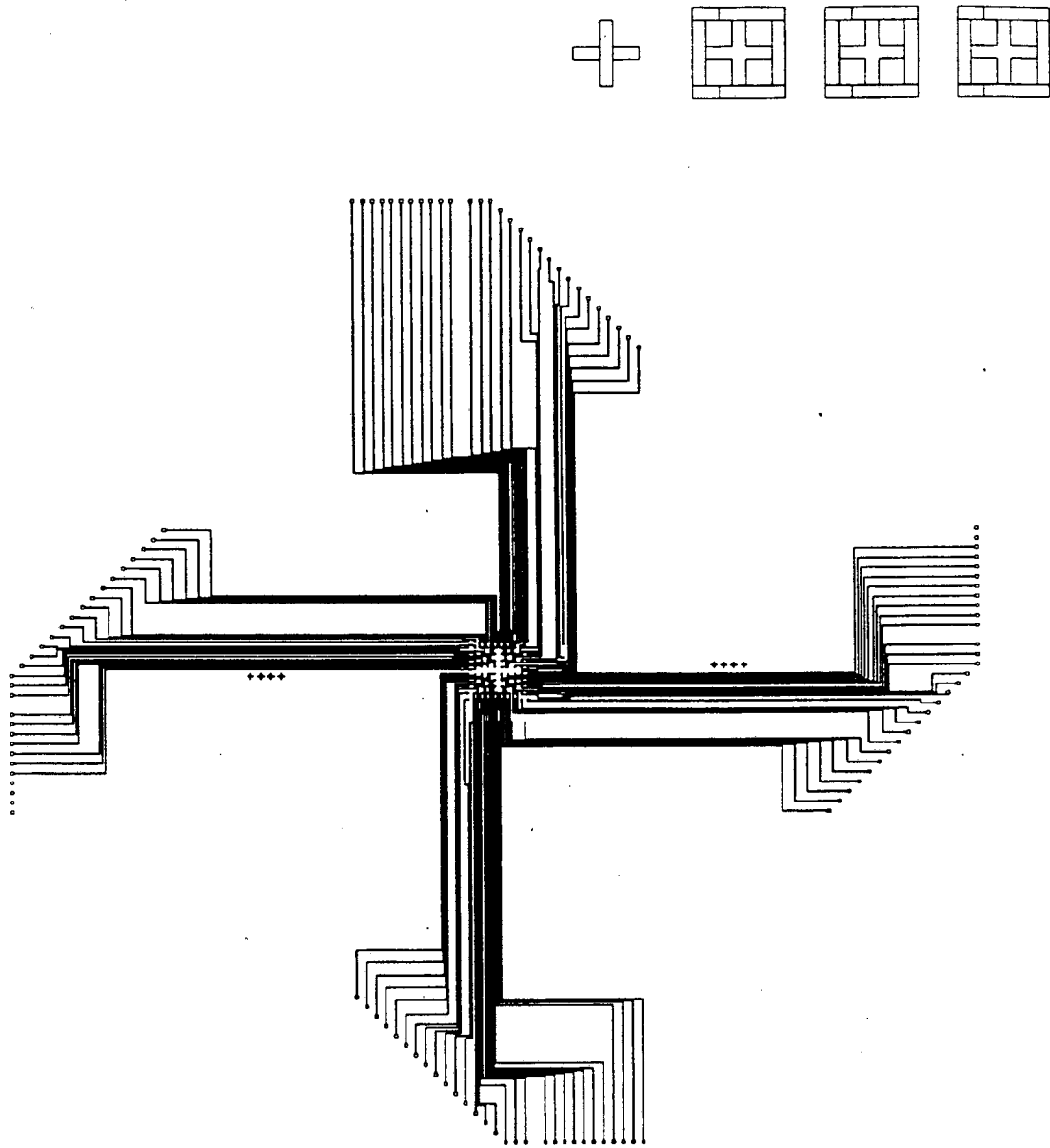
<b>Table B.3: In-house Micromosaic Project</b>		
<b>Equipment List</b>		
	<b>Equipment Name</b>	<b>Function</b>
<i>Process Equipment</i>		
1	Tylan Furnaces	CVD of SiO <sub>2</sub> and Si <sub>3</sub> N <sub>4</sub>
2	CPA Target Sputterer	Aluminum and titanium sputtering
3	Wet Sinks	Al etch, HMDS dip, KOH development
4	Eaton Resist Dispenser	Automated 4" wafer lithographic equipment
5	MTI Omnichuck	Automated development and stripping
6	Y1 Spinner	Manual photoresist spinning
7	YWR Oven	Hardbake of exposed, developed wafers
8	Kasper Contact Aligner	Contact exposure and lithography
9	Mask Copier	Contact exposure for 5" masks
10	Technics A/B	Si <sub>3</sub> N <sub>4</sub> plasma-enhanced CVD
11	Technics C	Photoresist descumming
12	Plasmatherm	Si <sub>3</sub> N <sub>4</sub> reactive ion etching and O <sub>2</sub> plasma ashing
13	Disco Saw	Wafer dicing
14	Randex Sputtering	Platinum sputtering
15	Ion Mill	Electrode definition by Ar ion milling
<i>Analytical Equipment</i>		
1	As200 profilometer	Depth profiling of Si <sub>3</sub> N <sub>4</sub> etching
2	Vickers	Line Thickness Measurements
3	I-V Probe Station	Resistivity Measurements
4	Reichert Microscope	Microphotography

<b>Table B.4: In-house Micromosaic Project</b>	
<b>Resistances to Individual Array Elements</b>	
<b>Electrode Number</b>	<b>Resistance (k<math>\Omega</math>)</b>
1	.217
2	.173
3	.198
4	.247
5	.212
6	.232
7	.263



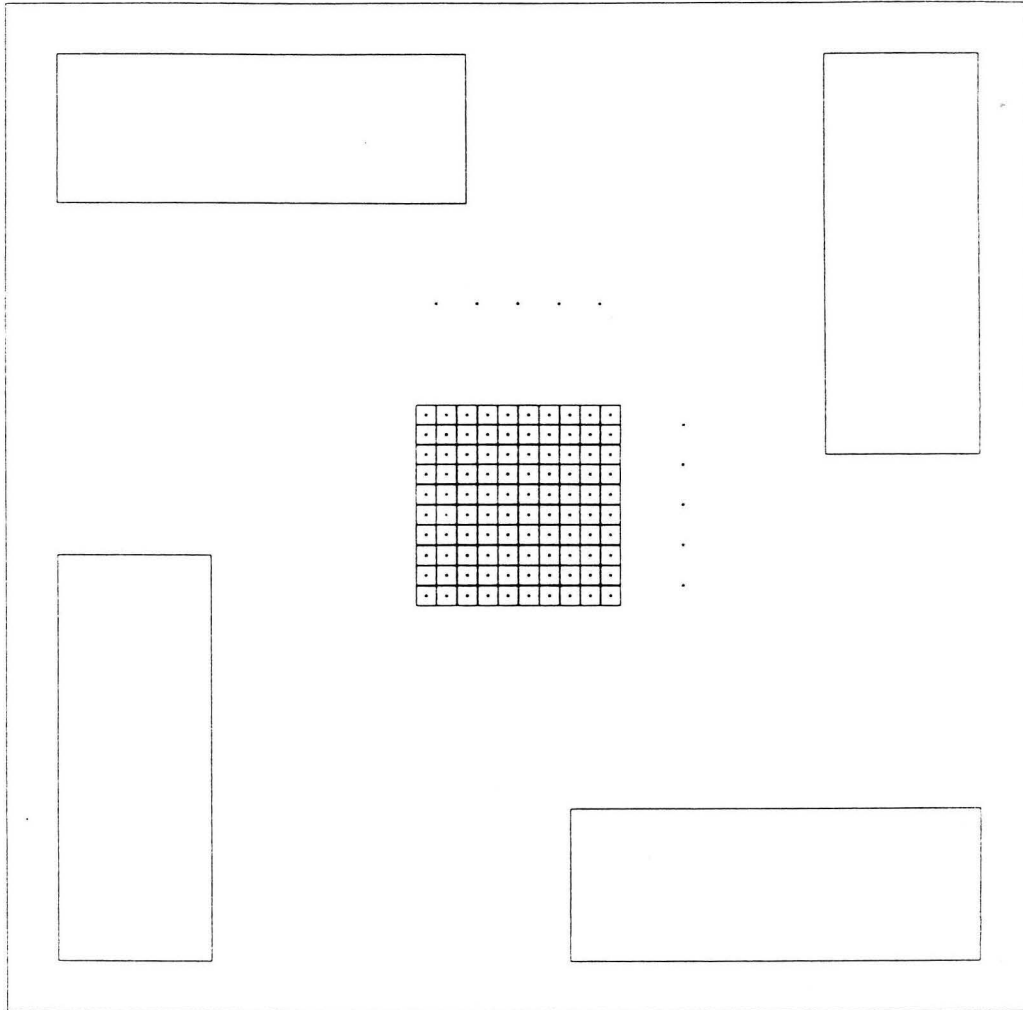
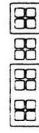
XBL 911-84

Figure B.1. Superimposed mask layouts for the fabrication of the re-designed micro-mosaic electrode.



XBL 911-83

Figure B.2. Mask layout for the fine aluminum wire layer (Mask 2).



XBL 911-81

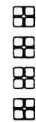


Figure B.3. Mask layouts for the segmented center of the micro-mosaic electrode.

XBL 911-128

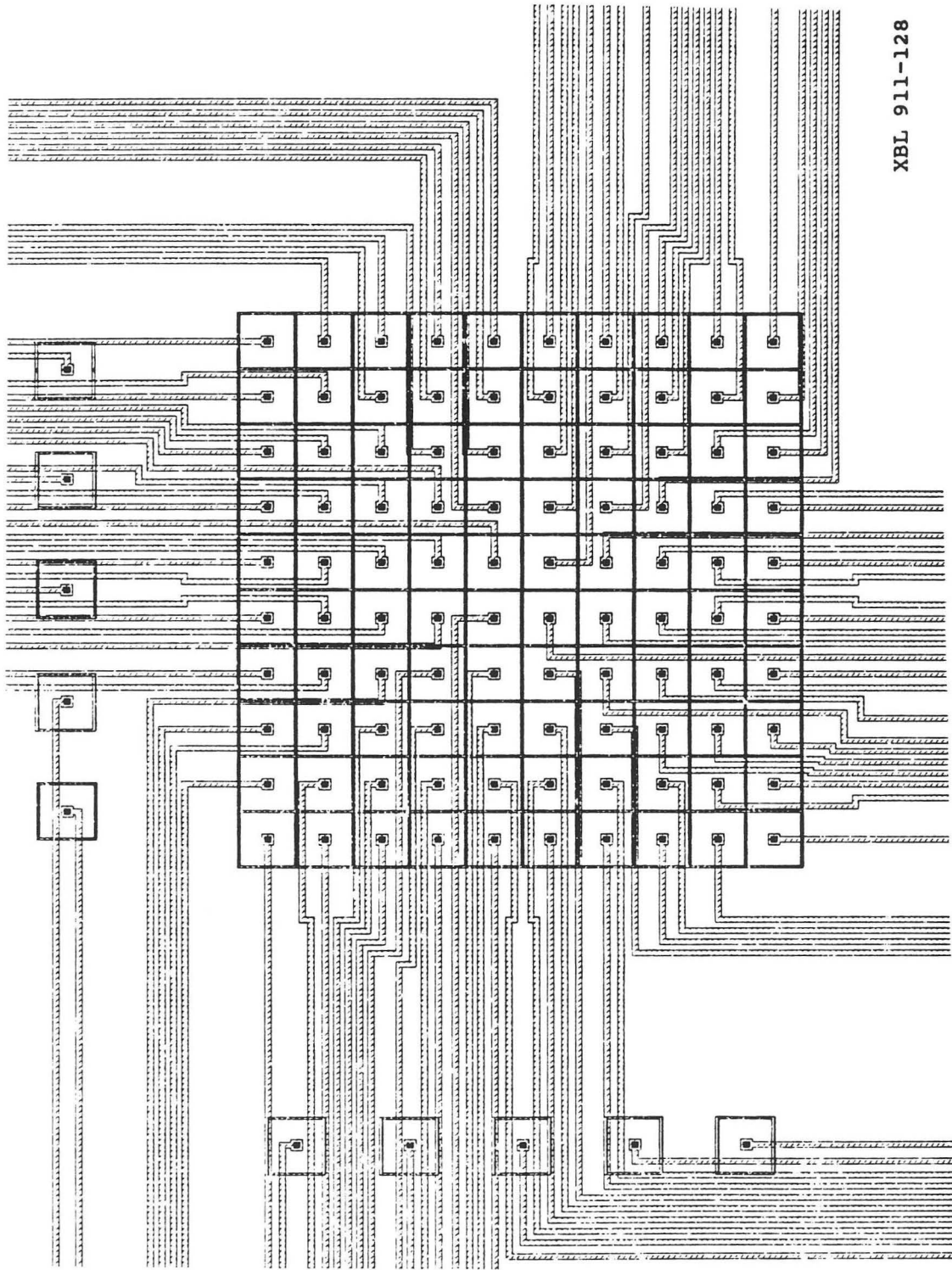
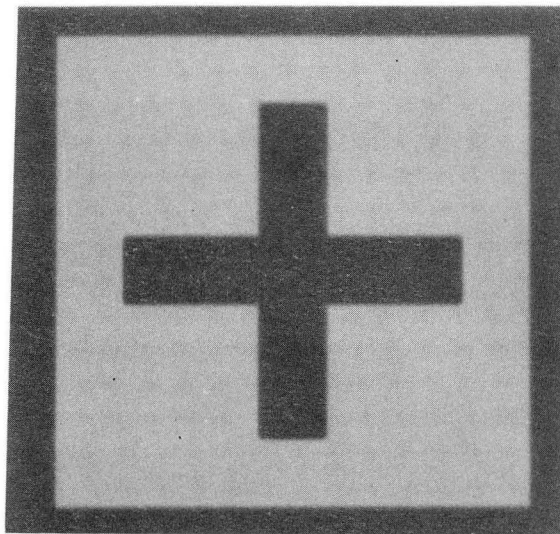
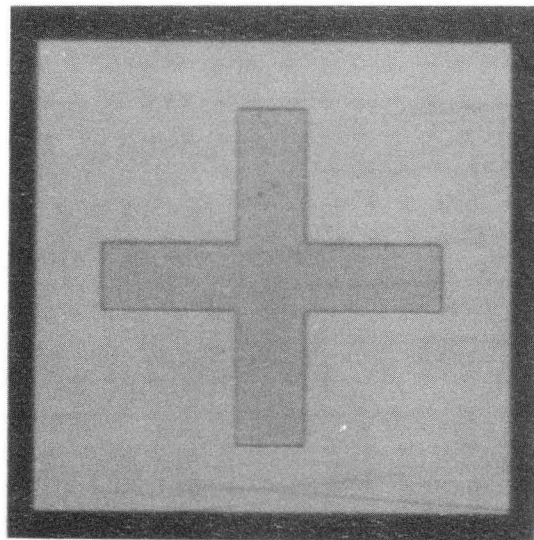


Figure B.4. Schematic of the wiring in the center of the micromosaic electrode.

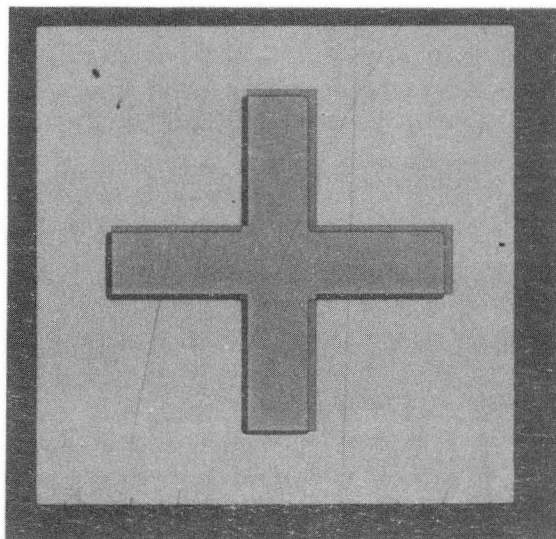




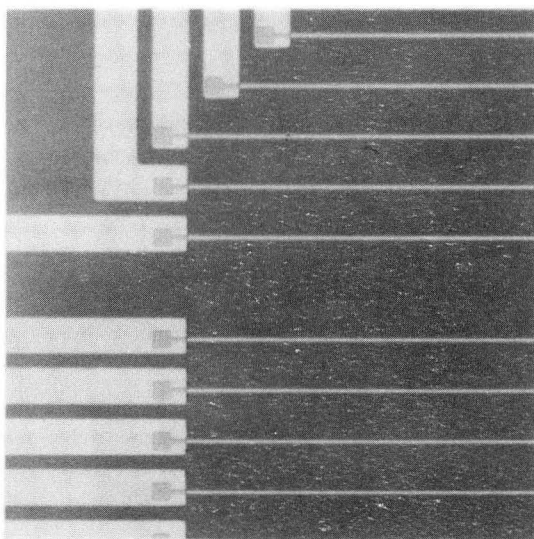
Open alignment mark



Filled alignment mark

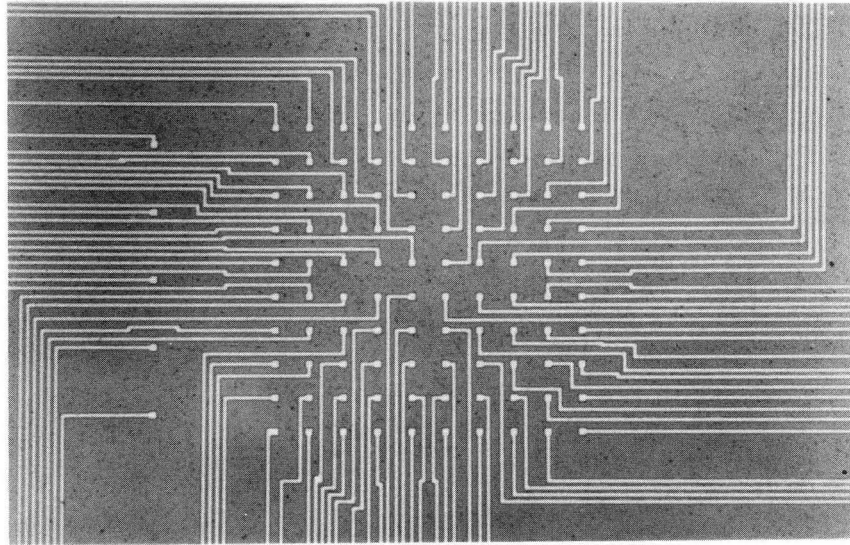


Maximum tolerable misalignment



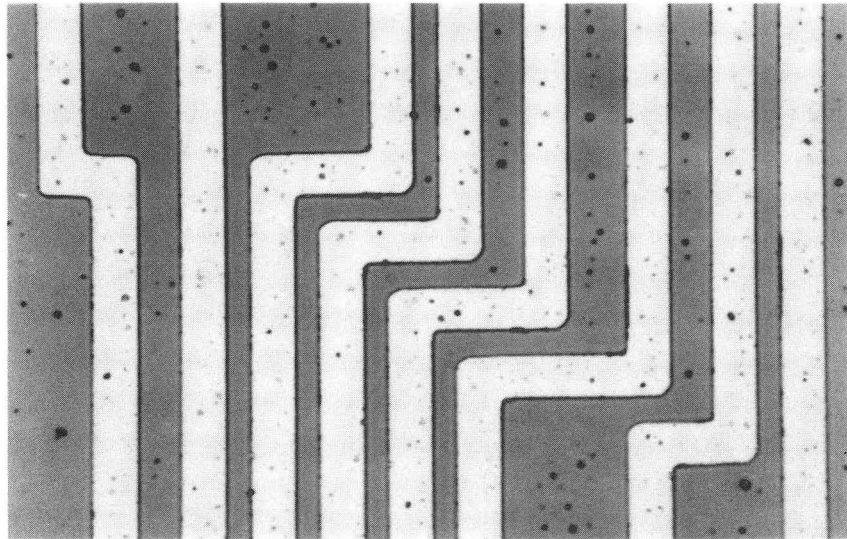
Resulting pad misalignment

Fig. B.5 Coarse Alignment Marks XBB 906-4900A



100  $\mu\text{m}$

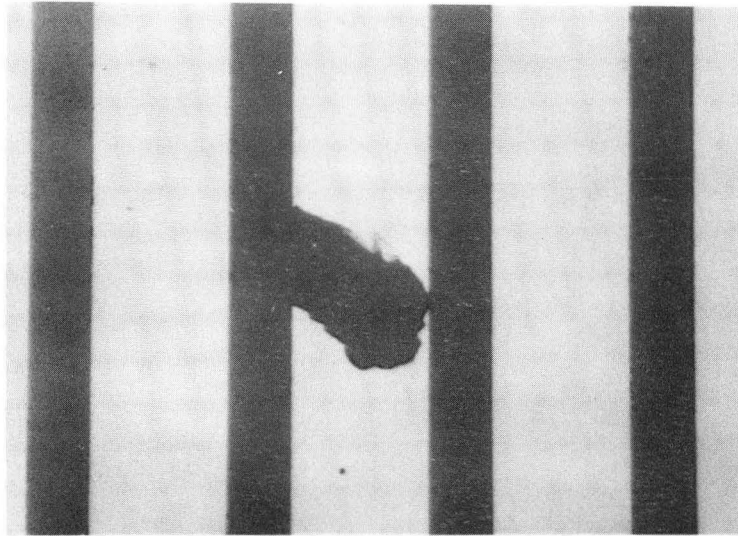
Center Region



10  $\mu\text{m}$

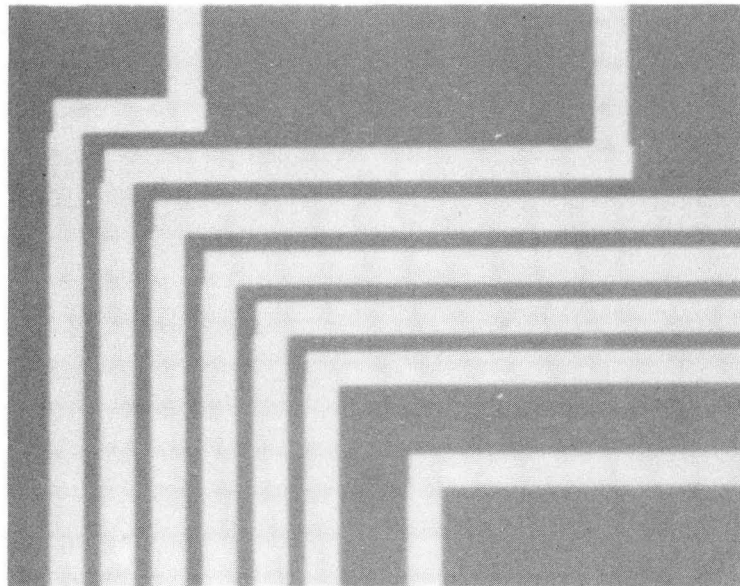
Closest Approach

Fig. B.6 Detail of fine aluminum layer showing the region under the segmented array, and the closest designed distance between lines. XBB 909-7449A



20  $\mu$ m

Exogenous Defects (Dust Particles)



20  $\mu$ m

Endogenous Defects (Mask Flaws)

Fig. B.7 Fabrication defects in aluminum lines. XBB 906-4891A

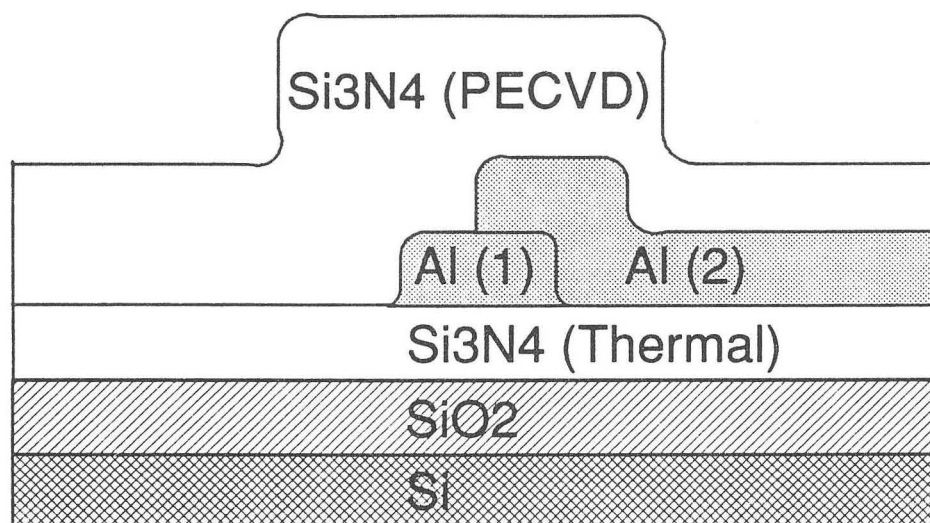


Figure B.8. Cross-section of the MME after PECVD of the Si<sub>3</sub>N<sub>4</sub> passivation layer at the largest wafer step-height.

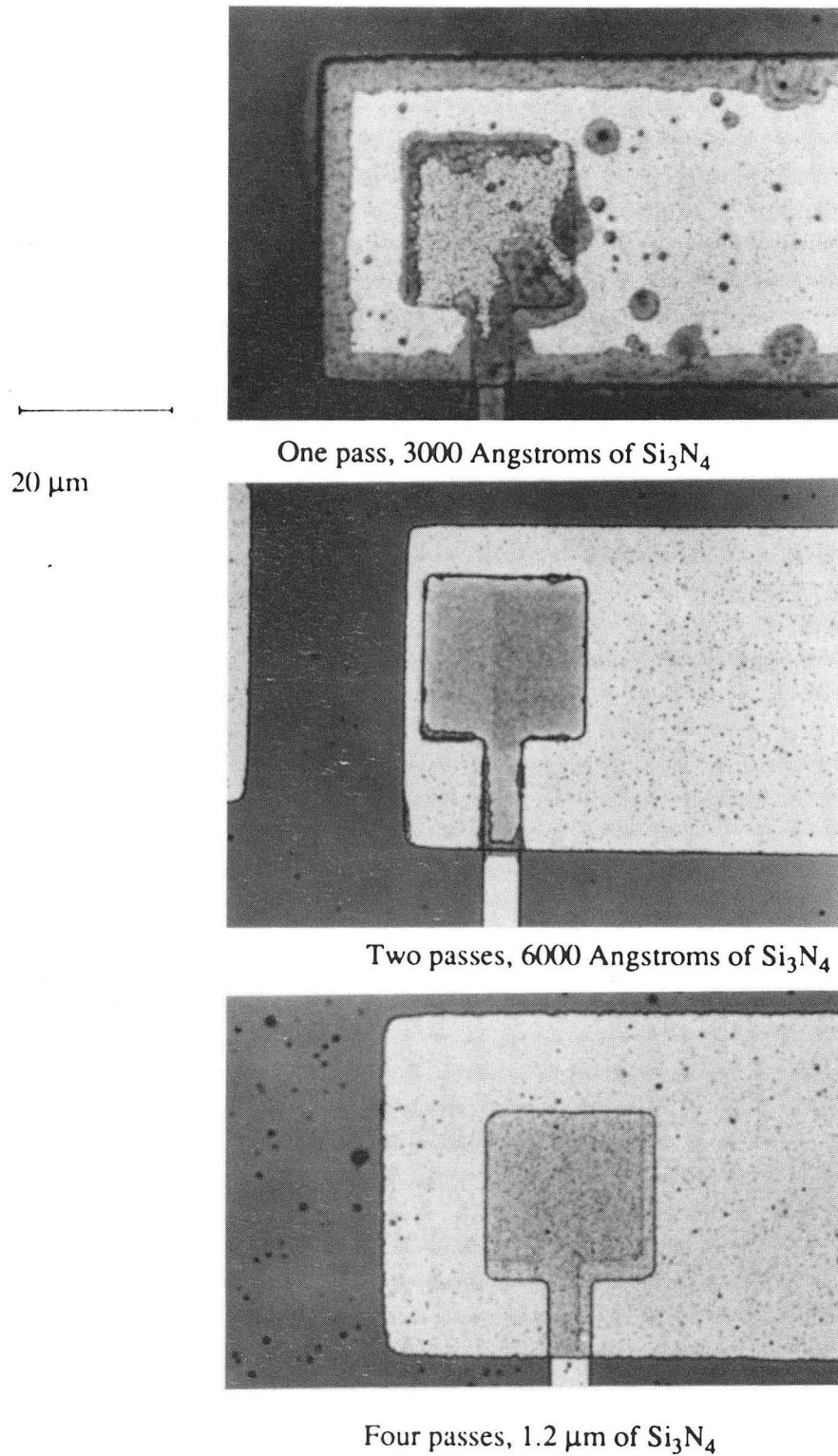


Fig. B.9 Corrosion resistance test in concentrated phosphoric acid. The 1.0  $\mu\text{m}$  step is covered by a  $\text{Si}_3\text{N}_4$  film of different thicknesses. CBB 909-7441A

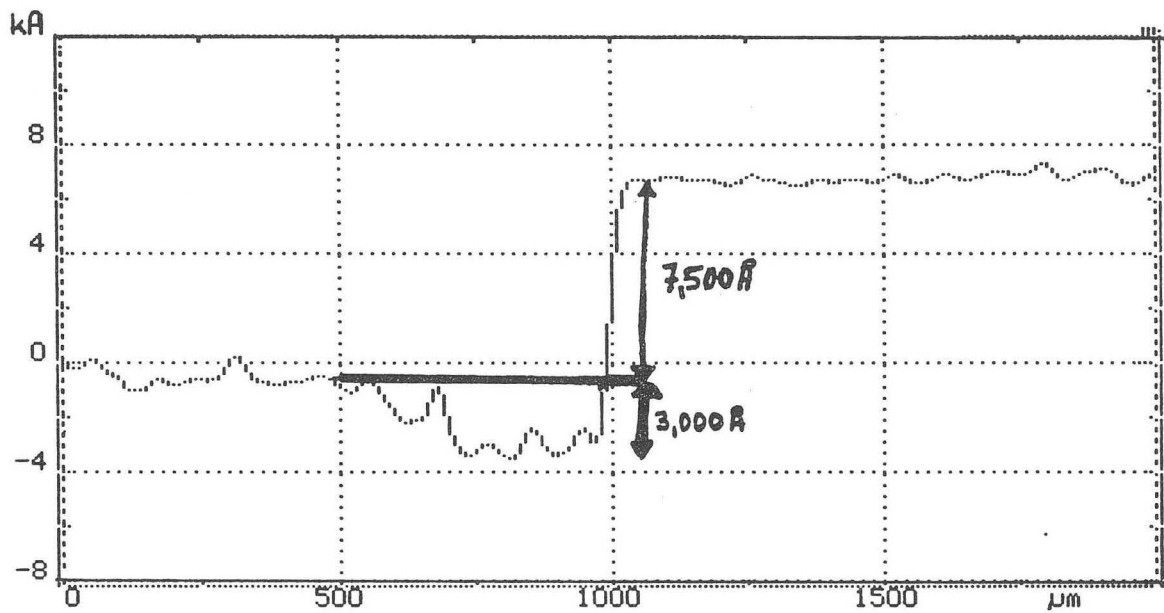
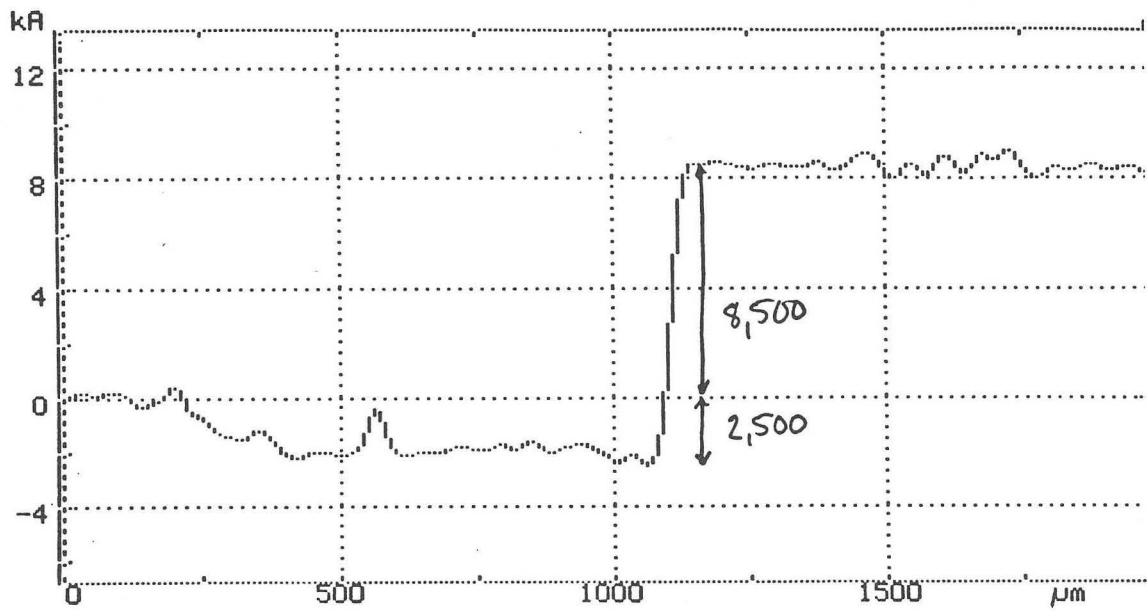


Figure B.10. Etch profiles at the peripheral pads. The corners of the large pads are preferentially etched. Five minutes etch time,  $\text{SF}_6$  plasma, at 70 Watts.

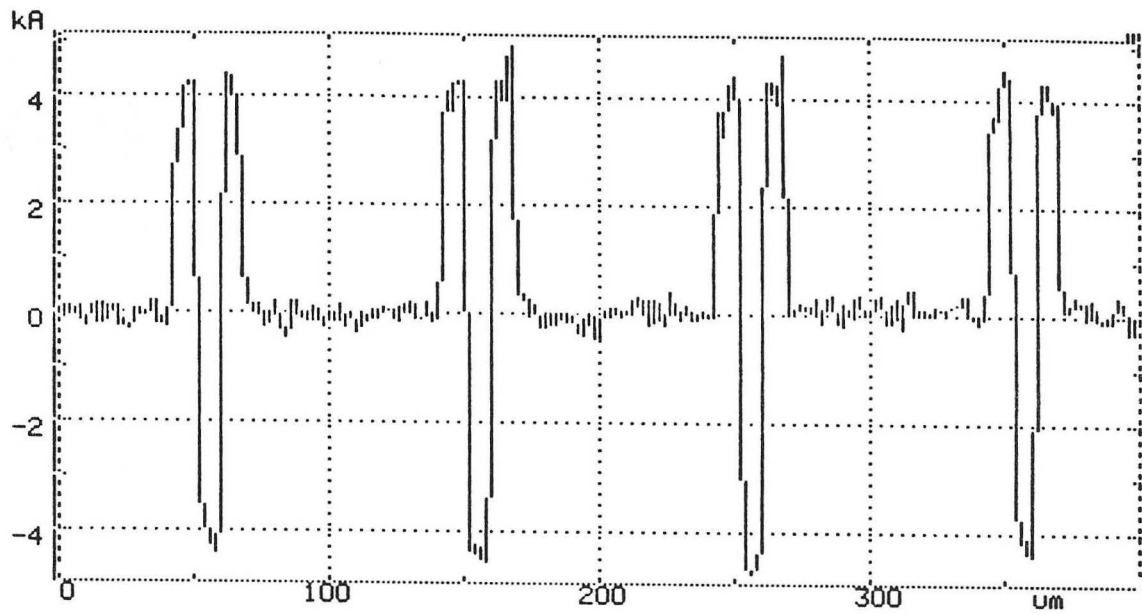


Figure B.11. Etch profile of the vias. Five minutes etch time,  $\text{SF}_6$  plasma, at 70 Watts.



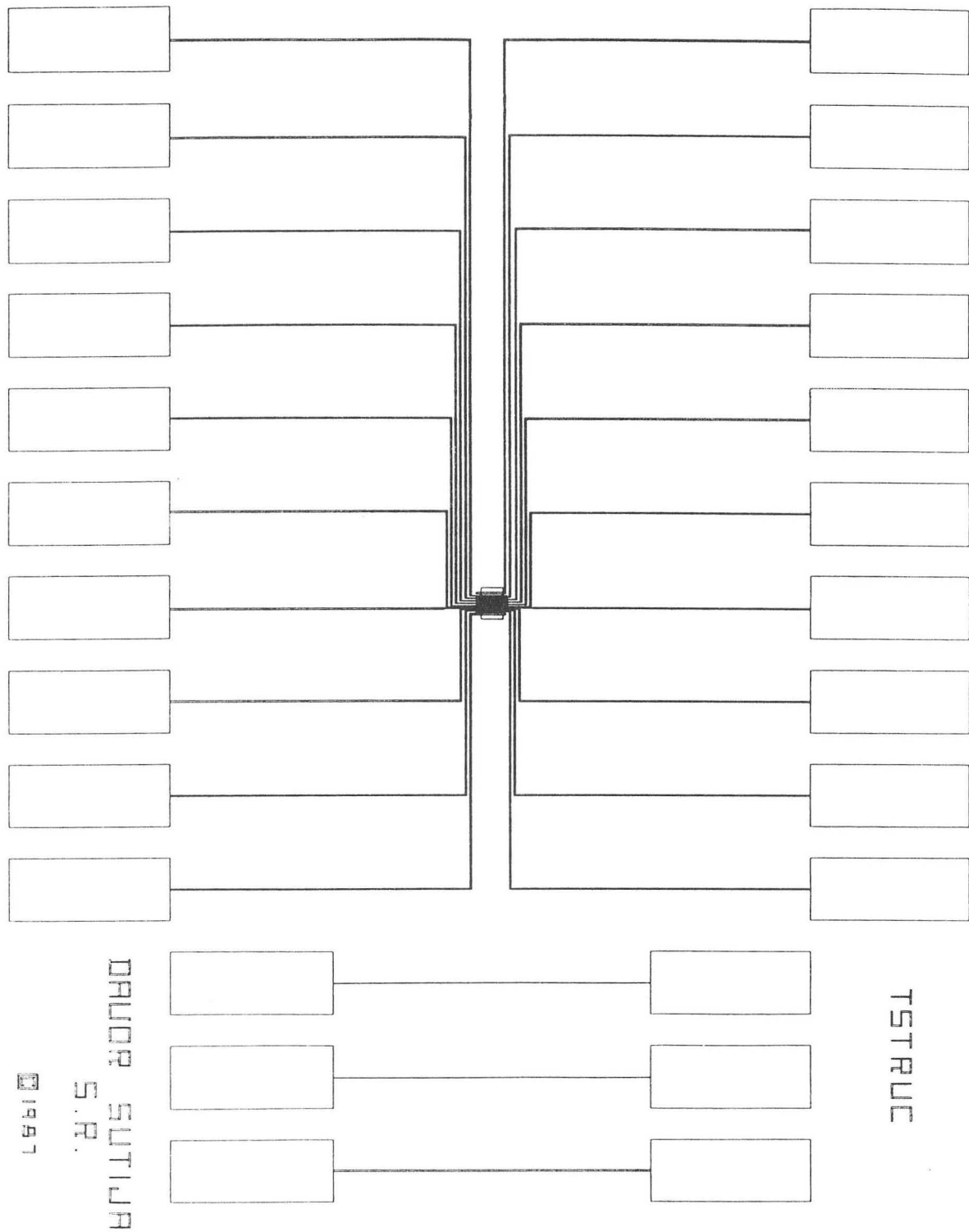


Figure B.12. TSTRUC lithographic mask; used to create titanium lines for tests of electrical conductivity and corrosion resistance.



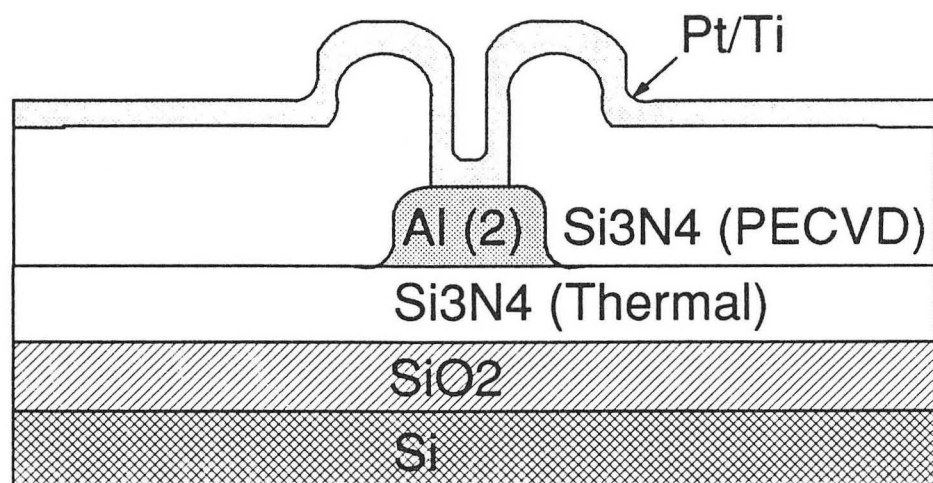
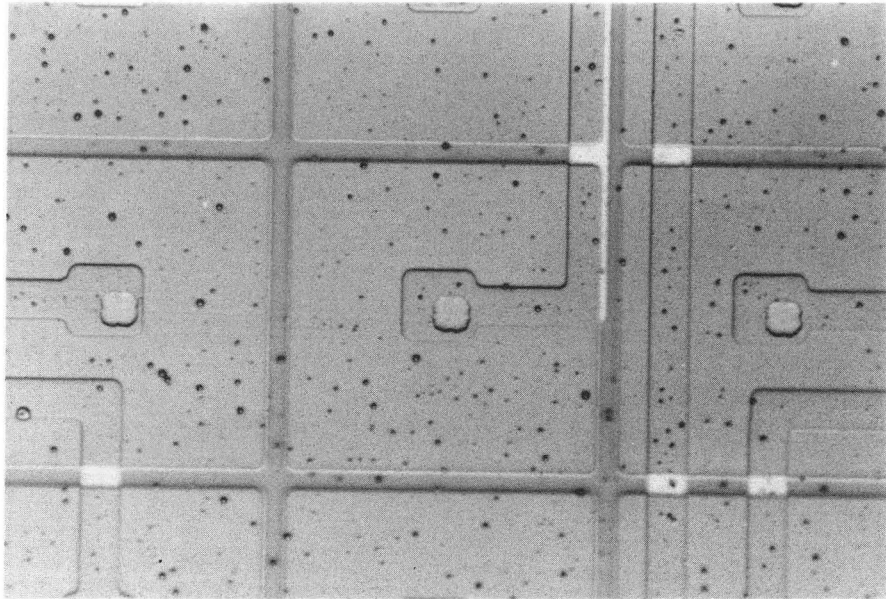


Figure B.13. Cross-section of the finished MME through the center of a segment, showing the via structure.



20  $\mu\text{m}$

Fig. B.14 A single segment of a completed MME array. The underlying aluminum layer is visible under the transparent silicon nitride and translucent Pt/Ti layers. The via is on target over the pad at the end of the aluminum wire. The milling lines are 4  $\mu\text{m}$  wide. XBC 911-390A

### Appendix C: An Impurity Analysis of 1M Zinc Bromide Electrolyte

Chemical analysis of solutions was done periodically in the UC College of Chemistry micro-analytical laboratory to test for the presence of impurities in the electrolyte which may have influenced zinc deposit morphology in the experiments reported in Chapter 3. The tests measured zinc by atomic absorption and halide ion concentration by titration, then determined the concentration of copper and iron. These two metallic impurities are present in the zinc halide salt used as a starting material. They are known to catalyze hydrogen evolution, and are removed by cementation with zinc powder at 70 °C (cf. Chap. 2). The table below gives typical results for a zinc bromide solution, nominally one molar in concentration:

<b>Atomic Absorption (AA) and Chemical Analysis</b>	
Element	Concentration
Zn	$5.85 \times 10^4$ ppm ( $0.91 \pm 0.1$ M)
Br	$1.97 \pm 0.1$ M
C	$0.22 \pm 0.3$ percent by weight (negligible)
N	$0.06 \pm 0.3$ percent by weight (negligible)
<b>Metallic Impurities</b>	
Element	Concentration
Fe	$6.6 \pm 2.0 \times 10^{-2}$ ppm by weight
Cu	$9.3 \pm 4.0 \times 10^{-2}$ ppm by weight

## Appendix D: Computer Programs for Statistical Analysis

The output from the Talysurf profilometer had to be converted to metric units and rewritten in standard ASCII format. This was accomplished by use of a basic program, called **Datprn** written and modified by Ken Jordan. Output files from Ken's program could be directly imported into LOTUS or FREELANC for plotting and analysis of the measured deposit profiles. Several other basic programs, written by the present author, converted and sorted the data into a standard format for autocorrelation analysis, Fourier analysis, and spectral power estimation. The first program, **Squish**, deleted the x-axis and printed out separate files for each profile. This was necessary because **Datprn** created only one output file for a series of 9 profiles on a single electrode surface, with the first data column reserved for the x-axis. The next program, **Split**, parsed the data from each scan into four equal portions, with the data points in each new file spaced four times further apart than in the original file. By doing this, and calculating separate Fourier spectra for each set, the variance in the estimate obtained for the power at each discrete frequency was reduced by 50%. This is possible because the striation spacing was much larger than the data spacing, and the power at high spectral frequencies was negligibly low.

After the listings of the basic programs, short LOTUS macros and MS-DOS batch files are given which prepared the data for zero-padding, then expedited analysis by allowing several spectra to be obtained in a batch mode without operator assistance. Finally, the annotated fortran code, adapted from **Numerical Recipes** [117], for the various analyses is listed. The following appendix gives the programs required for data acquisition from the experiments described in Part II.

## D.1 Basic Programs

### D.1.1 DATPRN

```

10 ' Program: DATPRN
20 ' Written by: Ken Jordan           3/10/89
30 '
40 ' This program will convert a *.DAT file created by the program
50 ' TS10.EXE (from Rank Precision Industries) and convert it into a
60 ' form useful to LOTUS.
70 '
80 ' input from user: Filename (no .DAT)
90 ' input from files: FILENAME.DAT
100 ' output to files: FILENAME.PRN
110 '
120 ' Revised by: Ken Jordan          5/31/89
130 ' This revision will handle three new commands from the new
140 ' version of TS10 (TS1087) (5.0). The new commands are
150 ' HTP, H%, T%
160 '
170 ' Revised by: Ken Jordan          10/03/89
180 ' This version will make multiple output *.PRN files from a single
190 ' *.DAT file containing several profiles (from TS1087 *.TEN files)
210 '
220 ' ***** Declare Variables
230 '
240 DIM TYPE(50),FILE$,I,I1,CODE,UNITSFOUND,
      NOOFPTS,CUTOFF,ASSESSED
250 DIM CODES$(50),MNG$(50),UCODE$(10),UNITS$(10),
      MODE$(6),Q$,A$,B$,ID$
260 DIM CUTOFFM(5),CUTOFFE(5),BLANK$,C$,NCODES%,
      APP$(32),TEMPFILES$,A,B
265 DIM Factor,OFactor,ONoOfPts,Columns,FC,True,False,Skip,HighB,LowB
270 '
280 ' ***** Main Program
290 '
300 GOSUB 2740 ' Titles
310 GOSUB 400 'Read Data
320 GOSUB 560 'Obtain Filename
330 IF FILE$="" THEN GOTO 370 'End Program
340 GOSUB 670 'Process TS10 file to LOTUS format
350 GOTO 320
360 '
370 PRINT "DATPRN: Normal End"

```

```

380 STOP
390 '
400 ' ***** SUBROUTINE:Read Data
410 '
420 READ NCODES%
430 FOR I=1 TO NCODES%:READ CODES$(I):NEXT I
440 FOR I=1 TO NCODES%:READ TYPE(I):NEXT I
450 FOR I=1 TO NCODES%:READ MNG$(I):NEXT I
460 FOR I=1 TO 10:READ UCODES$(I):NEXT I
470 FOR I=1 TO 10:READ UNITS$(I):NEXT I
480 FOR I=1 TO 6:READ MODE$(I):NEXT I
490 FOR I=1 TO 5:READ CUTOFFM(I):NEXT I
500 FOR I=1 TO 5:READ CUTOFFE(I):NEXT I
510 FOR I=1 TO 32:READ APP$(I):NEXT I
520 Q$=CHR$(34) ' Q$ = "
530 FOR I=1 TO 10:BLANK$=BLANK$+"    ":NEXT I
531 True=-1
532 False=0
540 RETURN
550 '
560 ' ***** Subroutine: Obtain Filename
570 '
580 FILE$=""
590 LOCATE 19,1:PRINT BLANK$
600 LOCATE 19,1
610 INPUT "TS 10 (version 5.0) filename? (No .DAT, <cr> to quit)",FILE$
615 IF FILE$="" THEN RETURN
620 FOR I=1 TO LEN(FILE$)
630  IF (MID$(FILE$,I,1)=".") THEN FILE$=LEFT$(FILE$,I-1):GOTO 650
640 NEXT I
641 '
650 LOCATE 19,1:PRINT BLANK$:LOCATE 19,1
653 INPUT "Skip, Start X (mm), End X (mm)? (1,0,1000 for all points)"
      ,Skip,LowB,HighB
655 IF (Skip<0) THEN Skip=1
657 IF LowB>HighB THEN B=LowB:LowB=HighB:HighB=B
659 RETURN
660 '
670 ' ***** Subroutine: Process TS10 File to LOTUS format
680 '
690 OPEN FILE$+".DAT" FOR INPUT AS #1
700 FC%=0
701 Factor=0:ONoOfPts=0
710 TEMPFILE$=FILE$
730 FC%=FC%+1
740 IF FC%<=32 THEN GOTO 780

```

```

750 PRINT "ERROR:More than 32 output files. Rest ignored."
760 GOTO 2340 'Error
770 '
780 IF LEN(TEMPFILE$)+LEN(APP$(FC%))>8 THEN
    TEMPFILE$=MID$(TEMPFILE$,1,8-LEN(APP$(FC%)))
785 LOCATE 19,1:PRINT BLANK$:LOCATE 19,1
790 PRINT "Processing ";FILE$;".DAT to ";TEMPFILE$+APP$(FC%);".PRN"
800 '
810 IF (EOF(1)=-1) THEN CLOSE #1:LOCATE 20,1:PRINT BLANK$:
    LOCATE 20,1:RETURN
820 LINE INPUT #1,ID$
830 LOCATE 20,1:PRINT BLANK$:LOCATE 20,1
840 PRINT ID$
850 '
860 OPEN TEMPFILE$+APP$(FC%)+".PRN" FOR OUTPUT AS #2
870 PRINT #2,Q$+ID$+Q$
880 '
890 ON ERROR GOTO 2340' Error
900 IF (EOF(1)=-1) THEN CLOSE #1:CLOSE #2:RETURN
910 INPUT #1,A$
920 IF A$=CHR$(12) THEN CLOSE #2:GOTO 730
930 GOSUB 2420 ' TrimString
940 IF A$="" THEN GOTO 900
950 GOSUB 2610 ' FindCode
960 IF CODE=0 THEN PRINT "ERROR:Unknown Code=";A$:GOTO 2340 'Error
970 '
980 'PRINT CODE$(CODE);TAB(5);TYPE(CODE);TAB(10);MNG$(CODE)
990 IF TYPE(CODE)=1 THEN GOSUB 1090 ' Type 1
1000 IF TYPE(CODE)=2 THEN GOSUB 1250 ' Type 2
1010 IF TYPE(CODE)=3 THEN GOSUB 1380 ' Type 3
1020 IF TYPE(CODE)=4 THEN GOSUB 1560 ' Type 4
1030 IF TYPE(CODE)=5 THEN GOSUB 1680 ' Type 5
1040 IF TYPE(CODE)=6 THEN GOSUB 1850 ' Type 6
1050 IF TYPE(CODE)=7 THEN GOSUB 2100 ' Type 7
1060 IF TYPE(CODE)=8 THEN GOSUB 2230 ' Type 8
1070 GOTO 900
1080 '
1090 ' ***** Subroutine: Type 1
1100 '
1110 IF LEN(A$)<=0 THEN INPUT #1,A$
1120 IF (CODE=1) THEN A$=Q$+MODE$(VAL(A$))+Q$
1130 IF (CODE<>2) THEN GOTO 1170
1140 A$=STR$(CUTOFFM(VAL(A$)))
1150 CUTOFF=VAL(A$)
1160 A$=A$+","+Q$+"mm"+Q$
1170 IF (CODE=3) THEN A$=STR$(VAL(A$)*1000)

```

```

1180 IF (CODE=4) THEN ASSESSED=VAL(A$)
1190 IF (CODE<>5) THEN 1220
1200 MMODE=VAL(A$)
1210 IF (MMODE=1) THEN A$=Q$+"(Inverted)" +Q$
      ELSE A$=Q$+"(Normal)" +Q$
1220 PRINT #2,Q$;MNG$(CODE);Q$;",";A$
1230 RETURN
1240 '
1250 ' ***** Subroutine: Type 2
1260 '
1270 IF LEN(A$)<=0 THEN INPUT #1,A$
1280 NOOFPTS=VAL(A$)
1290 FOR I1=1 TO NOOFPTS
1300 INPUT #1,A$
1310 PRINT #2,Q$;MNG$(CODE);Q$;",";Q$;"i=";I1;Q$;",";A$
1320 NEXT I1
1330 INPUT #1,B$
1340 GOSUB 1460 'DecodeUnits
1350 PRINT #2,Q$;B$;Q$
1360 RETURN
1370 '
1380 ' ***** Subroutine: Type 3
1390 '
1400 IF LEN(A$)<=0 THEN INPUT #1,A$
1410 INPUT #1,B$
1420 GOSUB 1460 ' DecodeUnits
1430 PRINT #2,Q$;MNG$(CODE);Q$;",";A$;",";Q$;B$;Q$
1440 RETURN
1450 '
1460 ' ***** Subroutine: DecodeUnits
1470 '
1480 UNITSFOUND=0
1490 FOR I1=1 TO 10
1500 IF B$=UCODE$(I1) THEN B$=UNIT$(I1):UNITSFOUND=1
1510 NEXT I1
1520 IF (UNITSFOUND<>0) THEN RETURN
1530 PRINT "Warning: Unknown Units=";B$;TAB(40);
      "Code Type=";TYPE(CODE)
1540 RETURN
1550 '
1560 ' ***** Subroutine: Type 4
1570 '
1580 IF LEN(A$)<=0 THEN INPUT #1,A$
1590 INPUT #1,B$
1600 A$=Q$+MNG$(CODE)+Q$+",";A$+",";Q$+"@";Q$+",";B$
1610 INPUT #1,B$

```



```

1620 GOSUB 1460 'DecodeUnits
1630 IF RIGHT$(MNG$(CODE),1)="a" THEN B$=B$+" depth"
      ELSE B$=B$+" heighth"
1640 A$=A$+",""+Q$+B$+Q$
1650 PRINT #2,A$
1660 RETURN
1670 '
1680 ' ***** Subroutine: Type 5
1690 '
1700 ' Note: This subroutine is only compatible with TS10 data files
1710 '       from version 5.0. Version 4.5 and lower do not have the
1720 '       second set of units, and the first set of units goes with
1730 '       the second number.
1740 '
1750 IF LEN(A$)<=0 THEN INPUT #1,A$
1760 INPUT #1,B$:GOSUB 1460 'DecodeUnits
1770 A$=Q$+MNG$(CODE)+Q$+",""+A$+",""+Q$+B$+" @"+Q$
1780 INPUT #1,C$
1790 INPUT #1,B$
1800 GOSUB 1460 'DecodeUnits
1810 A$=A$+",""+C$+",""+Q$+B$+Q$
1820 PRINT #2,A$
1830 RETURN
1840 '
1850 ' ***** Subroutine: Type 6
1860 '
1870 IF LEN(A$)<=0 THEN INPUT #1,A$
1875 IF (NoOfPts>ONoOfPts) THEN ONoOfPts=NoOfPts
1880 NOOFPTS=VAL(A$)
1890 INPUT #1,A$
1900 GOSUB 2610 'FindCode
1910 IF (CODE<>46) THEN PRINT "ERROR: TS10 file format error":GOTO 2340
1920 IF LEN(A$)<=0 THEN INPUT #1,A$
1930 SCALE=VAL(A$)
1935 OFactor=Factor
1940 Factor=Cutoff*Assessed/NoOfPts
1945 IF (Factor=OFactor) AND (NoOfPts<=ONoOfPts) THEN GOTO 1950
      ELSE GOTO 1990
1946 '
1950 Columns=1
1955 PRINT #2,Q$;"Vertical";Q$
1960 IF MID$(B$,1,2)="um" THEN PRINT #2,Q$;"um";Q$
1970 IF MID$(B$,1,2)="ui" THEN PRINT #2,Q$;"uin";Q$
1971 '
1980 GOTO 2020
1981 '

```

```

1990 Columns=2
1995 PRINT #2,Q$;"Horizontal";Q$;",";Q$;"Vertical";Q$
2000 IF MID$(B$,1,2)="um" THEN PRINT #2,Q$;"mm";Q$;",";Q$;"um";Q$
2010 IF MID$(B$,1,2)="ui" THEN PRINT #2,Q$;"in";Q$;",";Q$;"uin";Q$
2011 '
2020 T$kip=Skip ' Use T$kip because we want to reset for
      several columns of data.'
2022 FOR I=1 TO NOOFPTS
2023 IF I+T$kip-1>NoOfPts THEN T$kip=NoOfPts-I+1
2025 FOR I1=1 TO T$kip
2030 INPUT #1,A
2035 NEXT I1
2037 I=I+T$kip-1
2038 '
2040 B=I*Factor
2041 IF (B>LowB) AND (B<HighB) THEN InRange=True ELSE InRange=False
2045 IF (InRange=False) THEN GOTO 2070
2046 '
2050 IF (Columns=2) THEN PRINT #2,
      USING "##.####^",##.####^";B,A/SCALE
2060 IF (Columns=1) THEN PRINT #2, USING "##.####^";A/SCALE
2061 '
2070 NEXT I
2080 RETURN
2090 '
2100 ' ***** Subroutine: Type 7
2110 '
2120 IF LEN(A$)<=0 THEN INPUT #1,A$
2130 INPUT #1,C$
2140 A$=Q$+MNG$(CODE)+Q$+",";A$+",";Q$+"%" +Q$
2150 A$=A$+",";C$+",";Q$+"%" +Q$
2160 INPUT #1,C$
2170 INPUT #1,B$:GOSUB 1460 ' DecodeUnits
2180 A$=A$+",";C$+",";Q$+B$+Q$
2190 PRINT #2,A$
2200 'PRINT "type 7:";A$
2210 RETURN
2220 '
2230 ' ***** Subroutine: Type 8
2240 '
2250 IF LEN(A$)<=0 THEN INPUT #1,A$
2260 A$=Q$+MNG$(CODE)+Q$+",";A$+",";Q$+"% @" +Q$
2270 INPUT #1,C$
2280 INPUT #1,B$:GOSUB 1460 'DecodeUnits
2290 A$=A$+",";C$+",";Q$+B$+Q$
2300 PRINT #2,A$

```

```

2310 'PRINT "type 8:";A$
2320 RETURN
2330 '
2340 ' ***** Routine: Error
2350 '
2360 IF ERR=52 THEN PRINT "ERROR: End of File @ line";ERL
2370 IF ((ERR<>0) AND (ERR<>52)) THEN PRINT "ERROR ";ERR;" at line ";ERL
2380 PRINT "DATPRN: Abnormal End"
2390 CLOSE #1:CLOSE #2
2400 STOP
2410 '
2420 ' ***** Subroutine: TrimString
2430 ' This subroutine removes leading and trailing blanks from the
2440 ' string variable A$
2450 '
2460 FOR I=1 TO LEN(A$)
2470  IF ASC(MID$(A$,I,1))=255 THEN MID$(A$,I,1)=" "
2480  IF ASC(MID$(A$,I,1))<32 THEN MID$(A$,I,1)=" "
2490 NEXT I
2500 '
2510 FOR I=LEN(A$) TO 1 STEP -1
2520  IF (MID$(A$,I,1)<>" ") THEN A$=LEFT$(A$,I):GOTO 2560
2530 NEXT I
2540 A$="":RETURN
2550 '
2560 FOR I=1 TO LEN(A$)
2570  IF (MID$(A$,I,1)<>" ") THEN A$=MID$(A$,I):RETURN
2580 NEXT I
2590 GOTO 2540
2600 '
2610 ' ***** Subroutine: FindCode
2620 ' This subroutine finds the code number for the contents of A$
2630 '
2640 CODE=0
2650 FOR I=1 TO NCODES%
2660  IF CODE$(I)=MID$(A$,1,LEN(CODE$(I))) THEN CODE=I
2670 NEXT I
2680 IF (CODE<=0) THEN RETURN
2690 '
2700 IF (LEN(A$)<=LEN(CODE$(CODE))) THEN A$="":GOTO 2720
2710  A$=MID$(A$,LEN(CODE$(CODE))+1)
2720 RETURN
2730 '
2740 ' ***** Subroutine: Titles
2750 '
2760 CLS:PRINT "Program: DATPRN";TAB(50);"Version 3"

```

```

2770 PRINT TAB(50);"10/04/89"
2780 PRINT
2790 PRINT " This program will convert *.DAT files generated by"
2800 PRINT "the Rank Taylor Hobson Program TALYSURF 10 87 PC (C) to"
2810 PRINT "a *.PRN file for use in LOTUS (C)"
2820 RETURN
2830 '
2840 ' ***** Data Statements
2850 '
2860 ' Codes (TS10 codes used to identify numbers in *.DAT file)-----
2865 ' (These codes come from appendix A.1 or A.2 in the TS10 manual)
2870 ' (First data item is the number of codes)
2880 DATA 49
2890 '
2900 DATA A,B,D,E,F,G,H,HP,HV,I,J,K,L,M,N,O,P,Q,R,S,T,U,V,W,X,XV
2910 DATA Y,z,a,b,c,d,s,t,u,v,w,RK,RVK,RPK,MR1,MR2,AP,AV,RD,SD
2920 ' New Codes for new version TS1087 (version 5.0)
2930 DATA HTP,T%,H%
2940 '
2950 ' Code type (used to identify the type of data following the code)-
2960 '     type=1. number
2970 '         a single number follows the code
2980 '         (e.g. A,B,D,E,F,G)
2990 '     2. number, (value, value, ... ) units
3000 '         First number tells how many values follow.
3010 '         Last item is a units code (e.g. H,HP,HV)
3020 '     3. value, units
3030 '         a number and units code follow. (e.g. I,J,...)
3040 '     4. value, number, unit_code
3050 '         value, depth or heighth, U3 or U4
3060 '         (e.g. s,t,u,v)
3070 '         (HSC or TP% values)
3080 '     5. number, unit, value
3090 '         set zonewidth, U3 or U4, value (e.g. w)
3100 '         (Pc values)
3110 '     6. Special format.
3120 '         RD na
3130 '         SD nb
3140 '         n(1)
3150 '         n(2)
3160 '         ...
3170 '         n(i)
3180 '         ...
3190 '         n(na)
3200 '
3210 ' New types for new codes:

```

3220 ' 7. 1st % value, 2nd % value, dist, unit\_code  
 3230 ' (e.g. HTP)  
 3240 ' 8. percent\_value, depth, unit\_code  
 3250 ' (e.g. T%,H%)  
 3260 DATA 1,1,1,1,1,1,2,2,2,3,3,3,3,3,3,3,3,1,1,3,3,3,3,3,3  
 3270 DATA 3,3,3,3,4,4,4,4,5,3,3,3,3,3,3,6,6  
 3280 ' New Codes for 3 new commands in version 5.0 TS1087  
 3290 DATA 7,8,8  
 3300 '  
 3310 ' Data statements for meanings-----  
 3320 '  
 3330 DATA Mode,Cutoff,Magnification,Assessed,Measurement,Run,Rti,Rpi  
 3340 DATA Rvi,Ra,Rq,Ry,Rt,Rtm,Rv,Rp,Sm,LamQ,DelQ,Rsk,Rku,S,R3z,Rz  
 3350 DATA Rpm,Rvm,R3y,Wa,Wq,Wt,Wc,Wp,HSCa,HSCb,Tpa,Tpb,Pc,Rk  
 3360 DATA Rvk,Rpk,MR1,MR2,AP,AV,ReadData,DataScale  
 3370 ' New meanings for 3 new commands in version 5.0 TS1087  
 3380 DATA HTp,T%,H%  
 3390 '  
 3400 ' Data statements for units (unit codes first, then unit meanings)-  
 3410 ' (Table A.3 in TS10 manual)  
 3420 '  
 3430 DATA U0,U1,U2,U3,U4,U5,UA,UB,UC,UD  
 3440 DATA min,mm,in,um,uin,deg,/cm,/in,metric,imperial  
 3450 '  
 3460 ' Data statements for mode (Table A.4 in TS10 manual)-----  
 3470 '  
 3480 DATA "Roughness ISO", "Roughness PC", "Waviness PC", "Unfiltered"  
 3490 DATA WAVINESS ISO,Roughness Rk filter  
 3500 '  
 3510 ' Data statements for Cut-Off (Table A.5 in TS10 manual)-----  
 3520 ' (1st line is metric, 2nd line is imperial)  
 3530 DATA 0.08,0.25,0.8,2.5,8.0  
 3540 DATA 0.003,0.01,0.03,0.1,0.3  
 3550 '  
 3560 ' Data statements for APP\$() -----  
 3570 ' (Used to distinguish several output file from one input file)  
 3580 '  
 3590 DATA a,b,c,d,e,f,g,h,i,j,k,l,m,n,o,p,q,r,s,t,u  
 3600 DATA v,w,x,y,z,aa,ab,ac,ad,ae,af

### D.1.2 SQUISH

- 1 ' Program Squish
- 2 ' Written by D. Sutija, 10/89

```

3  ' Converts output from DATPRN into separate
4  ' files usable for SPD and autocorrelation analysis.
5    OPEN "INPUT.DAT" FOR INPUT AS #3
6    IF EOF(3) = -1 THEN CLOSE #3:STOP
10   INPUT #3, FILE$,TYPE$
20   OPEN FILE$+".PRN" FOR INPUT AS #1
25   OPEN FILE$+"C.PRN" FOR OUTPUT AS #2
30   FOR J = 1 TO 13
40     LINE INPUT #1, A$
50     PRINT#2, A$
60   NEXT J
70   IF EOF(1) = -1 THEN CLOSE #1:CLOSE #2: GOTO 6
75   IF TYPE$="2" THEN INPUT #1, B, C
80   INPUT #1, B, C
90   IF TYPE$="2" THEN PRINT #2, USING "##.###^", B, C
91   IF TYPE$="1" THEN PRINT #2, USING "##.###^", C
100  GOTO 70

```

#### D.1.3 SPLIT

```

1  ' Program SPLIT; Written by D. Sutija, 10/89
2  ' This Program divides a long data file into four equally-
3  ' spaced groups which may be SPD analyzed separately and
4  ' still represent the deposit profile. This technique
5  ' reduces the variance in the estimated power at each
6  ' discrete frequency. Use of SQUISH is not required first.

7    OPEN "INPUT.DAT" FOR INPUT AS #3
8    IF EOF(3) = -1 THEN CLOSE #3:STOP
10   INPUT #3, FILE$,TYPE$

20   OPEN FILE$+".PRN" FOR INPUT AS #1
25   OPEN FILE$+"A.PRN" FOR OUTPUT AS #4
26   OPEN FILE$+"B.PRN" FOR OUTPUT AS #5
27   OPEN FILE$+"C.PRN" FOR OUTPUT AS #6
28   OPEN FILE$+"D.PRN" FOR OUTPUT AS #7

30   FOR J = 1 TO 13
40     LINE INPUT #1, A$
50     PRINT#4, A$
51     PRINT#5, A$
52     PRINT#6, A$
53     PRINT#7, A$
60   NEXT J

```

```

70   IF EOF(1) = -1 THEN CLOSE #1:CLOSE #4:CLOSE #5:CLOSE #6:
      CLOSE #7: GOTO 2
75   IF TYPE$="2" THEN INPUT #1, B
80   INPUT #1, C
90   IF TYPE$="2" THEN PRINT #4, USING "##.###^",##.###^"; B , C
95   IF TYPE$="1" THEN PRINT #4, USING "##.###^"; C
96   IF EOF(1) = -1 THEN CLOSE #1:CLOSE #4:CLOSE #5:CLOSE #6:
      CLOSE #7: GOTO 2
100  IF TYPE$="2" THEN INPUT #1, B
110  INPUT #1, C
120  IF TYPE$="2" THEN PRINT #5, USING "##.###^",##.###^"; B , C
130  IF TYPE$="1" THEN PRINT #5, USING "##.###^"; C
131  IF EOF(1) = -1 THEN CLOSE #1:CLOSE #4:CLOSE #5:CLOSE #6:
      CLOSE #7: GOTO 2
140  IF TYPE$="2" THEN INPUT #1, B
150  INPUT #1, C
160  IF TYPE$="2" THEN PRINT #6, USING "##.###^",##.###^"; B , C
170  IF TYPE$="1" THEN PRINT #6, USING "##.###^"; C
171  IF EOF(1) = -1 THEN CLOSE #1:CLOSE #4:CLOSE #5:CLOSE #6:
      CLOSE #7: GOTO 2
180  IF TYPE$="2" THEN INPUT #1, B
190  INPUT #1, C
200  IF TYPE$="2" THEN PRINT #7, USING "##.###^",##.###^"; B , C
210  IF TYPE$="1" THEN PRINT #7, USING "##.###^"; C
300  GOTO 70
400  STOP ' The program should never get here.

```

## D.2 Lotus Macros and MS-DOS Batch Commands

### D.2.1 MACRO 'Macin'

```

/fin
{?}~
{right}
{branch a2}

```

### D.2.2 MACRO 'Macout'

```

{esc}{esc}/pf
{?}~
r{?}~
oouqgq
{esc}{esc}/pf

```

```
{?}~
r{esc}{right}.{end}{down}{?}~
oouqgq
{branch a6}
```

### D.2.3 Batch Files for Processing Multiple Data Sets

The first file run was "Dospd.bat" which stripped the extension off of the input data file, then ran "runstat.bat", which processed each profile through the autocorrelation and spectral power density estimation routines.

#### Dospd.bat

```
for %%f in (*.dat) do copy %%f + %%f *
for %%g in (*) do copy %%g *.prn
for %%h in (*) do call runspd %%h
del *
del *.prn
```

#### Runspd.bat

```
copy %1.prn data.prn
rename %1.prn %1.dat
fft512
copy fft.prn %1.fft
del fft.prn
del data.prn
copy %1.dat data.prn
autoc5
copy correl.prn %1.acr
del correl.prn
del data.prn
```



### D.3 Fortran Programs for SPD and Autocorrelation Analysis

#### D.3.1 SPD512

```

c
c   Program SPD512
c   Written by D. Sutija, revised by Sang Yi, a summer
c   undergraduate research assistant, July, 1990.
c   This program is used to call subroutine SPCTRM and
c   FOUR1 from Numerical Recipes to estimate
c   the power spectrum of a zinc deposit profile.
c   The program nine profiles from a print file generated
c   by LOTUS and appropriately renamed by the preceding batch
c   files. Each profile has already been split in four equivalent
c   850 data points (so this program may be run four times),
c   which are zero-padded and have an integral number of striations.
c   The subroutine SORT trims the input to obtain
c   512 equally spaced data points. A Parzen window is employed
c   to reduce noise caused by the finite number of data points.
c   Overlapping segments may be used to reduce variance.
c   K=1, M=512, Number of Data points = 2 * K * M = 1024.
c
  INTEGER M
  DIMENSION P(256,9), W1(1024,9)
  DIMENSION TEDAT(256)
  DIMENSION DATA(1024,9), SUM(256)
  WRITE (6,*) 'WRITE M, K=1,COLUMNS, ASSUMED FALSE'
  READ (5,*) M,KOU
  OPEN (8, FILE = 'INDATA.PRN')
  OPEN (2, FILE = 'CORREL.PRN')
  DO 100 I = 1,850
  READ (8,*) ( DATA (I,J) , J= 1,KOU )
100  CONTINUE
  DO 110 J = 1,KOU
  CALL SORT (DATA,J)
  KI = 1
  KST = 1
  KEND = 10
101  DO 102 I= KST, KEND, 2
  TEDAT(KI) = DATA(I,J)
  KI = KI + 1
102  CONTINUE
  TEDAT(KI) = DATA(KEND,J)
  KI = KI + 1

```

```
KST = KEND + 1
KEND = KEND + 10
IF (KEND .LT. 850) THEN
GOTO 101
ENDIF
TEDAT(511) = 0.D0
TEDAT(512) = 0.D0
DO 103 I = 1,512
DATA(I,J) = TEDAT(I)
103 CONTINUE
DO 104 I = 513,1024
DATA(I,J) = TEDAT(I-512)
104 CONTINUE
110 CONTINUE
OPEN (3, FILE = 'EXAM.PRN')
DO 120 I = 1,1024
WRITE(3,*) (DATA(I,J), J=1,KOU)
120 CONTINUE
CLOSE(3)
OPEN (3, FILE = 'EXAM.PRN')
CALL SPCTRM (P,M,W1)
CLOSE(3)
DO 201 J = 1, KOU
BIG = P(1,J)
DO 210 I = 1,M
IF (BIG .LT. P(I,J)) THEN
BIG = P(I,J)
ENDIF
210 CONTINUE
DO 220 I = 1,M
P(I,J) = P(I,J) / BIG
220 CONTINUE
201 CONTINUE
DO 230 I = 1,M
SUM(I) = 0.D0
DO 240 J = 1,KOU
SUM(I) = SUM(I) + P(I,J)
240 CONTINUE
230 CONTINUE
BIG = SUM(1)
DO 250 I = 1,M
IF (BIG .LT. SUM(I)) THEN
BIG = SUM(I)
ENDIF
250 CONTINUE
DO 260 I = 1,M
```

```

SUM(I) = SUM(I)/BIG
260 CONTINUE
DO 270 I = 1,M
WRITE (2,300) (P(I,J), J= 1,KOU)
270 CONTINUE
WRITE (2,*)
WRITE (2,*)
DO 280 I = 1,M
WRITE (2,300) SUM(I)
280 CONTINUE
300 FORMAT (9(1X,E11.4))
CLOSE(2)
CLOSE(3)
CLOSE(8)
STOP 'SUCCESSFUL COMPLETION'
END

```

SUBROUTINE SORT(DATA,J)

c  
c  
c  
c

This subroutine was written by Sang Yi, a  
summer undergraduate research assistant, July, 1990.

```

DIMENSION DATA(1024,9)
A= DATA(1,J)
B= DABS(DATA(1,J))
XA= A/B
C= DATA(850,J)
D= DABS(DATA(850,J))
XC= C/D
DO 310 I = 1,850
A= DATA(I,J)
B= DABS(DATA(I,J))
IF (B .LT. 1.D-4) THEN
GOTO 309
ENDIF
XB = A/B
IF (XA .NE. XB) THEN
GOTO 311
ENDIF
309 DATA(I,J) = 0.D0
310 CONTINUE
311 DO 320 I= 850,1,-1
A= DATA(I,J)
B= DABS(DATA(I,J))
IF (B .LT. 1.D-4) THEN
GOTO 319

```

```

ENDIF
XD= A/B
  IF (XC .NE. XD) THEN
    IN = I
    GOTO 321
  ENDIF
319 DATA(I,J) = 0.D0
320 CONTINUE
321  IF (XD .EQ. XB) THEN
    XC = XD
  ENDIF
DO 330 I= IN, 1, -1
A = DATA(I,J)
B = DABS(DATA(I,J))
  IF (D .LT. 1.D-4) THEN
    GOTO 329
  ENDIF
XD = A/B
  IF (XC .NE. XD) THEN
    GOTO 331
  ENDIF
329 DATA(I,J) = 0.D0
330 CONTINUE
331 RETURN
END

```

```

SUBROUTINE SPCTRM(P,M,K,OVRLAP,W1,W2)
LOGICAL OVRLAP
DIMENSION P(M), W1(4*M), W2(M)
WINDOW(J) = (1. - ABS(((J-1)-FACM)*FACP))
C WINDOW(J) = 1.
C WINDOW(J) = (1. - (((J-1)-FACM)*FACP)**2)
MM =M + M
M4 = MM + MM
M44 = M4 + 4
M43 = M4 + 3
DEN = 0.
FACM = M - 0.5
FACP = 1./(M+.5)
SUMW = 0.
DO 11 J = 1, MM
    SUMW = SUMW + WINDOW(J)**2
11 CONTINUE
DO 12 J = 1, M
    P(J) = 0.
12 CONTINUE

```

```

IF(OVRLAP) THEN
    READ (9,*) (W2(J), J = 1,M)
ENDIF
DO 18 KK = 1,K
    DO 15 JOFF = -1, 0, 1
        IF (OVRLAP) THEN
            DO 13 J = 1,M
                W1(JOFF+J+J) = W2(J)
13      CONTINUE
            READ(9,*) (W2(J), J = 1, M)
            JOFFN = JOFFN + MM
            DO 14 J = 1,M
                W1(JOFFN+J+J) = W2(J)
14      CONTINUE
            ELSE
                READ(9,*) (W1(J), J= JOFF+2, M4, 2)
            ENDIF
15      CONTINUE
            DO 16 J=1,MM
                J2= J+J
                W = WINDOW(J)
                W1 (J2) = W1(J2)*W
                W1 (J2-1) = W1(J2-1)*2
16      CONTINUE
                CALL FOUR1(W1, MM, 1)
                P(1) = P(1) + W1(1)**2 + W1(2)**2
                DO 17 J = 2,M
                    J2 = J+J
                    P(J) = P(J)+W1(J2)**2 + W1(J2-1)**2
                    *   +W1(M44-J2)**2 + W1(M43-J2)**2
17      CONTINUE
                DEN = DEN+SUMW
18      CONTINUE
                DEN = M4*DEN
                DO 19 J = 1,M
                    P(J) = P(J)/DEN
19      CONTINUE
            RETURN
        END

```

```

SUBROUTINE FOUR1(DATA, NN, ISIGN)
REAL*8 WR, WI, WPR, WPI, WTEMP, THETA
DIMENSION DATA( 2*NN )
N = 2 * NN
J=1
DO 21 I = 1,N,2

```

```

IF(J .GT. I) THEN
    TEMPR= DATA(J)
    TEMPI = DATA(J+1)
    DATA(J) = DATA(I)
    DATA(J+1) = DATA(I+1)
    DATA(I) = TEMPR
    DATA(I+1) = TEMPI
ENDIF
M = N/2
20 IF ( ( M .GE. 2 ) .AND. ( J .GT. M ) ) THEN
    J = J-M
    M = M/2
    GOTO 20
ENDIF
J = J+M
21 CONTINUE
MMAX = 2
22 IF ( N .GT. MMAX ) THEN
    ISTEP = 2 * MMAX
    THETA = 6.28318530717959D0 / ( ISIGN * MMAX )
    WPR = -2.D0 * DSIN (0.5D0 * THETA) ** 2
    WPI = DSIN(THETA)
    WR = 1.D0
    WI = 0.D0
    DO 23 M = 1, MMAX, 2
        DO 24 I = M,N,ISTEP
            J = I+ MMAX
            TEMPR = SNGL(WR) * DATA(J) - SNGL(WI) * DATA(J+1)
            TEMPI = SNGL(WR) * DATA(J+1) + SNGL(WI) * DATA(J)
            DATA(J) = DATA(I) = TEMPR
            DATA(I) = DATA(I+1) = TEMPI
            DATA(I+1) = DATA(I+1) + TEMPI
24 CONTINUE
            WTEMP = WR
            WR = WR * WPR - WI * WPI + WR
            WI = WI * WPR + WTEMP * WPI + WI
23 CONTINUE
            MMAX = ISTEP
            GOTO 22
        ENDO
    ENDO
    RETURN
END

```

### D.3.2 AutoC512

c This program will calculate the Auto-correlation of any  
 c set of 4096 real data points, as long as  $N=4096$ .  
 c This number is not arbitrary; for the algorithm to work  
 c properly, the length of the data set must be a power of 2.  
 c The file "Data" is opened and read, and the file ANS has the  
 c output: the correlation at negative lags are in ANS (N) down  
 c to ANS ( $N/2 + 1$ ) while the positive lags are in the first half  
 c of ANS. The subroutines used in this program are  
 c from Press et al., **NUMERICAL RECIPES**, which is available in  
 c machine-readable form from the publisher, Cambridge Univ. Press.  
 c

```

PROGRAM AUTOC512
INTEGER N
DIMENSION DATA (512)
COMPLEX ANS (512)
N=512

OPEN (UNIT=1,BLANK='NULL',MODE='READWRITE',
      FILE='DATA.PRN')
DO 10,I=1,512
  READ (1,*) DATA(I)
10  CONTINUE
  CLOSE(1)

CALL CORREL (DATA,DATA,N,ANS)

OPEN (UNIT=2,BLANK='NULL',MODE='READWRITE',
      FILE='CORREL.PRN')
DO 30,I=1,128
  WRITE (2,*) REAL(ANS(I))
  WRITE (2,*) IMAG(ANS(I))
30  CONTINUE
  CLOSE(2)
  STOP 'SUCCESSFUL COMPLETION'
  END
  
```

### D.3.2 MEMSPD

Program memspd  
 Implicit real\*8 (a-h, o-z)  
 Integer n,m

```

Real*8 fdt,pm
Dimension data(850,9), cof(20), wk1(850)
Dimension wk2(850), wkm(20), spectrum(1000,9)
Dimension sum(1000,1)
c n is the number of data points read along one profile
c m is the desired spectral density
c K is the total number of changes in m
c minc is the change in m
c kou is the number of columns incorporated in calculations
c kou should be either 9 or 1
  N = 400
  M = 15
  K = 1
  MINC = 5
  KOU = 9
  LIMIT = KOU * K
  JAW = 0
  Open (9,file= 'indata.prn')
  Open (2, file= 'outdata.prn')
  Do 80 i = 1,n
  Read (9,*) (data(i,1), l = 1,kou)
80  Continue
70  Do 75 ncol= 1, kou
  JAW = JAW +1
85  Call memcof(data,n,m,pm,cof,wk1,wk2,wkm,ncol)
  FDT = 0.d0
  Do 100 I = 1, 1000
  Spectrum (I,jaw) = evlmem (fdt,cof,m,pm)
  FDT = FDT + .0001d0
100 Continue
75  Continue
  M = M + MINC
  If (JAW .ne. LIMIT) Then
  Goto 70
  Endif
  Do 200 J = 1,LIMIT
  BIG = SPECTRUM(1,J)
  Do 205 i = 1,1000
  If (BIG .LT. SPECTRUM(I,J)) Then
  BIG = SPECTRUM(I,J)
  Endif
205 Continue
  Do 210 i = 1,1000
  SPECTRUM(I,J) = SPECTRUM(I,J)/BIG
210 Continue
200 Continue

```



```
KBG = 1
Do 300 KI= 1, K
  KSTOP = KOU*KI
  Do 225 i= 1,1000
    SUM(I,KI) = 0.D0
    Do 230 J = KBG, KSTOP
      SUM(I,KI) = SUM(I,KI) + SPECTRUM(I,J)
230  Continue
225  Continue
  KBG= KSTOP + 1
300  Continue
  Do 319 KI = 1,K
    BIG = SUM(1,KI)
    Do 320 I = 1,1000
      If (BIG .LT. SUM(I,KI)) then
        BIG = SUM(I,KI)
      Endif
320  Continue
    Do 321 I = 1,1000
      SUM(I,KI) = SUM(I,KI)/BIG
321  Continue
319  Continue
  Do 105 i = 1,1000
    Write (2,1000) (spectrum(i,j), j= 1,limit)
105  Continue
  Write (2,*)
  Write(2,*)
  Do 400 i =1,1000
    Write (2,1000) (sum(i,ki), ki= 1,k)
400  Continue
1000 Format (27(1X,E11.4))
  Close (9)
  Close (2)
  Stop
  End
```

## Appendix E - Basic Programs for Data Acquisition

### E.1 MUX

Upgrading of the data acquisition apparatus to a PC-based system required the use of new BASIC software for current control and for interfacing the PC with the NEFF multiplexer. The program used is called **MUX**, an abbreviation for multiplexer. The original version was written by Henry Chan of the UCB College of Chemistry Electronics Shop. It was later expanded and re-written by the author with the collaboration of Gerhard Matzen, a graduate co-worker. The accompanying machine language program for scanning of the multiplexer was also written by Mr. Chan.

```

10 REM PROGRAM MUX
20 REM
30 REM Original version written by Henry Chan, March, 1990
40 REM Revised and Annotated by Davor Sutija and Gerd Matzen, 1991
50 REM
60 REM -----
70 REM Start communications with GPIB board and 32-bit I/O boards
80 REM -----
85 REM
90 CLEAR ,58000!
100 IBINIT1=60000!
110 IBINIT2=IBINIT1+3
120 BLOAD "bib.m",IBINIT1:REM bib.m is Nat. Inst.'s Basic interface
130 CALL IBINIT1(IBFIND,IBTRG,IBCLR,IBPCT,IBSIC,IBLOC,IBPPC,IBBNA,
    IBONL,IBRSC,IBSRE,IBRSV,IBPAD,IBSAD,IBIST,IBDMA,IBEOS,
    IBTMO,IBEOT,IBRDF,IBWRTF,IBTRAP,IBDEV,IBLN)
140 CALL IBINIT2(IBGTS,IBCAC,IBWAIT,IBPOKE,IBWRT,IBWRTA,IBCMD,
    IBCMDA,IBRD,IBRDA,IBSTOP,IBRPP,IBRSP,IBDIAG,IBXTRC,IBRDI,
    IBWRTI,IBRDIA,IBWRTIA,IBSTA%,IBERR%,IBCNT%)
150 REM -----
160 REM Give the devices names/locations.
170 REM -----
180 PLOTTER$="DEV5":FUNCGEN$="DEV17":VOLTMETER$="DEV22"
190 CALL IBFIND(PLOTTER$,PLOTTER%)
200 CALL IBFIND(FUNCGEN$,FUNCGEN%)
210 CALL IBFIND(VOLTMETER$,VOLTMETER%)

```

```
220 J6=&H300:J8=&H304
230 OUT J6+3,&H80:REM This programs PIO12 #1 as all output
240 OUT J8+3,&H9B:REM This programs PIO12 #2 as all input
250 REM
260 REM -----
270 REM Load the machine code to scan the multiplexer channels
280 REM Define and read in channel #'s and sequence
290 REM -----
300 REM
310 BLOAD "scan1.com",58000!
320 SCAN1=58000!
330 DIM DATAARY%(256),CHARY%(256),REALARY(256)
340 READ CHCNT%:REM read in channel counts
350 DATA 103:REM 4 i,v channels and 100 array channels; (5,6) = K2.
360 FOR I=0 TO CHCNT%
370 READ CHARY%(I):REM Fill Array with selected channel scanning
    sequence
380 NEXT I
390 DATA &H0000,&H0001,&H0002,&H0003
400 DATA &H0063,&H0064,&H0066,&H0069,&H006D,&H0070
410 DATA &H0076,&H007A,&H007D,&H007F,&H0061,&H0062
420 DATA &H0065,&H0068,&H006C,&H0073,&H0077,&H007B
430 DATA &H007E,&H0024,&H005E,&H005F,&H0060,&H0067
440 DATA &H006B,&H0074,&H0078,&H007C,&H0025,&H0026
450 DATA &H005A,&H005B,&H005C,&H005D,&H006A,&H006F
460 DATA &H0079,&H0027,&H0028,&H0029,&H0054,&H0057
470 DATA &H0058,&h0053,&H0052,&H0003,&H002A,&H002B
480 DATA &H002C,&H002D,&H0051,&H0050,&H004F,&H004E
490 DATA &H0012,&H002E,&H002F,&H0034,&H0033,&H0030
500 DATA &H004D,&H004C,&H004B,&H001D,&H0013,&H000E
510 DATA &H0039,&H0038,&H0037,&H0036,&H004A,&H0049
520 DATA &H0020,&H001C,&H0018,&H000F,&H000B,&H003C
530 DATA &H003B,&H003A,&H0048,&H0022,&H001F,&H001B
540 DATA &H0017,&H0010,&H000C,&H0009,&H003E,&H003D
550 DATA &H0023,&H0021,&H001E,&H001A,&H0014,&H0011
560 DATA &H000D,&H000A,&H0008,&H003F
570 PRINT "DO YOU WANT TO CONTROL POTENTIAL OR
    CONTROL i(H2)?":PRINT
580 A$ = INPUT$(1)
590 IF ((A$ = "i") OR (A$ = "I")) THEN GOTO 870
600 REM
610 REM -----
620 REM POTENTIAL CONTROL
630 REM -----
640 REM
650 PRINT "POTENTIAL CONTROL"
```

```
660 PRINT "We are controlling potential K1 or K2."
670 PRINT
680 PRINT "Enter the name of this experiment."
690 INPUT "data file name?";FLNAME$
700 OPEN FLNAME$ FOR OUTPUT AS #1
710 PRINT #1, "CONTROLLED POTENTIAL EXPERIMENT"
720 INPUT "Enter constant potential
      (millivolts vs. Hg/HgSO4 ref.):";DV
730 PRINT #1, "The potential was";DV;"mV vs. Hg/HgSO4 ref."
740 PROFUNC$="FU0":CALL IBWRT(FUNCGEN%,PROFUNC$):REM DC OFFSET
750 CLOSE #1
760 FOR I=1 TO 1600:NEXT
770 AMP$="OF"+STR$(DV)+"MV"
780 IAM$="IOF":CALL IBWRT(FUNCGEN%,IAM$)
      :REM This has no real function
790 CALL IBRD(FUNCGEN%,RDS$)
      :REM This waits for last ibwrt to complete.
800 CALL IBWRT(FUNCGEN%,AMP$)
810 FOR I=1 TO 1600:NEXT:GOTO 1440
820 REM
830 REM -----
840 REM CURRENT CONTROL
850 REM -----
860 REM
870 PRINT
880 PRINT "CURRENT CONTROL"
890 PRINT "We are Controlling the current measured
      on the voltmeter."
900 PRINT "This program adjusts K2 to accomplish this."
910 PRINT
920 PRINT "1) CHECK THE SCALE ON THE RDE; SET TO 10 microA/Volt"
930 PRINT "2) CONNECT VOLTMETER TO I2 ON THE RDE3 POTENTIOSTAT"
940 PRINT "3) SET K2=K1 MANUALLY AS OUR STARTING POINT;"
950 PRINT "WE WILL CHANGE K2 BY 5mV AT A TIME
      UNTIL i=i(SET POINT)."
960 PRINT "4) CONNECT FUNCTION GENERATOR TO K2"
970 PRINT "5) Make sure that ONLY 1 segment is-on now."
980 PRINT
990 PRINT "We need to know the total cathodic
      current in microamps."
1000 INPUT "Enter constant i ";CI
1010 DI=-CI
1020 PRINT "Enter the file name for this experiment."
1030 INPUT "data file name?";FLNAME$
1040 OPEN FLNAME$ FOR OUTPUT AS #1
1050 PRINT #1, "CONTROLLED CURRENT EXPERIMENT"
```

```
1060 PRINT #1, "The cathodic current was";DI;
      "microamps per H2 segment."
1070 CLOSE #1
1080 REM
1090 REM -----
1100 REM Initialize function generator; set V=0mV.
1110 REM -----
1120 REM
1130 GOSUB 4010
1140 REM
1150 REM -----
1160 REM Adjust the current if it is not within specifications.
1170 REM -----
1180 REM
1190 CLS:PRINT "Adjusting for I":LOCATE 2,1
1200 PRINT "H2 Current", "Last read", "Last Pot. ", "New Pot."
1210 LOCATE 4,1:PRINT CI
1220 LOCATE 6,1:PRINT "Loop count"
1230 IAM$="IOF"
1240 CALL IBWRT(FUNCGEN%,IAM$)
1250 CALL IBRD(FUNCGEN%,RD$)
1260 FUNCAMP$=LEFT$(RD$,IBCNT%-2)
1270 LOOPCOUNT=0:REM RESET LOOP COUNT
1280 CALL IBRD(VOLTMETER%,RD$)
1290 METER$=LEFT$(RD$,IBCNT%-2)
1300 METER=VAL(METER$)
1310 PCURR=-10*METER
1320 LOCATE 4,15:PRINT PCURR,FUNCAMP$,AMP$;"      "
1330 LOCATE 6,11:PRINT "      ":LOCATE 6,11:PRINT LOOPCOUNT
1340 DEV=ABS(.02*DI)
1350 IF ABS(METER*10-DI) > DEV THEN GOSUB 3060:GOTO 1180
1360 REM
1370 REM -----
1380 REM Loop 10 times and check if current is stable.
1390 REM -----
1400 REM
1410 LOOPCOUNT=LOOPCOUNT+1
1420 IF LOOPCOUNT < 10 THEN 1280
1430 REM
1440 REM -----
1450 REM System is now ready for our experiment.
1460 REM -----
1470 REM
1480 REM -----
1490 REM Options for reading channels:
1500 REM -----
```

```

1510 REM
1520 PRINT "1) ENTER SPECIFIC CHANNELS TO BE READ"
1530 PRINT "2) USE ORIGINAL MICROMOSAIC FORMAT":PRINT
1540 PRINT "  DEFAULT IS #2"
1550 INPUT "ENTER CHOICE";CHOICE
1560 IF CHOICE = 1 THEN GOSUB 6020 : REM ENTER SPECIFIC CHANNELS
1570 REM
1580 REM -----
1590 REM CHOOSE BETWEEN AUTOSETTING AND ASSIGNING GAIN VALUES
1600 REM -----
1610 REM
1620 PRINT"1) ASSIGN GAIN VALUES MANUALLY"
1630 PRINT"2) AUTOSET THE GAIN":PRINT
1640 INPUT"ENTER CHOICE";CHOICE
1650 IF CHOICE < 1 OR CHOICE > 2 THEN GOTO 1640
1660 IF CHOICE = 1 THEN GOSUB 7010 : REM MANUAL GAIN CHOICE
1670 IF CHOICE = 2 THEN GOSUB 8000 : REM AUTOSET GAIN
1680 PRINT"Gain has been set."
1690 REM
1700 REM -----
1710 REM Data Acquisition Program:
1720 REM -----
1730 REM
1740 LOOP2COUNT=1
1750 LOCATE 8,1
1760 OUT J6+1,0:OUT J6+2,1:OUT J6+2,0
1770 FOR I=0 TO 4000:NEXT:REM delay
1780 BEEP:CLS:PRINT "Type any key to start experiment":PRINT
1790 IF INKEY$="" THEN 1790:REM wait until any key is depressed
1800 TIMES$ = "0.00"
1810 CALL SCAN1 (CHCNT%,DATAARY%(0),CHARY%(0))
1820 PRINT : PRINT "Elapsed time (sec.):" TIMER
1830 REM
1840 REM -----
1850 REM Finished scan; calculate data values and print.
1860 REM -----
1870 REM
1880 OPEN FLNAME$+MID$(STR$(LOOP2COUNT),2)+".PRN"
      FOR OUTPUT AS #1
1890 INPUT "How many bubble columns were used
      in this run?"; BUB$
1900 PRINT #1, "THE NUMBER OF BUBBLE COLUMNS WAS", BUB$
1910 FOR I=0 TO CHCNT%
1920 GAIN%=CHARY%(I)/&H1000:IF GAIN%<0 THEN GAIN%=GAIN%+16
1930 IF (DATAARY%(I) AND &H3FFE)=&H3FFE
      THEN GOSUB 5050 :GOTO 2170

```

```

1940 IF DATAARY%(I) = &HC000 THEN GOSUB 5050 :GOTO 2170
1950 DATAARY%(I) = ((DATAARY%(I) AND &H7FF8)/8)
1960 SIGN = 1 : IF DATAARY%(I) <> (DATAARY%(I) AND &H7FF)
      THEN SIGN = -1
1970 DATAARY%(I) = (DATAARY%(I) AND &H7FF)
1980 REALARY(I) = (DATAARY%(I)/2^11*10.24/(2^GAIN%))*SIGN
1990 IF SIGN < 0 THEN REALARY(I) =
      SIGN*(10.24/2^GAIN%) - REALARY(I)
2000 REM
2010 REM Done: store channel # in temp and print out data:
2020 REM
2030 TEMP = CHARY%(I) AND &HFF
2040 PRINT "Channel " TEMP;:PRINT,
2050 PRINT USING "##.##";REALARY(I);:PRINT " gain = "; GAIN%
2060 ROW = INT( (I - 4) /10)+1
2070 COLUMN = I - ((ROW - 1) * 10 + 3)
2080 IF I < 4 GOTO 2110
2090 PRINT #1, "Ch.";TEMP,
2100 PRINT #1, USING "SEG. (## , ##), I = ";ROW,COLUMN;
2110 IF I = 0 THEN PRINT #1, "POTENTIAL E1 = ";
2120 IF I = 1 THEN PRINT #1, "CURRENT I1 (mA) = ";
2130 IF I = 2 THEN PRINT #1, "POTENTIAL E2 = ";
2140 IF I = 3 THEN PRINT #1, "TOTAL H2 CURRENT (I = 10uA) = ";
2150 PRINT #1, USING "-##.##";REALARY(I),
2160 PRINT #1, " Gain = "; GAIN%
2170 NEXT I
2180 CLOSE #1
2190 PRINT:PRINT
2200 PRINT "finishing scan # "; LOOP2COUNT
2210 LOOP2COUNT = LOOP2COUNT + 1
2220 INPUT "Do you want another loop (y/n) ";KY$
2230 IF (KY$="y") OR (KY$="Y") THEN CLS:GOTO 1750
2240 IF (KY$<>"n") AND (KY$<>"N") THEN GOTO 2220
2250 PRINT "Ending program"
3000 END
3010 REM -----
3020 REM End of main program
3030 REM -----
3040 REM
3050 REM -----
3060 REM SUBROUTINE 1: Adjusts amplitude of function generator
3070 REM -----
3080 REM
3090 IF RIGHT$(FUNCAMP$,2) = "VO" THEN SCALE = 1000
3100 IF RIGHT$(FUNCAMP$,2) = "MV" THEN SCALE = 1
3110 FUNCAMP = VAL(MID$(FUNCAMP$,3))*SCALE

```

```

3120 IF METER*10 > DI THEN NEWAMP=NEWAMP-5
3130 IF METER*10 < DI THEN NEWAMP=NEWAMP+5
3140 IF ABS(NEWAMP) >= 2000 THEN BEEP
      :LOCATE RUN1:PRINT "OVER 2 V":GOTO 3170
3150 AMP$="OF"+STR$(NEWAMP)+"MV"
3160 CALL IBWRT(FUNCGEN%,AMP$)
3170 FOR DELAY=1 TO 2000:NEXT
3180 RETURN
3190 REM
4000 REM -----
4010 REM INITIALIZATION SUBROUTINE -----
4020 REM -----
4030 REM
4040 PROFUNC$="FU0":CALL IBWRT(FUNCGEN%,PROFUNC$)
      :REM needs 1500 MS to complete
4050 RD$=SPACE$(56)
4060 AMP$="OF 0.0MV"
4070 IAM$="IOF":CALL IBWRT(FUNCGEN%,IAM$)
      :REM This has no real function
4080 CALL IBRD(FUNCGEN%,RD$)
      :REM This waits for last ibwrt to complete.
4090 CALL IBWRT(FUNCGEN%,AMP$)
4100 FOR I=1 TO 1600:NEXT
4110 CALL IBRD(VOLTMETER%,RD$)
4120 METER$=LEFT$(RD$,IBCNT%-2)
4130 METER=VAL(METER$)
4140 RETURN
5000 REM
5010 REM -----
5020 REM SATURATION BYPASS AND GAIN RESETTING SUBROUTINE
5030 REM -----
5040 REM
5050 IF (DATAARY%(I) AND &H8000) THEN SIGN$="-" ELSE SIGN$="+"
5060 T = CHARY%(I) AND &HFF
5070 PRINT "CHANNEL No.",T,"IS SATURATED";
      SIGN$;"GAIN WILL BE LOWERED."
5080 GAIN% = CHARY%(I)/&H1000
      : IF GAIN% < 0 THEN GAIN% = GAIN% + 16
5090 IF GAIN% > 0 THEN GAIN% = GAIN% - 1: GOTO 9010: RETURN
5100 IF NOT PASS1 THEN PASS1=1:GOTO 5120
5110 IF I=OLDI+1 THEN 5160 ELSE OLDI=I
5120 FOR J=I TO CHCNT%-1
5130 CHARY%(J)=CHARY%(J+1)
5140 NEXT J
5150 CHCNT%=CHCNT%-1
5160 RETURN

```



```
6000 REM
6010 REM -----
6020 REM SUBROUTINE: Enter specific channels to be read.
6030 REM -----
6040 REM
6050 INPUT"ENTER THE NUMBER OF MULTIPLEXER CHANNELS";CHCNT%
6060 IF CHCNT% <0 OR CHCNT% > 128
      THEN PRINT"OUT OF RANGE":GOTO 6050
6070 FOR I = 1 TO CHCNT%
6080 INPUT "ENTER CHANNEL NUMBER CHOICE";CHARY%(I)
6090 REM CORRECT CHANNEL NUMBER CHOICE
6100 CHARY%(I) = CHARY%(I) - 1
6110 NEXT I
6120 RETURN
7000 REM
7010 REM -----
7020 REM SUBROUTINE: Manual Choice of Gain ----
7030 REM -----
7040 REM
7050 INPUT "ENTER CHOICE OF GAIN";GAIN%
7060 FOR I = 1 TO CHCNT%
7070 GOSUB 9010 : REM SET GAIN
7080 NEXT I
7090 INPUT "DO YOU WANT A DIFFERENT GAIN FOR A
      SPECIFIC CHANNEL (Y/N)";TEMP$
7100 IF (TEMP$ <> "Y") OR (TEMP$ <> "y") THEN 7200
7110 INPUT "ENTER CHANNEL NUMBER";TEMP1
7120 REM CORRECT THE GAIN OF A SPECIFIC CHANNEL
7130 TEMP1 = TEMP1 - 1
7140 INPUT "ENTER CHOICE OF GAIN FOR THIS CHANNEL";GAIN%
7150 FOR I = 1 TO CHCNT%
7160 TEMP2 = CHARY%(I) AND &HFF
7170 IF TEMP2 = TEMP1 THEN GOSUB 9010 : REM SET GAIN
7180 NEXT I
7190 GOTO 7090
7200 RETURN
8000 REM
8010 REM -----
8020 REM SUBROUTINE AUTOSET THE GAIN -----
8030 REM -----
8040 REM
8050 REM -----
8060 REM set the gain by interacting with the system
8070 REM -----
8080 REM
8090 DEAD% = 0
```

```

8100 CHCNTTEMP% = 1
8110 CALL SCAN1 (CHCNT%,DATAARY%(0),CHARY%(0))
8120 FOR I = 1 TO CHCNT%
8130 CHARYTEMP%(1) = CHARY%(I)
8140 CALL SCAN1 (CHCNTTEMP%,DATAARY%(1),CHARYTEMP%(1))
8150 GAIN% = CHARY%(I)/&H1000
      :IF GAIN% < 0 THEN GAIN% = GAIN% +16
8160 REM change dataary% to mirror multiplexer output
8170 DATAARY%(1) = ((DATAARY%(1) AND &H7FF8)/8)
8180 SIGN = 1: IF DATAARY%(1) <> (DATAARY%(1) AND &H7FF)
      THEN SIGN = -1
8190 REM CHANGE DATAARY IF VALUE IS NEGATIVE
8200 TEMP2 = 0
8210 IF SIGN > 0 THEN 8280
8220 TEMP2 = 2^11-1
8230 FOR N=0 TO 10
8240 TEMP1% = INT(DATAARY%(1)/2^N)
8250 IF TEMP1% AND 1 THEN TEMP2 = TEMP2 - 2^N
8260 NEXT N
8270 DATAARY%(1) = TEMP2 : TEMP2 = 0
8280 REM FIND WHAT THE CORRECT GAIN SHOULD BE.
8290 FOR N = 0 TO 10
8300 TEMP1% = INT(DATAARY%(1)/2^N)
8310 IF TEMP1% AND 1 THEN TEMP2 = 0 ELSE TEMP2 = TEMP2 + 1
8320 NEXT N
8330 GAIN% = TEMP2
8340 IF GAIN% > 0 THEN GAIN% = GAIN% - 1
8350 IF GAIN% > 9 THEN PRINT "Warning!! Ch. ";
      CHARY%(I) AND &HFF; "is dead"
8360 IF GAIN% > 9 THEN DEAD% = DEAD% + 1
8370 GOSUB 9010 : REM SET GAIN
8380 NEXT I
8390 PRINT: PRINT "Number of dead segments: ", DEAD%
8400 FOR J=1 TO 2000: NEXT
8410 RETURN
9000 REM
9010 REM -----
9020 REM GAIN SETTING SUBROUTINE-----
9030 REM -----
9040 REM
9050 TEMP3=(&HFFF AND CHARY%(I))
9060 TEMP4=GAIN%*(16^3)+TEMP3
      :IF TEMP4 > 32767 THEN TEMP4 = TEMP4 - 65536!
9070 CHARY%(I) = TEMP4
9080 RETURN
9090 END:REM NEVER GET HERE!

```

LAWRENCE BERKELEY LABORATORY  
UNIVERSITY OF CALIFORNIA  
INFORMATION RESOURCES DEPARTMENT  
BERKELEY, CALIFORNIA 94720